Modelling Antarctic ice shelf, ocean, and sea ice interactions under present-day and future climate scenarios

Author:
Naughten, Kaitlin

Publication Date:
2018

DOI:
https://doi.org/10.26190/unsworks/20546

Modelling Antarctic ice shelf, ocean, and sea ice interactions under present-day and future climate scenarios

Kaitlin Naughten

A dissertation submitted in fulfilment
of the requirements for the degree of
Doctor of Philosophy

Climate Change Research Centre
ARC Centre of Excellence for Climate System Science
UNSW Sydney

14 May 2018

Supporting Publications and Presentations

The following publications and presentations have developed over the course of writing this thesis.

Publications

- Naughten, K.A., Galton-Fenzi, B.K., Meissner, K.J., England, M.H., Brassington, G.B., Colberg, F., Hattermann, T., and Debernard, J.B. (2017). Spurious sea ice formation caused by oscillatory ocean tracer advection schemes. *Ocean Modelling* 116:108-117, doi:10.1016/j.ocemod.2017.06.010.
- Naughten, K.A., Meissner, K.J., Galton-Fenzi, B.K., England, M.H., Timmermann, R., Hellmer, H.H., Hattermann, T., and Debernard, J.B. (2018). Intercomparison of Antarctic ice-shelf, ocean, and sea-ice interactions simulated by MetROMS-iceshelf and FESOM 1.4. *Geoscientific Model Development* 11:1257-1292, doi:10.5194/gmd-11-1257-2018.
- Naughten, K.A., Meissner, K.J., Galton-Fenzi, B.K., England, M.H., Timmermann, R., and Hellmer, H.H. (2018). Future projections of Antarctic ice shelf melting based on CMIP5 scenarios. *Journal of Climate*, in press, doi:10.1175/JCLI-D-17-0854.1.

Presentations

Please note my previous surname Alexander.

- Poster presentation - Alexander, K.A., Meissner, K.J., Galton-Fenzi, B.K., and England, M.H. *Projections of ice shelf basal melting and sub-ice shelf*

circulation changes in a warming climate. IGS International Symposium on Contemporary Ice-Sheet Dynamics, Cambridge, UK (August 2015)

- Poster presentation - Alexander, K.A., Galton-Fenzi, B.K., Meissner, K.J., England, M.H., Hattermann, T., Debernard, J.B., Hellmer, H.H., Timmermann, T., and Sein, D. *A new circumpolar model of ice-shelf/ ocean/sea-ice interaction.* IGS International Symposium on Interactions of Ice Sheets and Glaciers with the Ocean, La Jolla, USA (July 2016)

- Oral presentation - Alexander, K.A., Galton-Fenzi, B.K., Meissner, K.J., England, M.H., Hattermann, T., and Debernard, J.B. *Interesting bugs I have had with MetROMS and how I fixed them.* ROMS Asia-Pacific Workshop, Hobart, TAS (October 2016)

- Poster presentation - Alexander, K.A., Meissner, K.J., Galton-Fenzi, B.K., and England, M.H. *Spurious sea ice formation caused by oscillatory advection schemes in an S-coordinate ocean model.* ARCCSS Annual Workshop, Lorne, VIC (November 2016)

- Oral presentation - Naughten, K.A., Meissner, K.J., Galton-Fenzi, B.K., England, M.H., Hellmer, H.H., Timmermann, R., Nakayama, Y., Debernard, J.B., and Hattermann, T. *Intercomparison of two ice-shelf/ ocean/sea-ice models on a circumpolar Antarctic domain.* IGS/IACS/ CliC International Symposium on the Cryosphere in a Changing Climate, Wellington, New Zealand (February 2017)

- Oral presentation - Naughten, K.A., Meissner, K.J., Galton-Fenzi, B.K., England, M.H., Hattermann, T., Debernard, J.B., Brassington, G.B., Colberg, F., Timmermann, R., Hellmer, H.H., and Nakayama, Y. *Simulation of ocean/sea-ice/ice-shelf interactions with MetROMS and FESOM.* COSIMA Workshop, Sydney, NSW (May 2017)

- Oral presentation - Naughten, K.A., Meissner, K.J., Galton-Fenzi, B.K., England, M.H., Timmermann, R., Hellmer, H.H., Hattermann, T., and Debernard, J.B. *Intercomparison of Southern Ocean, sea ice, and ice shelf interactions simulated by two models.* ARCCSS Annual Workshop, Canberra, ACT (October 2017)

- Poster presentation - Naughten, K.A., Meissner, K.J., Galton-Fenzi, B.K., Timmermann, R., and Hellmer, H.H. *Future projections of Antarctic ice shelf melting.* ARCCSS Annual Workshop, Canberra, ACT (October 2017)

- Oral presentation - Naughten, K.A., Meissner, K.J., Galton-Fenzi, B.K., England, M.H., Timmermann, R., Hellmer, H.H., Hattermann, T., and Debern-

ard, J.B. *Intercomparison of Antarctic ice shelf, ocean, and sea ice interactions simulated by two models.* AMOS-ICSHMO, Sydney, NSW (February 2018)

- Oral presentation - Naughten, K.A., Meissner, K.J., Galton-Fenzi, B.K., Timmermann, R., and Hellmer, H.H. *Future projections of Antarctic ice shelf melting based on CMIP5 scenarios.* AMOS-ICSHMO, Sydney, NSW (February 2018)

Acknowledgements

Every PhD student has a supervisor, but very few are lucky enough to have a supervisor like Katrin Meissner. Since the day we started working together, Katrin has been the most incredible mentor. She has guided me through every facet of academic life, and has helped me build confidence, experience, and perspective. One of my greatest hopes for my career is that I can be the kind of supervisor, for my own future students, that Katrin has been for me.

When I started my PhD, all I knew was that I wanted to study "something about ice shelves". The fact that my project matured so far beyond that point is due in large part to Ben Galton-Fenzi. Ben's enthusiasm, expertise, and knack for project design compelled me to become his student soon after my first visit to Hobart. He connected me with models, observations, and researchers from around the world, which has shaped not only my PhD but also the rest of my career. Our lively conversations about the philosophy of debugging and the future of ice-shelf/ocean modelling have made me sure that science is what I want to do for the rest of my life.

As with any model development project, my PhD involved a lot of twists and turns, dead ends, and days (or weeks) of feeling absolutely stuck. At these times, it was invariably helpful to seek the advice of my final supervisor, Matthew England. Matt seems to have an instinctive sense of how to approach scientific challenges, due to his years of experience with physical oceanography and coupled modelling. For this reason, conversations with Matt never failed to point me in the right direction, and I believe my PhD would have taken much longer without his support. I am also grateful to Matt for his excellent written feedback, his advice regarding experimental design, and for getting me started in ocean swimming.

Several external collaborators also played instrumental roles in this project. Ralph Timmermann and Hartmut Hellmer hosted my visit to the Alfred Wegener Institut, introduced me to FESOM, and continued to provide advice and guidance throughout the rest of the project. Ralph went above and beyond during the last 6 months of my PhD, providing extensive and thorough advice on FESOM meshes and paper

revisions. Next, Tore Hattermann perhaps shaped my PhD more than anyone else when I happened to sit beside him at a conference and he told me about MetROMS. Since then, Tore has been a valued collaborator and a reliable co-author. I'd also like to thank the rest of the MetROMS master development team, particularly Jens Debernard, for undertaking this coupling project and for allowing me to jump on board.

Other members of the Antarctic modelling community generously offered advice during the MetROMS development process, including Michael Dinniman, Paul Holland, Petra Heil, Elizabeth Hunke, Matthew Mazloff, and Xylar Asay-Davis. I learned a lot from these discussions and I feel very lucky to have made so many contacts in the community.

A number of other colleagues have helped to make this thesis a reality. Gary Brassington and Frank Colberg provided the upwind limiters code used in Chapter 4, as well as advice regarding its implementation. Nicholas Hannah offered his unmatched computing expertise whenever I had a particularly difficult bug in parallel processing. Assistance with FESOM configuration and mesh generation was provided by Yoshihiro Nakayama, Dmitry Sein, Marta Kasper, and Lukrecia Stulic. In Chapter 2, Jean-Baptiste Salle, Violaine Pellichero, and Takeshi Tamura provided observational datasets for model comparison. Ariaan Purich shared her analysis of sea ice trends in CMIP5 projections. Willem Huiskamp assisted with the formatting of this thesis. Finally, Xylar Asay-Davis, John Klinck, and five anonymous reviewers provided helpful comments on the three publications resulting from this project.

This PhD was funded by an Australian Government scholarship under the Australian Postgraduate Award and Research Training Program schemes. The scholarship was supplemented by a UNSW Research Excellence Award and by the Climate Change Research Centre at UNSW. The Australian Research Council's Centre of Excellence for Climate System Science (ARCCSS) and the Antarctic Climate & Ecosystems Cooperative Research Centre (ACE CRC) provided travel funding and professional development opportunities. Travel funding was also provided by Katrin Meissner. None of this research would have been possible without the computing resources awarded to us by the National Computational Infrastructure (NCI) through the Merit Allocation Scheme, the Intersect allocation scheme, and the UNSW HPC at NCI Scheme.

Now, the non-science-related thank yous.

I'd like to thank my family for their support from across the ocean. To my mum, Sheila Pursey, whose good wishes I could feel every single day of my PhD. To my sister Helen Alexander, for our conversations about academia that helped me

make decisions about my future. And to my sisters Megan MacCormack and Ailsa Desender, for our conversations about everything-but-academia, because sometimes I just needed to get my mind off of work.

I made so many friends during my PhD, probably more friends than I've had at any other stage of my life. Now that we are all scattered around the world I am so excited to meet up with you during conferences and holidays for many years to come. I would like to thank the entire CCRC for building such a positive work environment, and lively social scene, in which I could thrive. A few friends in particular deserve special mention. Shannon Bengtson was a marvellous companion during the last year of my PhD, and kept my spirits up everywhere from the CCRC to the running trail to the emergency room. Zoë Thomas was a close friend from the beginning, and the time we spent hanging out together was always a highlight of the week. My deepest gratitude goes to Ariaan Purich for her unending support, advice, and encouragement, and for many trips out to the meadow[1]. And of course to Willem Huiskamp, my Brother in Science, for a lifelong friendship forged in swimming, tea breaks, bird photography, commiseration, and comic relief.

To Kevin, with all my love, very much and always.

> We know this world is good enough
> because it has to be.
> Allow the hope that we will meet
> again out in the winter wheat.
> — John K. Samson

[1] John Green (2017), Turtles All the Way Down, Penguin Australia, page 208.

Abstract

This thesis uses two ocean/sea-ice/ice-shelf models to advance our understanding of physical processes in Antarctic ice shelf cavities and over the surrounding continental shelf, and to project how these environments may change in the future. A new circumpolar Antarctic configuration of the MetROMS model (ROMS: Regional Ocean Modelling System coupled to CICE: Community Ice CodE) is developed, and is compared to the Finite Element Sea-ice/ice-shelf Ocean Model (FESOM). Future projections of ice shelf basal melt rates through the 21st century are also produced using FESOM.

Both models exhibit reasonable agreement with available observations, but share many of the same biases, such as an underestimation of ice shelf melt rates in the Amundsen and Bellingshausen Seas, insufficient summer sea ice cover, and weakening transport of the Antarctic Circumpolar Current. The major limitations on model performance appear to be (i) excessive smoothing of the topography in FESOM, which is necessary to ensure numerical stability; (ii) spurious diapycnal mixing inherent in the terrain-following coordinates of MetROMS; and (iii) potential biases in the atmospheric reanalysis used to force the models.

The development process of the new MetROMS configuration is chronicled, and particular attention is given to a mechanism of numerical error that was found to be producing excessive sea ice. In particular, oscillatory ocean tracer advection schemes cause spurious supercooling and consequently sea ice formation, leading to a range of dynamic and thermodynamic impacts which degrade the simulation. Careful choice of advection schemes, increased parameterised diffusion, or the application of flux limiters can avoid this problem.

Future projections with FESOM, under four 21st-century atmospheric forcing scenarios, all exhibit increased ice shelf basal melting in every sector of Antarctica. Total ice shelf basal mass loss from the continent increases by between 41% and 129%. The main mechanism of melting is an increased presence of warm Circumpolar Deep Water, which is better preserved on the continental shelf due to reduced convection, primarily from weakened sea ice formation. Other projections include freshening of

High Salinity Shelf Water, weakening of the Antarctic Circumpolar Current, and a reduction in winter sea ice extent.

Contents

List of Figures

List of Tables

List of Abbreviations

AABW	Antarctic Bottom Water
AAIW	Antarctic Intermediate Water
AASW	Antarctic Surface Water
ACC	Antarctic Circumpolar Current
ACCESS	Australian Community Climate and Earth-System Simulator
AIS	Antarctic Ice Sheet
BRIOS	Bremerhaven Regional Ice-Ocean Simulations
cDrake	Dynamics and Transport of the Antarctic Circumpolar Current in Drake Passage
CDW	Circumpolar Deep Water
CICE	Community Ice CodE
CMIP5	Coupled Model Intercomparison Project phase 5
COARE	Coupled-Ocean Atmosphere Response Experiment
CROCO	Coastal and Regional Ocean COmmunity model
DJF	Southern Hemisphere summer (December, January, February)
DSW	Dense Shelf Water
EAP	Elastic-Anisotropic-Plastic
ECHAM5	ECMWF HAMburg model version 5
EVP	Elastic-Viscous-Plastic
FESOM	Finite Element Sea-ice/ice-shelf Ocean Model
FRIS	Filchner-Ronne Ice Shelf
GCM	General Circulation Model
GM	Gent-McWilliams parameterisation
HadCM3	Hadley Centre Coupled Model version 3
HadGEM2	Hadley Centre Global Environment Model version 2
HCf	Heat content relative to the in-situ freezing point
HSIMT	High-order Spatial Interpolation at the Middle Temporal level
HSSW	High Salinity Shelf Water
ISOMIP	Ice Shelf-Ocean Model Intercomparison Project
ISW	Ice Shelf Water

JJA	Southern Hemisphere winter (June, July, August)
KPP	K-Profile Parameterisation
LSSW	Low Salinity Shelf Water
MAM	Southern Hemisphere autumn (March, April, May)
MCDW	Modified Circumpolar Deep Water
MCT	Model Coupling Toolkit
MetROMS	Norwegian Meteorological Institute (MetNO) branch of ROMS
MIP	Model Intercomparison Project
MISOMIP	Marine Ice Sheet-Ocean Model Intercomparison Project
MMM	Multi-model mean
MPDATA	Multidimensional Positive Definite Advection Transport Algorithm
MPI	Message Passing Interface
NADW	North Atlantic Deep Water
NSIDC	National Snow and Ice Data Centre
OMIP	Ocean Model Intercomparison Project
POP	Parallel Ocean Program
RACMO	Regional Atmospheric Climate MOdel
RCP	Representative Concentration Pathway
RIMBAY	Revised Ice Model Based on frAnk pattYn
rms	root-mean-squared
ROMS	Regional Ocean Modelling System
RSBW	Ross Sea Bottom Water
RSUP3	Rotated Split UPstream 3rd order
RTopo	Refined Topography data set
SON	Southern Hemisphere spring (September, October, November)
WOCE	World Ocean Circulation Experiment
WSBW	Weddell Sea Bottom Water

List of Symbols

A_U	amplitude of zonal tidal transport
A_V	amplitude of meridional tidal transport
c_{pw}	specific heat of seawater
C	concentration of tracer at grid box face
C_d	drag coefficient at ice shelf base
D	reference boundary layer depth in ice shelf cavity
f	Coriolis parameter
h	bathymetry
n	tidal component
P^*	sea ice strength coefficient
Pr	Prandtl number
r	slope parameter measuring steepness of topography
S	salinity
Sc	Schmidt number
T	temperature
T_f	surface freezing point
T_{if}	in-situ freezing point
u	zonal velocity
u_{tide}	RMS tidal velocity
u^*	friction velocity at ice shelf base
u^*_{min}	lower bound for u^* representing molecular diffusion
v	meridional velocity
V	volume
z	depth
z_{ice}	ice shelf draft
α	clipping parameter for upwind flux limiters
γ_S	salt exchange coefficient at ice shelf base
γ_T	heat exchange coefficient at ice shelf base
κ	turbulence term at ice shelf base
ν	kinematic viscosity

ρ density

Chapter 1

Introduction

1.1 The role of ice shelves

Sea level rise is perhaps one of the most troubling repercussions of modern climate change. Just a few metres of global sea level rise could inundate many of the world's major coastal cities and entire island nations, possibly forcing their abandonment. While mass loss from the Antarctic Ice Sheet (AIS) currently makes up a relatively small fraction of observed sea level rise (*Church et al.*, 2013), we can expect this contribution to continue to increase. Part of the evidence for this comes from paleoclimate warming events, which show that sea level rise was dominated by ice sheet mass loss (*Deconto and Pollard*, 2016; *Dutton et al.*, 2015). This situation is concerning because the AIS has enormous sea level rise potential: if the entire ice sheet disintegrated, global sea level would rise by 58 m (*Fretwell et al.*, 2013).

Ice shelves exist on the edges of the AIS, and are fed by glaciers flowing out from the interior of Antarctica. Rather than resting on bedrock, ice shelves extend out from the continent to float on the ocean surface. For this reason, removing an ice shelf through melting or calving does not directly contribute to sea level rise. However, ice shelves hold back the rest of the ice sheet, slowing down its flow in what is known as the buttressing effect. Removing an ice shelf can cause the source glaciers to accelerate, which contributes to the negative mass balance of Antarctica (*Rignot et al.*, 2011; *Zwally and Giovinetto*, 2011) and ultimately global sea level rise. Indeed, glaciers on the Antarctic Peninsula thinned and accelerated following the collapse of the Larsen B Ice Shelf in 2002 (*Rignot et al.*, 2004; *Scambos et al.*, 2004).

Through the buttressing effect, ice shelves play a vital role in stabilising the AIS. Unfortunately, ice shelves are also the parts of the AIS that are most at risk, because

they are the only parts of the ice sheet in contact with the ocean. A warming ocean is more effective than a warming atmosphere at melting Antarctic ice, due to its high heat capacity as well as its warmer temperatures in this region. Additionally, a warming ocean is threatening because over 40% of the AIS (by area) rests on bedrock that is below sea level (*Fretwell et al.*, 2013) (Figure 1.1). This provides the potential for seawater to melt its way beneath these regions of the ice sheet, unpinning ice from the bedrock and melting it from the bottom up.

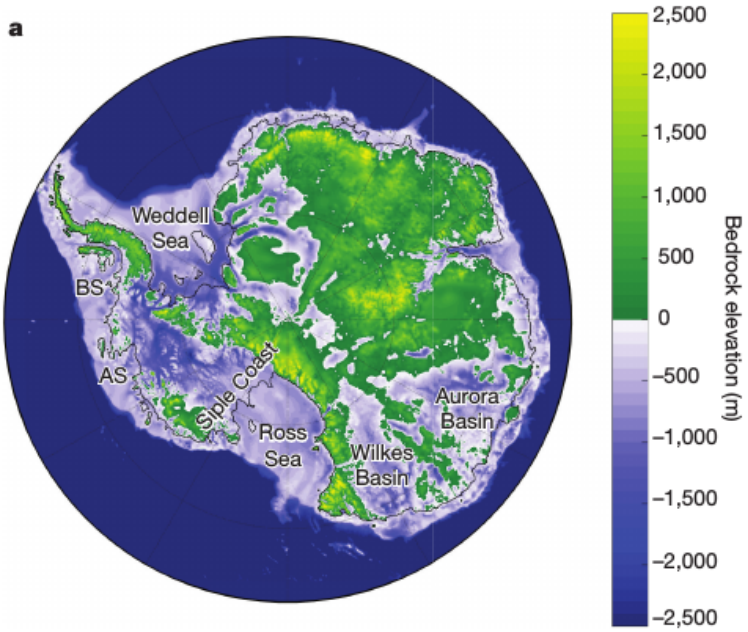

Figure 1.1: Elevation of bedrock (m) underlying AIS and the surrounding ocean. Regions below sea level (negative elevation) are shades of blue. Reproduced from Figure 1a of *Deconto and Pollard* (2016).

The effects of climate change on ice shelf basal melting are already becoming apparent. Satellite observations by *Paolo et al.* (2015) indicate that ice shelf volume loss is accelerating (Figure 1.2), driven by a combination of increased basal melting and increased strain rates from faster-flowing glaciers. *Pritchard et al.* (2012) find evidence of thinning for 20 of 54 Antarctic ice shelves, and attribute this thinning to basal melting. Given these changes, and their implications for AIS stability, it is clear that a better understanding of processes on the Antarctic continental shelf and beneath ice shelves is vital to constrain estimates of future sea level rise.

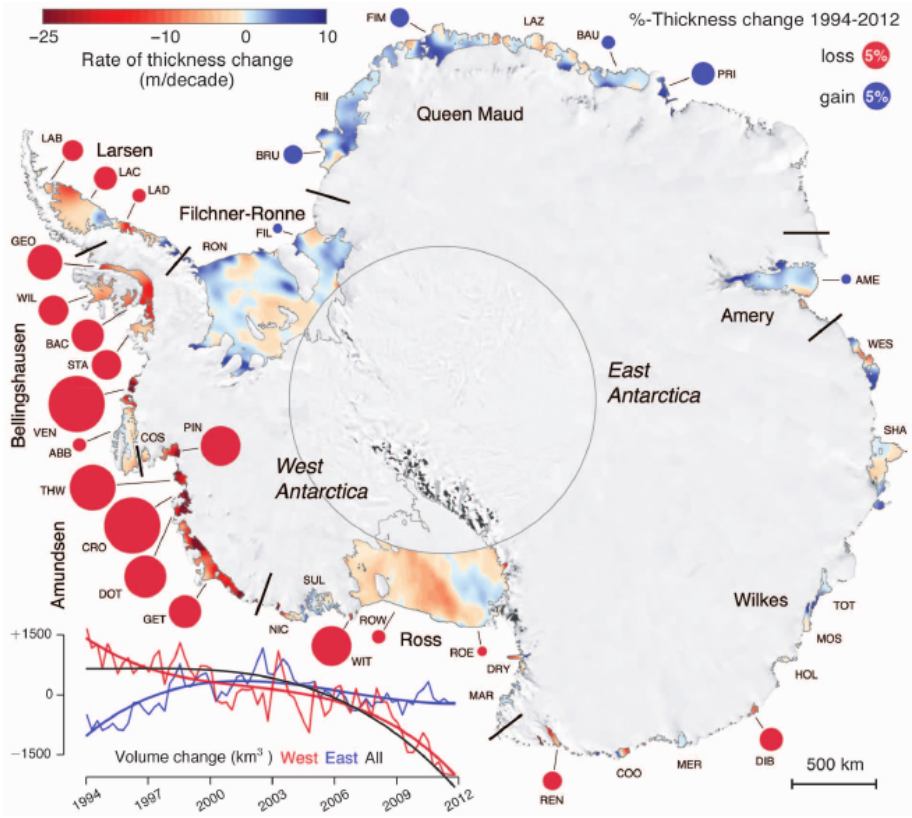

Figure 1.2: Ice shelf volume loss from 1994 to 2012, reproduced from Figure 1 of *Paolo et al.* (2015). Red and blue shading on the ice shelves shows the regional rates of thickness change in m/decade. Red and blue circles show the percentage change in thickness over the 18-year period, integrated over individual ice shelves. Red circles indicate ice loss, blue circles indicate ice gain, and the area of each circle is scaled by the magnitude of the change. The timeseries in the bottom left shows total volume change in km^3 for all West Antarctic (red) and East Antarctic (blue) ice shelves, with the polynomial fits overlaid. The polynomial fit for all ice shelves is also shown in black.

1.2 Cavity and continental shelf processes

An ice shelf cavity (Figure 1.3) is a region of the ocean between an ice shelf and the seafloor, bounded laterally by the ice shelf front (where the outflowing glacier calves into icebergs) and the grounding line (where the ice sheet detaches from the bedrock). Some of the water masses and circulation patterns in ice shelf cavities are influenced by sea ice processes. The residual seawater from sea ice formation, salinized through brine rejection and with temperature near the surface freezing point, is known as High Salinity Shelf Water (HSSW) or Low Salinity Shelf Water (LSSW) depending on the magnitude of the brine rejection. It sinks due to its density, and may circulate into an ice shelf cavity. Since the freezing point of seawater decreases with depth, sinking HSSW or LSSW becomes warmer than the in-situ freezing point, and will cause melting if it comes into contact with the ice shelf base. The resulting

meltwater is called Ice Shelf Water (ISW), with temperature near the in-situ freezing point. As it is largely fresh, ISW rises in a plume along the sloping ice shelf base. As it rises it may become supercooled and form frazil ice, which accretes on the ice shelf base and forms marine ice.

This circulation pattern - HSSW or LSSW causing melting and ISW refreezing - is known as the ice pump (*Lewis and Perkin*, 1986), and was also termed "Mode 1 melting" by *Jacobs et al.* (1992). It is driven by the pressure dependence of the freezing temperature of seawater, and redistributes ice from deep water to shallower water. If there was no glacial flow from the continent, the ice shelf base would eventually become completely horizontal. In reality, the non-zero flow of the source glacier allows the ice shelf to maintain its sloped base.

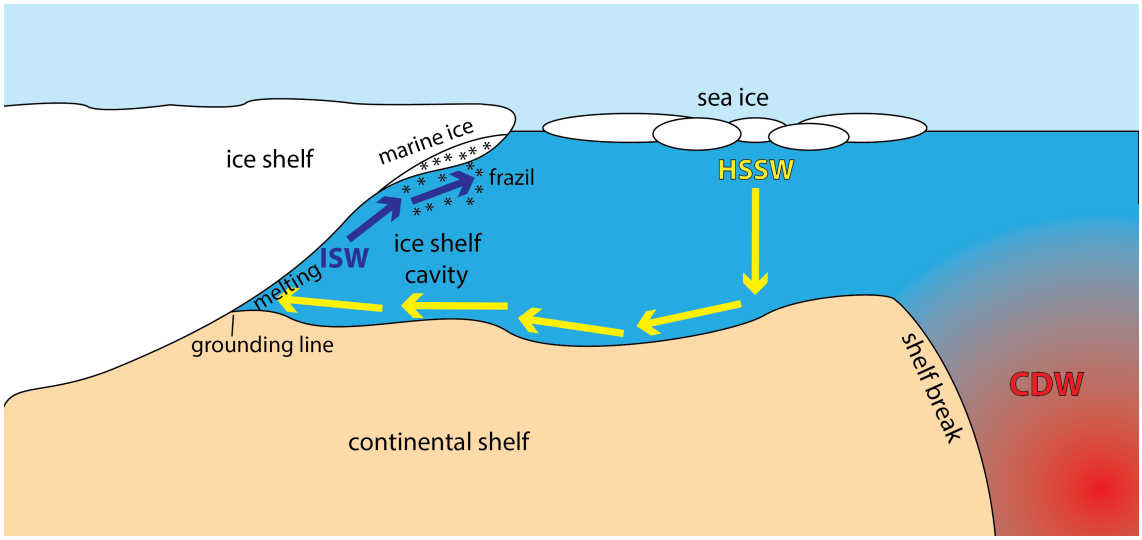

Figure 1.3: Illustration of some of the processes described in this section. High Salinity Shelf Water (HSSW) forms as the result of sea ice production, then sinks and travels into an ice shelf cavity (yellow arrows). When HSSW comes into contact with the ice shelf base, it causes melting. The result is Ice Shelf Water (ISW), which rises along the ice shelf base (blue arrows) and then supercools, forming frazil and ultimately marine ice. Circumpolar Deep Water (CDW) is also shown offshore, and its relative warmth is indicated by red shading.

The absence of sea ice can also cause ice shelf melting, as it exposes the ocean surface to solar heating. This fresh, sun-warmed surface layer is called Antarctic Surface Water (AASW), and it may subduct into ice shelf cavities and/or laterally melt the ice shelf front, a process known as "Mode 3 melting" (*Jacobs et al.*, 1992).

Finally, intrusions of warm Circumpolar Deep Water (CDW, $> 0°C$) into ice shelf cavities can drive intense basal melting, termed "Mode 2 melting" by *Jacobs et al.* (1992). CDW is formed as deep water in the North Atlantic, travels southward, and upwells to intermediate depths in the Southern Ocean. Transport of CDW onto the continental shelf is the result of multiple processes, including eddies (*Stewart and Thompson*, 2015), tidal mixing (*Wang et al.*, 2013), and barotropic Kelvin waves

(*Spence et al.*, 2017). Direct intrusions of CDW are also possible in some regions, depending on bathymetry. For example, a series of troughs across the continental shelf break of the Amundsen Sea provides channels for CDW to regularly access ice shelf cavities in the region (*Assmann et al.*, 2003; *Thoma et al.*, 2008). Since CDW gains its properties from North Atlantic surface waters and takes 500-1000 years to reach the Southern Ocean (*Sallée et al.*, 2013a), warming of CDW due to climate change is not expected in the near future. However, wind-driven changes in the water mass structure of the Southern Ocean could lead to shoaling of the CDW temperature maximum, bringing it closer to the continental shelf (*Spence et al.*, 2014). These changes have already been observed in the Amundsen and Bellingshausen Seas (*Schmidtko et al.*, 2014). Furthermore, weakened sea ice formation and the associated reduced convection could favour more direct transport of CDW onto the continental shelf (*Timmermann and Hellmer*, 2013).

Processes on the Antarctic continental shelf have important consequences for the ventilation of oceans worldwide by deep water masses. Dense Shelf Water (DSW) is salinized by a combination of sea ice formation (HSSW) and marine ice formation (refreezing ISW) (*Ohshima et al.*, 2013). This water mass is exported from the continental shelf and ultimately forms Antarctic Bottom Water (AABW), which travels into the abyssal plains of every ocean basin (*Kusahara and Hasumi*, 2014).

1.3 Ice-shelf/ocean/sea-ice modelling

Antarctica is perhaps the very definition of "remote", and conditions there are extreme, posing major challenges for the manual collection of observations (*Rintoul et al.*, 2010). Semi-automated observing networks, such as Argo floats (*Roemmich et al.*, 2009), have historically been unable to withstand the crushing force of sea ice. Modern Argo floats are more resilient, but the number of measurements beneath sea ice is still limited. Some measurements are also collected by tagged seals which dive beneath sea ice (*Roquet et al.*, 2013). This dataset is promising, but is not yet seasonally or spatially comprehensive, and does not extend beneath ice shelves. Remote sensing techniques can provide some information, such as sea ice concentration (*Fetterrer et al.*, 2017) or inferred ice shelf basal melt rates (*Rignot et al.*, 2013), but their scope is still limited. Key processes such as sub-ice shelf circulation, DSW export, and CDW intrusions remain almost entirely unmonitored.

For these reasons, numerical modelling has a critical role to play in improving our understanding of the Antarctic continental shelf and ice shelf cavities. Models provide information which complements observations at a fraction of the cost, and their

output can be used to guide priorities for future observations. Furthermore, models have the ability to project future changes in the system, and to estimate its sensitivity to a changing climate.

Numerical modelling of ocean/ice-shelf interaction traces back to the 1980s, with the two-dimensional model of *Hellmer and Olbers* (1989). Their pioneering work was later refined by *Holland and Jenkins* (1999) into what is known as the "three-equation parameterisation" of the heat flux, salt flux, and in-situ freezing point at a given ice-shelf/ocean interface. In the years since, this parameterisation has been adapted into numerous three-dimensional ocean models, both regional and global, and with both interactive and prescribed sea ice (*Dinniman et al.*, 2016).

These models typically assume a static ice shelf geometry. Rates of melting and refreezing at the ice shelf base are calculated, but not actually applied to the ice draft. Instead, it is assumed that any changes in ice thickness from melting and refreezing are exactly offset by glacial dynamics and surface accumulation. The alternative is to couple with an ice sheet model, a particularly challenging task given the very different timescales involved in ocean and ice sheet processes, and the potential for spurious grounding line instabilities. Ice-sheet/ocean coupling is an emerging field, and active model development is underway at numerous institutions (*Asay-Davis et al.*, 2016). So far, the only published ice-sheet/ocean models involve regional (*Timmermann and Goeller*, 2017) or idealised (e.g., *De Rydt and Gudmundsson*, 2016; *Jordan et al.*, 2017) configurations.

1.4 Aims of thesis

This thesis makes use of two ocean/sea-ice models, both including static ice shelves, and forced with a prescribed atmospheric state. MetROMS consists of the regional ocean model ROMS (Regional Ocean Modelling System) (*Shchepetkin and McWilliams*, 2005) coupled to the sea ice model CICE (Community Ice CodE) (*Hunke et al.*, 2015), for which a circumpolar Antarctic configuration has been newly developed as part of this thesis. FESOM (Finite Element Sea-ice/ice-shelf Ocean Model) (*Wang et al.*, 2014; *Danilov et al.*, 2015; *Timmermann et al.*, 2012) is a global ocean/sea-ice model with an unstructured mesh allowing spatially varying resolution.

The aims of this thesis are threefold:

1. **To develop a new circumpolar Antarctic configuration of ROMS including interactive sea ice.** Previous ice-shelf/ocean simulations with ROMS did not include sea ice, and instead represented its effects with pre-

scribed surface fluxes of heat, salt, and momentum (*Galton-Fenzi et al.*, 2012; *Cougnon et al.*, 2013; *Gwyther et al.*, 2014). These configurations also featured much smaller regional domains, encompassing several ice shelves at most. Alternatively, the configuration of *Dinniman et al.* (2015) has a circumpolar Antarctic domain with ice shelves and includes the sea ice model of *Budgell* (2005). However, given the numerous advantages of CICE, including a more sophisticated representation of sea ice processes, a larger user base, and the ability to run on separate processors to ROMS, it was decided that pursuing a parallel effort to *Dinniman et al.* was warranted.

2. **To conduct a comprehensive intercomparison of MetROMS and FESOM on a realistic circumpolar Antarctic domain.** Model intercomparison projects (MIPs) provide valuable opportunities to benchmark models, identify areas of relative strengths and weaknesses, and guide future development. In the ice-shelf/ocean modelling community, intercomparison has so far been limited to idealised domains without interactive sea ice (*Hunter*, 2006; *Asay-Davis et al.*, 2016). An intercomparison project which systematically examines every region of the Antarctic continental shelf is therefore of great value to the community.

3. **To produce future projections of ice shelf melt rates using carefully selected and bias-corrected CMIP5 atmospheric forcing.** As articulated in Section 1.1, a major motivation behind ice-shelf/ocean modelling is to better predict future sea level rise. Projections of 21st-century changes in ice shelf melt rates and sub-ice shelf processes are an essential step towards this goal. However, the only published projections to date were forced with uncorrected output from CMIP3 (Coupled Model Intercomparison Project phase 3) models, and focused on the southern Weddell Sea (*Hellmer et al.*, 2012; *Timmermann and Hellmer*, 2013; *Hellmer et al.*, 2017; *Timmermann and Goeller*, 2017). This thesis aims to produce new simulations using the most recent generation of CMIP projections, accounting for mean-state CMIP biases, and examining the entire Antarctic continental shelf.

The remainder of this thesis is organised as follows:

- Chapter 2 presents an intercomparison of ice shelf, ocean, and sea ice interactions in MetROMS and FESOM. Here the two models are described and their architectures and design choices are compared. The period 1992-2016 is simulated by MetROMS and by two configurations of FESOM which differ only in resolution. Sub-ice shelf processes in eight regions of the Antarctic coastline are compared between these three simulations, as well as water mass properties

on the continental shelf, sea ice conditions, and large-scale Southern Ocean circulation and drift. The model output is evaluated against observations where they are available. This chapter has been published in *Geoscientific Model Development* (*Naughten et al.*, 2018).

- Chapter 3 chronicles the development pathway MetROMS took to reach its final configuration in Chapter 2, and the challenges faced along the way. This is presented as a series of case studies, describing model defects and biases and how they were diagnosed and overcome. Sensitivity studies are performed which recreate the original problems and isolate their effects. One case study is also presented for FESOM. Issues which persist in MetROMS are analysed, and options for future development are discussed.

- Chapter 4 expands on one of the case studies mentioned in Chapter 3: namely, the undesirable effects of oscillatory ocean tracer advection schemes on coupled sea ice models. When oscillatory advection errors cause the near-surface ocean temperature to drop below the freezing point, sea ice forms. The dynamic and thermodynamic impacts of this spurious sea ice are analysed in MetROMS simulations. The susceptibility of different advection schemes to this problem is assessed, and flux limiters are introduced to remove dispersive error from one advection scheme. This chapter has been published in *Ocean Modelling* (*Naughten et al.*, 2017).

- Chapter 5 applies the high-resolution FESOM configuration from Chapter 2 to the question of future ice shelf melt rates. A suite of four 21st-century atmospheric forcing scenarios is created, by selecting the CMIP5 models in best agreement with historical atmospheric reanalyses over the Southern Ocean, and linearly bias-correcting their output for two different RCP (Representative Concentration Pathway) scenarios. The products are used to force FESOM simulations, and the resulting projections of ice shelf melt rates, water mass properties, Southern Ocean circulation, and sea ice formation and melt are analysed. A parallel control simulation with repeated historical forcing is also presented to assess model drift. This chapter has been accepted at *Journal of Climate*.

- Finally, Chapter 6 summarises the results of this thesis and presents ideas for future work.

Note that Chapters 2, 4, and 5 are designed to be standalone manuscripts suitable for publication, and have been only slightly modified from their published or accepted state, as detailed in the chapter preambles. Some repetition is therefore inherent in the motivation and model description sections. All references have been consolidated

in a single bibliography at the end of this thesis.

Chapter 2

Intercomparison of Antarctic ice shelf, ocean, and sea ice interactions simulated by MetROMS-iceshelf and FESOM 1.4

Preamble

This chapter is based on the paper "Intercomparison of Antarctic ice-shelf, ocean, and sea-ice interactions simulated by MetROMS-iceshelf and FESOM 1.4" by Kaitlin A. Naughten, Katrin J. Meissner, Benjamin K. Galton-Fenzi, Matthew H. England, Ralph Timmermann, Hartmut H. Hellmer, Tore Hattermann, and Jens B. Debernard, which was published in *Geoscientific Model Development* in April 2018. I have secured copyright permission to reproduce the publication within this thesis. Compared to the published paper, the version reproduced here has several minor additions and clarifications, including the addition of Figure 2.2 and Section 2.4.1.5. None of these changes affect the main conclusions of the study. Cross-references to other thesis chapters have also been added.

Despite the extensive author list, I completed the majority of the work for this publication: installing and configuring the models, designing and running simulations, analysing results, and writing the paper. My supervisors Katrin Meissner, Ben Galton-Fenzi, and Matthew England gave me advice throughout the process. Ben Galton-Fenzi also provided the ROMS ice shelf code. Ralph Timmermann

and Hartmut Hellmer provided the FESOM code, and Ralph Timmermann also answered questions about the design of FESOM. Tore Hattermann and Jens Debernard provided the MetROMS coupling code. All co-authors provided comments on the manuscript.

Abstract

An increasing number of Southern Ocean models now include Antarctic ice shelf cavities, and simulate thermodynamics at the ice-shelf/ocean interface. This adds another level of complexity to Southern Ocean simulations, as ice shelves interact directly with the ocean and indirectly with sea ice. Here we present the first model intercomparison and evaluation of present-day ocean/sea-ice/ice-shelf interactions, as simulated by two models: a circumpolar Antarctic configuration of MetROMS (ROMS: Regional Ocean Modelling System coupled to CICE: Community Ice CodE) and the global model FESOM (Finite Element Sea-ice/ice-shelf Ocean Model), where the latter is run at two different levels of horizontal resolution. From a circumpolar Antarctic perspective, we compare and evaluate simulated ice shelf basal melting and sub-ice shelf circulation, as well as sea ice properties and Southern Ocean water mass characteristics as they influence the sub-ice shelf processes. Despite their differing numerical methods, the two models produce broadly similar results, and share similar biases in many cases. Both models reproduce many key features of observations, but struggle to reproduce others, such as the high melt rates observed in the small warm-cavity ice shelves of the Amundsen and Bellingshausen Seas. Several differences in model design show a particular influence on the simulations. For example, FESOM's greater topographic smoothing can alter the geometry of some ice shelf cavities enough to affect their melt rates; this improves at higher resolution, since less smoothing is required. In the interior Southern Ocean, the vertical coordinate system affects the degree of water mass erosion due to spurious diapycnal mixing, with MetROMS' terrain-following coordinate leading to more erosion than FESOM's z-coordinate. Finally, increased horizontal resolution in FESOM leads to higher basal melt rates for small ice shelves, through a combination of stronger circulation and small-scale intrusions of warm water from offshore.

2.1 Introduction

The Antarctic Ice Sheet (AIS) has significant potential to drive sea level rise as climate change continues (*Deconto and Pollard*, 2016; *Golledge et al.*, 2015; *Rignot*

et al., 2014; *Mengel and Levermann*, 2014). Paleo records indicate that the AIS was a major contributor to sea level change in past climate events (*Cook et al.*, 2013; *Miller et al.*, 2012; *Raymo and Mitrovica*, 2012; *Dutton et al.*, 2015; *O'Leary et al.*, 2013), and the mass balance of the modern-day AIS is already negative (*Rignot et al.*, 2011; *Zwally and Giovinetto*, 2011; *Shepherd et al.*, 2012). The ocean is an important driver of AIS retreat (*Golledge et al.*, 2017; *Joughin and Alley*, 2011), as 40% of the ice sheet by area is grounded below sea level (*Fretwell et al.*, 2013). This geometry provides the potential for the ocean to melt large regions of the AIS from below. For example, the Amundsen sector of West Antarctica has bedrock geometry favourable for a marine ice sheet instability, and unstable retreat may have already begun (*Rignot et al.*, 2014).

The ocean directly interacts with the AIS through ice shelves, which are the floating extensions of the land-based ice sheet. The properties of ice shelf cavities, the pockets of ocean between ice shelves and the seafloor, determine the basal melt rates of each ice shelf which ultimately affect the mass balance of the AIS through dynamical processes (*Dupont and Alley*, 2005). The seawater in ice shelf cavities can be sourced from several different water masses, which affect its temperature and salinity. Many of these source water masses are influenced by sea ice processes (*Jacobs et al.*, 1992; *Nicholls et al.*, 2009).

A better understanding of ocean/sea-ice/ice-shelf interactions in Antarctica is crucial, particularly given their importance for future sea level rise. However, these interactions take place in observation-deficient regions. In particular, there are very few direct measurements inside ice shelf cavities, and observations are also scarce in the sea ice covered regions of the Southern Ocean (*Rintoul et al.*, 2010). Nonetheless, some measurements have been made at great expense (e.g. *Nicholls et al.*, 2006; *McPhail et al.*, 2009; *Venables and Meredith*, 2014). While ice shelf basal melt rates can be inferred using remote sensing methods (*Rignot et al.*, 2013; *Depoorter et al.*, 2013), large uncertainties remain regarding the circulation patterns driving these melt rates, and no predictions for the future can be made based on these data.

Consequently, much of our understanding of ocean/sea-ice/ice-shelf interactions is based on numerical modelling. In recent years an increasing number of ocean models have begun to resolve ice shelf cavities and simulate thermodynamic processes at the ice shelf base (*Dinniman et al.*, 2016 and references therein; *Mathiot et al.*, 2017). Given the variety of models involved, and the relative lack of observations to constrain their tuning, it is desirable to conduct model intercomparison projects (MIPs, see e.g. *Meehl et al.* (2000)) by which several models run the same experiment and their output is compared. The resulting insights into model similarities and differences can ideally be attributed to model design choices, with the aim of guiding

future development.

To date, the only MIPs considering ice shelf cavities are the ongoing ISOMIP experiments (Ice Shelf-Ocean Model Intercomparison Project) (*Hunter*, 2006; *Asay-Davis et al.*, 2016) which use idealised domains and simplified forcing, and do not include coupled sea ice models. The ISOMIP experiments are undoubtedly valuable, and are likely to provide particular insights regarding the response of cavity circulation to warm versus cold forcing. However, idealised experiments such as ISOMIP should be complemented by intercomparisons over more realistic domains, with observationally derived forcing and coupled sea ice models. These model configurations are already being used to better understand processes in observed cavities (*Timmermann et al.*, 2012; *Galton-Fenzi et al.*, 2012) and to provide future projections of ice shelf melt (*Timmermann and Hellmer*, 2013; *Hellmer et al.*, 2012, 2017), so analysis of the similarities and differences between such models is timely. Another important benefit of realistic domains is the opportunity to compare model output to available observations, even if these observations are limited. Therefore, an element of model evaluation, as well as model intercomparison, can be included.

In this chapter we present such an intercomparison of two ocean models, both including ice shelf thermodynamics and sea ice components, from a circumpolar Antarctic perspective. We focus on ice shelf basal melt and sub-ice shelf circulation across eight regions of the Antarctic coastline, but also consider interior Southern Ocean and sea ice processes as they affect ice shelf cavities. The model output is compared to relevant observations where available. Finally, key findings and their implications, as well as possibilities for future model development, are discussed.

2.2 Model descriptions

Two coupled ocean/sea-ice/ice-shelf models are included in this intercomparison: MetROMS-iceshelf (hereafter MetROMS) and FESOM 1.4 (hereafter FESOM). We run FESOM at two different resolutions, for a total of three experiments (see Section 2.3). In this section we describe the two models and compare their scientific design.

2.2.1 Overview

MetROMS consists of the regional ocean model ROMS (Regional Ocean Modelling System) (*Shchepetkin and McWilliams*, 2005) including ice shelf thermodynamics (*Galton-Fenzi et al.*, 2012), coupled to the sea ice model CICE (Community Ice

CodE) (*Hunke et al.*, 2015) using the coupler MCT (Model Coupling Toolkit) (*Larson et al.*, 2005; *Jacob et al.*, 2005). The coupling was implemented by the Norwegian Meteorological Institute (*Debernard et al.*, 2017) and is described in Section 4.3.5. We use the development version 3.7 of the ROMS code, version 5.1.2 of CICE, and version 2.9 of MCT.

FESOM (Finite Element Sea-ice/ice-shelf Ocean Model) is a global ocean model (*Wang et al.*, 2014) with an internally coupled sea ice model (*Danilov et al.*, 2015; *Timmermann et al.*, 2009) and ice shelf thermodynamics (*Timmermann et al.*, 2012). It has an unstructured mesh in the horizontal, consisting of triangular elements which allow for spatially varying resolution. The numerical methods associated with the unstructured mesh are detailed by *Wang et al.* (2008) and *Wang et al.* (2014), while the implementation of the ice shelf component is discussed in *Timmermann et al.* (2012).

2.2.2 Domain and resolution

Our configuration of MetROMS has a circumpolar Antarctic domain with a northern boundary at 30°S. Horizontal resolution is quarter-degree scaled by cosine of latitude, and the South Pole is relocated to achieve approximately equal resolution around the Antarctic coastline. This leads to resolutions (defined as the square root of the area of each grid box) of approximately 15-20 km in the Antarctic Circumpolar Current (ACC), 8-10 km on the Antarctic continental shelf, and 5 km or finer at the southernmost grounding lines of the Ross, Filchner-Ronne, and Amery Ice Shelves (Figure 2.1a).

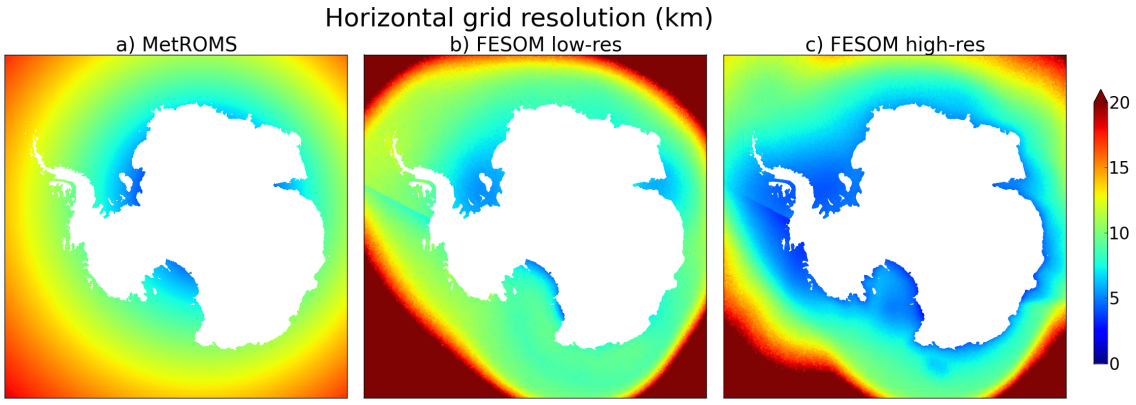

Figure 2.1: Horizontal resolution (km) of the MetROMS grid and both FESOM meshes around Antarctica. Resolution is defined as the square root of the area of each grid box (MetROMS) or triangular element (FESOM). Note that values above 20 km are not differentiated.

Our FESOM setup has a global domain with spatially varying horizontal resolution. Here we define resolution in FESOM as the square root of the area of each triangular element. However, this metric may not be truly comparable to MetROMS. When discussing resolution, the real question is the smallest flow features that are captured by a mesh of a certain spacing. In models with such different numerical methods as MetROMS (finite-volume) and FESOM (finite-element), the smallest resolved feature may scale differently with the mesh spacing. Numerical dissipation and stabilisation built into different time-stepping routines can also influence this "effective resolution". Furthermore, MetROMS employs a staggered Arakawa C-grid for the ocean and B-grid for the sea ice (*Arakawa and Lamb*, 1977), by which different variables are calculated at different locations within each grid box (Figure 2.2a). In FESOM, all variables are calculated at the same locations (Figure 2.2b). There is some evidence that this design tends to resolve fewer features of fluid flow (*Haidvogel and Beckmann*, 1999), and indeed FESOM appears to have a lower effective resolution than finite-difference C-grid models with comparable nominal grid spacing.

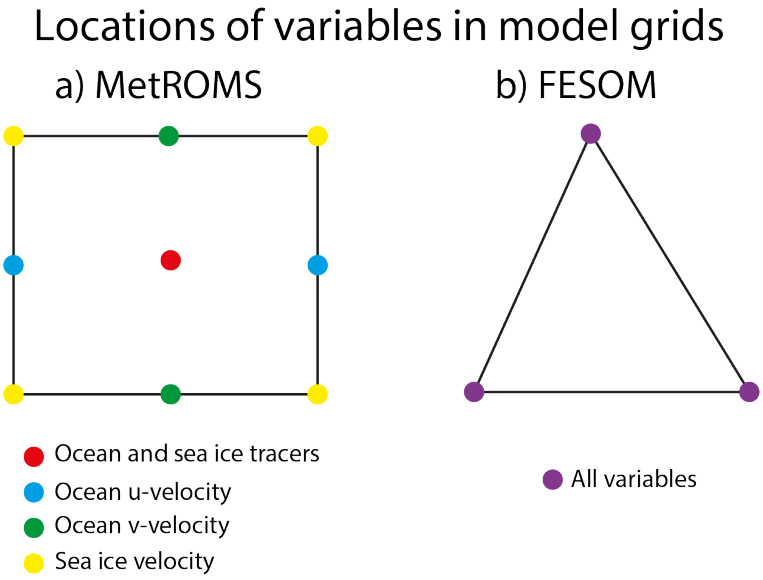

Figure 2.2: Schematic showing the locations of variables in the (a) MetROMS and (b) FESOM grids. MetROMS consists of an Arakawa C-grid for the ocean (red, blue, and green points), and an Arakawa B-grid for the sea ice (red and yellow points). FESOM calculates all variables at the same locations (purple points).

To account for these uncertainties, as well as to investigate the importance of resolution on FESOM's performance, we have prepared two meshes: "low-resolution" (Figure 2.1b) and "high-resolution" (Figure 2.1c). During mesh generation, resolution is distributed based on distance from the coastline (using a hyperbolic tangent function) as well as individually defined patches of increased resolution, which are then smoothed together using Gaussian filters. The high-resolution mesh has approximately double the number of 2D nodes as the low-resolution mesh, but these

extra nodes are not evenly spaced throughout the domain. Outside the Southern Ocean, the two meshes have virtually identical resolution (not shown), ranging from 150-225 km in the abyssal Pacific, Atlantic, and Indian Oceans, and 50-75 km along coastlines. These regions of the domain are not the focus of the current study, so coarse resolution here is acceptable, and provides computational savings. Resolution is finer along coastlines compared to the abyssal ocean so that the shape of the coastline is preserved, and so that processes on the continental shelf are adequately resolved. Next, the ACC is the subject of some analysis in these simulations, so more resolution is concentrated in the open Southern Ocean, ranging from 20-100 km for the low-resolution mesh and 15-50 km for the high-resolution mesh. Resolution continues to refine on the Antarctic continental shelf (approximately 8-10 km for low-resolution, 5-7 km for high-resolution) and further refine in ice shelf cavities (5-10 km for low-resolution, 3-7 km for high-resolution), corresponding to the regions of focus for this study. The greatest difference between the two meshes occurs in the Amundsen and Bellingshausen Seas, with approximate resolution of 11 km for the low-resolution mesh and 4 km for high-resolution.

In the vertical, MetROMS has 31 terrain-following levels using the s-coordinate system, with increasing vertical resolution near the surface and bottom, and coarsest resolution in the interior. FESOM employs a hybrid z-sigma vertical coordinate system, with the same discretisation for both the low- and high-resolution meshes. The region south of the 2500 m isobath surrounding Antarctica, which includes all ice shelf cavities as well as the continental shelf and slope, has sigma-coordinates with 22 levels. The remainder of the domain has z-coordinates, comprised of 38 levels weighted towards the surface. Both models are free-surface, which leads to time-varying vertical levels in MetROMS, but only affects the uppermost layer in FESOM.

In both models, the use of terrain-following coordinates in the thin water columns of ice shelf cavities leads to enhanced vertical resolution, often finer than 1 m in MetROMS, which limits the time step. Our configuration of ROMS requires a baroclinic time step of 5 minutes for stability, with 30 barotropic time steps for each baroclinic. In CICE, the time step is 30 minutes for both dynamic and thermodynamic processes, and ocean/sea-ice coupling is also performed every 30 minutes. FESOM is run with a time step of 10 minutes for the low-resolution mesh and 9 minutes for high-resolution. The sea ice model operates on the same time step as the ocean component.

Resolution, domain size, and time step length all have important consequences for computational cost. MetROMS is the most expensive of the three models, requiring approximately 2660 CPU hours for each year of simulation. On the same computing

facility, low-resolution FESOM requires approximately 730 CPU hours per year, while high-resolution FESOM requires approximately 1940 CPU hours per year. Despite MetROMS' smaller domain than FESOM, and often lower resolution on the Antarctic continental shelf, it nonetheless has the largest number of 3D grid points among the three models, which explains its relative expense. These extra grid points are due to higher resolution throughout the open Southern Ocean, and more vertical layers than FESOM in most regions.

2.2.3 Smoothing of bathymetry and ice shelf draft

Steep bathymetry can be problematic for terrain-following coordinate ocean models, as it has the potential to introduce pressure gradient errors (*Haney*, 1991). Both ROMS (*Shchepetkin and McWilliams*, 2003) and FESOM (*Wang et al.*, 2008) are designed to minimise this issue with the splines density Jacobian method for the calculation of the pressure gradient force, which reduces errors compared to the standard density Jacobian method. Nevertheless, a particular challenge arises at ice shelf fronts, which in reality are cliff faces that can reach several hundred metres in depth, but which models must represent as sloping surfaces. This substantial change in surface layer depth over as little as one grid cell creates steeply sloping vertical layers with a large pressure gradient, and numerical errors in the pressure gradient calculation could drive spurious circulation patterns across the given ice shelf front.

In both models, some amount of smoothing of the bathymetry and ice shelf draft is necessary for numerical stability and to reduce pressure gradient errors. On the other hand, excessive smoothing could alter the geometry of the ice shelf cavities to the point where circulation is affected. An oversmoothed ice shelf front would be too shallow and gently sloping, providing a pathway for warm surface waters to easily enter the cavity, where in reality the ice shelf front constitutes a vorticity barrier which may limit water mass exchanges (*Nicholls et al.*, 2009). However, in some cavities small-scale processes do allow significant water mass exchange at the ice shelf front (*Arzeno et al.*, 2014), so oversmoothing may compensate for these unresolved processes. Near the grounding lines at the backs of ice shelf cavities, oversmoothing would remove the deepest ice which melts most easily (*Lewis and Perkin*, 1986). In this situation the water column thickness would be overestimated, allowing for greater transport of warm water to the grounding line. In a coupled ice-sheet/ocean model, *Timmermann and Goeller* (2017) demonstrated that increased water column thickness due to a thinning ice shelf can more than compensate for the reduced melting expected from the elevated in-situ freezing point at the ice shelf base. Therefore, a delicate balance must be struck when smoothing model

topographies, in order to achieve the most accurate simulation.

We prepared the MetROMS and FESOM domains using bathymetry, ice shelf draft, and land/sea masks from the RTopo-1.05 dataset (*Timmermann et al.*, 2010). MetROMS follows a 3-step smoothing procedure similar to that of *Lemarié et al.* (2012). First, the "deep ocean filter" consists of a single pass of a Hanning filter (window size 3) over the bathymetry h, with variable coefficients designed to remove isolated seamounts. Next, a selective Hanning filter is repeatedly applied to both $\log(h)$ and $\log(z_{ice})$, where z_{ice} is the ice shelf draft, until the slope parameter $r = |h_i - h_{i+1}|/(h_i + h_{i+1})$ satisfies the condition $r < 0.25$ everywhere (and similarly for z_{ice}). This selective filter has coefficients scaled by the gradient of h or z_{ice}, meaning that regions which are already smooth enough will not become oversmoothed. Finally, both h and z_{ice} undergo a final two passes of a regular Hanning smoother to remove 2D noise. Note that this separate treatment of bathymetry and ice shelf draft does not directly consider water column thickness, for which some large gradients may remain.

The smoothing procedure in FESOM is the same as described by *Nakayama et al.* (2014). The source bathymetry and ice shelf draft are first averaged over 4-minute ($\frac{1}{15}^\circ$) intervals. Then Gaussian filters are applied to both fields, with spatially-varying radii scaled by the desired final resolution. For this reason, high-resolution regions of the domain receive less smoothing than lower-resolution regions. The ice shelf draft undergoes one pass of the Gaussian filter, while the bathymetry undergoes four passes with larger radii. Following interpolation to the unstructured mesh, the ice shelf draft field receives selective smoothing to satisfy the critical steepness limitation of *Haney* (1991) at all points. This procedure limits the slope of the ice shelf draft, and extremely high resolution may be necessary to preserve steep slopes.

Another region of concern is the grounding line, where water column thickness approaches zero and vertical layers converge. Estimates of pressure gradient error, such as that of *Haney* (1991), scale inversely with the vertical layer thickness and can therefore diverge near the grounding line. To alleviate this problem, a minimum water column thickness of 50 m is enforced. In both models, the bathymetry is artificially deepened where necessary to satisfy this condition during the smoothing process. An alternate approach would be to fill the affected cells with land rather than deepen them, but this would alter the grounding line locations determined by RTopo, which we wished to preserve.

2.2.4 Ocean mixing

ROMS includes several options for tracer advection (*Shchepetkin and McWilliams*, 2005), and the choice of advection scheme is known to impact the simulation. The centered and Akima fourth-order tracer advection schemes are dominated by dispersive error, which can lead to undershoots of the freezing point and spurious sea ice formation in our MetROMS configuration (Chapter 4). On the other hand, the upwind third-order tracer advection scheme is dominated by dissipative error, which can result in high levels of diapycnal mixing for some simulations (*Lemarié et al.*, 2012; *Marchesiello et al.*, 2009). Indeed, problematic diapycnal mixing related to the upwind third-order scheme was observed in decadal-scale simulations with our configuration of MetROMS (Section 3.7). Therefore, the 25-year MetROMS simulation we present here uses the Akima fourth-order tracer advection scheme (*Shchepetkin and McWilliams*, 2005), combined with explicitly parameterised Laplacian diffusion applied along isoneutral surfaces, at a level strong enough to smooth out most dispersive oscillations. This configuration shows minimal spurious sea ice formation, comparable to a simulation with flux-limited (i.e. locally monotonic) upwind third-order advection (Chapter 4), and exhibits less spurious diapycnal mixing than the upwind scheme. The diffusivity coefficient is 150 m^2/s, which applies to the largest grid cell (approx. 24 km resolution) and is scaled linearly for smaller cells. Advection of momentum uses the upwind third-order scheme in the horizontal and the centered fourth-order scheme in the vertical (*Shchepetkin and McWilliams*, 2005), and is combined with parameterised biharmonic viscosity along geopotential surfaces, with a coefficient of 10^7 m^4/s (scaled by grid size as with diffusivity).

FESOM computes advection of momentum using the characteristic Galerkin method, and advection of tracers using the explicit second-order flux-corrected-transport scheme (*Wang et al.*, 2014). The Laplacian approach is used to explicitly parameterise both diffusivity and viscosity, with coefficients 600 m^2/s and 6000 m^2/s respectively. These values apply to a reference area of 5800 km^2, and are scaled to the area of each triangular element, scaling with the square root for diffusivity and linearly for viscosity. At 10 km resolution (element area of 100 km^2), the resulting diffusivity is 78.8 m^2/s, compared to 62.4 m^2/s in ROMS. The analogous viscosity terms cannot be directly compared between ROMS and FESOM, since they do not use the same parameterisation.

A flow-dependent Smagorinsky viscosity term is also applied in FESOM (*Smagorinsky*, 1963, 1993; *Wang et al.*, 2014). In z-coordinate regions, tracer diffusion is rotated along isoneutrals, and the Gent-McWilliams eddy parameterisation is used (*Gent and McWilliams*, 1990; *Gent et al.*, 1995; *Wang et al.*, 2014). In sigma-

coordinate regions, diffusivity and viscosity are both applied along constant-sigma surfaces.

For weakly stratified regions such as the Southern Ocean, the choice of vertical mixing parameterisation can have a significant impact on simulated convection (*Timmermann and Beckmann*, 2004). MetROMS employs the Large-McWilliams-Doney interior closure scheme (*Large et al.*, 1994) which includes the KPP boundary layer parameterisation. We implement the same KPP modification as in *Dinniman et al.* (2011), which imposes a minimum surface boundary layer depth based on surface stress, in the case of stabilising conditions. This modification is designed to address problems with excessive stratification during periods of rapid sea ice melt, and follows principles similar to the FESOM vertical mixing parameterisation discussed below. A shallow bias in mixed layer depths during the melt season is problematic for the accurate simulation of Southern Ocean water masses, particularly in the Weddell Sea (*Timmermann and Beckmann*, 2004).

The vertical mixing scheme in our configuration of FESOM (*Timmermann et al.*, 2009) consists of the Richardson number dependent parameterisation of *Pacanowski and Philander* (1981), modified to have maximum vertical diffusivities and viscosities of 0.05 m^2/s. Over a depth defined by the Monin-Obukhov length, calculated as a function of surface stress and buoyancy forcing, an extra 0.01 m^2/s is applied to both vertical diffusivity and viscosity. This combination was found by *Timmermann and Beckmann* (2004) to produce the most realistic representation of water masses in the Weddell Sea, avoiding the excessive open-ocean convection which is characteristic of traditional convective adjustment. We also tested the KPP parameterisation (without the modification used by MetROMS) in short simulations with our FESOM configuration (not shown). At least on the 5-year timescale, hydrography in the offshore Weddell Sea was very similar between KPP and the modified Pacanowski-Philander scheme. It is possible that longer simulations would show more divergence, and this warrants further investigation.

2.2.5 Ice shelf thermodynamics

With terrain-following coordinates, it is relatively straightforward to include ice shelf cavities in an Antarctic domain. In both ROMS and FESOM, all of the terrain-following vertical layers subduct beneath the ice shelves. The pressure of the ice shelf draft must be considered in the calculation of the pressure gradient. ROMS vertically integrates the density of water displaced by ice, and assumes the density of this displaced water is a linear function of depth, with coefficient $\frac{\partial \rho}{\partial z} = 4.78 \times 10^{-3}$ kg/m^4 and intercept given by the density in the first model layer. FESOM computes

the pressure gradient force from the vertically integrated horizontal density gradient and assumes that the horizontal pressure gradient is zero at the ice shelf base. High-order interpolation for density is done in the vertical to compute horizontal density gradients as accurately as possible.

ROMS and FESOM simulate ice shelf thermodynamics: the heat and salt fluxes associated with melting and refreezing at the ice shelf base. However, any net melting or freezing is not actually applied to the ice shelf geometry. It is assumed that glacial flow of the ice shelf, surface accumulation, and basal melting are in dynamic equilibrium such that the geometry remains constant. Removing this assumption necessitates coupling with an ice sheet model, which has recently been accomplished for FESOM (*Timmermann and Goeller*, 2017) and is under development for ROMS (*Gladstone et al.*, 2017). Ice-sheet/ocean coupling is an emerging field of climate modelling, and the first generation of models will be compared and evaluated as part of the MISOMIP experiments (Marine Ice Sheet-Ocean Model Intercomparison Project) (*Asay-Davis et al.*, 2016).

Both ROMS and FESOM (*Galton-Fenzi*, 2009; *Galton-Fenzi et al.*, 2012; *Timmermann et al.*, 2012) implement the 3-equation parameterisation of *Hellmer and Olbers* (1989) refined by *Holland and Jenkins* (1999). The heat and salt exchange coefficients γ_T and γ_S have the form

$$\gamma_T = \frac{u^*}{\kappa + 12.5\,\mathrm{Pr}^{\frac{2}{3}} - 6} \qquad \text{and} \qquad \gamma_S = \frac{u^*}{\kappa + 12.5\,\mathrm{Sc}^{\frac{2}{3}} - 6} \tag{2.1}$$

where Pr is the Prandtl number and Sc is the Schmidt number (both dimensionless constants) and u^* is the friction velocity in m/s, calculated as

$$u^* = \max\left(\sqrt{C_d\,(u^2 + v^2)}, u^*_{min}\right) \tag{2.2}$$

where C_d is the drag coefficient (3×10^{-3} in ROMS, 2.5×10^{-3} in FESOM), u and v are the horizontal ocean velocity components in the uppermost vertical layer, and u^*_{min} is a lower bound for u^* which represents molecular diffusion (10^{-3} in ROMS, 2.5×10^{-4} in FESOM). While the effect of the different drag coefficient between the models is likely to be negligible, the larger minimum u^* in ROMS will cause stronger melting in locations with very weak flow, such as at the grounding line (*Gwyther et al.*, 2016).

The turbulence term κ in Equation 2.1 has a different formulation between the two models. FESOM follows a very similar approach to *Jenkins* (1991), by which

$$\kappa = 2.12\ \log\left(u^*\frac{D}{\nu}\right) - 3 \tag{2.3}$$

where $D = 10$ m is a reference boundary layer depth, and $\nu = 1.95 \times 10^{-6}$ m^2/s is the kinematic viscosity. ROMS instead uses a simplified version of *McPhee et al.* (1987)'s approach, by which

$$\kappa = \begin{cases} 2.5 \log\left(\frac{\left(5300 \text{ m}^{-2}\text{s}\right)(u^*)^2}{|f|}\right) + 7.12 & \text{if } u^* > 10^{-3} \text{ m/s and } |f| > 10^{-8} \text{ s}^{-1} \\ 0 & \text{otherwise} \end{cases} \tag{2.4}$$

where f is the Coriolis parameter in s^{-1}.

While refreezing is implicit in the 3-equation formulation, none of our configurations include an explicit frazil ice model such as that of *Smedsrud and Jenkins* (2004) or *Galton-Fenzi et al.* (2012). A frazil ice scheme does not yet exist in FESOM, so activating this option in MetROMS alone would bias the intercomparison.

2.2.6 Sea ice

MetROMS includes the sea ice model CICE (*Hunke et al.*, 2015) which is a multi-layer, multi-category model widely used in global coupled models as well as regional and uncoupled setups. Our configuration of CICE has seven ice layers plus one snow layer, and five ice thickness categories. It is externally coupled to ROMS, i.e. runs on separate processors, with communication driven by the coupler MCT (*Larson et al.*, 2005; *Jacob et al.*, 2005). There are six baroclinic ocean time steps (5 minutes) for each sea ice time step (30 minutes), and the coupler exchanges fields every sea ice time step. Having longer time steps for the sea ice than for the ocean is computationally favourable, but it also introduces lags in ocean/sea-ice interactions, because the coupled fields are time-averaged over the previous 30 minutes.

FESOM's sea ice model is described by *Danilov et al.* (2015). It has a single ice layer (plus one snow layer) and a single thickness category. It is internally coupled with the ocean, running on the same processors and the same time step. While the FESOM sea ice model is generally less complex than CICE, it nonetheless has been shown to reproduce key features of observed Arctic and Antarctic sea ice (*Timmermann et al.*, 2009).

Our configuration of CICE uses the "mushy" thermodynamics scheme of *Turner et al.* (2013a). It also includes the level-ice melt pond parameterisation of *Hunke et al.* (2013), and the Delta-Eddington radiation scheme (*Briegleb and Light*, 2007). In FESOM, sea ice thermodynamics follows *Parkinson and Washington* (1979) with the zero-layer approach to heat conduction (*Semtner*, 1976).

For sea ice dynamics, CICE uses elastic-anisotropic-plastic rheology (*Tsamados*

et al., 2013) with the ridging-based ice strength formulation of *Rothrock* (1975). FESOM has elastic-viscous-plastic rheology (*Bouillon et al.*, 2013) including a linear formulation of ice strength with coefficient $P^* = 15,000$ N/m^2. Sea ice transport follows an incremental remapping approach in CICE (*Lipscomb and Hunke*, 2004), with the ridging participation and redistribution functions of *Lipscomb et al.* (2007). FESOM uses a backward Euler implicit advection scheme for sea ice transport.

2.2.7 Surface exchange scheme

While MetROMS and FESOM are forced with the same atmospheric state (see Section 2.3.2), the resulting surface fluxes differ based on the bulk formulae implemented by the models. Our configuration of FESOM uses constant exchange coefficients for heat and momentum fluxes, while MetROMS' exchange coefficients vary in time and space. For ocean/atmosphere fluxes (in ROMS), these coefficients are based on the COARE (Coupled-Ocean Atmosphere Response Experiment) protocol (*Fairall et al.*, 1996). For sea-ice/atmosphere fluxes, CICE includes a stability-based atmospheric boundary interface (*Hunke et al.*, 2015). These differences in bulk formulae may affect the simulations, particularly the momentum fluxes which have consequences for ACC transport, Ekman pumping, and sea ice formation and drift. A comparison of ocean surface stress (not shown) reveals that these momentum fluxes are typically stronger in MetROMS, by up to 30%.

2.3 Experimental design

For this intercomparison, we simulated the 25-year period 1992-2016 using three model configurations: MetROMS, low-resolution FESOM, and high-resolution FESOM (Figure 2.1).

2.3.1 Initial conditions

All simulations are initialised using monthly-averaged observational or reanalysis products for January 1992. Initial ocean temperature and salinity are taken from the ECCO2 reanalysis (*Menemenlis et al.*, 2008; *Wunsch et al.*, 2009), and extrapolated into ice shelf cavities using a nearest-neighbour method in Cartesian space. This leads to an initial warm bias in most cavities, but the resulting high melt rates drive strong sub-ice shelf circulation that flushes out the cavities during the first year or two of simulation, allowing more realistic sub-ice shelf conditions to quickly

develop. An alternate approach, which we also tested, was to initialise cavities at the local freezing point, so that initial melt rates were zero. These simulations took much longer to equilibrate, because the absence of ice shelf meltwater led to weak circulation in cavities, and therefore longer residence times. Initialising cavities based on observations was not feasible due to the scarcity of measurements.

Sea ice is initialised using the NOAA/NSIDC Climate Data Record for Passive Microwave Sea Ice Concentration (*Meier et al.*, 2013). Wherever the observed Antarctic sea ice concentration exceeds 0.15, the model is initialised with concentration 1, ice thickness of 1 m, and snow thickness of 0.2 m. This is the same method used in Chapter 4 and is similar to that of *Kjellsson et al.* (2015). FESOM, having a global domain, also requires initial conditions for Arctic sea ice. We follow the same method as for the Antarctic, but set the initial ice thickness to 2 m, since Arctic sea ice tends to be thicker (*Kwok and Cunningham*, 2008; *Worby et al.*, 2008). Initial ocean velocity, sea ice velocity, and sea surface height are set to zero.

Our experiments do not include a proper spinup to a quasi-equilibrium state. For the purposes of this intercomparison around the Antarctic margin and continental shelf, as well as in the ice shelf cavities, we argue a full spinup is not worth the computational expense. The processes we focus on - onshore flow, dense shelf water formation, and ocean/ice-shelf interaction - equilibrate much more quickly than the interior ocean. For example, area-averaged basal melt rates in our experiments stabilise within 5-10 years for most ice shelves. Since melt rates are a function of water mass properties and of circulation, this result indicates that processes in ice shelf cavities have spun up within the first decade of simulation.

2.3.2 Atmospheric forcing

MetROMS and FESOM are both forced with the ERA-Interim atmospheric reanalysis (*Dee et al.*, 2011) using 6- and 12-hourly fields over the years 1992-2016. Due to differing implementations of model thermodynamics, the two models are forced with different combinations of atmospheric variables. Both models utilise 6-hourly fields for near-surface air temperature, pressure, and winds, which are linearly interpolated to each time step. Near-surface humidity is derived from ERA-Interim's 6-hourly fields for dew point temperature; this conversion is performed in advance for MetROMS, but at run-time for FESOM. Both models read 12-hourly fields for precipitation (split into rain and snow) and evaporation, which are not interpolated in time but rather applied at a constant rate with a step change every 12 hours, as they represent total fluxes over the given 12-hour period.

MetROMS diagnoses incoming shortwave radiation from ERA-Interim's 6-hourly total cloud cover, which is interpolated to each time step. Incoming longwave radiation is calculated internally. In FESOM, incoming shortwave and longwave radiation are read directly from ERA-Interim, as 12-hourly fields which are applied as step changes.

To account for the influence of iceberg calving on the Southern Ocean freshwater budget, both models are forced with an additional surface freshwater flux representing iceberg melt. For this field we use the output of *Martin and Adcroft* (2010), who modelled icebergs as interactive Lagrangian particles in the ocean component of a GCM simulation. The initial sizes of icebergs at calving fronts were determined from a statistical distribution constrained by observations. *Martin and Adcroft*'s monthly climatology of iceberg melt is interpolated to each time step in our simulations, and repeated annually. River runoff from other continents is not considered.

2.3.3 Surface salinity restoring

A persistent feature of many Southern Ocean models (*Kjellsson et al.*, 2015; *Heuzé et al.*, 2015; *Sallée et al.*, 2013b; *Turner et al.*, 2013b; *Goosse and Fichefet*, 2001) is spuriously deep convection in the Weddell Sea, leading to an unrealistic open-ocean polynya as warm Circumpolar Deep Water is brought to the surface. The possible causes of this widespread model bias include insufficient surface freshwater flux (*Kjellsson et al.*, 2015) as well as insufficient summer mixed layer depths (*Timmermann and Beckmann*, 2004). In both circumstances, salinity in the subsurface Winter Water layer increases until the weakly stratified water column becomes unstable and overturns.

MetROMS is prone to deep convection in the Weddell Sea, and while tuning of the sea ice dynamics and ocean vertical mixing helped to delay the onset of convection, the only permanent solution we found was surface salinity restoring. Such restoring affects the salt budget and may contribute to drift in the total salt content of the ocean, although it prevents drift in the surface layer. This may impact the density structure of the Southern Ocean, and particularly the ACC, as well as damping interannual variability. However, these shortcomings were deemed preferable to spurious deep convection for the purposes of our analysis. We restore MetROMS to the World Ocean Atlas 2013 monthly climatology of surface salinity (*Zweng et al.*, 2013), linearly interpolated to each model time step and repeated annually. Restoring has a timescale of 30 days and affects the uppermost layer, whose thickness is time-varying but generally ranges from 1-3 m. We exclude the Antarctic continental shelf from this restoring (defined as regions south of 60°S with bathymetry shallower

than 1500 m, as well as all ice shelf cavities), as significant freshening of Antarctic Bottom Water occurs otherwise. Given the relatively scant observations on the continental shelf making up the World Ocean Atlas products, restoring in this region would not be appropriate.

FESOM does not develop spurious deep convection in the Weddell Sea, even for long simulations without restoring. Possible reasons for this differing behaviour between MetROMS and FESOM are discussed in Section 2.4.2.1. Nonetheless, we apply the same surface salinity restoring to FESOM as we do to MetROMS, so that the experiments are as similar as possible. Restoring in FESOM is scaled with a constant depth of 10 m, which is the depth of the surface layer in z-coordinate regions, neglecting free surface variations. We do not restore north of 30°S, as this region is outside the MetROMS domain.

2.3.4 Northern boundary conditions

MetROMS, with its regional circumpolar domain, has lateral boundary conditions at 30°S. The ECCO2 reanalysis (*Menemenlis et al.*, 2008; *Wunsch et al.*, 2009) provides temperature, salinity, and meridional velocity (v) as monthly averages over the transient period 1992-2016. Sea surface height is taken from the AVISO annual mean climatology (*AVISO*, 2011) which is a single time record. Note that tides are not considered, as discussed further in Section 2.5.

We follow the method described in Section 4.3.3 to ensure stability at the open boundary: zonal velocity u is clamped to zero, the bathymetry is modified to be constant in latitude over the northernmost 15 rows of the domain, and a sponge layer is applied over these rows (in which the diffusivity coefficient linearly increases to 10 times its background value, and the viscosity coefficient to 100 times). Northern boundary conditions are applied using the Chapman scheme for sea surface height (*Chapman*, 1985), the Flather scheme for barotropic v (*Flather*, 1976), and the radiation-nudging scheme for baroclinic v, temperature, and salinity (*Marchesiello et al.*, 2001).

The presence of lateral boundary conditions derived from observations may give MetROMS an advantage for the accurate simulation of Southern Ocean water masses, compared to FESOM which has a global domain. However, this intercomparison focuses on the continental shelf and ice shelf cavities. These regions are relatively far-field from 30°S, compared to the ACC and the interior Southern Ocean which are more tightly coupled to the boundary conditions. For the relatively short (25-year) simulations shown here, it is unlikely that continental shelf water masses will be

significantly influenced by nudging at 30°S. Longer simulations would likely show a larger response.

2.4 Results

2.4.1 Ocean

2.4.1.1 Drake Passage transport

The ACC has the strongest transport of any ocean current in the world, and is key to the thermal isolation of Antarctica. Transport of the ACC is influenced by the Southern Hemisphere westerly winds as well as the density structure of the Southern Ocean. By convention, zonal transport of the ACC is evaluated through Drake Passage and is time-averaged to remove the seasonal cycle. With respect to observations, Drake Passage transport was previously thought to lie around 134 Sv (*Cunningham et al.*, 2003). However, recent improvements in measuring systems have suggested a higher value. As part of the cDrake project (Dynamics and Transport of the Antarctic Circumpolar Current in Drake Passage), *Donohue et al.* (2016) estimated a Drake Passage transport of 173.3 ± 10.7 Sv.

For our simulations, zonal transport through Drake Passage is calculated at 67°W over the period 2002-2016. The first 10 years of the simulation (1992-2001) are excluded as spinup. This time-averaged Drake Passage transport, including the standard deviation in annual averages, is 126.8 ± 3.4 Sv in MetROMS, 158.6 ± 2.8 Sv in low-resolution FESOM, and 152.6 ± 3.1 Sv in high-resolution FESOM. Compared to the observations of *Donohue et al.* (2016), the values from all three of our simulations are too low, especially in MetROMS. This occurs despite MetROMS' stronger surface stress than in FESOM (Section 2.2.7). Additionally, the MetROMS and low-resolution FESOM simulations exhibit downward trends in Drake Passage transport over 2002-2016, which are statistically significant at the 95% level: -0.28 Sv/y in MetROMS and -0.17 Sv/y in low-resolution FESOM. This weakening of the ACC may be driven by degradation of Southern Ocean interior water masses due to spurious diapycnal mixing, as discussed in Section 2.4.1.4. Furthermore, drift in the density structure may result from non-closure of the surface freshwater budget, which is globally unconstrained by the bulk-flux approach of our simulations.

Since interior Southern Ocean processes operate on much longer timescales than our experiments, and would require long spin-ups to equilibrate, simulated ACC transport should be interpreted with caution and is not the focus of this intercom-

parison project. Nonetheless, from a model development perspective it is useful to discuss the strengths and weaknesses of MetROMS and FESOM in the open Southern Ocean. This region has been a major research focus for global ocean models in recent years (e.g. *Downes et al.*, 2015), and models which are able to accurately simulate both the ACC and the Antarctic continental shelf will likely be in demand in the near future.

2.4.1.2 Mixed layer depth

The surface mixed layer represents the portion of the ocean which is directly influenced by the atmosphere. The depth of the mixed layer is a key indicator of the strength of convection, and heat loss to the atmosphere resulting from convection will influence water mass properties. Deep wintertime mixed layers adjacent to the Antarctic coast are often the result of strong sea ice formation in polynyas, a process which is examined in Section 2.4.2.3.

We calculate mixed layer depth using the density criterion of *Sallée et al.* (2013b): the shallowest depth at which the potential density is at least 0.03 kg/m^3 greater than at the surface (or at the ice shelf interface, in the case of ice shelf cavities). Summer (DJF) and winter (JJA) mixed layer depth in each simulation, averaged over the period 2002-2016, are shown in Figure 2.3 for the entire Southern Ocean, and Figure 2.4 zoomed into the Antarctic continental shelf. Figure 2.3 also includes climatological observations by *Pellichero et al.* (2017) recalculated to use the same definition of mixed layer depth as the models. We have not included these observations in Figure 2.4, as they are less reliable on the continental shelf due to insufficient measurements.

In the ACC in summer (top row of Figure 2.3), MetROMS shows a ring of deeper mixed layers around 100 m surrounding the region stratified by sea ice meltwater. This spatial pattern agrees well with observations, but the magnitude somewhat disagrees, as MetROMS' mixed layers are too deep in the ACC and too shallow elsewhere. FESOM has a much more uniform summer mixed layer depth which is 45 m (corresponding to the fourth layer in z-coordinate regions) throughout most of the ACC, and generally shallower in the sigma-coordinate region of the continental shelf. Both models have significantly deeper mixed layers in winter (bottom row of Figure 2.3, note different colour scale) with the largest values in the northern branch of the ACC where mode and intermediate waters subduct. Observations indicate this feature should be strongest in the Pacific and Australian sectors. MetROMS shows local maxima in both regions, but the magnitude in the Pacific sector (approx. 250 m) is still quite low. FESOM only captures this feature in the Pacific sector, but

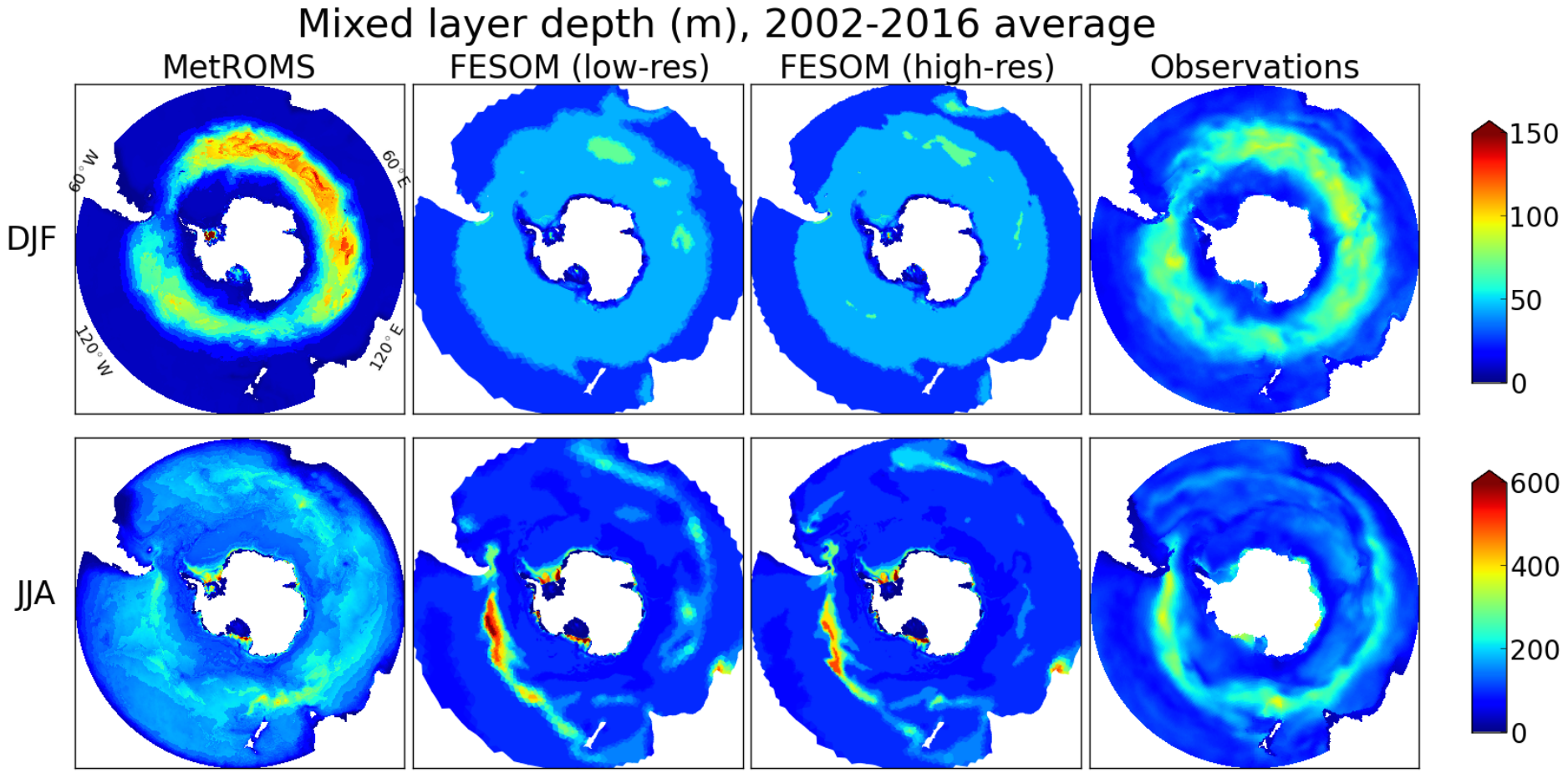

Figure 2.3: Mixed layer depth (m), calculated as the shallowest depth where potential density is at least 0.03 kg/m^3 greater than at the surface or ice shelf base. Results are shown for MetROMS, low-resolution FESOM, and high-resolution FESOM averaged over the years 2002-2016 for summer (DJF) and winter (JJA), as well as climatological observations by *Pellichero et al.* (2017) recalculated with the same definition of mixed layer depth. Note the different colour scale for summer and winter.

here it attains mixed layer depths in excess of 500 m which exceeds observations. This overestimation is less pronounced at high resolution. Elsewhere in the ACC, FESOM's mixed layer depths (approx. 100 m) more or less agree with observations, while in MetROMS they are too deep (approx. 200 m). The tendency of MetROMS to have deeper mixed layers than FESOM may be influenced by the differing surface stress between the two models (Section 2.2.7).

Zooming into the continental shelf, the water column is largely stratified in summer (top row of Figure 2.4) but shows active regions of dense water formation in winter (bottom row of Figure 2.4, note different colour scale). Both MetROMS and FESOM form dense water in the inner Ross and Weddell Seas, with regions of mixed layer depth exceeding 500 m. Convection appears to be stronger in FESOM where these regions are deeper and more widespread, due to stronger sea ice production (Section 2.4.2.3). In the Weddell Sea, dense water formation is split into two regions on either side of the Filchner-Ronne Ice Shelf front, with shallower mixed layers in the middle. In the Ross Sea, both models show somewhat stronger convection on the western side of the Ross Ice Shelf front, near McMurdo Sound, in agreement with observations (*Jacobs et al.*, 1979). A small region of dense water formation in western Prydz Bay, adjacent to the Amery Ice Shelf, is also present in both models. These regions are in agreement with observed bottom water formation sites (*Foldvik et al.*, 2004; *Gordon et al.*, 2015; *Herraiz-Borreguero et al.*, 2016). FESOM also exhibits deep mixed layers (> 500 m) in the Amundsen Sea, which were observed in 2012 but are not a consistent feature of this region (*Dutrieux et al.*, 2014). The presence of CDW on the Amundsen Sea continental shelf is sensitive to mixed layer depth, as a completely destratified water column filled with cold shelf water will prevent the development of a warmer bottom layer (*Petty et al.*, 2013, 2014). This mechanism has been proposed as a cause of cold biases in Amundsen Sea ice shelf cavities, and subsequent underestimation of ice shelf melt rates, in FESOM (*Nakayama et al.*, 2014). In our simulations these deep mixed layers have some dependence on resolution, as they cover nearly the entire Amundsen Sea at low resolution but are more restricted to the ice shelf fronts at high resolution. Similarly, low-resolution FESOM exhibits locally deepened mixed layers (approx. 250 m) near the southern entrance of George VI Ice Shelf in the Bellingshausen Sea, while this feature is absent at high resolution.

Mixed layer depths in ice shelf cavities show no significant seasonality (note the different colour scales for summer and winter in Figure 2.4), and are generally shallow (< 50 m) except near regions of persistent refreezing, which forms marine ice. This process increases salinity at the ice shelf base as fresh water is removed in the form of frazil ice, providing a buoyancy forcing. Regions of marine ice formation are detailed in Section 2.4.3, but their signature can be seen here. The most affected region is the

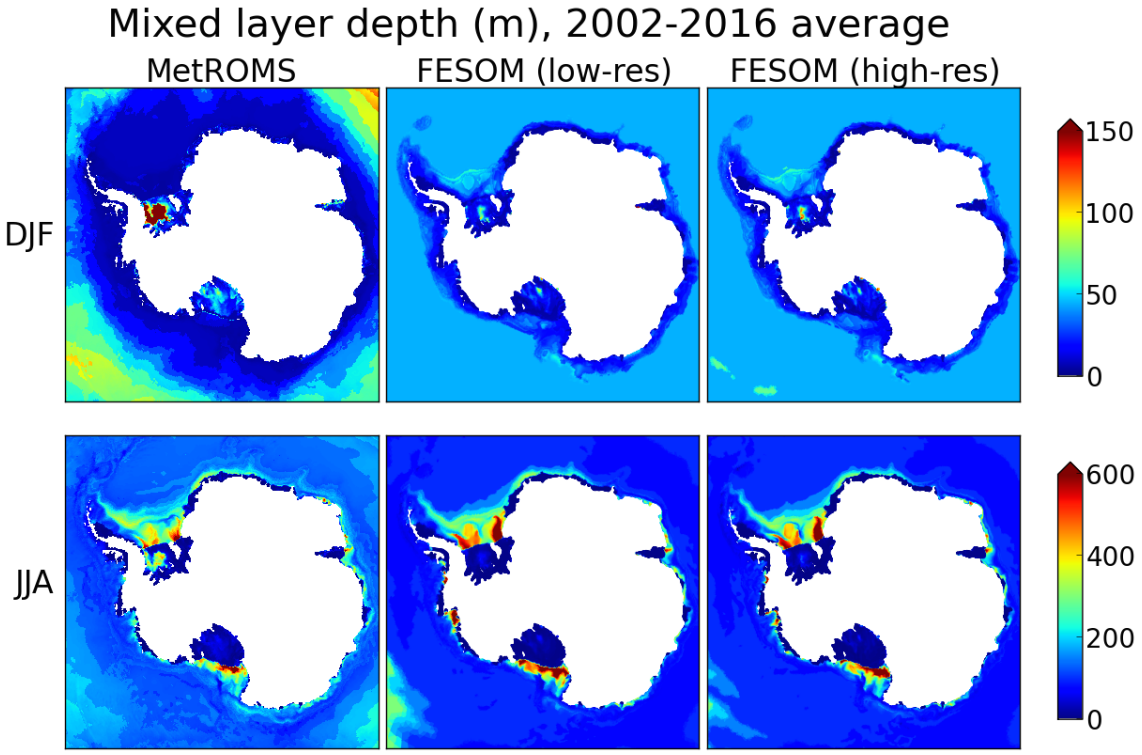

Figure 2.4: As Figure 2.3 for each model simulation, zoomed into the Antarctic continental shelf.

central Ronne Ice Shelf, which has mixed layer depths of 300-400 m in MetROMS, 50-80 m in low-resolution FESOM, and 70-120 m in high-resolution FESOM. Refreezing in this region is indeed stronger and more widespread in MetROMS than in FESOM (Section 2.4.3.1). All three simulations exhibit mixed layer depths exceeding 50 m in much of the Ross Ice Shelf, which has large areas of refreezing (Section 2.4.3.5). Only MetROMS shows increased mixed layer depths (approx. 70 m) along the western edge of the Amery Ice Shelf, which is a region of refreezing in MetROMS but not in FESOM (Section 2.4.3.3). Due to the lack of observations in ice shelf cavities, the true mixed layer depths in these regions are unknown.

2.4.1.3 Water mass properties

Ice shelf melt rates and sea ice formation both influence, and are influenced by, water mass properties on the continental shelf. Figure 2.5 plots the temperature/salinity (T/S) distribution south of 65°S in each simulation, averaged over 2002-2016, and colour-coded based on depth. In this section we identify the different water masses represented in Figure 2.5, and compare their properties between the two models. Due to a scarcity of year-round measurements on the continental shelf, it is not feasible to create a comparable figure using observations. However, limited observations of some water masses exist, and are compared to the simulated water mass properties

in the text below.

Just above the surface freezing temperature (dashed black lines in Figure 2.5, approx. $-2°C$) are two subsurface water masses (100-500 m depth). Low Salinity Shelf Water (LSSW, < 34.5 psu) and High Salinity Shelf Water (HSSW, > 34.5 psu) are both the result of sea ice formation, but HSSW is more affected by strong brine rejection. LSSW shows similar properties in all three simulations, with minimum salinities around 33.75 psu. HSSW is saltier in low-resolution FESOM (up to 35.1 psu) than in high-resolution FESOM (up to 35 psu). This is the main difference between the two FESOM simulations, which are otherwise very similar in terms of water mass properties. MetROMS has fresher HSSW than either FESOM simulation, with maximum salinities of approximately 34.8 psu. The differing salinity of HSSW in each simulation corresponds to the relative rates of sea ice production, analysed in Section 2.4.2.3.

At the higher end of the HSSW salinity range, and with temperatures up to $-1°C$, is surface water (0-50 m) from the Ross Sea polynya. This water mass is more prominent in the FESOM distributions than in MetROMS, due to its higher salinity. As with HSSW, FESOM's Ross Sea polynya is saltier at low resolution.

The remainder of the surface water (50 m or shallower) is Antarctic Surface Water (AASW) which has lower salinity, generally < 34 psu, with temperatures between the surface freezing point and $1°C$. A spread of points with particularly low salinity (< 33.7 psu) represents narrow embayments on the western side of the Antarctic Peninsula, from which meltwater cannot easily escape.

The water mass below the surface freezing temperature is called Ice Shelf Water (ISW). The only way that a water mass can fall below this line (neglecting numerical error in tracer advection) is from interaction with an ice shelf base. The freezing temperature of seawater decreases with depth, due to enhanced pressure, and at the deepest grounding lines it can approach $-3°C$. Water which melts or refreezes at the ice shelf base will retain this freezing temperature until it is modified by mixing or by melting/freezing at a different depth.

The temperature/salinity distributions of ISW follow distinct diagonals, where the slope is the dilution ratio of melting/freezing ice in seawater (*Gade*, 1979). The three deepest ice shelf cavities form the most prominent diagonals in Figure 2.5, which are separate from each other due to the differing salinities of ISW produced in each cavity. In order of increasing salinity, these diagonals represent the Amery, the Filchner-Ronne, and the Ross Ice Shelf cavities. ISW beneath the Ross Ice Shelf is saltiest in low-resolution FESOM and freshest in MetROMS, consistent with the HSSW which feeds the cavity. In the Amery and Filchner-Ronne cavities,

high-resolution FESOM displays deeper water masses than low-resolution FESOM, which is due to its better representation of deep ice near the grounding line (Sections 2.4.3.3 and 2.4.3.1).

The remaining water masses, in the deep Southern Ocean, have much longer residence times and are therefore not fully spun up. Comparing their simulated properties is useful to assess model drift (see also Section 2.4.1.4), but they should be evaluated with caution.

Antarctic Bottom Water (AABW) is the deepest water mass (1000 m or deeper) with simulated salinity > 34.5 psu and intermediate temperature (-1°C to 1.5°C). In both MetROMS and FESOM, the deepest AABW (below 2000 m) forks into two distinct branches on either side of 34.7 psu. The lower-salinity branch is Weddell Sea Bottom Water (WSBW) and the higher-salinity branch is Ross Sea Bottom Water (RSBW). Limited observations of these two water masses are available through the World Ocean Circulation Experiment (WOCE) Atlas (*Koltermann et al.*, 2011; *Talley*, 2007): track A23 through the Weddell Sea (considering only the section south of 65°S, which has approximate longitude 20°W, and below 2000 m) and track S4P through the Ross Sea (considering only the section between 150°E and 130°W, which has latitude 67°S, and below 2000 m). In these tracks, the salinity of WSBW ranges from 34.65 to 34.7 psu, and RSBW from 34.68 to 34.72 psu. The models' tendency for WSBW to be fresher than RSBW is therefore supported by observations, and both models are also in agreement with the observed salinity of WSBW. However, they both overestimate the salinity of RSBW compared to these observations, particularly FESOM which approaches 34.8 psu. Both water masses have more uniform salinity in MetROMS than in FESOM, which is reflected by narrower red lines in Figure 2.5.

The same WOCE tracks measure temperatures from -0.8°C to -0.2°C for WSBW,

Figure 2.5 (following page): Temperature-salinity distribution south of 65°S for MetROMS, low-resolution FESOM, and high-resolution FESOM, averaged over the years 2002-2016, and coloured based on depth (note nonlinear colour scale). Each grid box (in MetROMS) or triangular prism (in FESOM) is sorted into 1000×1000 temperature and salinity bins. The depth shown for each bin is the volume-weighted average of the depths of the grid boxes or triangular prisms within that bin. The dashed black line in each plot is the surface freezing point, which has a slightly different formulation between MetROMS and FESOM due to the different sea ice thermodynamics schemes. The dotted grey lines are potential density contours in kg/m^3-1000. Labels show different water masses: AABW = Antarctic Bottom Water, WSBW = Weddell Sea Bottom Water, RSBW = Ross Sea Bottom Water, CDW = Circumpolar Deep Water, MCDW = Modified Circumpolar Deep Water, LSSW = Low Salinity Shelf Water, HSSW = High Salinity Shelf Water, AASW = Antarctic Surface Water, ISW = Ice Shelf Water. Slanted labels below the freezing point line show specific ice shelves' contributions to ISW.

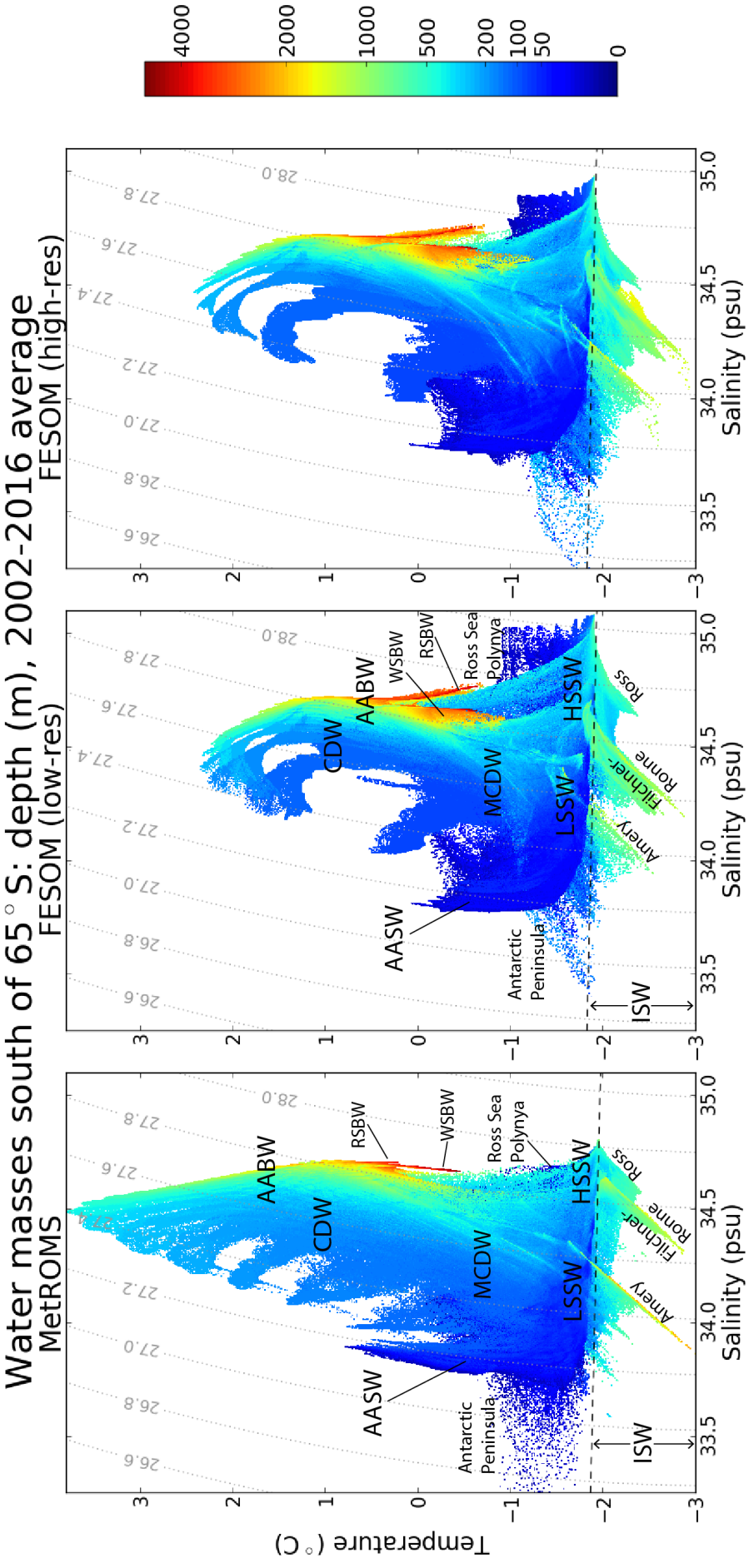
Water masses south of 65°S: depth (m), 2002-2016 average
MetROMS
FESOM (low-res)
FESOM (high-res)
4000
2000
1000
500
200
100
50
0
AABW
CDW
MCDW
LSSW
HSSW
AASW
ISW
RSBW
WSBW
Ross Sea Polynya
Antarctic Peninsula
Ross
Filchner-Ronne
Amery
Temperature (°C)
Salinity (psu)

and −0.4°C to 0.8°C for RSBW. The observed tendency for WSBW to be colder than RSBW is apparent in MetROMS (−0.5°C to 0.75°C for WSBW, 0.25°C to 0.75°C for RSBW) but the two water masses have approximately the same temperature in FESOM (−1°C to 1°C). The colder varieties of RSBW are absent in MetROMS, while FESOM reaches temperatures which are significantly colder than WOCE observations. In both models, simulated WSBW is too warm. However, these observations do not sample the full spatial extent of the water masses, so the true temperature and salinity may have a larger range.

Circumpolar Deep Water (CDW) is shallower than AABW (200-1000 m) and warmer (> 0°C). In MetROMS, the temperature of CDW can exceed 3°C, while it stays below approx. 2.5°C in FESOM. The warmer CDW in MetROMS is consistent with increased southward spreading of warmer CDW from the north around most of the continent, as discussed in Section 2.4.1.4. Observations of CDW in this region suggest a temperature range of 0.3°C to 2.5°C (*Schmidtko et al.*, 2014). Both models exhibit curling, finger-like structures on the low-salinity (left) side of the CDW distribution. These features represent meanders of the ACC over the boundary of 65°S, and these meanders transport different properties southward in different geographical locations. As CDW enters the subpolar gyres, it mixes with other water masses to produce cooler Modified Circumpolar Deep Water (MCDW).

2.4.1.4 Deep ocean drift

As our experiments do not include a full spin-up, it is useful to examine changes in the properties of deep water masses during the simulations, and compare the different ways the models are drifting. Some of these changes may be forced, as our forcing period 1992-2016 is not a steady-state climate. Other changes may be due to model deficiencies, such as artificial diapycnal mixing (by which water masses over-mix) or sea ice biases affecting deep water formation.

Figure 2.6 shows meridional slices of temperature and salinity along 0°E (Greenwich Meridian), comparing the ECCO2 initial conditions for January 1992 (a) with the January 2016 monthly average for MetROMS (b), low-resolution FESOM (c), and high-resolution FESOM (d). Greater smoothing of the FESOM bathymetry compared to MetROMS or ECCO2 is apparent, as deep ocean seamounts in the coarse-resolution regions north of 55°S are less pronounced. This is somewhat alleviated with higher resolution.

Antarctic Intermediate Water (AAIW), the subsurface water mass north of approx. 50°S characterised by relatively low salinity (< 34.5 psu, shown as a black contour in Figure 2.6), shows some degree of erosion in all three simulations. Difficulty

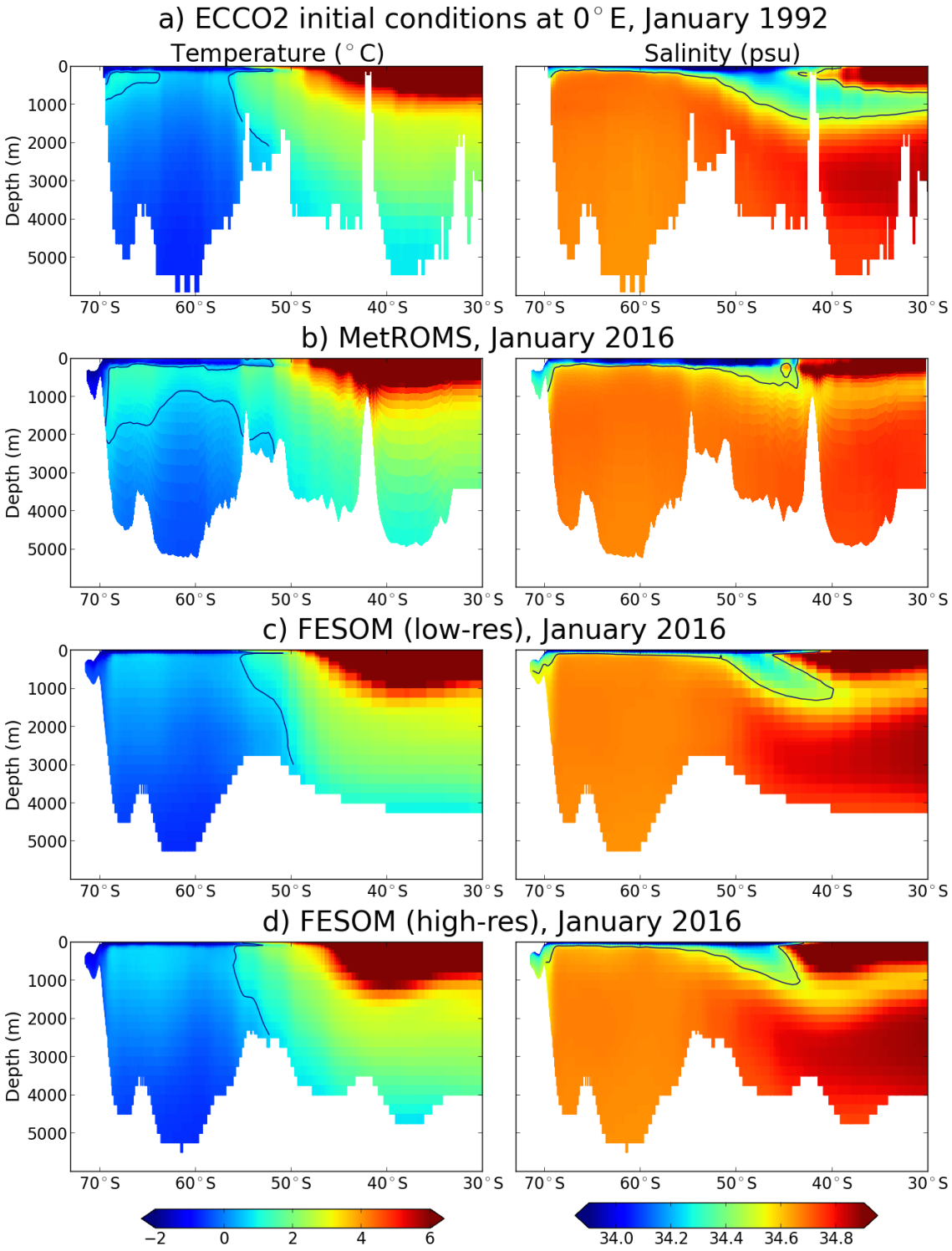

Figure 2.6: Temperature in °C (left) and salinity in psu (right) interpolated to 0°E (Greenwich Meridian). Black contours show the 0.75°C isotherm and the 34.5 psu isohaline. (a) Initial conditions for January 1992, from the ECCO2 reanalysis (*Menemenlis et al.*, 2008; *Wunsch et al.*, 2009). (b), (c), (d) January 2016 monthly average for MetROMS, low-resolution FESOM, and high-resolution FESOM respectively.

preserving AAIW is a very common problem among ocean models and is generally attributed to spurious diapycnal mixing (*England*, 1993; *England et al.*, 1993) with a potential contribution from errors in surface forcing (*Griffies et al.*, 2009). The

erosion is most severe in MetROMS, and is combined with freshening of the underlying North Atlantic Deep Water (NADW). Since MetROMS has terrain-following coordinates throughout the entire domain, whereas FESOM has z-coordinates everywhere except the Antarctic continental shelf, MetROMS would indeed be expected to be more prone to diapycnal mixing in the deep ocean (*Griffies et al.*, 2000), particularly around steep regions of bathymetry such as seamounts. The degree of AAIW erosion in MetROMS depends on the tracer advection scheme (*Marchesiello et al.*, 2009; *Lemarié et al.*, 2012), and our choice of the Akima advection scheme over the upwind third-order scheme (Section 2.2.4) was motivated by the less severe diapycnal mixing in Akima. In FESOM, AAIW is slightly better preserved at low resolution than at high resolution. This agrees with the results of *Marchesiello et al.* (2009) showing that in non-eddy-resolving regimes, spurious diapycnal mixing tends to increase as resolution is refined.

Another notable feature in Figure 2.6 is the larger volume of warm CDW (> 0.75°C, shown as a black contour) south of 60°S in MetROMS. A slight warming of the underlying AABW is also apparent, likely due to spurious entrainment of the CDW through diapycnal mixing. The cause of this increased CDW upwelling in MetROMS is not obvious. Warming and shoaling of CDW around most regions of Antarctica has been observed over recent decades, and attributed to changes in wind stress (*Schmidtko et al.*, 2014; *Spence et al.*, 2014, 2017). With these observations in mind, it is possible that this behaviour is due to MetROMS' surface exchange scheme, which leads to stronger surface stress than in FESOM (Section 2.2.7). However, CDW upwelling is also sensitive to the tracer advection scheme in MetROMS, and is more severe with the upwind third-order advection scheme (Section 3.7). Therefore, some component of numerical error could be an additional contributing factor.

2.4.1.5 Antarctic Slope Front

The Antarctic Slope Front (ASF), which separates the cold waters of the continental shelf from warmer offshore CDW, is a key determinant of cross-shelf transport (*Whitworth et al.*, 1998). The density gradient across the ASF is associated with a geostrophic current, the Antarctic Slope Current, which travels westward along the continental slope. This current is absent on the western side of the Antarctic Peninsula (including the Amundsen and Bellingshausen Seas), where observed cross-shelf transport of CDW is plentiful.

Examination of the barotropic zonal velocity simulated by each model reveals an Antarctic Slope Current of approximately 0.1 m/s travelling along the continental shelf break of East Antarctica and the Weddell Sea. The current is generally nar-

rower and faster in MetROMS than in either FESOM simulation, which may be due to MetROMS' rougher topography. In West Antarctica, all three simulations show significantly weakened zonal transport, in agreement with observations (*Whitworth et al.*, 1998). However, some westward flow is still apparent, especially in FESOM. This indicates that cross-shelf transport of CDW is inhibited in the Amundsen and Bellingshausen Seas.

2.4.2 Sea ice

2.4.2.1 Concentration and extent

Sea ice concentration (the fraction of each grid cell covered by ice) and extent (the area of grid cells with concentration exceeding 0.15) are the most convenient variables for model evaluation, due to the availability of satellite observations. These variables are largely a reflection of atmospheric conditions, but are also influenced by ocean processes, such as upwelling of warmer water from below, and the pathway of the ACC. Here we compare with the NOAA/NSIDC Climate Data Record of Passive Microwave Sea Ice Concentration (*Meier et al.*, 2013) and the NSIDC Sea Ice Index version 2 for sea ice extent (*Fetterrer et al.*, 2016). We examine monthly averages for February and September, which are the months of minimum and maximum Antarctic sea ice extent, respectively, over the period 1992-2015 (observations for 2016 were not yet available at the time of writing).

Figure 2.7 compares time-averaged sea ice concentration (a) as well as timeseries of total sea ice extent (b) for February and September, between NSIDC observations, MetROMS, low-resolution FESOM, and high-resolution FESOM. All three of our simulations underestimate the sea ice minimum, which is a common bias seen in other standalone ocean/sea-ice models forced with ERA-Interim (*Kusahara et al.*, 2017) as well as in fully coupled GCMs (*Turner et al.*, 2013b). The majority of simulated February sea ice is in the Weddell Sea (Figure 2.7a, top row), which agrees with observations, although in both FESOM simulations it extends too far northeast into the Weddell Gyre. Observed patches of coastal ice in the Amundsen and Bellingshausen Seas, as well as along the coast of East Antarctica, are largely absent in MetROMS and almost completely absent in FESOM. The timeseries in Figure 2.7b (top panel) reveal that all three simulations underestimate February total sea ice extent by approximately a factor of 2 compared to observations. However, they all display some of the observed interannual variability, such as the high in 2008 and the low in 2011, likely because observed sea ice cover is imprinted on the ERA-Interim atmospheric fields used to force the models.

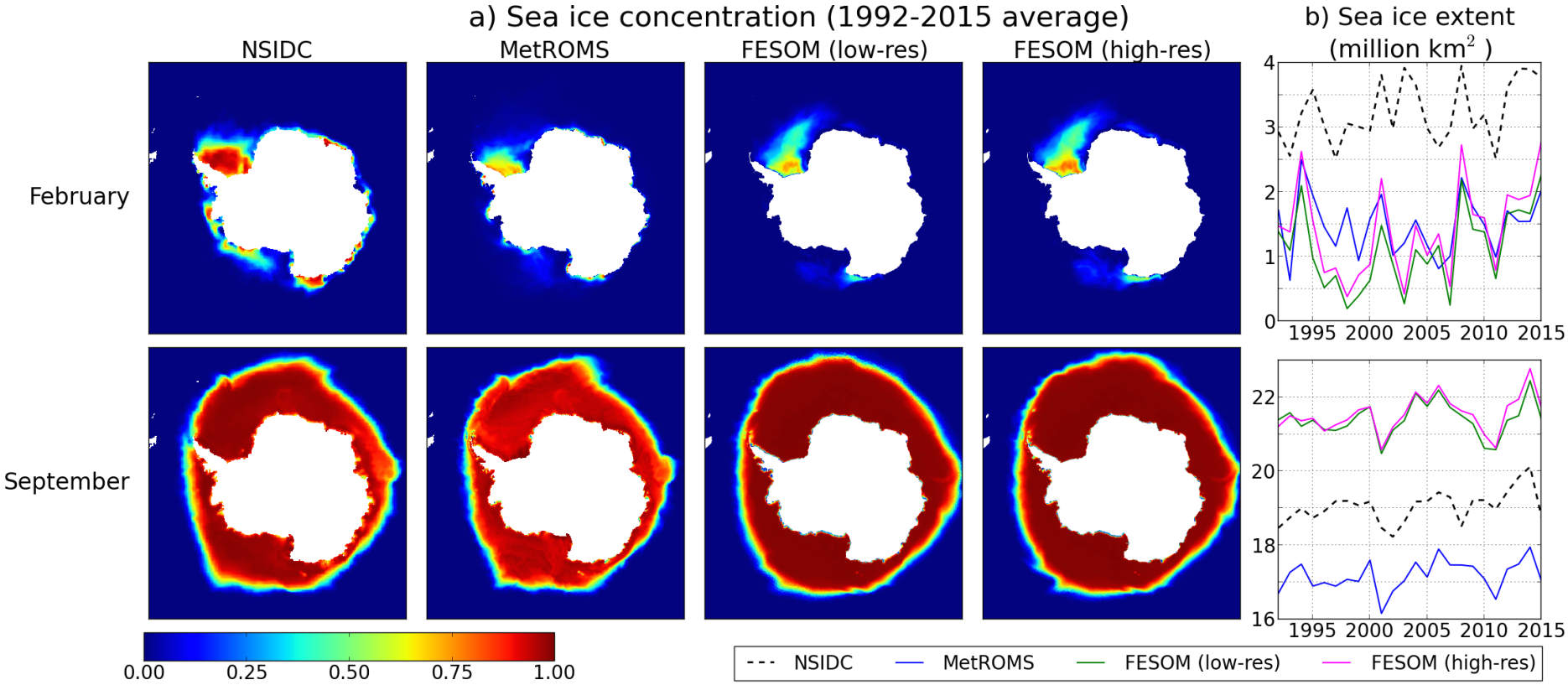

Figure 2.7: (a) 1992-2015 mean Antarctic sea ice concentration for February (top) and September (bottom), comparing NSIDC observations (NOAA/NSIDC Climate Data Record of Passive Microwave Sea Ice Concentration) (*Meier et al.*, 2013), MetROMS, low-resolution FESOM, and high-resolution FESOM. (b) Timeseries of total Antarctic sea ice extent in millions of km^2 for February (top) and September (bottom), comparing NSIDC observations (NSIDC Sea Ice Index version 2) (*Fetterrer et al.*, 2016), MetROMS, low-resolution FESOM, and high-resolution FESOM.

In FESOM, the sea ice minimum is slightly greater at high resolution. This difference is driven by summertime conditions in the southern Weddell Sea and the east coast of the Antarctic Peninsula. In the low-resolution mesh, smoother bathymetry near the peninsula allows a spurious southward excursion of the southern boundary of the ACC in summer, which carries warmer water into the region and melts more sea ice.

The sea ice maximum in September is well captured by all three simulations, which exhibit zonal asymmetry in line with observations (Figure 2.7a, bottom row). Sea ice concentrations throughout most of the ice pack are lower in MetROMS (approx. 0.94) than in both FESOM simulations (approx. 0.995). Observations from NSIDC fall in the middle (approx. 0.97), which is not significantly different from either model if observational uncertainty is considered. Nonetheless, this difference between the models influences the air-sea fluxes, which are modulated by the sea ice concentration. For example, the ocean in MetROMS will experience slightly greater wind stress than in FESOM, and therefore more turbulent mixing. In particular, sea ice concentration affects the air-sea heat fluxes, which may shed some light on the spurious Weddell Sea deep convection seen in MetROMS (without surface salinity restoring) but not in FESOM, as described in Section 2.3.3. Winter sea ice concentrations far below 1 in MetROMS allow frazil ice to form in the middle of the ice pack, rather than being restricted to coastal polynyas. This introduces a positive feedback by which brine rejection increases the sea surface salinity, causing destabilisation of the water column and upwelling of warm water, which melts surrounding sea ice and exposes more open water to the cold atmosphere. By contrast, FESOM's winter sea ice has concentrations near 1 almost everywhere, which shields the ocean surface from atmospheric heat fluxes and the resulting frazil ice formation and brine rejection. However, differences in vertical mixing schemes between the two models could also affect their sensitivity to spurious Weddell Sea deep convection (*Timmermann and Beckmann*, 2004), as discussed in Section 2.2.4.

While the general pattern of both models' September sea ice agrees with observations, the northern edge of the ice pack is too far south in MetROMS and too far north in FESOM, which is possibly related to differences in mixed layer depth (Section 2.4.1.2) or in the path of the ACC. These discrepancies are reflected in the timeseries of September sea ice extent (Figure 2.7b, bottom panel) where the NSIDC observations fall between the MetROMS and FESOM simulations. Interannual variability is well represented, with both models reproducing many of the highs and lows seen in the observations. No significant difference in winter sea ice cover is apparent between the low-resolution and high-resolution FESOM simulations.

2.4.2.2 Thickness

Sea ice thickness is influenced by both thermodynamics (sea ice formation and melt) and dynamics (sea ice transport). Observations of sea ice thickness are scarce and have large uncertainties (*Holland et al.*, 2014). A comprehensive evaluation of MetROMS and FESOM with respect to sea ice thickness is therefore difficult, although a comparison of the two models can still be made. Figure 2.8 shows seasonal averages of sea ice effective thickness (concentration times height) in each simulation, averaged over 1992-2016.

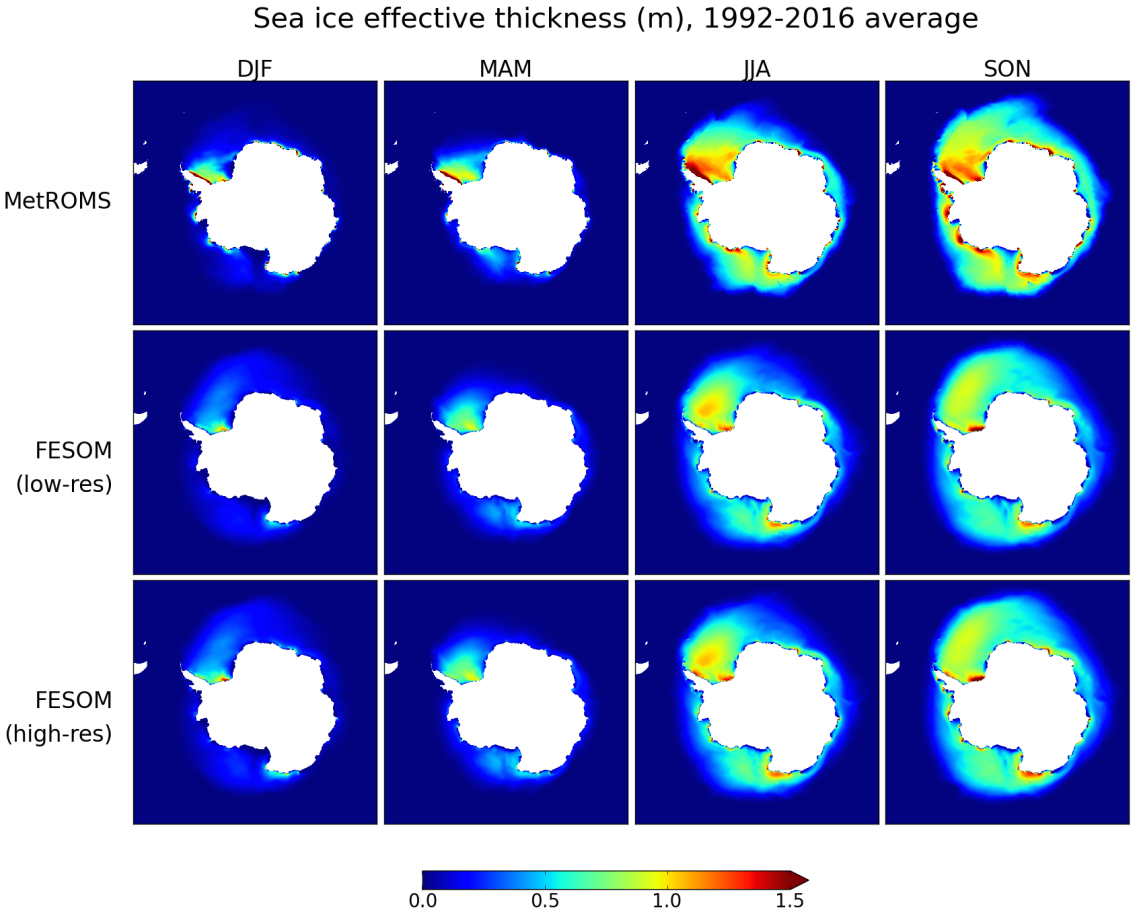

Figure 2.8: 1992-2016 mean seasonal Antarctic sea ice effective thickness (concentration times height, measured in metres) for MetROMS, low-resolution FESOM, and high-resolution FESOM.

Sea ice is generally thicker in MetROMS than in either FESOM simulation, particularly in the Weddell Sea, the Amundsen and Bellingshausen Seas, and along the coastline of East Antarctica. This difference may be due to complex dynamic processes such as ridging and rafting, which are not considered by single-layer sea ice models such as the one used in FESOM. However, FESOM's coastal sea ice is slightly thicker at high resolution, particularly in the Amundsen and Bellingshausen Seas.

In MetROMS, a particularly thick region of sea ice (approx. 3 m) exists on the western edge of the Weddell Sea, along the Antarctic Peninsula. This feature is also present in IceSAT observations (*Kurtz and Markus*, 2012; *Holland et al.*, 2014), and in-situ measurements of second-year ice in the western Weddell Sea find thicknesses of 2.4 to 2.9 m (*Haas et al.*, 2008). The region of thick ice is less pronounced, but still visible, in the high-resolution FESOM simulation. In low-resolution FESOM, the southward excursion of the southern boundary of the ACC in summer (see Section 2.4.2.1) prevents multi-year ice from building up in this region, so the feature is mostly absent. All three simulations show some sign of the Ronne Polynya in winter (JJA) and spring (SON), with thinner sea ice near the Ronne Depression. Thicker ice is present directly in front of the Filchner Ice Shelf, especially in FESOM.

Both models generally agree with the thickness climatology of *Worby et al.* (2008), who found that most Antarctic sea ice is thinner than 1 metre, with the exception of the western Weddell Sea where a significant proportion of ice is between 1 and 2 metres thick.

2.4.2.3 Sea ice production

As discussed in Section 2.4.1.2, the strength of sea ice formation is a key determinant of mixed layer depth, particularly in coastal polynyas on the Antarctic continental shelf where most sea ice is formed. Figure 2.9 compares sea ice production in each simulation to the observation-based estimate of *Tamura et al.* (2016). Sea ice production is integrated over 1° longitude bins on the continental shelf (defined as in Section 2.3.3), and averaged over the observed period 1992-2013. Note that *Tamura et al.*'s calculation is integrated daily, but sea ice production in the models is calculated based on 5-day averaged fluxes. These fluxes account for both melting and freezing, so sea ice production is only accumulated over 5-day periods with net freezing. As a result, diagnosed sea ice production in the models may be underestimated in regions which switch between melting and freezing on the 1-5 day timescale, but this discrepancy is expected to be small.

Compared to *Tamura et al.*, all three simulations overestimate sea ice production in the Ross and Weddell Seas; this bias is somewhat larger in FESOM and is slightly alleviated at high resolution. In Prydz Bay, all three simulations display a peak in sea ice formation; here FESOM agrees with observations, but MetROMS produces an overestimate. Further east in the Australian Sector, the models struggle to capture the observed peaks in sea ice formation seen in small coastal polynyas, such as the Dalton Polynya near 120°E. The Amundsen Polynya (approx. 110°W) is also not well captured by the models. However, further east in the Amundsen

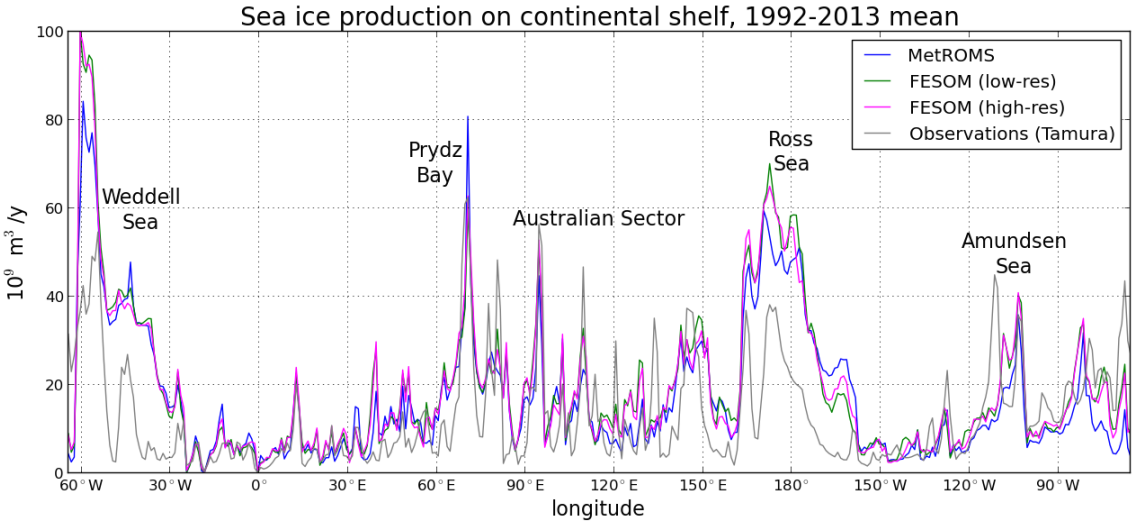

Figure 2.9: Sea ice production (10^9 m^3/y) on the continental shelf (defined as regions south of 60°S with bathymetry shallower than 1500 m), integrated over 1° longitude bins. Results are shown for MetROMS, low-resolution FESOM, high-resolution FESOM, and the observation-based estimate of *Tamura et al.* (2016) which uses ERA-Interim heat fluxes for its calculation.

Sea (approx. 105°W), near the Pine Island and Thwaites Ice Shelf fronts, FESOM overestimates sea ice production. The implications of these regional biases for water mass properties and ice shelf melt rates are discussed in Section 2.4.3.

Note that *Tamura et al.*'s calculation makes use of heat flux values from ERA-Interim, in addition to satellite observations of sea ice. Therefore, if biases in ERA-Interim are affecting our simulations, they may also be affecting *Tamura et al.*'s estimates to some extent.

2.4.3 Ice shelf cavities

Basal melting of Antarctic ice shelves comprises a substantial source of freshwater entering the Southern Ocean. *Rignot et al.* (2013) estimate, based on observations for the period 2003-2008, that total ice shelf basal mass loss occurs at a rate of 1325±235 Gt/y. This estimate is prone to errors in the calculation of basal melting at ice shelf fronts (where separating basal melting from calving is not straightforward) and relies on atmospheric reanalyses which in turn have limited observations from which to downscale. Another observation-based estimate, by *Depoorter et al.* (2013), is similar at 1454 ± 174 Gt/y.

All three model simulations underestimate total ice shelf basal mass loss with respect to these observations, roughly by a factor of two. The simulated mass loss, averaged over 2002-2016, is 642 Gt/y for MetROMS, 586 Gt/y for low-resolution FESOM, and 739 Gt/y for high-resolution FESOM. A closer examination of individual ice shelves

	MetROMS	**FESOM low-res**	**FESOM high-res**	**Rignot et al.**
1. Filchner-Ronne	46.0 (-)	113.8	115.4	155.4 ± 45
2. Eastern Weddell Region				
Brunt & Riiser-Larsen	29.2 (+)	33.4 (+)	34.6 (+)	9.7 ± 16
Fimbul & Jelbart & Ekstrom	30.3	41.8 (+)	52.4 (+)	26.8 ± 14
Nivl	3.4	5.4	5.9	3.9 ± 2
Lazarev	2.9 (-)	4.9	4.9	6.3 ± 2
Baudouin & Borchgevink	28.4	35.7	36.5	21.6 ± 18
Prince Harald	5.4 (+)	2.1 (+)	2.6 (+)	-2 ± 3
3. Amery	91.0 (+)	71.0 (+)	71.4 (+)	35.5 ± 23
4. Australian Sector				
West	11.5 (-)	10.2 (-)	12.7 (-)	27.2 ± 10
Shackleton	14.3 (-)	17.4 (-)	22.7 (-)	72.6 ± 15
Totten & Moscow University	9.5 (-)	4.4 (-)	9.3 (-)	90.6 ± 8
Mertz	4.1 (-)	2.6 (-)	4.6 (-)	7.9 ± 3
5. Ross Sea				
Ross	53.8	95.1 (+)	112.0 (+)	47.7 ± 34
Sulzberger	14.0 (-)	6.5 (-)	9.2 (-)	18.2 ± 3
Nickerson	5.3	2.0 (-)	4.1	4.2 ± 2
6. Amundsen Sea				
Getz	88.1 (-)	21.3 (-)	30.6 (-)	144.9 ± 14
Dotson	9.1 (-)	1.6 (-)	3.7 (-)	45.2 ± 4
Thwaites	7.4 (-)	2.5 (-)	5.9 (-)	97.5 ± 7
Pine Island	20.5 (-)	1.9 (-)	9.5 (-)	101.2 ± 8
7. Bellingshausen Sea				
Abbot	25.0 (-)	21.9 (-)	36.3	51.8 ± 19
Stange	6.1 (-)	5.1 (-)	10.9 (-)	28.0 ± 6
George VI	48.4 (-)	14.0 (-)	32.5 (-)	89.0 ± 17
Wilkins	8.1	8.6	11.3	18.4 ± 17
8. Larsen Ice Shelves				
Larsen C	18.2	35.2	54.7	20.7 ± 67
Larsen D	2.9	2.1	3.3	1.4 ± 14
Total Antarctica	642 (-)	586 (-)	739 (-)	1325 ± 235

Table 2.1: Ice shelf basal mass loss (Gt/y) for all ice shelves with area exceeding 5000 km^2 as measured by *Rignot et al.* (2013). In some cases multiple ice shelves have been combined (eg Brunt & Riiser-Larsen) because the boundaries between them in the model domains are not distinct. The ice shelves have been sorted into the eight regions analysed in Section 2.4.3. Values are shown for the MetROMS, low-resolution FESOM, and high-resolution FESOM simulations averaged over the years 2002-2016, and are compared to the range of observational estimates given by *Rignot et al.* for the period 2003-2008. Mass loss values from model simulations are marked with (-) or (+) if they fall below or above (respectively) the range given by *Rignot et al.*

shows that the bias in our simulations is a regional phenomenon. Table 2.1 compares simulated basal mass loss to *Rignot et al.*'s estimates for 25 ice shelves, organised into eight regions. The model biases are summarised in Figure 2.10, which plots the difference between the simulated values and *Rignot et al.*'s central estimates, as well as the uncertainty range, for each ice shelf. All three simulations underestimate mass loss for ice shelves in the Amundsen Sea, Bellingshausen Sea, and Australian Sector. These three regions include many warm-cavity ice shelves which, despite their small areas, exhibit substantial basal mass loss in observations. Ice shelves

in the remaining five regions generally show either agreement between our model simulations and *Rignot et al.*'s observations, or an overestimation of mass loss by the models (with the main exception being MetROMS' underestimation of the Filchner-Ronne Ice Shelf). The following sections will analyse these eight regions in more detail.

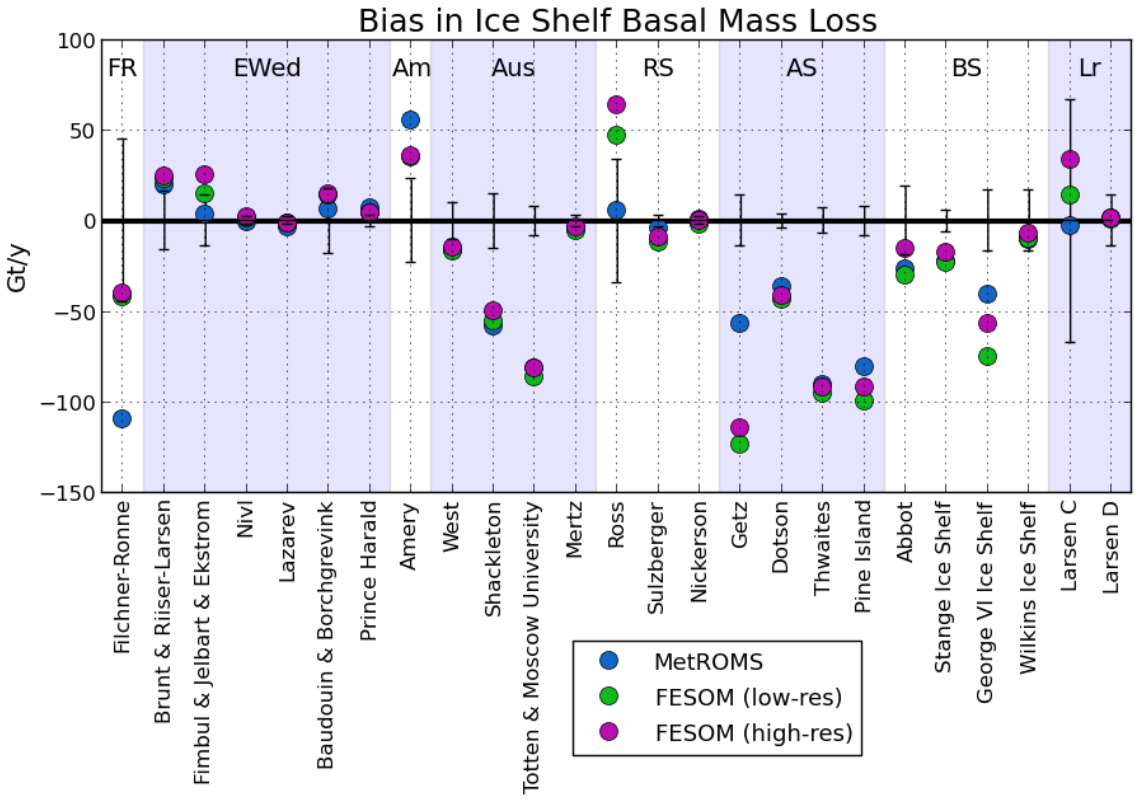

Figure 2.10: Difference between simulated ice shelf basal mass loss (2002-2016 average) and the central estimate given by *Rignot et al.* (2013) for each ice shelf in Table 2.1, in MetROMS (blue), low-resolution FESOM (purple), and high-resolution FESOM (green). The uncertainty ranges of *Rignot et al.* are also shown with black error bars. The eight regions specified in Table 2.1 are labelled as follows: FR = Filchner-Ronne, EWed = Eastern Weddell Region, Am = Amery, Aus = Australian Sector, RS = Ross Sea, AS = Amundsen Sea, BS = Bellingshausen Sea, Lr = Larsen Ice Shelves.

While biases in ice shelf mass loss are largely region-specific, several overarching factors are worth mentioning here. First, neither MetROMS nor FESOM considers the effects of tides. Since the heat and salt transfer coefficients in both models depend on ocean velocity adjacent to the ice shelf base, tidal currents would be expected to increase both melting and refreezing rates in all ice shelf cavities. Tides also cause enhanced vertical mixing, which further influences melt rates (*Gwyther et al.*, 2016). Next, insufficient horizontal resolution is likely to cause an underestimation of eddy transport of warm CDW onto the continental shelf; this phenomenon is discussed more fully in Section 2.4.3.6. Finally, biases in the ERA-Interim atmospheric forcing could affect water mass properties and therefore ice shelf melt

rates; this is difficult to test due to a lack of observations around Antarctica. Note also that the area of a given ice shelf in model simulations does not necessarily agree with the area used in *Rignot et al.*'s calculations, particularly for small ice shelves which are not well resolved by the models. Such disagreements may bias our comparison. However, a comparison of area-averaged basal melt rates rather than area-integrated basal mass loss (not shown) shows essentially the same biases. Furthermore, a comparison with the mass loss estimates of *Depoorter et al.* (2013) yields a similar pattern of biases.

The average annual minimum in total basal mass loss (calculated over 5-day averages between 2002 and 2016) is 490 Gt/y for MetROMS, 323 Gt/y for low-resolution FESOM, and 379 Gt/y for high-resolution FESOM. The corresponding average annual maximum values are 1017 Gt/y, 1589 Gt/y, and 1988 Gt/y respectively. Note that the seasonal cycle is larger in FESOM than in MetROMS, which is likely related to greater summertime melting near ice shelf fronts. Transport of warm AASW into ice shelf cavities is enhanced by FESOM's more significant smoothing of the ice shelf front, as discussed in the following sections.

Interannual variability in ice shelf melting is relatively small. In all three simulations, the standard deviation in annually averaged mass loss from individual ice shelves is typically 10-20% of their 2002-2016 mean. Furthermore, the mean and median of the annually averaged values are typically very similar (within 10% of each other) which indicates that the long-term average is not skewed by a few years of unusually high or low melt. The main exceptions are the Larsen C and D Ice Shelves in FESOM, which experience large spikes in mass loss in some summers but not others. This behaviour is tied to the sea ice cover, as FESOM occasionally has ice-free summers along the peninsula, allowing warmer AASW to develop. In MetROMS, the Shackleton Ice Shelf shows the highest interannual variability in mass loss. Here a few cells on the western edge of the ice shelf are undercut by the Antarctic Coastal Current, bringing periodic pulses of high melt.

To aid our intercomparison, we have categorised the water in ice shelf cavities into five water masses based on discrete temperature and salinity bounds, defined in Table 2.2: ISW, MCDW, HSSW, LSSW, and AASW. Figure 2.11 plots the percent volume of each water mass in ice shelf cavities, for the eight regions specified in Table 2.1 as well as the total for all Antarctic ice shelf cavities. These proportions are based on temperature and salinity fields averaged over 2002-2016 for each simulation, and neglect the seasonal cycle. AASW, which is mostly a summertime phenomenon, may therefore be obscured. For Antarctica as a whole (Figure 2.11i), both FESOM simulations have more MCDW and HSSW, and less ISW and LSSW, than in MetROMS. These differences are more pronounced in low-resolution FE-

SOM, while high-resolution FESOM is more similar to MetROMS. The water mass proportions in each region (Figure 2.11a to 2.11h), and consequently the reasons for the overarching differences between the three models, will be analysed in the following sections.

	T (°C)	S (psu)
ISW	$T < T_f$	
AASW	$T \geq T_f$	$S < 34$
LSSW	$T_f \leq T \leq -1.5$	$34 \leq S < 34.5$
HSSW	$T_f \leq T \leq -1.5$	$S \geq 34.5$
MCDW	$T > -1.5$	$S \geq 34$

Table 2.2: Potential temperature (T) and salinity (S) ranges used to categorise water masses in ice shelf cavities in Figure 2.11. T_f is the surface freezing point as in Figure 2.5. All acronyms are the same as in Figure 2.5.

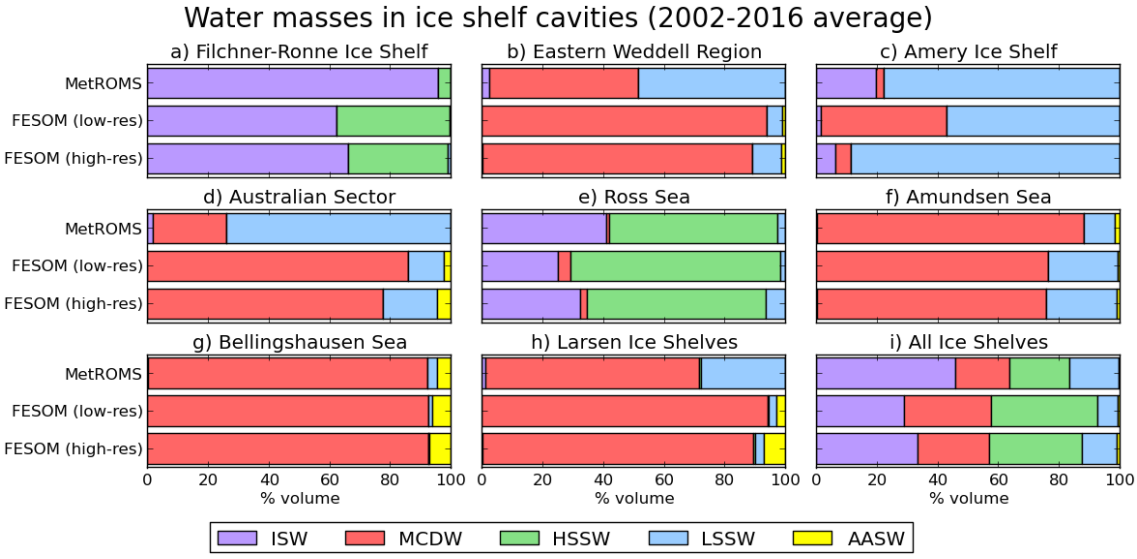

Figure 2.11: Proportions of different water masses (defined in Table 2.2) as percentage volumes in ice shelf cavities for each simulation, based on temperature and salinity fields averaged over 2002-2016. Results are shown for the eight regions specified in Table 2.1 (a-h) as well as the total for all Antarctic ice shelves (i). All acronyms are the same as in Figure 2.5.

2.4.3.1 Filchner-Ronne Ice Shelf

The Filchner-Ronne Ice Shelf (FRIS) is the largest ice shelf in the Weddell Sea region and the second largest (by area) in Antarctica. However, its melt rates are quite low away from the grounding line, leading to relatively modest basal mass loss for its size. For both FESOM simulations, basal mass loss for FRIS falls within the range of observations given by *Rignot et al.* (Table 2.1.1). MetROMS significantly underestimates this rate, simulating about half the lower bound given by *Rignot et al.*. Figure 2.12a shows the spatial distribution of this mass loss in the three

simulations, with two-dimensional ice shelf melt/freeze fields averaged over 2002-2016.

Circulation patterns in the FRIS cavity have been inferred from a few sub-ice shelf observations (*Nicholls and Østerhus*, 2004; *Nicholls and Johnson*, 2001) and feature anticyclonic flow around Berkner Island, a cyclonic gyre in the Filchner Ice Shelf cavity, and HSSW inflow into the western Ronne Ice Shelf cavity via the Ronne Depression. MetROMS displays the anticyclonic flow around Berkner Island (Figure 2.12b), which is stronger on the western and southern sides, corresponding with locally increased melt rates. Circulation in the Filchner Ice Shelf cavity is weak but mostly cyclonic. However, the observed refreezing immediately east of Berkner Island (*Joughin and Padman*, 2003; *Rignot et al.*, 2013) is absent.

In FESOM, southward flow of HSSW on the western flank of the Filchner Depression drives a relatively strong anticyclonic gyre in the Filchner cavity. Melting is therefore apparent on the western side of the Filchner Ice Shelf front, with refreezing associated with outflow in the east. This pattern is opposite to observations and may be caused by FESOM's strong HSSW formation in the Filchner Depression, as evidenced by deep wintertime mixed layers in Figure 2.4. Melting at the Filchner Ice Shelf front is stronger in the low-resolution FESOM simulation than the high-resolution, with vigorous melting immediately east of Berkner Island. This feature is likely due to the slightly smoother ice shelf front in the low-resolution simulation (Figure 2.12e), which allows for greater transport of warm AASW into the cavity. At the southern coast of Berkner Island, FESOM's inflowing current splits into two branches, one continuing westward along the southern edge of the Ronne Ice Shelf cavity, and the other turning northward to continue the cyclonic flow around the island.

In the Ronne Ice Shelf cavity, observations by *Rignot et al.* as well as *Joughin and Padman* (2003) indicate significant areas of refreezing in the interior combined with melting at the ice shelf front. MetROMS captures both of these features. FESOM exhibits refreezing in the interior (albeit weaker than in MetROMS) but also at the ice shelf front, with a band of melting between the two regions. At the western edge of the cavity, a narrow band of refreezing associated with outflow is present in both MetROMS and FESOM, which agrees with observations by *Nicholls et al.* (2004).

In MetROMS, the strongest melting occurs in the pockets of deep ice at the back of the cavity. Compared to the remote sensing observations of *Joughin and Padman* (2003), MetROMS overestimates melt rates in these regions of the Filchner Ice Shelf, but underestimates them for the Ronne Ice Shelf. In FESOM, melting is weaker and more widespread along these grounding line regions, which more or less agrees with *Joughin and Padman*'s observations for the Filchner grounding line, although melt

rates in the interior Filchner Ice Shelf are too high. These grounding line regions are largely bypassed by the gyre transporting HSSW through the Filchner cavity, and therefore remain cooler and fresher. There may also be a small effect from FESOM's greater smoothing of the ice shelf draft, which causes the deepest ice to shoal by approximately 100 m. All else being equal, shallower ice melts more slowly due to its increased in-situ freezing point. In this situation, the increase is approximately 0.076°C, which is likely to be overwhelmed by other factors. The pockets of deep ice are better preserved in the high-resolution FESOM mesh than the low-resolution, and show no significant changes in melt rate. Instead, the slightly thinner water column further inhibits HSSW transport to these grounding line regions, where the temperature is slightly cooler. This tendency for changes in velocity to offset changes in the in-situ freezing point in the FRIS cavity was demonstrated by *Timmermann and Goeller* (2017) for a fully coupled configuration with an evolving ice shelf draft.

Other FESOM simulations focusing on FRIS exhibit somewhat different melt rate patterns. For example, *Timmermann and Goeller* (2017) simulate more vigorous melting near the grounding line, as well as a larger area of refreezing in the interior Ronne Ice Shelf which does not quite extend to the ice shelf front. However, these simulations used a different atmospheric forcing dataset, which may influence sea ice formation patterns and consequently sub-ice shelf circulation. Additionally, the mesh used by *Timmermann and Goeller* has higher resolution at the FRIS grounding line (approx. 1 km), which may allow for better representation of ocean velocities beneath the deepest ice.

With respect to water mass properties, Figure 2.11a reveals that the FRIS cavity in MetROMS is almost entirely filled with ISW, with a small contribution from HSSW ($< 5\%$). This dominance of ISW indicates that it has a relatively long simulated residence time in the FRIS cavity. FESOM's stronger dense water formation in the Filchner Depression means that HSSW has a much larger presence (approx. 40%), indicating more rapid flushing of the cavity; this effect is slightly lessened at high resolution. As a result, FESOM has warmer and saltier bottom water than MetROMS in most of the FRIS cavity (Figures 2.12c and 2.12d). However, observations south of Berkner Island (*Nicholls and Johnson*, 2001) reveal bottom

Figure 2.12 (following page): The Filchner-Ronne Ice Shelf cavity in MetROMS (left), low-resolution FESOM (middle), and high-resolution FESOM (right). All fields are averaged over the period 2002-2016. (a) Ice shelf melt rate (m/y). (b) Vertically averaged ocean velocity (m/s), where the colour scale shows magnitude and the arrows show direction. (c) Bottom water temperature (°C). (d) Bottom water salinity (psu). (e) Ice shelf draft (m) as seen by each model. In (b), (c), and (d), the ice shelf front is contoured in black. Rn = Ronne Ice Shelf, Fi = Filchner Ice Shelf, RDp = Ronne Depression, FDp = Filchner Depression, BI = Berkner Island.

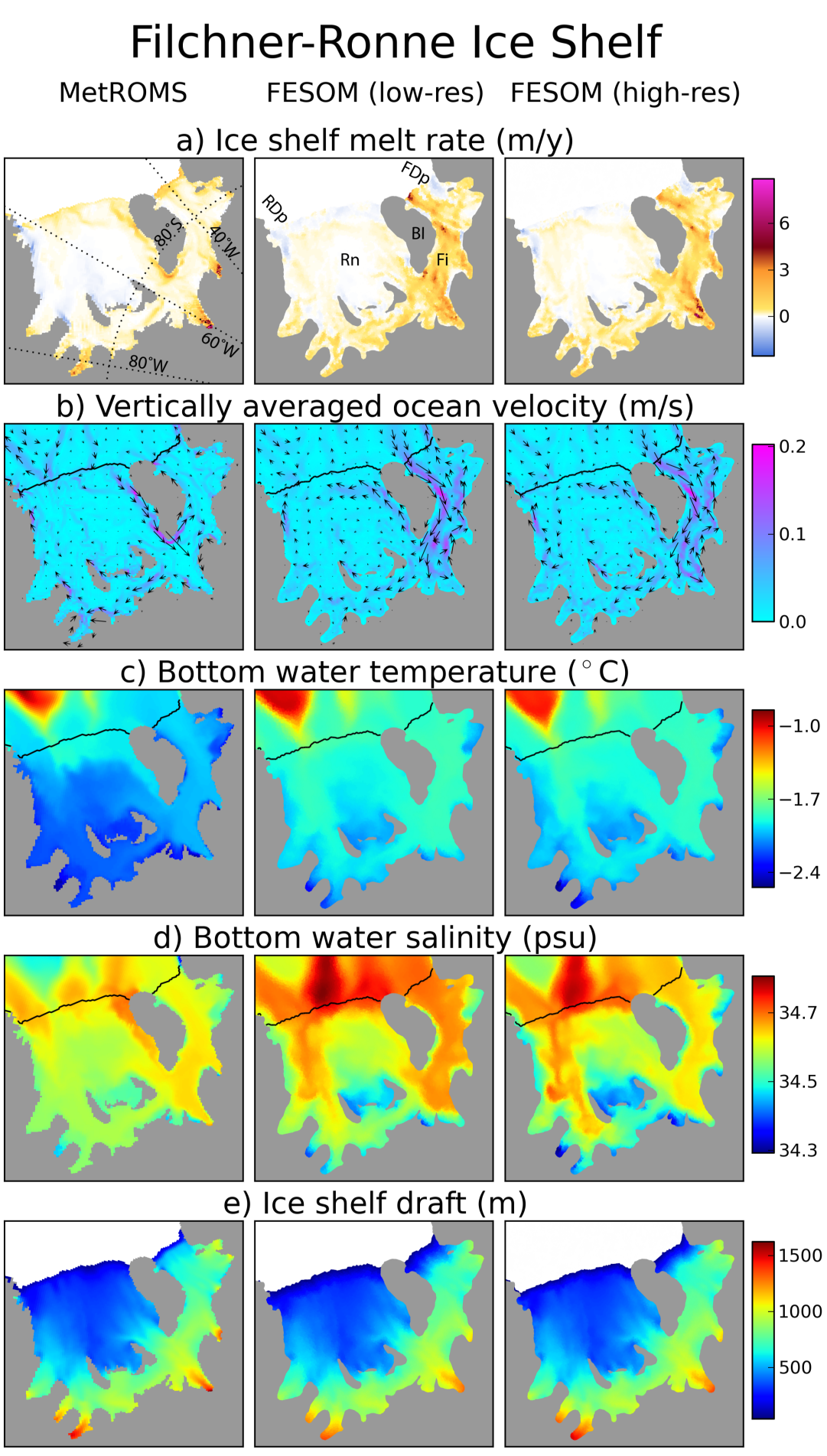
Filchner-Ronne Ice Shelf
MetROMS
FESOM (low-res)
FESOM (high-res)
a) Ice shelf melt rate (m/y)
80°S
40°W
60°W
80°W
RDp
FDp
Bl
Rn
Fi
6
3
0
b) Vertically averaged ocean velocity (m/s)
0.2
0.1
0.0
c) Bottom water temperature (°C)
−1.0
−1.7
−2.4
d) Bottom water salinity (psu)
34.7
34.5
34.3
e) Ice shelf draft (m)
1500
1000
500

water temperatures around −2.2°C, which implies that both MetROMS and FESOM are too warm. The fact that MetROMS still underestimates total basal mass loss, despite a warm bias, suggests that its relatively weak circulation and long residence time are to blame for low melt rates.

The exceptionally large tides of the Weddell Sea (*Foldvik et al.*, 1990), with tidal velocities up to 1 m/s (*Robertson et al.*, 1998), are understood to have a strong impact on FRIS melt rates. Indeed, inclusion of tides in one regional model of the southern Weddell Sea caused basal mass loss from FRIS to approximately double (*Makinson et al.*, 2011). Another model (*Mueller et al.*, 2018) found no significant change in total mass loss, but rather an amplification of existing melt and freeze patterns. As mentioned previously, neither MetROMS nor FESOM considers these effects.

2.4.3.2 Eastern Weddell Region

We define the Eastern Weddell region as the line of ice shelves east of FRIS, stretching along the coastline of Queen Maud Land, from the Brunt Ice Shelf in the west to the Prince Harald Ice Shelf in the east. Compared with the values given by *Rignot et al.* (Table 2.1.2), all three simulations overestimate basal mass loss from the combined Brunt and Riiser-Larsen Ice Shelves as well as the Prince Harald Ice Shelf. Both FESOM simulations also overestimate mass loss from the combined Fimbul, Jelbart, and Ekstrom Ice Shelves. Simulated mass loss for the other ice shelves in the Eastern Weddell region generally falls within the observational estimates. However, some of the ice shelves are so small that they are barely resolved by the MetROMS grid or the low-resolution FESOM mesh, particularly the Nivl, Lazarev, and Prince Harald Ice Shelves.

A notable feature of the Eastern Weddell region is an overhang of some ice shelf fronts past the continental shelf break, which in our simulations allows the Antarctic Coastal Current to undercut the ice shelf (Figure 2.13b). This process is particularly strong in MetROMS, where increased velocity corresponds with vigorous melting at the fronts of the Brunt, Riiser-Larsen, and Fimbul Ice Shelves, with weaker melting or refreezing further back in the cavities (Figure 2.13a). This pattern more or less agrees with observations by *Langley et al.* (2014) for the Fimbul Ice Shelf. FESOM has a weaker coastal current than MetROMS in this region, and melting is less concentrated at the ice shelf fronts. In general, melting is stronger in the high-resolution FESOM simulation than the low-resolution.

Observations of Eastern Weddell ice shelf cavities are scarce, but mooring data does exist for the Fimbul Ice Shelf (*Hattermann et al.*, 2012). It reveals a generally

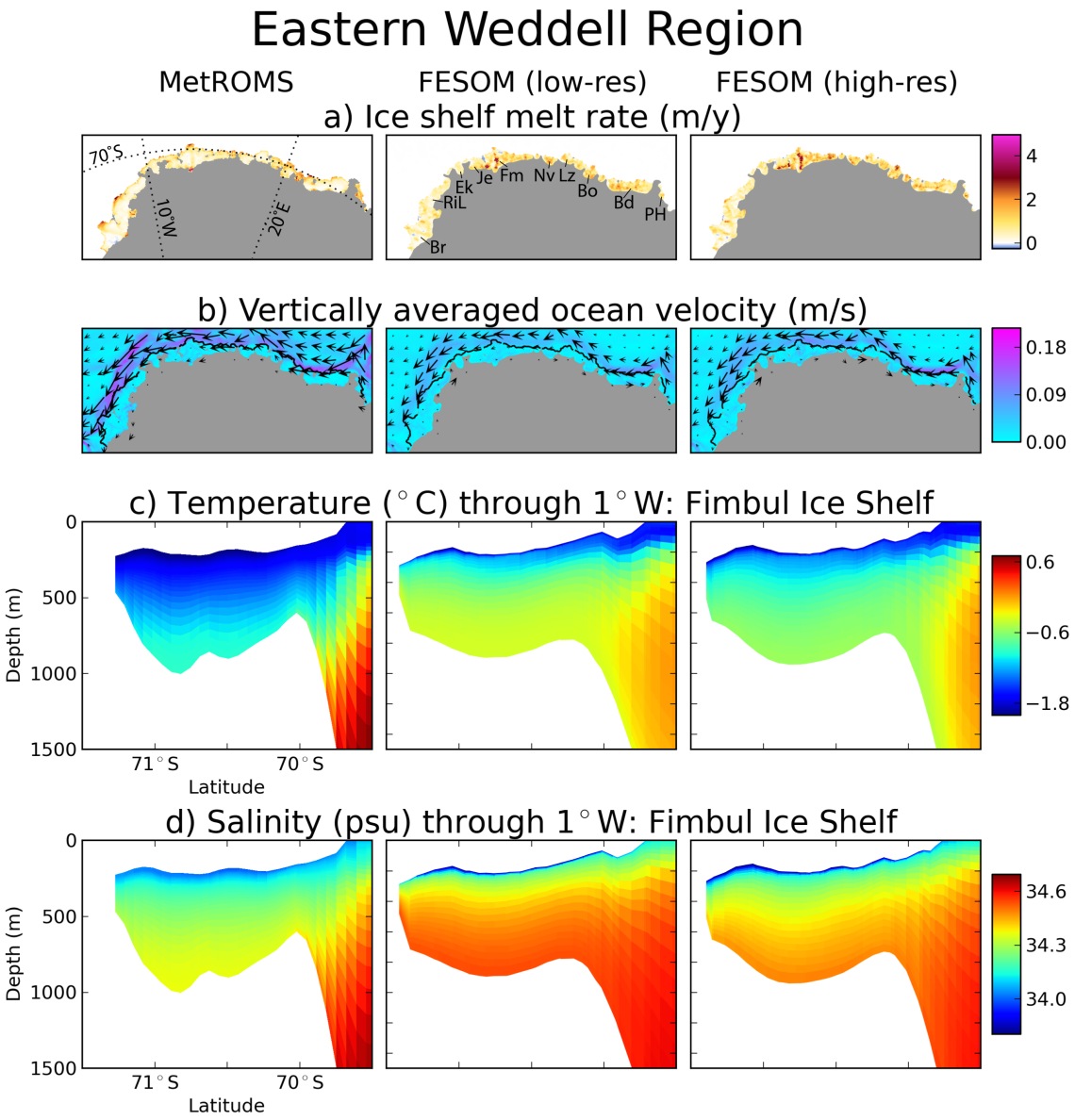

Figure 2.13: (a), (b): As Figure 2.12a and 2.12b for the Eastern Weddell ice shelf cavities. (c) Temperature (°C) and (d) salinity (psu) interpolated to 1°W, through the Fimbul Ice Shelf. Br = Brunt Ice Shelf, RiL = Riiser-Larsen Ice Shelf, Ek = Ekstrm Ice Shelf, Je = Jelbart Ice Shelf, Fm = Fimbul Ice Shelf, Nv = Nivl Ice Shelf, Lz = Lazarev Ice Shelf, Bo = Borchgrevink Ice Shelf, Bd = Baudouin Ice Shelf, PH = Prince Harald Ice Shelf.

cold cavity with temperatures around −1.9°C and salinities around 34.3 psu, with occasional intrusions of warmer, saltier MCDW at depth, and seasonal melting at the ice shelf front driven by AASW. For comparison, Figures 2.13c and 2.13d plot meridional slices of simulated temperature and salinity through the Fimbul Ice Shelf cavity at 1°W. All three of our simulations show a warmer and (in the case of FESOM) saltier cavity than seen in the range of mooring readings (see Figure 2 of *Hattermann et al.*). It appears that MCDW is mixing too readily into the cavity, particularly in FESOM where the continental shelf break is more gently sloping due to smoothing of the bathymetry (Figures 2.13c and 2.13d, first column vs.

second and third columns). The high-resolution FESOM mesh has a slightly steeper continental shelf break than the low-resolution mesh, and the cavity is slightly cooler and fresher, indicating that oversmoothing of the continental shelf break may be a contributing factor in the increased transport of MCDW.

For the Eastern Weddell region as a whole, FESOM has proportionally more MCDW in ice shelf cavities than MetROMS, as evidenced by Figure 2.11b. As for the Fimbul, this effect is slightly lessened at high resolution. The Eastern Weddell cavities in MetROMS are more dominated by LSSW (approx. 50%) with a small amount of ISW ($< 5\%$). Traces of AASW are present in both FESOM simulations but not in MetROMS, although it may still exist on a seasonal basis.

2.4.3.3 Amery Ice Shelf

All three model simulations overestimate basal mass loss from the Amery Ice Shelf, by about 50% above the upper bound given by *Rignot et al.* for MetROMS, and about 20% for both FESOM simulations (Table 2.1.3). However, the sources of this bias are quite different between the two models.

In MetROMS, the majority of melting occurs near the grounding line (Figure 2.14a), which has one of the deepest ice shelf drafts in Antarctica (> 2000 m) (*Galton-Fenzi et al.*, 2008). A cyclonic circulation pattern is apparent (Figure 2.14b), with refreezing along the western side of the cavity. This spatial distribution of melting and freezing agrees with observations (*Wen et al.*, 2010; *Rignot et al.*, 2013) and with previous modelling (*Galton-Fenzi et al.*, 2012), but the melting at the grounding line appears to be too strong (> 40 m/y) and the refreezing too weak and over an insufficient area. These two biases combine to cause the overestimation of total basal mass loss simulated by MetROMS. It is possible that both biases could be addressed with an explicit frazil ice parameterisation with multiple size classes, as *Galton-Fenzi et al.* (2012) showed that including such a parameterisation in ROMS both reduced melting at the grounding line and increased refreezing on the western side of the cavity. Additionally, the back of the Amery Ice Shelf cavity is very steep and not well resolved by MetROMS, which could lead to pressure gradient errors causing excessive melt.

FESOM exhibits much weaker melting than MetROMS at the back of the cavity, even though bottom water temperatures are at least as warm (Figure 2.14c). We attribute this discrepancy at least partly to shoaling of the ice shelf draft from oversmoothing in our FESOM setups, which raises the in-situ freezing point and therefore reduces melting. The Amery draft is so steep that in order for a FESOM mesh to preserve the > 2000 m deep ice near the grounding line, resolution of 1.5

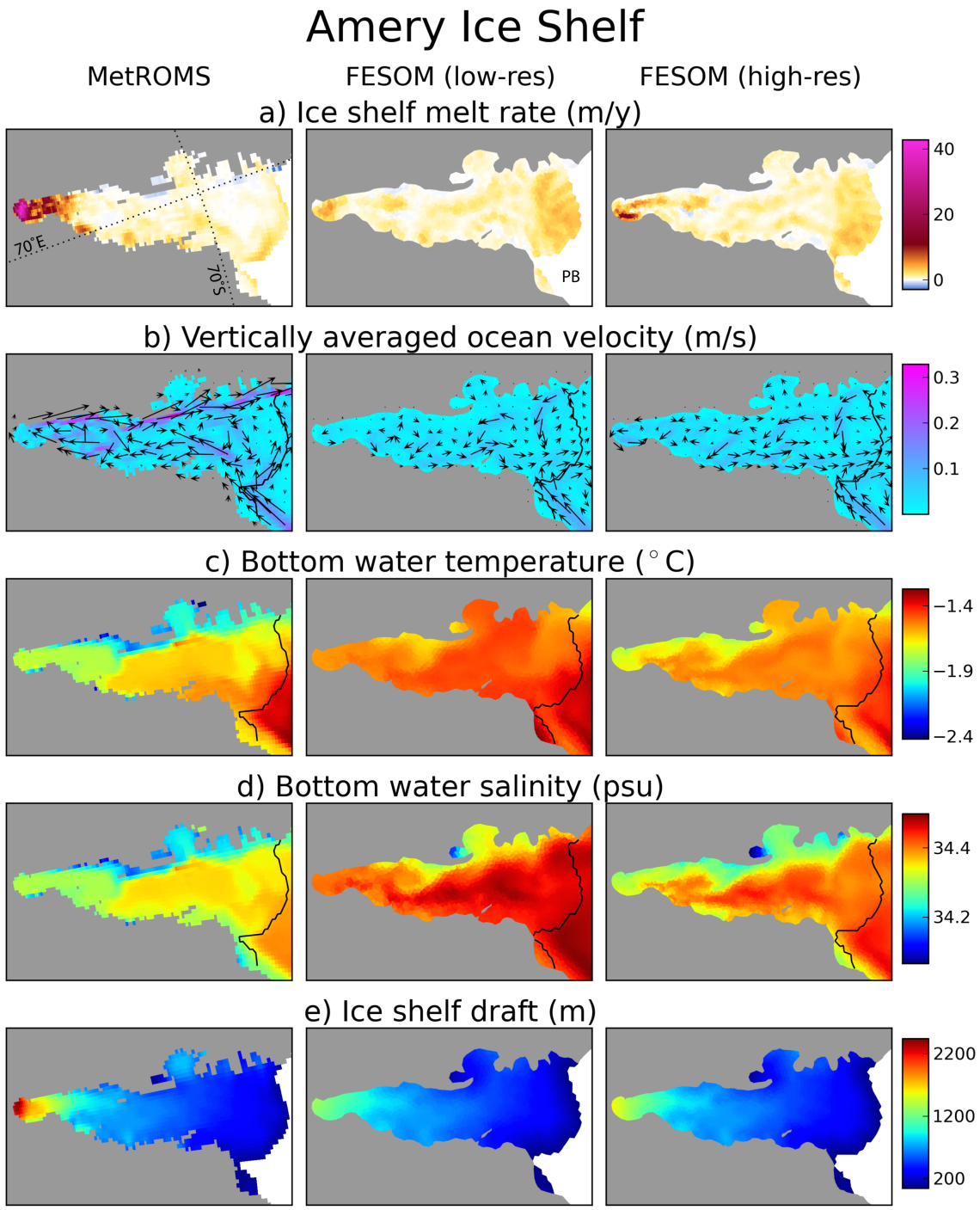

Figure 2.14: As Figure 2.12, for the Amery Ice Shelf cavity. PB = Prydz Bay.

km or finer is required throughout the entire cavity. However, experimentation with such a mesh revealed severe time step limitations: even a 1 minute time step was prone to numerical instabilities, compared to the 10 minute and 9 minute time steps which are stable for the two FESOM meshes we present here. Due to the computational expense, we chose not to pursue simulations with this experimental mesh. Nonetheless, some improvement can be seen between the low-resolution mesh and the high-resolution mesh (Figure 2.14e), in which the deep ice has shoaled by ap-

proximately 1000 m and 800 m respectively compared to the source topography. The corresponding increases in the in-situ freezing point are 0.76°C and 0.61°C. In the high-resolution simulation, melt rates near the grounding line exceed 10 m/y on the eastern flank, which is approximately double that of the low-resolution simulation. Such a strong response is not due to the in-situ freezing point alone, which is only modestly different between the two simulations. Increased velocities near the back of the cavity, possibly due to the steeper ice draft or better resolved currents, also have an effect.

In both FESOM simulations, significant melting also occurs near the ice shelf front and throughout the outer third of the ice shelf, at a higher rate (up to 5 m/y) than in MetROMS. This melting is somewhat lessened at high resolution, offsetting the increased melt rates at the grounding line. It occurs primarily in summer, leading to a large seasonal cycle in total basal mass loss for the entire ice shelf. Average annual minimums and maximums (calculated over 5-day averages between 2002 and 2016) are 27 Gt/y and 451 Gt/y for low-resolution FESOM, and 30 Gt/y and 309 Gt/y for high-resolution FESOM. In comparison, MetROMS has an average annual minimum of 78 Gt/y and maximum of 119 Gt/y. The seasonality and resolution-dependence of melting in the outer third of the cavity suggest that it is driven by warm AASW subducting beneath an oversmoothed ice shelf front. Circulation in FESOM is predominantly anticyclonic, with no significant areas of refreezing. This reversed circulation shows little sensitivity to the improved cavity geometry at high resolution, indicating that it is more likely driven by hydrography, as for the Filchner Ice Shelf (Section 2.4.3.1).

Bottom water in FESOM is warmer and saltier than in MetROMS throughout the cavity (Figures 2.14c and 2.14d); these differences are lessened at higher resolution. Figure 2.11c indicates that the Amery cavity is dominated by LSSW in both MetROMS and high-resolution FESOM, with smaller contributions from ISW (5-20%) and MCDW ($< 5\%$). Low-resolution FESOM has significantly more MCDW in the cavity (approx. 40%), which may be tied to oversmoothing of the continental shelf break as for the Fimbul Ice Shelf (Section 2.4.3.2).

2.4.3.4 Australian Sector

Travelling east from the Amery, the remainder of the Australian sector of Antarctica contains numerous small ice shelves along the coast of Wilkes Land, including the West, Shackleton, Totten, and Mertz Ice Shelves. *Rignot et al.* estimate relatively high melt rates for these ice shelves, which all three of our simulations fail to capture (Table 2.1.4).

There are several potential reasons for this consistent underestimation. First, the observed production of HSSW which drives the majority of melting for cold-cavity ice shelves (*Jacobs et al.*, 1992) is enhanced in this region by many small polynyas which are kept open by grounded icebergs (*Kusahara et al.*, 2010; *Gwyther et al.*, 2014) and coastline geometry (*Tamura et al.*, 2008). Neither MetROMS nor FESOM considers grounded icebergs in the configurations used here, which may explain why sea ice production is underestimated in this region (Section 2.4.2.3), implying a lack of HSSW. In fact, Figure 2.11d reveals no year-round presence of HSSW in Australian sector ice shelf cavities for any of the three simulations. The dominant water mass from sea ice formation is instead LSSW, which is fresher and less dense.

Whether enhanced production of HSSW would lead to a decrease or increase in basal melting depends on the local hydrography. For example, flooding a cavity with relatively cold HSSW formed in coastal polynyas could prevent any nearby MCDW from accessing the cavity, in which case stronger polynyas would lead to decreased melt rates (*Cougnon et al.*, 2013; *Khazendar et al.*, 2013; *Gwyther et al.*, 2014). Indeed, MCDW has recently been observed in front of the Totten Ice Shelf (*Greenbaum et al.*, 2015; *Rintoul et al.*, 2016; *Silvano et al.*, 2017) which could be a factor in its considerable melt rate. However, MCDW can only access the cavity through a trough in the continental shelf which was previously unknown and therefore not included in RTopo-1.05 (*Greenbaum et al.*, 2015). Even if this trough was included in the bathymetry datasets used by MetROMS and FESOM, the models would likely not resolve such a small-scale feature without increased resolution. As seen in Figure 2.11d, a significant amount of MCDW is still present in Australian sector ice shelf cavities for all three simulations (approx. 20% in MetROMS, 85% in low-res FESOM, and 75% in high-res FESOM). However, the fairly wide temperature range of water masses we consider to be MCDW (Table 2.2) means that the degree of modification is important for ice shelf melting.

Simulated ice shelf melt rates are shown for the Australian sector in Figure 2.15a. Melt rates in MetROMS are generally more concentrated at the ice shelf front, and in FESOM more uniform throughout the cavities. As suggested by FESOM's greater proportion of MCDW in Figure 2.11d, FESOM has slightly warmer and (in

the case of low-resolution FESOM) saltier bottom water in most ice shelf cavities (Figures 2.15b and 2.15c). This is despite the fact that bottom water offshore of the continental shelf is warmer in MetROMS (approx. 0.5°C) than in either FESOM simulation (approx. −0.2°C), and indicates that cross-shelf heat transport is stronger in FESOM. Melt rates are enhanced in the high-resolution FESOM simulation compared to low-resolution, and in most cases are also higher than MetROMS. This pattern is likely due to stronger circulation as shown for the Totten Ice Shelf in Figure 2.15d. The MetROMS grid and low-resolution FESOM mesh cannot adequately resolve circulation in such a small cavity, which is represented by only a few dozen grid boxes or triangular elements. Resolution is still less than ideal for the high-resolution FESOM mesh, but this simulation manages to develop an anticyclonic gyre beneath the ice shelf. Stronger transport through the cavity at high resolution, as well as increased transfer coefficients due to the faster velocity, causes basal mass loss for the Totten Ice Shelf to more than double compared to the low-resolution FESOM simulation, even though temperatures are slightly higher in the latter simulation. By comparison, the ROMS configuration of *Gwyther et al.* (2014) for the Totten region was even higher resolution (approx. 3 km), and instead simulated a cyclonic gyre.

Figure 2.15 (following page): (a), (b), (c): As Figure 2.12a, 2.12c, and 2.12d for the Australian Sector ice shelf cavities. The dashed black lines in (b) and (c) show the 1500 m isobath, which approximates the continental shelf break. (d) As Figure 2.12b, zoomed into the Totten Ice Shelf cavity (region outlined in the rightmost panel of (a)). We = West Ice Shelf, Sh = Shackleton Ice Shelf, Tt = Totten Ice Shelf, MU = Moscow University Ice Shelf, Mz = Mertz Ice Shelf.

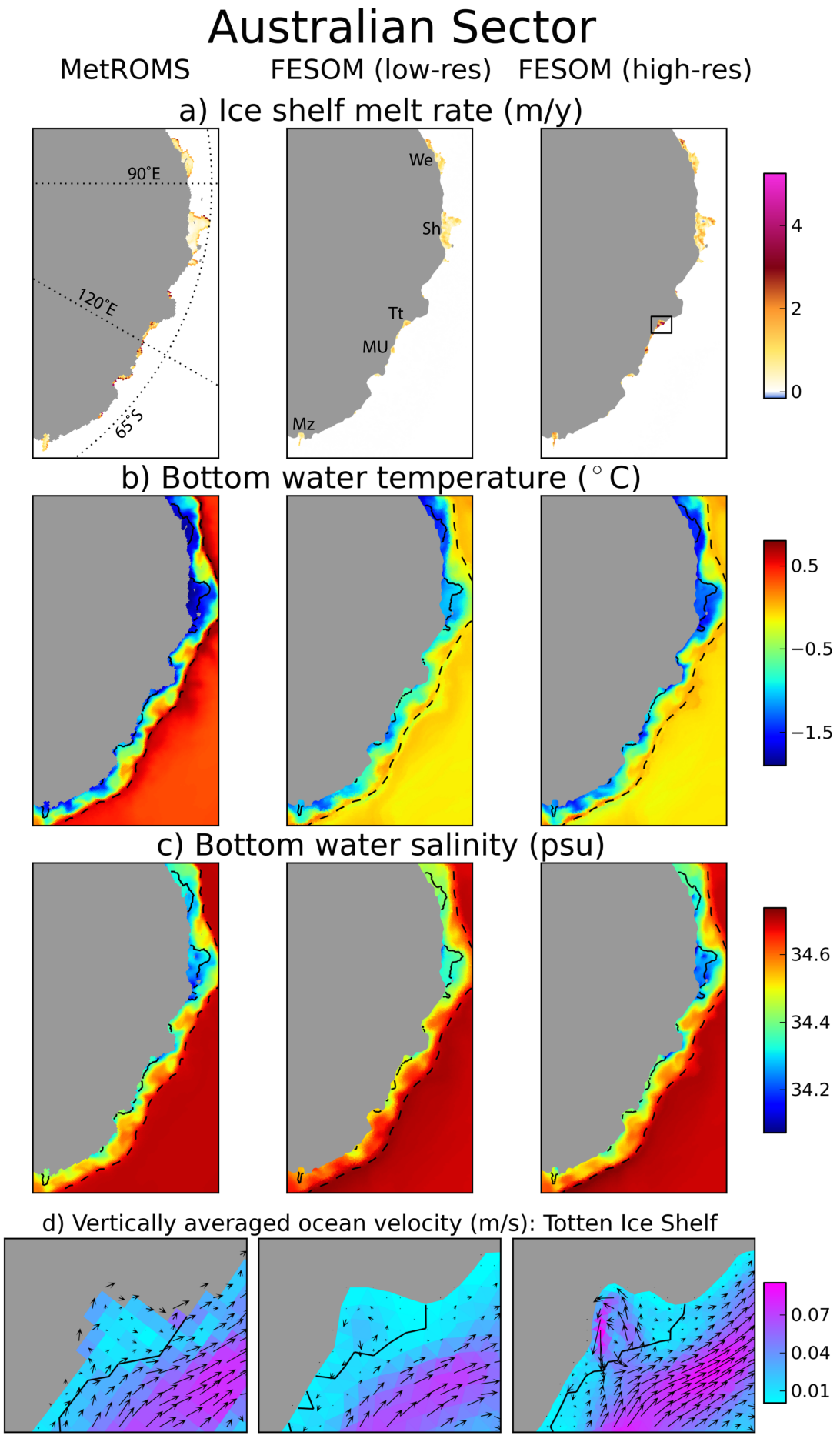
Australian Sector
MetROMS
FESOM (low-res)
FESOM (high-res)
a) Ice shelf melt rate (m/y)
90°E
120°E
65°S
We
Sh
Tt
MU
Mz
4
2
0
b) Bottom water temperature (°C)
0.5
−0.5
−1.5
c) Bottom water salinity (psu)
34.6
34.4
34.2
d) Vertically averaged ocean velocity (m/s): Totten Ice Shelf
0.07
0.04
0.01

2.4.3.5 Ross Sea

For the Ross Ice Shelf, the largest in Antarctica (by area), MetROMS falls within *Rignot et al.*'s estimate of basal mass loss while both FESOM simulations produce an overestimate (Table 2.1.5). In this region we also include the nearby Sulzberger Ice Shelf, for which all three simulations underestimate basal mass loss, and the Nickerson Ice Shelf, for which MetROMS and high-resolution FESOM agree with *Rignot et al.*'s observations, but low-resolution FESOM produces a slight underestimate.

All simulations show predominantly anticyclonic circulation beneath the Ross Ice Shelf, with inflow in the west and outflow in the east (Figure 2.16b), in agreement with observations (*Reddy et al.*, 2010). A similar system of interconnected gyres is seen in all three simulations, although circulation near the back of the cavity is stronger in MetROMS.

Patterns of refreezing are similar between simulations (Figure 2.16a), with large areas of refreezing near the back of the cavity concentrated around Steers Head and Crary Ice Rise. FESOM also displays relatively strong refreezing near the edge of McMurdo Ice Shelf, particularly in the high-resolution simulation, which has been observed (*Langhorne et al.*, 2015).

The Ross Ice Shelf front is exceptionally steep and requires smoothing in all three simulations for numerical stability. This smoothing allows relatively warm AASW to slide under the ice shelf front, which is visible as tongues of warm water in meridional temperature slices through 180°E (Figure 2.16c). The low-resolution FESOM simulation exhibits this problem most severely, but it is reduced at high resolution as the ice shelf front requires less smoothing. The interior of the cavity is warmer in FESOM than in MetROMS, and (particularly at low resolution) saltier (Figure 2.16d). This is due to an increased presence of HSSW, which is warmer and saltier than the ISW which is more prominent in MetROMS (Figure 2.11e). The increased HSSW is in turn due to stronger sea ice formation in FESOM, as discussed in Section 2.4.2.3. These differences in hydrography explain why melting in the outer third of the cavity remains stronger in FESOM than in MetROMS even when the oversmoothing of the ice shelf front has been addressed with higher resolution.

FESOM also displays stronger melting east of Roosevelt Island, where a small amount of relatively warm MCDW enters the cavity (not shown). This water mass has been observed (*Reddy et al.*, 2010; *Jacobs and Comiso*, 1989) and is likely not a model artifact. Indeed, *Paolo et al.* (2015) detect ice shelf thinning in this region over the period 1994-2012.

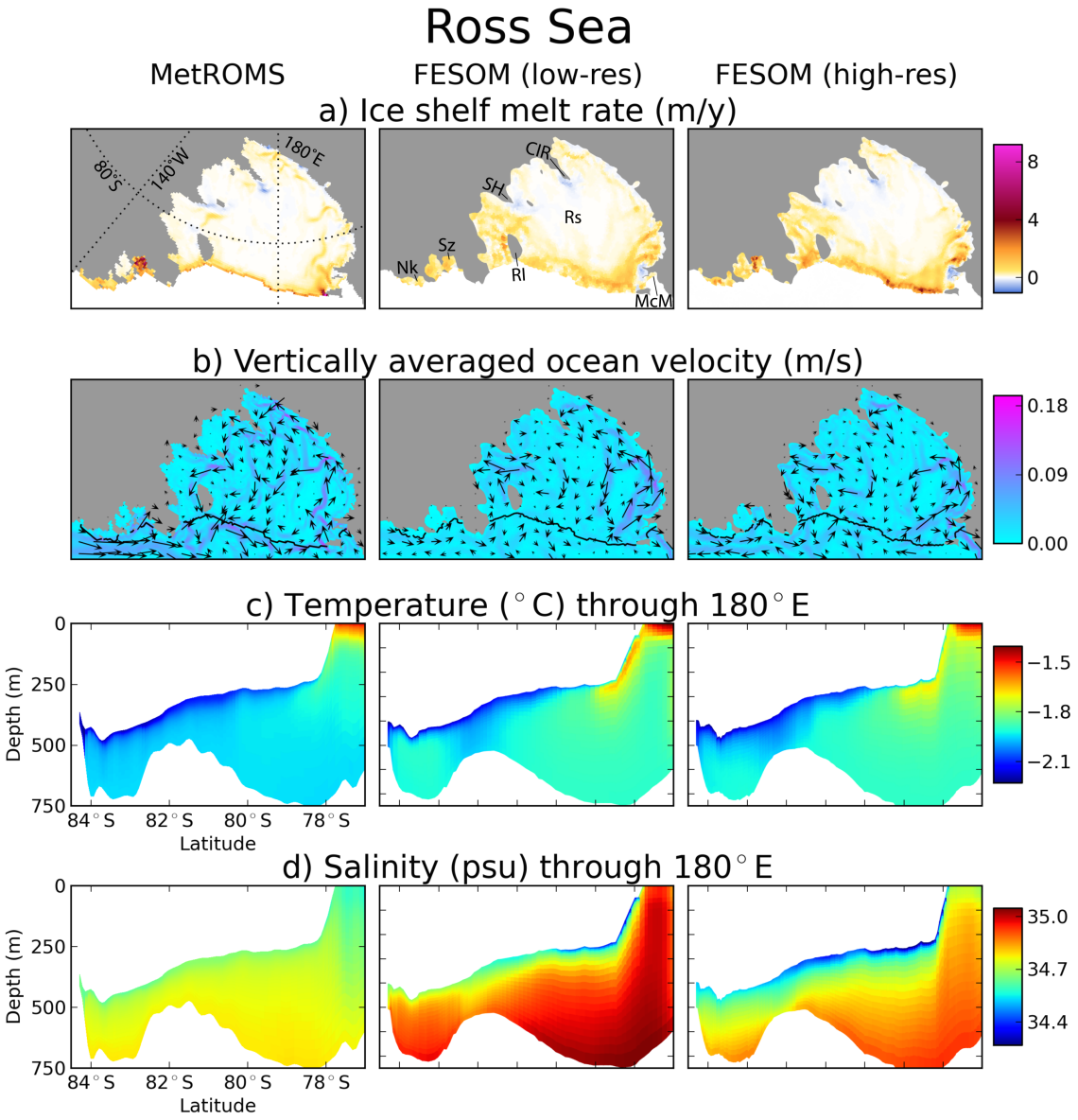

Figure 2.16: (a), (b): As Figure 2.12a and 2.12b for the Ross Sea ice shelf cavities. (c) Temperature (°C) and (d) salinity (psu) interpolated to 180°E, through the Ross Ice Shelf. Rs = Ross Ice Shelf, Sz = Sulzberger Ice Shelf, Nk = Nickerson Ice Shelf, McM = McMurdo Ice Shelf, RI = Roosevelt Island, CIR = Crary Ice Rise, SH = Steers Head.

2.4.3.6 Amundsen Sea

Ice shelves in the Amundsen Sea have been the subject of much attention in recent years, due to observed intrusions of unmodified CDW causing rapid basal melting and grounding line retreat (*Hellmer et al.*, 1998; *Jacobs et al.*, 2011; *Jenkins et al.*, 2010; *Wåhlin et al.*, 2010). The Amundsen Sea has the highest ice shelf melt rates of any sector of Antarctica, corresponding to large basal mass loss coming from a handful of relatively small ice shelves. However, all three of our simulations severely underestimate these mass loss values, as shown in Table 2.1.6.

There are several likely reasons for this systematic bias, the first and most well-studied being resolution. Intrusion of CDW onto the continental shelf of the Amundsen Sea depends on small-scale features in the bathymetry, which cannot be resolved by model grids coarser than approx. 5 km (*Nakayama et al.*, 2014). Of the three simulations in this intercomparison, only high-resolution FESOM falls within this threshold. Eddy transport of heat is also an important factor for cross-shelf CDW exchange. In order to fully resolve this process, resolutions of 1 km or finer are required (*St-Laurent et al.*, 2013), which none of our simulations have. A partial representation of eddy transport would be expected from eddy-permitting simulations (approx. 2-4 km on the Antarctic continental shelf), which high-resolution FESOM attains in the Amundsen and Bellingshausen Seas. The latitude-dependence of the Rossby radius of deformation means that eddies are much smaller, and therefore more computationally expensive to resolve, in the polar regions compared to the tropics and the mid-latitudes.

In FESOM, CDW transport into the Amundsen Sea has been shown to be sensitive to the depth of transition between sigma-coordinates and z-coordinates, with a shallower transition favouring the transport of warmer CDW due to the better alignment of z-coordinates with isopycnals in this region (*Nakayama et al.*, 2014). Our simulations have a relatively deep transition of 2500 m, which supports the on-shore transport of cooler CDW. Additionally, the very deep mixed layers in the Amundsen Sea which develop in both FESOM simulations (Sections 2.4.1.2 and 2.4.2.3) produce a slope front which further blocks CDW from the continental shelf. Any warm water flowing along the bottom is eroded by the convection of cold LSSW.

All three simulations underestimate bottom water temperature throughout the continental shelf (Figure 2.17b), which has been observed at approx. 1°C in the Pine Island Ice Shelf cavity (*Jacobs et al.*, 2011; *Jenkins et al.*, 2010) and 0.5 to 1.2°C throughout the Amundsen Sea (*Dutrieux et al.*, 2014). Temperatures are warmer in MetROMS (approx. -0.2°C) than in both FESOM simulations (approx. -1.7°C for low-resolution and -1°C for high-resolution), leading to higher melt rates (Figure 2.17a). All three simulations are dominated by MCDW in this region (Figure 2.11f), however FESOM has a larger presence of LSSW than MetROMS due to the deep mixed layers discussed previously. Consistent with the reduced cross-shelf transport of CDW, the Antarctic Slope Front in this region (see Section 2.4.1.5) is stronger in

Figure 2.17 (following page): (a), (b), (c): As Figure 2.15a, 2.15b, and 2.15c for the Amundsen Sea ice shelf cavities. The dashed black lines in (b) and (c) show the 1500 m isobath. (d) As Figure 2.15d, zoomed into the Pine Island Ice Shelf cavity (region outlined in the rightmost panel of (a)). PI = Pine Island Ice Shelf, Th = Thwaites Ice Shelf, Do = Dotson Ice Shelf, Gz = Getz Ice Shelf.

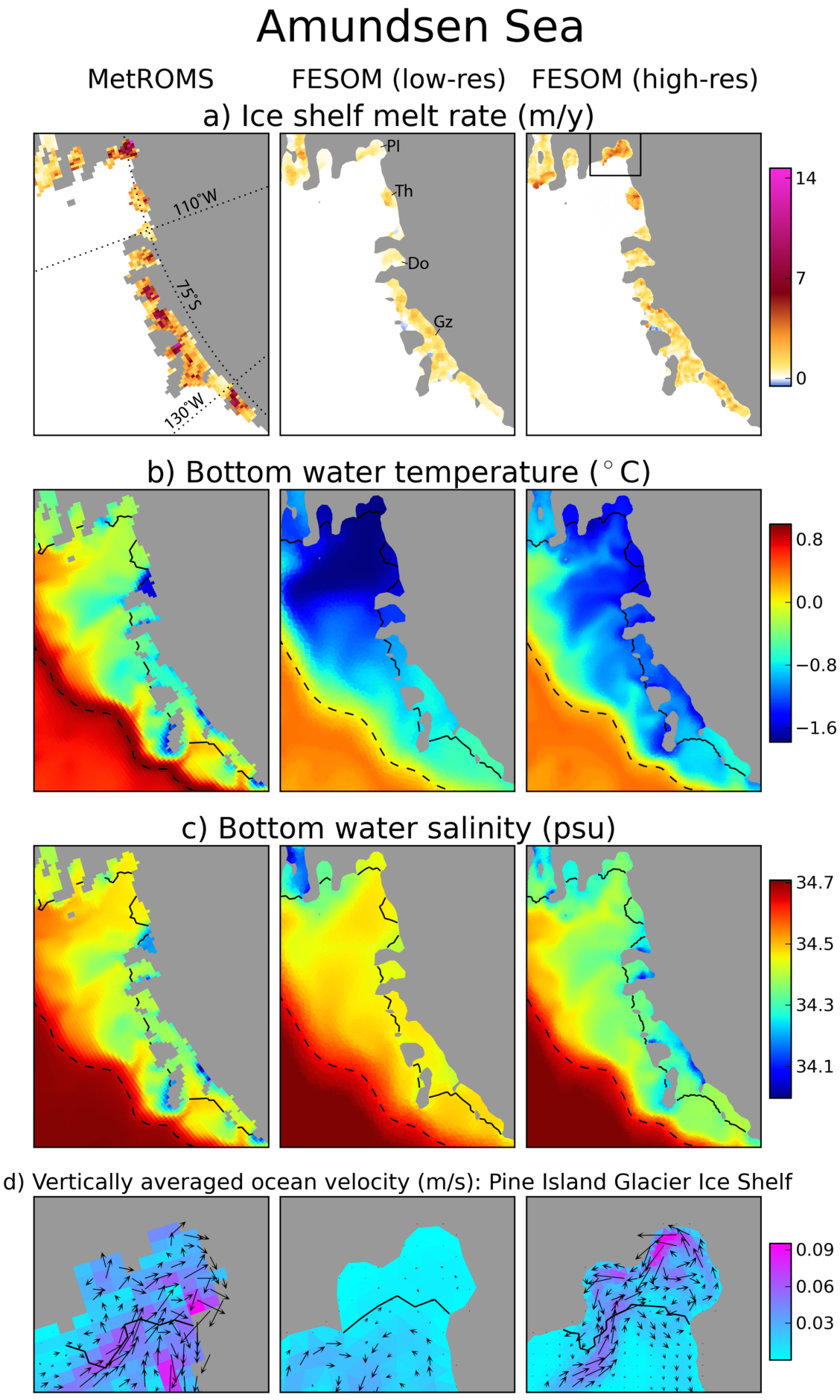
Amundsen Sea
MetROMS
FESOM (low-res)
FESOM (high-res)
a) Ice shelf melt rate (m/y)
110°W
75°S
130°W
Pl
Th
Do
Gz
14
7
0
b) Bottom water temperature (°C)
0.8
0.0
−0.8
−1.6
c) Bottom water salinity (psu)
34.7
34.5
34.3
34.1
d) Vertically averaged ocean velocity (m/s): Pine Island Glacier Ice Shelf
0.09
0.06
0.03

FESOM than in MetROMS.

Increasing the resolution in FESOM causes a substantial increase in basal mass loss for all Amundsen Sea ice shelves (Table 2.1.6). These changes are most pronounced for the Pine Island Ice Shelf, where mass loss increases by approximately a factor of 5. A major contributor to this increased melting is better resolution of troughs in the bathymetry which provide a pathway for warmer water to access the continental shelf. In the easternmost trough, near the Thwaites and Pine Island Ice Shelves, bottom water temperature increases by approximately 1°C as a result of increased resolution. Salinity also decreases throughout the Amundsen Sea, due to entrainment from additional meltwater (Figure 2.17c).

Melting is further enhanced in the high-resolution FESOM simulation due to stronger circulation, as shown for the Pine Island Ice Shelf in Figure 2.17d. As for the Totten Ice Shelf (Section 2.4.3.4), circulation in this small cavity is not well resolved by MetROMS or low-resolution FESOM, but high-resolution FESOM develops an anticyclonic gyre which increases melt rates due to larger friction velocities.

2.4.3.7 Bellingshausen Sea

Similarly to the Amundsen Sea, observations of the nearby Bellingshausen Sea show intrusions of unmodified CDW, particularly beneath George VI Ice Shelf in the east (*Jenkins and Jacobs*, 2008) as well as into Marguerite Bay (*Moffat et al.*, 2009). Again, all three model simulations largely fail to capture the observed CDW intrusions, and as a result underestimate basal mass loss for the Stange and George VI Ice Shelves (Table 2.1.7). MetROMS and low-resolution FESOM also produce an underestimate for the Abbot Ice Shelf, while high-resolution FESOM agrees with *Rignot et al.*'s observations. All three simulations agree with observations for the Wilkins Ice Shelf. The increase in melting between the low-resolution and high-resolution FESOM simulations is substantial, with basal mass loss more than doubling for the Stange and George VI Ice Shelves. However, this still falls below the range of observations.

As in the Amundsen Sea, insufficient resolution as well as the depth of the sigma-z transition in FESOM could be playing a role in the simulated lack of CDW in-

Figure 2.18 (following page): (a), (b), (c): As Figure 2.15a, 2.15b, and 2.15c for the Bellingshausen Sea ice shelf cavities. The dashed black lines in (b) and (c) show the 1500 m isobath. (d) As Figure 2.15d, zoomed into the George VI Ice Shelf cavity (region outlined in the rightmost panel of (a)). GVI = George VI Ice Shelf, Wi = Wilkins Ice Shelf, St = Stange Ice Shelf, Ab = Abbot Ice Shelf, MB = Marguerite Bay, RE = Ronne Entrance.

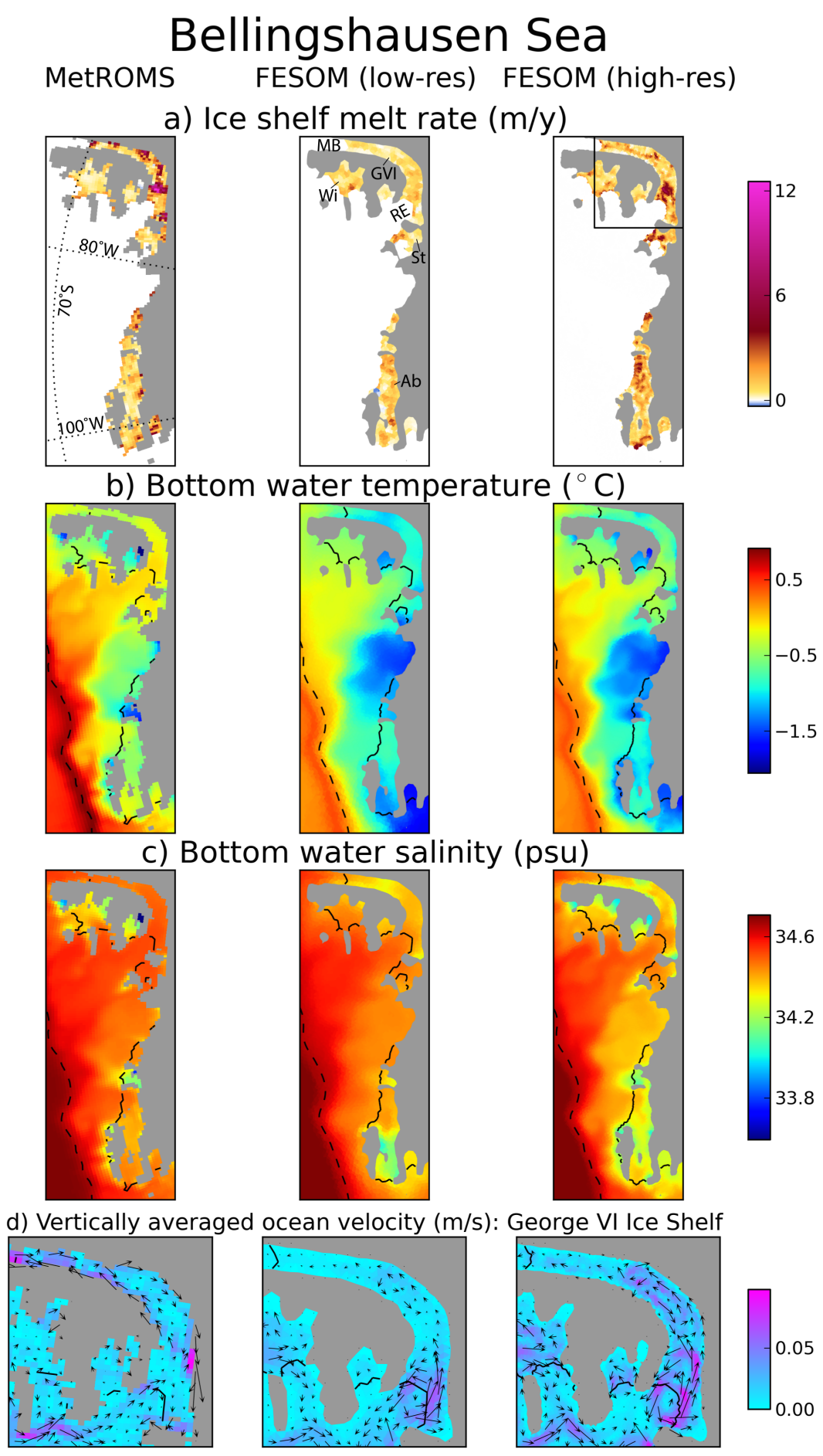
Bellingshausen Sea
MetROMS
FESOM (low-res)
FESOM (high-res)
a) Ice shelf melt rate (m/y)
MB
GVI
Wi
RE
St
Ab
80°W
70°S
100°W
12
6
0
b) Bottom water temperature (°C)
0.5
−0.5
−1.5
c) Bottom water salinity (psu)
34.6
34.2
33.8
d) Vertically averaged ocean velocity (m/s): George VI Ice Shelf
0.05
0.00

trusions. Observations suggest that the dominant mechanism for cross-shelf CDW transport in this region is eddies shed from the ACC (*Martinson and McKee*, 2012), which none of our simulations fully resolve. The sensitivity of Bellingshausen Sea temperatures to model resolution was further demonstrated by *Graham et al.* (2016), whose ROMS simulations exhibited greater onshore heat transport at 1.5 km resolution compared to 4 km resolution, due to increased eddy activity. However, the FESOM simulations of *Timmermann et al.* (2012) had much higher melt rates in the Bellingshausen Sea than our FESOM simulations, despite similar resolution and the same sigma-z transition. Since *Timmermann et al.* forced FESOM with the NCEP/NCAR atmospheric reanalysis rather than ERA-Interim, differences in atmospheric forcing could also be a factor.

MetROMS has generally warmer bottom water in the Bellingshausen Sea than either FESOM simulation (Figure 2.18b), leading to stronger melting in some regions (Figure 2.18a). In Ronne Entrance, extending into the southern end of the channel-shaped George VI Ice Shelf, MetROMS displays an intrusion of MCDW (approx 0°C). High-resolution FESOM also has warmer bottom water here than low-resolution FESOM (approx -0.25°C and -0.75° respectively). For all three simulations, however, bottom water temperatures in this region and in Marguerite Bay fall well below the observed 1°C (*Jenkins and Jacobs*, 2008). As in the Amundsen Sea, the increased meltwater in high-resolution FESOM compared to low-resolution FESOM leads to lower salinities in most regions of the Bellingshausen Sea (Figure 2.18c). MetROMS displays pockets of exceptionally cold and fresh water (approx. -2°C and 33.6 psu) in some ice shelf cavities, which is the result of poor resolution preventing meltwater from efficiently circulating out of semi-isolated regions, as discussed in Section 2.4.1.3. All three simulations show a dominance of MCDW in the Bellingshausen Sea region (Figure 2.11g), with a smaller presence of AASW ($< 5\%$).

Beneath George VI Ice Shelf (Figure 2.18d), FESOM displays inflow at the southern end of the channel in Ronne Entrance, and outflow at the northern end into Marguerite Bay. This circulation agrees with the direction of net transport inferred from observations (*Jenkins and Jacobs*, 2008). Some outflow is also apparent in Ronne Entrance, as part of an anticyclonic gyre, but the rest of the gyre splits off and flows through the cavity. These circulation patterns are similar in both FESOM simulations, but they are stronger at high resolution. In MetROMS, south-to-north transport is apparent along the western edge of the cavity, but also north-to-south transport along the eastern edge. This channel-shaped cavity is narrower and not well resolved by MetROMS, sometimes only 2 grid boxes wide.

2.4.3.8 Larsen Ice Shelves

The Larsen Ice Shelves on the eastern coast of the Antarctic Peninsula are undergoing a period of dramatic change, with the collapse of Larsen A in 1995 and Larsen B in 2002 (*Rott et al.*, 1996; *Rack and Rott*, 2004), followed by a major calving of Larsen C in July 2017 (*Hogg and Gudmundsson*, 2017). However, these breakup events are thought to be mainly driven by atmospheric processes rather than basal melting (*Pritchard et al.*, 2012). Basal processes are actually thought to stabilise the Larsen C Ice Shelf through the production of marine ice by refreezing (*Holland et al.*, 2009). Additionally, tidal forcing is likely to be important for the spatial distribution of melting (*Mueller et al.*, 2012).

For all three simulations presented here, simulated basal mass loss for the Larsen C and Larsen D Ice Shelves falls within the range of estimates given by *Rignot et al.* (Table 2.1.8). For the larger Larsen C Ice Shelf, basal mass loss is approximately doubled in the low-resolution FESOM simulation compared to MetROMS, with a further increase of approximately 50% in high-resolution FESOM. Note that the RTopo-1 dataset used to generate the model domains does not include Larsen A or Larsen B, as it was published following their collapse.

Ice shelf melt rate (a), vertically averaged velocity (b), and bottom water temperature (c) are shown for all three simulations in Figure 2.19. The stronger melting in FESOM corresponds to stronger circulation, travelling from north to south beneath the ice shelf. These differences are due to the lower summer sea ice concentration along the peninsula in FESOM compared to MetROMS, as seen in Figure 2.7. The absence of sea ice means the ocean surface is less sheltered from wind stress, and develops stronger seasonal currents which extend into the cavity. Additionally, more AASW is allowed to develop in FESOM compared to MetROMS, as seen in Figure 2.11h. By contrast, wintertime area-averaged melt rates are similar in all three simulations (not shown). The low-resolution FESOM simulation also has warmer bottom water and more MCDW in the cavities than either MetROMS or high-resolution FESOM, consistent with the southward excursion of the southern boundary of the ACC as discussed in Section 2.4.2.2.

Observations suggest extensive areas of refreezing beneath the southern Larsen C Ice Shelf (*Holland et al.*, 2009; *Rignot et al.*, 2013). Both FESOM simulations show small regions of refreezing here, but not to the same extent as observations. MetROMS shows no regions of net refreezing at all. This discrepancy may be due to the lack of small-scale ice shelf thickness variability in the smoothed ice shelf drafts.

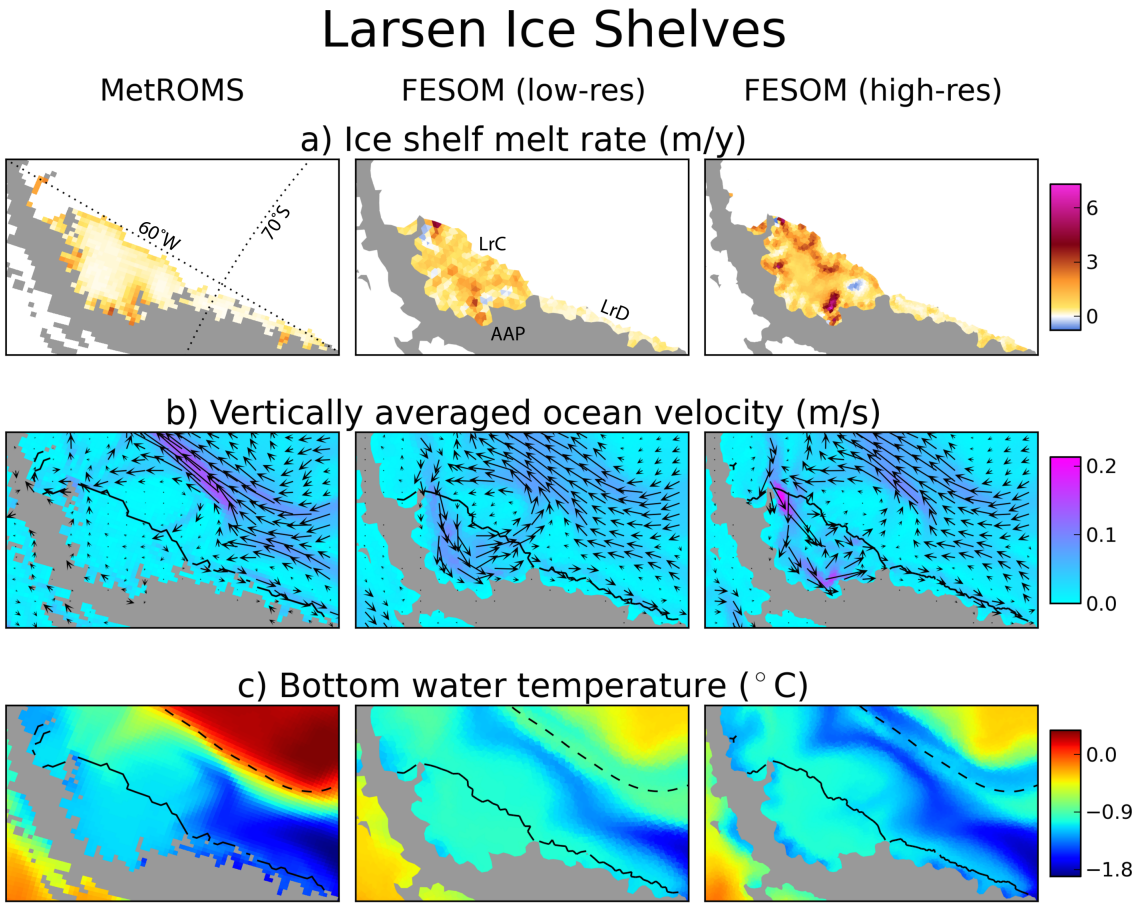

Figure 2.19: (a), (b), (c): As Figure 2.12a, 2.12b, and 2.15b for the Larsen ice shelf cavities. The dashed black line in (c) shows the 1500 m isobath. LrC = Larsen C Ice Shelf, LrD = Larsen D Ice Shelf, AAP = Antarctic Peninsula.

2.5 Discussion

Despite large variations in ocean/ice-shelf interaction, sub-ice shelf circulation, and continental shelf processes across different regions of the Antarctic coastline, several consistent themes have emerged in the simulation of these regions by the MetROMS and FESOM models. In some cases these patterns can be directly linked to model design, and can therefore provide guidance for future model development. In other cases, the interaction of several different model design choices makes this attribution more difficult.

Apparent in nearly all regions is the influence of sea ice on ocean/ice-shelf interactions. Since many of the prominent Southern Ocean water masses are governed by sea ice formation and melt, it is not surprising that simulated sea ice would have a discernible effect on the processes in ice shelf cavities. First, the location and rate of sea ice formation impacts the properties of shelf water masses flowing into the ice shelf cavities. MetROMS generally exhibits weaker dense water formation than either FESOM simulation, as evidenced by shallower mixed layers on the Antarctic

continental shelf (Figure 2.4), lower sea ice production (Figure 2.9), and a reduced presence of HSSW in ice shelf cavities (Figure 2.11). For the Filchner-Ronne and Ross Ice Shelves, this results in colder, fresher cavities with generally lower basal melt rates. Depending on the ice shelf, this may lead to better or worse agreement with observed basal mass loss. In FESOM, the excessive volume of HSSW produced by sea ice formation in the Filchner Depression is likely the culprit for its reversed direction of transport through the FRIS cavity. In the Amundsen and Bellingshausen Seas, FESOM has unrealistically deep mixed layers driven by sea ice formation, which fill the shelf with LSSW and extract the heat of any warm bottom layer. This contributes to the cold bias in these regions and the underestimation of basal melt rates. This mechanism is known to be sensitive to the atmospheric forcing (*Petty et al.*, 2013, 2014; *Nakayama et al.*, 2014), although there is clearly some model-dependence since these deep mixed layers are not present in MetROMS. The relationship between sea ice production, cross-shelf CDW transport, and ice shelf basal melting was also investigated by *Timmermann and Hellmer* (2013) in the context of future climate projections.

Simulated summer sea ice extent is too low in all three simulations, which exposes a larger area of the ocean to surface heating and drives increased summertime melting of ice shelf fronts. This behaviour is exacerbated by smoothing of the ice shelf front which allows the warm surface waters to slide further back into the cavity, as seen for the Ross Ice Shelf in both models and the Amery Ice Shelf in FESOM. The question of ice shelf smoothing will be discussed later in this section, but it is also worth considering the potential causes of low summer sea ice and how this might be ameliorated. The fact that both models underestimate the sea ice minimum by a similar amount, despite MetROMS' more sophisticated sea ice physics, suggests that atmospheric forcing could be part of the problem. Atmospheric general circulation models (GCMs) consistently overestimate the amount of solar radiation reaching the Southern Ocean in summertime due to biases in cloud cover (*Trenberth and Fasullo*, 2010; *Williams et al.*, 2013; *Bodas-Salcedo et al.*, 2016), and while atmospheric reanalyses such as ERA-Interim perform better than GCMs, some biases persist (*Naud et al.*, 2014). For future work, it would be worthwhile to force MetROMS or FESOM with the output of a high-resolution regional atmospheric model, such as RACMO (Regional Atmospheric Climate Model) which has previously been used for downscaling ECMWF reanalyses over Antarctica (*Lenaerts et al.*, 2012). The resulting impact (if any) on cloud cover, radiation, and summer sea ice extent would be useful to quantify. Another potential contributor to low summer sea ice in our simulations is the fact that grounded icebergs are not considered. In addition to enhancing polynya activity (as described in Section 2.4.3.4), grounded icebergs

increase the extent of fast ice, which is anchored to the coast and better survives the summer melt (*Fraser et al.*, 2012).

Another model characteristic which influences ice shelf melt rates is the degree of smoothing of the bathymetry and the ice shelf draft. This problem is more severe in FESOM, which for a given horizontal resolution requires more smoothing than MetROMS to ensure numerical stability, but it is also apparent for MetROMS at the Ross Ice Shelf front. Indeed, steep ice shelf fronts are some of the most affected regions, as smoothing allows warm AASW to slide into the ice shelf cavity and cause seasonal spikes in melt rates. However, a lack of observations means that the true amplitude of this seasonal cycle is unknown, and strong summertime melting is not necessarily unrealistic. This smoothing might also compensate for the absence of tides in both models, and for unresolved eddies, given that these processes similarly drive water mass exchanges across the ice shelf front (*Arzeno et al.*, 2014). Another environment in which smoothing is problematic is the continental shelf break, which is too gently sloping in some regions of the FESOM mesh, such as near the Fimbul Ice Shelf (Figure 2.13c). This allows MCDW to mix up the slope more easily, and indeed FESOM has a greater presence of MCDW than MetROMS in many ice shelf cavities (Figure 2.11). Finally, the steeply sloping Amery Ice Shelf draft is a particularly challenging feature for the FESOM mesh to adequately represent without considerable computational expense. In order to satisfy steepness limitations, the deep ice near the back of the cavity shoals, particularly in the coarse-resolution mesh, which raises the in-situ freezing point at the ice shelf base and contributes to reduced melting.

All three of these problems improve with increased resolution, as less smoothing is required. High-resolution FESOM represents steep ice shelf drafts more accurately than low-resolution FESOM, leading to fewer AASW intrusions beneath the Ross and Amery Ice Shelf fronts, and higher melt rates near the back of the Amery. The continental shelf break is also better preserved, and as a result the proportion of MCDW in ice shelf cavities decreases in almost every sector (Figure 2.11). Increased resolution is a straightforward solution to oversmoothing, and FESOM's unstructured mesh is ideal for targeting problematic regions without requiring increased resolution everywhere. However, since the maximum stable time step of the model is a function of the smallest element rather than the average element, the impact of this approach on computational cost can still be substantial, as we found when experimenting with resolution in the Amery Ice Shelf cavity. Therefore, in the future it may be worthwhile to experiment with different topographic smoothing methods, which may uncover options to minimise the trade-off between numerical stability and geometric accuracy. Another worthwhile approach would be to investigate al-

ternative methods for the calculation of the horizontal pressure gradient force, such as that of *Engwirda et al.* (2017), which may permit more steeply sloping layers and therefore less topographic smoothing.

Another way in which resolution impacts ice shelf melt rates in FESOM is by affecting the strength of sub-ice shelf circulation and the friction velocity at the ice shelf base. The high-resolution FESOM simulation is able to resolve circulation patterns beneath small ice shelves, such as the Totten, Pine Island, and George VI Ice Shelves, whereas the low-resolution simulation shows more or less stagnant cavities with lower melt rates. Furthermore, the well-studied impact of resolution on Amundsen Sea CDW intrusions (*Nakayama et al.*, 2014) is apparent in our simulations, with bottom water temperature on the continental shelf increasing by up to 1°C as a result of better-resolved troughs in the bathymetry. However, both FESOM simulations still have a cold bias in the Amundsen Sea, due to deep wintertime mixed layers in this region. Convection fills the continental shelf with LSSW and erodes any CDW intruding into the bottom layer. This behaviour is driven by sea ice formation, and has been shown to be sensitive to the atmospheric dataset used (*Nakayama et al.*, 2014). The relatively deep transition between sigma and z coordinates in our FESOM simulations is also known to inhibit CDW intrusions. Finally, *Stewart and Thompson* (2015) found that mesoscale eddies are vital to onshore CDW transport. None of our simulations fully resolve eddies on the Antarctic continental shelf, which would require resolution of approximately 1 km (*St-Laurent et al.*, 2013), although high-resolution FESOM is eddy-permitting (2-4 km) in the Amundsen and Bellingshausen Seas.

FESOM's hybrid vertical coordinate system, with z-coordinates in most of the domain, is advantageous for the accurate simulation of the interior Southern Ocean and the ACC. Both FESOM and MetROMS exhibit some erosion of AAIW during the simulation, but the erosion is more severe in MetROMS due to spurious diapycnal mixing associated with terrain-following coordinates in the deep ocean. This degradation of deep water masses could explain the relatively weak Drake Passage transport simulated by MetROMS. However, terrain-following coordinates as used by both MetROMS and FESOM have other benefits on the continental shelf/slope and within ice shelf cavities. In particular, they avoid the considerable sensitivity of ice shelf melt rates to vertical resolution which is seen in z-coordinate models of ice shelf cavities (*Gwyther*, 2016; *Mathiot et al.*, 2017). On the other hand, z-coordinate cavities are not susceptible to pressure gradient errors at the ice shelf front, and do not introduce time step limitations at the grounding line (*Mathiot et al.*, 2017).

None of our simulations include tides, which would increase ice shelf melt rates through enhanced mixing and higher friction velocities. Tidal amplitudes are par-

ticularly large in the Weddell Sea, and the inclusion of tides has been shown to have a significant effect on simulated FRIS melt rates (*Makinson et al.*, 2011; *Mueller et al.*, 2018). While tides do exist as an option in the ROMS code, their implementation requires specifying tidal elevation and/or tidal currents at lateral boundaries, from which the tidal signal propagates throughout the domain. In our MetROMS domain, the northern boundary at 30°S requires a strong sponge layer of increased diffusivity and viscosity to prevent numerical instabilities, which is likely to modify any tidal signal specified at the boundary. Additionally, the ice shelf cavities are much further from the boundary than is typical for simulations investigating tide/ice-shelf interactions, which generally have smaller domains focusing on a single ice shelf (*Padman et al.*, 2009; *Mueller et al.*, 2018). We experimented with tides in our MetROMS setup, but they triggered northern boundary instabilities leading to large oscillations in ACC transport and subsequently CDW upwelling. In FESOM, tides have only been applied in regional configurations such as the Ross Sea (*Wang et al.*, 2013) using a similar method to ROMS. Nonetheless, future model development to successfully implement tides in our MetROMS and FESOM domains would be valuable, and in particular may improve MetROMS' simulated basal mass loss for FRIS. An alternative approach better suited to large domains could be to implement the complete lunisolar tides of *Thomas et al.* (2001), which have been successfully incorporated into two global ocean models (*Müller et al.*, 2010).

Finally, we must acknowledge that while the three-equation parameterisation for ice-shelf/ocean interaction is widely used, it relies on turbulent transfer coefficients which are largely unconstrained by observations. Little is known about the basal roughness of ice shelves, and thus the spatial and temporal variations in the corresponding drag coefficient are not generally included in models. The thermodynamics of the boundary layer at the ice-shelf/ocean interface are also influenced by the choice of vertical mixing scheme (*Gwyther et al.*, 2015). A more sophisticated treatment of marine ice formation, such as the explicit frazil ice models of *Smedsrud and Jenkins* (2004) and *Galton-Fenzi et al.* (2012), may improve simulated patterns of refreezing. Furthermore, alternative parameterisations of ice shelf basal melt are being explored by the community (*Jenkins*, 2011, 2016), which may provide valuable intercomparisons with the three-equation parameterisation in the future.

2.6 Conclusions

We have presented the first published model intercomparison of circumpolar Antarctic ocean/sea-ice/ice-shelf interactions over a realistic domain. While we find that both MetROMS and FESOM underestimate total basal mass loss from ice shelves,

this is a regional bias largely confined to small, warm-cavity ice shelves which are not well resolved by the model configurations considered here. With respect to simulated sub-ice shelf circulation, some ice shelf cavities show agreement with the direction of transport inferred from observations (such as the Ross Ice Shelf in both models, the Amery Ice Shelf in MetROMS, and the George VI Ice Shelf in FESOM) and others show disagreement (such as the George VI Ice Shelf in MetROMS, and the Amery and Filchner-Ronne Ice Shelves in FESOM). FESOM's simulation of ice shelf cavities improves at higher resolution, suggesting that further refinement of resolution is justified as available computational power continues to increase. Sea ice extent in both MetROMS and FESOM mostly agrees with observations, although both models underestimate the summer sea ice minimum, and MetROMS requires surface salinity restoring to prevent a spurious open-ocean polynya from forming in the Weddell Sea. Sea ice production is too strong in the Ross and Weddell Seas compared to observations, and too weak in the small coastal polynyas of the Australian Sector. In the interior Southern Ocean and the ACC, FESOM has an advantage due to its vertical coordinate system, which is locally z-coordinate compared to MetROMS' terrain-following coordinate which covers the entire domain. Our results are dependent on the ERA-Interim atmospheric reanalysis and are influenced by any biases it may contain over the Southern Ocean, including its known underestimation of summertime cloud cover which leads to excessive sea ice melt. We conclude that realistic intercomparisons of simulated ice shelf cavities are valuable for guiding model development. Future studies including a greater variety of models, alternative atmospheric forcing datasets, and ideally more observations, would be worthwhile as these coupled ocean/sea-ice/ice-shelf models continue to be developed by the community.

Chapter 3

Challenges in developing coupled ocean/sea-ice/ice-shelf models

Preamble

Every new configuration of an Earth system model goes through an iterative process of debugging and tuning. Here this process is chronicled for the circumpolar Antarctic configuration of MetROMS, the final version of which was evaluated in Chapter 2. This chapter therefore "looks behind the curtain" of model development, an iterative trial-and-error process which is rarely discussed in the literature, but which can offer many valuable lessons and insights.

3.1 Introduction

A substantial portion of this PhD project was devoted to developing the circumpolar Antarctic configuration of MetROMS. At the time of commencement, the structural code handling all communication between ROMS and CICE had already been completed by the master MetROMS development team (*Debernard et al.*, 2017), appropriate for several Arctic domains which are now in use. In theory, the most significant change required to adapt the code for an Antarctic domain was the addition of thermodynamic ice shelf cavities. However, this only involved a relatively simple merge of *Galton-Fenzi* (2009)'s ice shelf code from another branch of ROMS. Many more challenges transpired over the course of development which took much longer to address. The circumpolar Antarctic configuration features a larger domain, lower resolution, different forcing, and different processes than the Arctic configurations previously considered by MetROMS. Finding the best combination of parameterisa-

tions therefore required additional experimentation. Furthermore, several problems in the MetROMS code only became apparent under certain combinations of options, which were first used by the circumpolar Antarctic configuration. Some of the problems discovered during this project impacted all MetROMS configurations, and the corrections were passed to the master branch as part of long-term collaborative development. This project therefore afforded a unique view of the model development process, beginning with an unusable model configuration bearing little resemblance to reality, and ending with well-performing simulations which reproduce many features of observations (Chapter 2). This chapter explores some of the problems and challenges that were encountered along the way.

Pipitone and Easterbrook (2012), in the context of climate modelling, define a software defect as "any problem that is worth fixing". This perspective goes beyond the colloquial definition of "bugs" as programming mistakes resulting from human error. It also includes modelling choices which are unsuitable but not strictly incorrect, such as parameterisations which perform poorly under the given boundary conditions. In an analysis of defect density in two GCMs and one stand-alone ocean model, *Pipitone and Easterbrook* (2012) conclude that software quality in these models is equal to or higher than large open-source software projects such as the Apache http server project. However, they note that "the less frequently used configurations of the models may include many more unnoticed code faults", a caveat which is acutely experienced during the development of new configurations such as those presented here.

Defects in climate models, particularly those resulting from human error, are not traditionally communicated in the scientific literature. Model description papers typically detail the set of parameterisations and design choices which worked, without indicating those that did not. However, the community can learn a great deal by discussing model defects and sharing case studies of memorable bugs and how they were fixed. Even human error can tell us something interesting about the climate system, since models are virtual laboratories which allow the simulation of extreme (and in these cases, inadvertent) sensitivity studies. More practically, communicating challenges overcome during model development is of benefit to other developers working towards similar goals, who may face similar challenges. This discussion builds up the community's body of knowledge about the best ways to configure a model, even if it consists of sharing all the worst ways to configure a model.

In this project, model development took the form of an iterative process of defect-fixing and evaluation. Issues with the simulation, i.e. the outward symptoms of model defects, were investigated, diagnosed, and addressed one at a time. This typically involved substantial experimentation in which multiple potential solutions

were tested. After each defect was resolved, the new simulation was evaluated against available observations for a variety of metrics. These included net ice shelf melt rates, sea ice extent and thickness, water mass properties, and Drake Passage transport. The next issue on which to focus attention was determined based on the results. The simulations did not always improve monotonically as defects were addressed, due to compensating errors (see *Oreskes et al.* (1994)). If the symptoms of one defect were masking the symptoms of another, fixing the first defect tended to make the simulation look worse, not better.

When does such a process end? In the midst of development, the answer appeared to be "never". Nonetheless, the circumpolar Antarctic configuration of MetROMS eventually reached a point where it was deemed fit for purpose. Model biases remained, but the effort required to implement the likely solutions (or the additional computational cost associated with those solutions) outweighed the expected benefit. Returning to the nomenclature of *Pipitone and Easterbrook* (2012), these problems were deemed "not worth fixing", at least in the context of this PhD.

The remainder of this chapter consists of case studies of defects found in MetROMS which were addressed during development, as well as one case study for FESOM (Section 3.9). While some defects resulting from human error are described, the analysis focuses more on unsuitable parameterisations and design choices. Sensitivity studies showing the effects of some unsuitable choices are presented, and compared to the baseline intercomparison simulations of Chapter 2. Finally, pathways for future development of the circumpolar Antarctic configuration of MetROMS are discussed.

3.2 Computational and coupling challenges

MetROMS implements "external coupling" of sea ice, by which the sea ice model (CICE) runs on separate processors, a separate timestepping loop, and a slightly different grid to the ocean model (ROMS). Communication between the two components is facilitated by the coupler MCT. This approach is distinct from the "internal coupling" used by models such as FESOM, where the sea ice routines are strictly a subset of the ocean code. External coupling can be beneficial for computational efficiency, as it allows for a larger timestep in the sea ice model than in the ocean, as well as the opportunity to optimise the distribution of processors between the two models ("load balancing"). However, particular complexities are inherent in external coupling, some of which are discussed below.

3.2.1 Periodic boundaries

During initial tests with the circumpolar Antarctic domain, patches of zeros in ocean-to-ice coupling fields (surface salinity, freeze/melt potential, etc.) were visible along the periodic boundary in CICE. This was due to an inconsistency in the ROMS-MCT and CICE-MCT interfaces. When a two-dimensional field is passed from ROMS to CICE (or vice versa), MCT first unravels the field into a one-dimensional array, which is reassembled after the transfer. However, the master MetROMS code did not consider the case of a domain with periodic boundaries, such as the east-west periodic boundary in the circumpolar Antarctic domain. This led to complications with halo points (also known as ghost points), artificial indices beyond the boundary of the domain which are introduced to complete the stencils of numerical differentiation. ROMS handles halo points differently at periodic boundaries, and as a result the unravelling of two-dimensional arrays passed from ROMS to CICE was not the inverse of the reassembling. Certain indices near the periodic boundary were never updated from their initial value of zero, meaning that all of the ocean coupling fields as seen by CICE had patches of zeros at these indices. A modification to the unravelling routine in the ROMS-MCT interface fixed this problem.

It later became apparent that ROMS included halo points in its exported coupling fields, which CICE treated as computational points and then added halo points of its own. For rectangular domains with four open lateral boundaries, and no sea ice at these boundaries, this mismatch does not strictly matter. All of the domains used by the developers of the master MetROMS code meet these criteria. However, the periodic boundary in the circumpolar Antarctic domain posed a much more serious problem: CICE was seeing two extra columns of cells at this boundary, spherical geometry notwithstanding. To address this issue, the ROMS-MCT interface was modified to exclude halo points from exported coupling fields, and the CICE grid was remade without the extra halo points. This revision, while clearly necessary, did not lead to any obvious differences in the large-scale behaviour of the simulations.

3.2.2 Domain decomposition

While benchmarking MetROMS to determine the optimum load balancing, the coupled model displayed extremely poor scalability, in that doubling or tripling the number of processors led to a negligible decrease in walltime. Analysis of MPI (Message Passing Interface) commands revealed the limiting factor to be CICE, which was spending a significant proportion of time on communication rather than calculation. The culprit was found to be domain decomposition, i.e. how the model

grid was partitioned into tiles for assigning to processors. MetROMS was decomposing the CICE domain into approximately square tiles, with multiple rows and columns. This tiling would be appropriate for a rectangular domain where sea ice is distributed more or less evenly. However, in a circumpolar Antarctic domain extending as far north as 30S, only the southernmost few rows of tiles ever contained sea ice. Tiles in the northern part of the domain had no calculations to do, but still had to communicate with each other. A more efficient decomposition of this domain comprised a single row of tall, slender tiles. The effect of activating this option in CICE was immediate: the coupled model sped up by a factor of three.

3.2.3 Staggered grids

Once it was appropriate to run multi-year simulations with MetROMS, it became apparent that certain cells in the model grid were prone to slowly developing extreme sea ice thicknesses, reaching spurious values of up to several kilometres. To call this "unrealistically thick" would be a gross understatement. However, the adjacent cells always had realistic sea ice thicknesses, typically between 1 and 2 metres. Closer examination of the affected cells revealed that they were all isolated on three sides by either land or ice shelves (which CICE also treats as land).

As mentioned in Section 4.3.5, ROMS and CICE share the same horizontal grid cells to simplify coupling. However, the location of momentum variables within those cells (edges vs corners) is not the same, as ROMS uses the staggered Arakawa C-grid (*Arakawa and Lamb*, 1977) while CICE uses the staggered Arakawa B-grid. The C-grid permits single-cell channels, meaning ROMS has no difficulty with points which are isolated on three sides. However, CICE's B-grid forces both components of sea ice velocity to be zero in such cells. Sea ice can therefore freeze and melt, but not advect. If freezing exceeds melting, the sea ice thickness will grow indefinitely without affecting the neighbouring cells.

All affected cells were identified using an automated process. In total, 119 cells on the Antarctic continental shelf were surrounded on three sides by land or ice shelves. To address this situation, the affected cells were altered in four different ways:

1. Fill with land
2. Fill with ice shelf (with ice shelf draft extrapolated from neighbouring cells)
3. Turn a neighbouring ice shelf point into an open ocean point
4. Turn a neighbouring land point into an open ocean point (with bathymetry extrapolated from neighbouring cells)

This choice was made manually for each cell, depending on the local coastline geometry.

3.3 Drake Passage transport

Zonal transport of the Antarctic Circumpolar Current (ACC) is a useful metric for evaluation of Southern Ocean models (*Sen Gupta et al.*, 2009; *Russell et al.*, 2006). The ACC is driven by the Southern Hemisphere westerly winds as well as the meridional density gradient across the Southern Ocean. It is limited by drag along the ocean floor, and by eddies which act to flatten isopycnals and reduce the density gradient.

ACC transport is typically calculated from a meridional slice through Drake Passage (67°W in this analysis), which also includes the transport of the counteracting Antarctic Coastal Current. As discussed in Section 2.4.1.1, observation-based estimates of Drake Passage transport historically lay around 134 Sv (*Cunningham et al.*, 2003) but the true value is now thought to be higher, such as *Donohue et al.* (2016)'s estimate of 173.3 ± 10.7 Sv.

3.3.1 Directional challenges

The first calculation of total Drake Passage transport in MetROMS revealed that it was going in the wrong direction. It started out weak (approx. 75 Sv) and then collapsed, becoming negative after several years of simulation and stabilising around -125 Sv. This was approximately the right magnitude, but the wrong sign.

At this time, the northern boundary of the model domain was at 50°S, bisecting the westerly winds. Upstream momentum in the ACC was inhibited, leading to relatively slow ocean velocities. Extending the model domain to 30°S increased velocities in the ACC, and Drake Passage transport at the beginning of the simulation approximately doubled to 140 Sv. However, during spinup this eastward flow still collapsed, becoming negative in a matter of years.

The culprit of the backwards-flowing Drake Passage transport was found to be, strangely enough, a unit error for humidity as seen by the sea ice model. The input atmospheric forcing fields included relative humidity, but CICE assumed it to be specific humidity, which is approximately 3 orders of magnitude smaller. Humidity in CICE is only used for the calculation of incoming longwave radiation, which was approximately doubled due to the extremely large humidity values. As a result,

surface melting of sea ice was unrealistically strong (approx. 30 cm/day), and this freshwater flux was not properly offset by the salt flux of sea ice formation when it was replenished, due to the concurrent salt conservation issue discussed in Section 3.5.1. Very low salinities (10-20 psu) resulted around the Antarctic coastline. The effect of this excessive freshwater on the density structure of the continental shelf was to drive an extremely strong Antarctic Coastal Current. Over time, the transport of this westward current through Drake Passage became strong enough to overpower the eastward-flowing ACC.

3.3.2 Viscosity parameterisations

Once the humidity units were corrected in CICE, simulated Drake Passage transport was of the right direction, but now it was unrealistically strong. This was a consequence of the Laplacian viscosity parameterisation which was then used to parameterise subgrid-scale mixing of momentum in ROMS. To analyse the relationship between viscosity parameterisations and ACC transport, this section compares the MetROMS simulation from Chapter 2, which uses the biharmonic visocisty parameterisation, with an additional simulation which uses Laplacian viscosity (coefficient of 1500 m^2/s, scaled linearly with grid size).

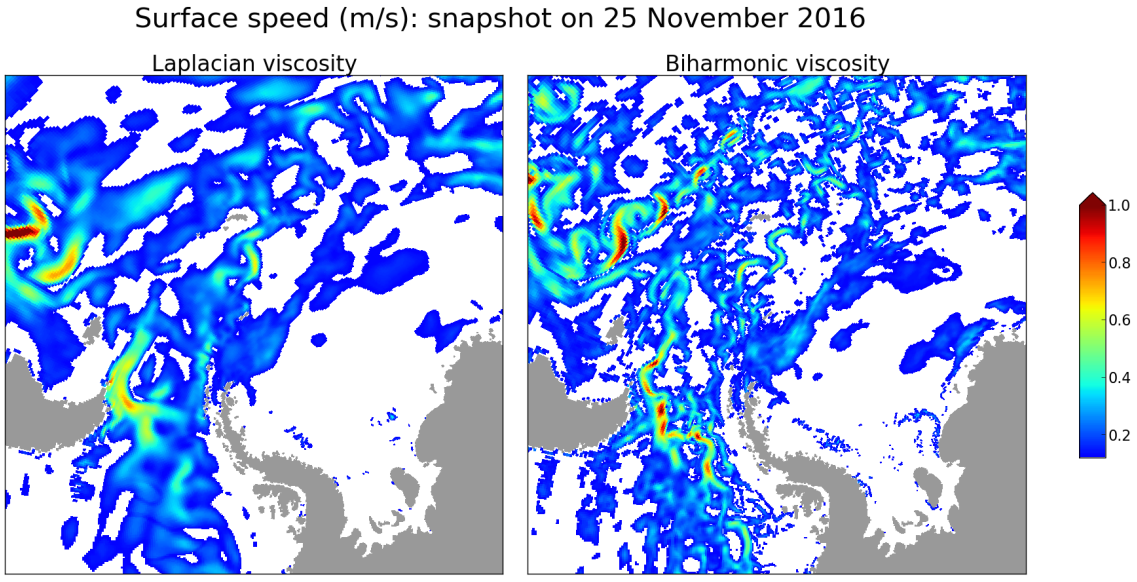

Figure 3.1: Surface speed in m/s in a section of the model domain including Drake Passage, at a single timestep on 25 November 2016. Values below 0.12 m/s are masked. Subgrid-scale mixing of momentum is parameterised using either Laplacian viscosity or biharmonic viscosity. The latter simulation is the same MetROMS simulation analysed in Chapter 2.

As demonstrated by *Griffies and Hallberg* (2000), the Laplacian parameterisation tends to overly damp eddies compared to the more scale-selective biharmonic para-

meterisation. Ideally, viscosity parameterisations should mimic the effects of unresolved eddies while leaving the resolved eddies untouched, but the Laplacian scheme instead suppresses the resolved eddies. This effect can be seen in MetROMS, as shown in Figure 3.1 with snapshots of surface speed at a single timestep for the two simulations. The simulation using biharmonic viscosity is clearly more eddy-rich than the Laplacian simulation.

One effect of these eddies, as mentioned previously, is to flatten isopycnals and weaken ACC transport. Therefore, a simulation with overly damped eddies (and in the absence of a parameterisation such as that of *Gent and McWilliams* (1990)) can be expected to have steeper isopycnals and a stronger ACC. Indeed, the simulation using Laplacian viscosity displays relatively strong Drake Passage transport which continues to strengthen throughout the simulation (Figure 3.2). Over the period 2002-2016 (excluding the first 10 years as spinup), average Drake Passage transport is 182.8 Sv with an increasing trend of 1.17 Sv/y (significant at the 95% level). In comparison, the simulation using biharmonic viscosity has an average Drake Passage transport of 126.8 Sv over the same period, with a significant decreasing trend of -0.29 Sv/y.

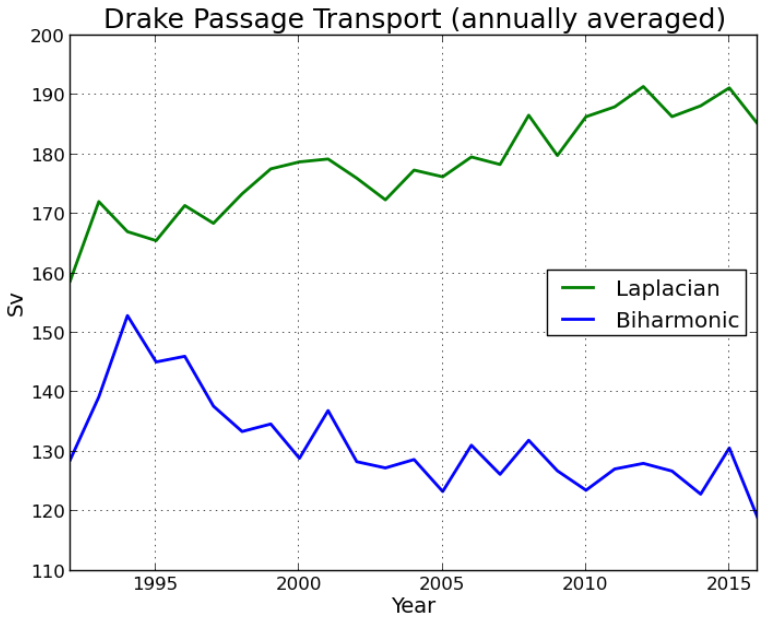

Figure 3.2: Timeseries of annually averaged Drake Passage transport during the two 25-year simulations described in Figure 3.1.

The stronger transport resulting from Laplacian viscosity is arguably in better agreement with observations, if one excludes the lower historical estimates and only considers *Donohue et al.* (2016)'s results (173.3 ± 10.7 Sv). However, the biharmonic simulation's representation of eddies is clearly more realistic. The relatively low and downward-drifting Drake Passage transport seen in the latter simulation is likely due to spurious diapycnal mixing (see Section 3.7) which erodes deep water masses and

weakens the meridional density gradient. Therefore, transport in the Laplacian simulation - which is only just within observations and shows no sign of stabilisation - may be the result of compensation between diapycnal mixing and eddy suppression.

Some models, such as FESOM (see Section 2.2.4), instead combine Laplacian viscosity with the Gent-McWilliams (GM) parameterisation (*Gent and McWilliams*, 1990) which mimics the flattening effects of eddies on isopycnals. However, GM does not exist in the ROMS code, and implementation would be difficult with terrain-following vertical coordinates. Indeed, FESOM only applies the GM parameterisation in the z-coordinate part of the domain.

3.4 Open boundary conditions

As described in Section 2.3.4, the circumpolar Antarctic domain requires northern boundary conditions at 30°S for temperature, salinity, velocity, and sea surface height. However, the numerical treatment of these boundary conditions is not trivial, and several options exist in the ROMS code. Open boundaries are a source of artifacts and instabilities in many domains, which is a disadvantage for regional ocean models, compared to global models such as FESOM for which boundary conditions are unnecessary.

3.4.1 Volume conservation

Initially the circumpolar Antarctic domain was found to be losing volume from the northern boundary, causing the Southern Ocean to slowly drain. After several years the model "blew up", i.e. self-terminated due to extreme velocities, near the grounding lines of ice shelf cavities. Here the water column is exceptionally thin, which limits the model timestep. Further reductions in water column thickness due to volume loss therefore led to violations of CFL stability conditions.

This scenario occurred even if the boundary conditions for v (meridional velocity) were modified to ensure volume conservation. The problem instead lay in the numerical treatment of these boundary conditions. Experimentation with the available options revealed that the Flather scheme for barotropic velocity (*Flather*, 1976) and the Chapman scheme for sea surface height (*Chapman*, 1985) was the only combination of numerical methods that prevented a persistent loss of volume. In these methods, differences between the simulated fields and the specified boundary conditions are radiated out of the domain at the speed of external gravity waves.

3.4.2 Boundary instabilities

When the biharmonic viscosity parameterisation was enabled (Section 3.3.2), instabilities began to occur near 30°S. Strong jets were forming along the boundary, particularly off the east coast of South America. These instabilities were due to discontinuities between the ECCO2 boundary conditions and the simulated fields near the boundary. They were previously suppressed by the more stable and diffuse Laplacian parameterisation for viscosity.

Stability was ultimately ensured by following the same approach as the Southern Ocean State Estimate simulations, which use a similar circumpolar domain (Matthew Mazloff, personal communication). As described in Section 4.3.3, this procedure consists of three steps: zonal velocity is clamped to zero at the northern boundary, the bathymetry is modified to be constant in y over the northernmost 3° latitude of the domain, and a sponge layer of linearly increasing diffusivity and viscosity is applied over this region.

3.5 Coastal polynyas

A persistent problem with this MetROMS configuration was a lack of coastal polynyas, i.e. regions of open water surrounded by sea ice and adjacent to the coast. In reality, strong southerly katabatic winds push sea ice away from the Antarctic coast in certain regions and expose the ocean surface to the cold atmosphere, which creates more sea ice (*Barthélemy et al.*, 2012; *Mathiot et al.*, 2010). This conveyer-belt of sea ice formation drives the production of HSSW and ultimately AABW. These coastal polynyas were almost completely absent in MetROMS, resulting in reduced convection which allowed warm CDW to access the continental shelf and cause unrealistically strong basal melting of ice shelves. The absence of coastal polynyas was due to a combination of four factors, described below.

3.5.1 Salt conservation

As detailed in Section 4.3.5, ROMS removes supercooling from ocean cells every timestep, and sends the corresponding amount of energy ("freeze potential") to CICE for frazil ice formation. In earlier versions of the MetROMS code, ROMS also calculated the salt fluxes of this frazil formation, increasing ocean salinity by an amount proportional to the freeze potential. Frazil is not pure ice, and ROMS assumed a constant value for its initial salinity. However, the mushy thermody-

namics scheme in CICE (*Turner et al.*, 2013a) allows sea ice salinity to evolve, and the initial salinity of frazil ice varies. The ocean/sea-ice coupling therefore did not conserve salt. This led to a positive feedback of surface freshening and stabilisation of the water column, shutting down the convection necessary to keep coastal polynyas open. To address the salt conservation issue, the frazil ice formation code was modified so that salt fluxes were calculated by CICE rather than ROMS, which properly accounted for the varying initial salinity. This led to slight improvement in the appearance of coastal polynyas, with higher sea surface salinity and generally lower sea ice concentrations.

3.5.2 Frequency of wind forcing

Initially, this MetROMS configuration used monthly-averaged atmospheric forcing from the ERA-Interim reanalysis (*Dee et al.*, 2011). For the wind fields, which exhibit substantial short-term variability, one effect of monthly averaging is to reduce the maximum wind speed in the domain at any given time. In particular, the strong southerly katabatic winds become weaker and more diffuse, with smoother gradients. This reduces their ability to transport sea ice away from the coast. Indeed, switching to atmospheric forcing at 6- and 12-hourly intervals increased wind stress on the sub-monthly timescale, leading to more coastal polynya activity.

Similarly, *Kim and Stössel* (1998) found that forcing a coupled ocean/sea-ice model with daily wind fields led to increased sea ice formation, extent, and thickness compared to a simulation forced with a monthly climatology. They attribute these changes to increased turbulent heat fluxes, which have a nonlinear dependence on wind speed in bulk flux parameterisations (*Fairall et al.*, 1996).

3.5.3 Spurious sea ice formation

Coastal polynyas were also being suppressed in MetROMS due to the excessive sea ice produced by oscillatory ocean tracer advection schemes, which are prone to spurious supercooling. This phenomenon is fully explored in Chapter 4. After switching from the centered fourth-order advection scheme to the upwind third-order scheme including flux limiters, coastal sea ice became thinner and polynya activity increased.

3.5.4 Grid resolution mismatch

While the previous three changes led to marked improvements in the representation of coastal polynyas, particularly around East Antarctica, major disagreements remained between MetROMS' sea ice and available observations. Simulated summer sea ice extent was too high, which is the opposite bias to most models (*Turner et al.*, 2013b). The substantial Ross Sea polynya (*Meier et al.*, 2013) was virtually nonexistent in MetROMS. Instead, sea ice on the continental shelf of the Ross and Weddell Seas became thicker and thicker, with a monotonically increasing age tracer showing that the ice was approximately as old as the simulation itself. At the same time, sea ice offshore was thinning. It was clear that something was inhibiting the export of sea ice from the continental shelf, particularly in the Ross and Weddell Seas where most sea ice is formed. Simulations that varied the sea ice dynamics parameters, such as drag coefficients, turning angles, and ice strength coefficients, had little effect on the export. Eventually, comparison with an independent CICE simulation (Nicholas Hannah, personal communication) revealed that the sea ice divergence term in MetROMS was extremely low. This variable depends only on sea ice velocity and grid resolution, and it became apparent that the problem lay with the latter.

One of the MetROMS domains used by the master development team has a constant horizontal resolution of 20 km, which was originally hard-coded into CICE rather than being read from the grid file. The developers later fixed this shortcut in the master code, but the update was never transferred to the ice shelf branch due to a version control issue. Since the circumpolar Antarctic MetROMS domain has variable Cartesian resolution which is finer than 20 km in most of the domain (averaging 10 km in sea ice covered regions), the divergence term was damped to the point of nearly shutting down all sea ice deformation. Fixing this mismatch led to a pronounced increase in sea ice export, with associated improvements in sea ice thickness, concentration, and polynya activity. The representation of coastal polynyas in the final version of MetROMS more or less agrees with observations (Section 2.4.2.1).

Note that the simulations in Chapter 4 were completed after the grid resolution mismatch was addressed, and show that coastal polynyas still remain sensitive to spurious sea ice formation from oscillatory advection schemes.

3.6 Weddell Sea deep convection

Near the centre of the Weddell Sea Gyre, MetROMS is prone to developing unrealistic deep convection. Figure 3.3 plots temperature and salinity slices through 13°W for a simulation with no surface salinity restoring, but which is otherwise identical to the simulation analysed in Chapter 2. During the first September of the simulation (top row of Figure 3.3), the offshore Weddell Sea is weakly stratified. A colder, fresher mixed layer (approx. −1.5°C, 34.5 psu) overlays warmer, saltier Circumpolar Deep Water (CDW, > 0°C, > 34.6 psu). The mixed layer is at its maximum annual depth (100-150 m), and later forms the subsurface Winter Water layer which buffers seasonally shallow mixed layers from the CDW.

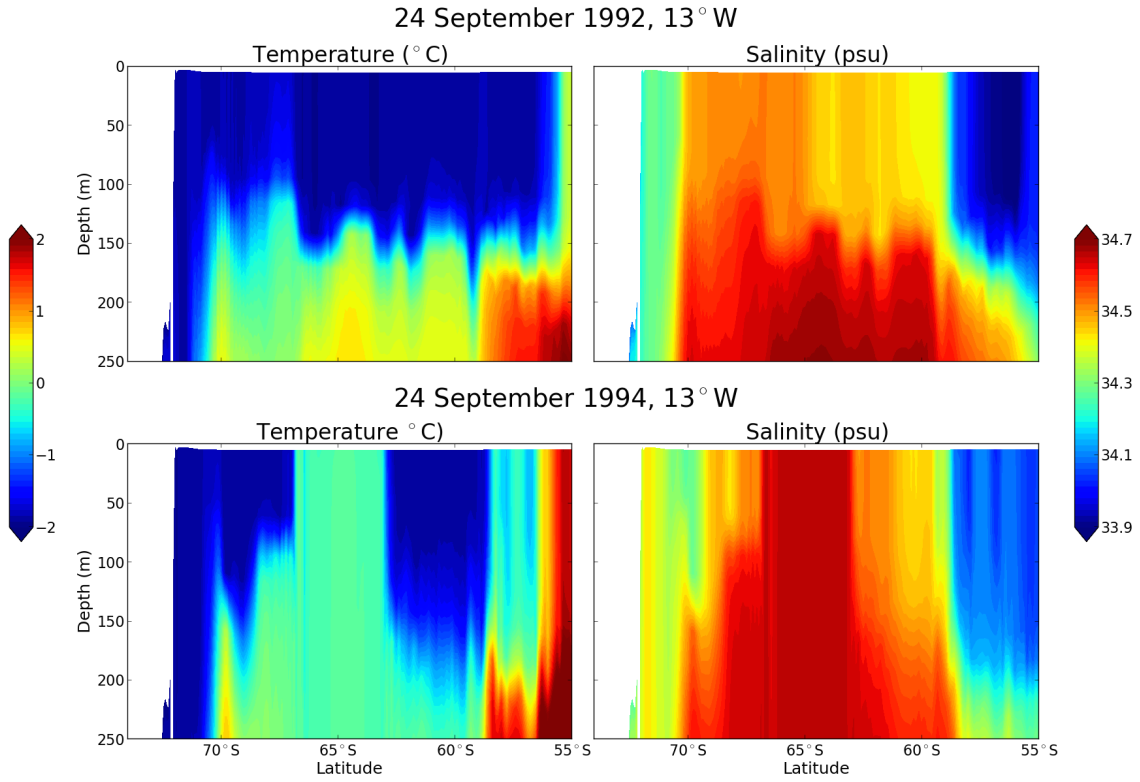

Figure 3.3: Meridional slices of temperature (°C) and salinity (psu) interpolated to 13°W, during a simulation with no surface salinity restoring. The top row shows conditions during the first spring (5-day average centered on 24 September 1992) and the bottom row during the third spring (24 September 1994).

Two years later (bottom row of Figure 3.3), the first deep convection event occurs. The water column homogenises near 65°S, with uniform temperature (approx. −0.25°C) and salinity (approx. 34.65 psu) through at least the upper 250 m of the water column. Figure 3.4a shows that this convection actually extends much deeper, with the local surface boundary layer depth (as calculated by the KPP parameterisation) in excess of 2000 m. The surface warming associated with the convection melts the sea ice in this region (Figure 3.4b), forming an open-ocean polynya which

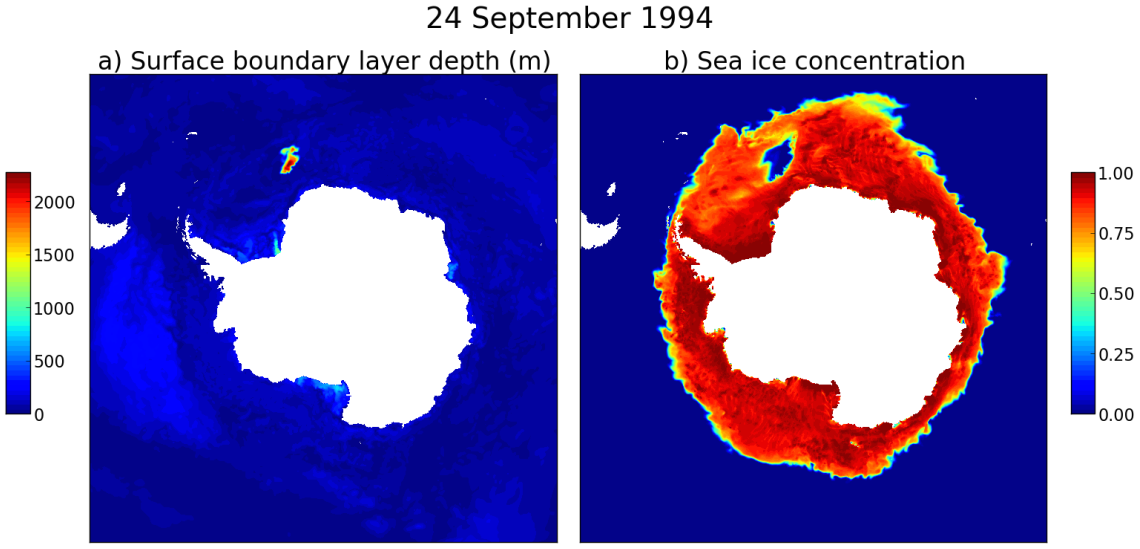

Figure 3.4: Conditions during the third spring (5-day average centered on 24 September 1994) of the simulation shown in Figure 3.3. (a) Depth of the surface boundary layer (m) as calculated by the KPP parameterisation. (b) Sea ice concentration (fraction).

is characteristic of this model bias. Furthermore, CDW becomes cooler and fresher in the Weddell Sea due its newfound atmospheric connection, and this signal gradually spreads through the rest of the domain following the pathway of Weddell Sea Bottom Water.

The conundrum is that Weddell Sea deep convection has been known to occur in observations, but only very occasionally. For example, the Weddell Polynya of 1974-1976 exhibited full depth open-ocean convection (*Gordon*, 1978) but was not observed again until the spring of 2017 (*Fetterrer et al.*, 2017). The sporadic nature of this convection suggests a connection to interannual variability in atmospheric conditions. In contrast, most CMIP5 models simulate such convection as a permanent fixture of both the Weddell and Ross Seas (*Heuzé et al.*, 2013). This model bias is so pervasive that even ocean reanalyses constrained by observations exhibit unrealistic deep convection (*Aguiar et al.*, 2017). At least in MetROMS, there does not appear to be any link between the onset of deep convection and specific atmospheric conditions beyond the seasonal cycle. During the many test simulations performed to investigate this issue, deep convection consistently began in spring (when surface salinity was highest following months of sea ice formation), but the year of onset varied widely depending on the model configuration. Atmospheric variability therefore appears to be overwhelmed by a bias in the model configuration itself.

The causes of simulated deep convection in the Weddell Sea have been investigated by previous studies. *Timmermann and Beckmann* (2004) demonstrated the importance of vertical mixing schemes, and showed that traditional convective adjustment

is especially prone to this problem. Even in more sophisticated mixing schemes, a shallow bias in summertime mixed layer depth prevents fresher surface water from being mixed down into the underlying Winter Water. The salinity of the Winter Water layer instead increases until the water column becomes unstable and overturns. *Kjellsson et al.* (2015) found a similar sensitivity to vertical mixing, but also showed that the surface freshwater budget has a role to play. Neglecting iceberg meltwater, or initialising with insufficient sea ice, causes salinity to increase in the mixed layer (and therefore the Winter Water, due to their seasonal connection), eventually triggering deep convection.

In this configuration of MetROMS, three improvements to the model design helped to delay the onset of convection. First, evaporation was originally calculated internally by ROMS as a function of simulated sea surface temperature. A warm bias in summer led to excessive evaporation, and in the absence of a coupled atmosphere model, this evaporation was not compensated by higher humidity and eventually increased precipitation. Rather, the freshwater was permanently lost, contributing to a positive salinity drift in the mixed layer. To address this problem, evaporation is instead prescribed from ERA-Interim as part of the atmospheric forcing.

Next, the CICE configuration originally used elastic-viscous-plastic (EVP) sea ice rheology. These simulations displayed excessive ridging, which displaced sea ice from the centres of the subpolar gyres and instead built up thicker ridges along the coast and along the boundaries of the gyres. Sea ice in the centre of the Weddell Gyre was relatively thin with lower concentration, and therefore sensitive to the frazil-open water feedback described in Section 2.4.2.1. Elastic-anisotropic-plastic (EAP) rheology yields better results, with a smoother and more realistic distribution of sea ice thickness in the subpolar gyres. These differences may be a result of several unrealistic assumptions made by the EVP formulation which are not present in EAP (*Tsamados et al.*, 2013). First, EVP treats sea ice as a continuum, assuming that ice floes are significantly smaller than the grid resolution. However, this domain has a relatively high resolution of approx. 10 km in sea ice covered regions, which could resolve the largest floes. Furthermore, EVP assumes that sea ice is isotropic, i.e. its properties do not depend on the orientation of individual floes. This assumption is contradicted by satellite observations, which reveal roughly diamond-shaped floes which interlock with a preferred orientation (*Tsamados et al.*, 2013). The EAP rheology implemented in CICE models this anisotropy on the sub-grid scale and makes no assumptions about the floe size. The resulting impacts on sea ice dynamics have been shown to improve simulated sea ice thickness in an Arctic domain, in a similar manner to the results described here for the Antarctic (*Tsamados et al.*, 2013).

Finally, the mixed layer was unrealistically shallow in summer, which contributed to salinity drift in the Winter Water layer as described above. To address this problem, the KPP modification of *Dinniman et al.* (2011) was implemented. Under stabilising conditions, the surface boundary layer depth is set to a theoretical minimum based on surface stress.

These three improvements are assessed here by individually removing them from the baseline simulation. Figure 3.5 plots timeseries of total sea ice area in four different simulations. The baseline simulation (as in Figures 3.3 and 3.4) exhibits occasional deep convection, but this does not melt enough ice to significantly impact the total area, which remains more or less stable during the 10 year simulation (black line). By contrast, simulations with EVP rheology (red line) or internally calculated evaporation (green line) display a steep decline in annual sea ice maxima. In these simulations, the Weddell Sea polynya enters an unstable state where the convective region grows larger every year, melting more and more ice from the Atlantic sector. Removing the KPP modification (blue line) originally leads to larger sea ice maxima than the baseline simulation, but these maxima decline more quickly than in any other simulation.

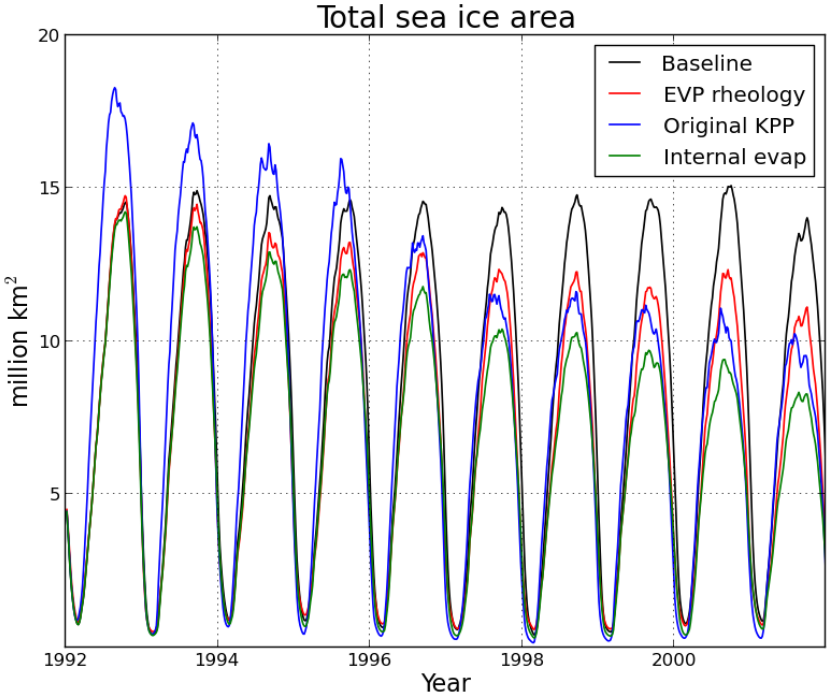

Figure 3.5: Timeseries of total sea ice area during four different simulations: "Baseline" = simulation shown in Figures 3.3 and 3.4. "EVP rheology" = simulation with elastic-viscous-plastic sea ice rheology instead of elastic-anisotropic-plastic. "Original KPP" = simulation without the KPP modification of *Dinniman et al.* (2011). "Internal evap" = simulation where evaporation is calculated internally by ROMS, instead of prescribed from ERA-Interim.

In longer simulations with repeated 1992-2005 forcing (following FESOM's control simulation in Chapter 5), the baseline simulation eventually enters the same unstable state where deep convection increases every year. The only permanent solution that was found to this problem was surface salinity restoring, which is used for the simulation in Chapter 2. Salinity drift in the mixed layer is therefore suppressed, and the water column never becomes unstable.

The main disadvantage of salinity restoring is the limitations it places on the types of simulations for which the model is appropriate. In particular, future projections such as those performed by FESOM (Chapter 5) should allow the surface salinity to evolve based on changes in atmospheric forcing, sea ice processes, and circulation, rather than being restored to a present-day climatology. MetROMS' need for surface salinity restoring was one reason why it was ultimately deemed unsuitable for such experiments.

3.7 Erosion of deep water masses

The susceptibility of terrain-following coordinate ocean models to spurious diapycnal mixing, leading to erosion of deep water masses, is a well known problem (*Griffies et al.*, 2000) and was demonstrated in ROMS by *Marchesiello et al.* (2009). Dissipative error is a consequence of the along-level diffusivity inherent in the upwind third-order scheme for tracer advection (*Shchepetkin and McWilliams*, 2005), which can align poorly with isopycnals in regions of steep bathymetry. To address this issue, *Marchesiello et al.* developed the RSUP3 advection scheme (Rotated Split UPstream 3rd order) in which the hyperdiffusive term is split from the upwind third-order scheme, rotated along geopotential surfaces, and added to the biharmonic diffusion operator. Alternatively, *Arango* (2010) demonstrated that the Akima advection scheme (*Shchepetkin and McWilliams*, 2005) performs better than the upwind third-order scheme with regards to diapycnal mixing.

The MetROMS simulation analysed in Chapter 2 uses the Akima advection scheme. Two additional simulations over the same 25-year period (1992-2016) were completed for comparison in this section. The first uses the upwind third-order advection scheme, with flux limiters as in Chapter 4; note that the addition of flux limiters had no discernible impact on diapycnal mixing. The second simulation uses the RSUP3 advection scheme developed by *Marchesiello et al.* (2009), but with the hyperdiffusive term rotated along isoneutrals as in *Lemarié et al.* (2012) rather than along geopotentials. These three simulations exhibit different levels of erosion of Southern Ocean deep water masses, as shown in Figure 3.6 with temperature and

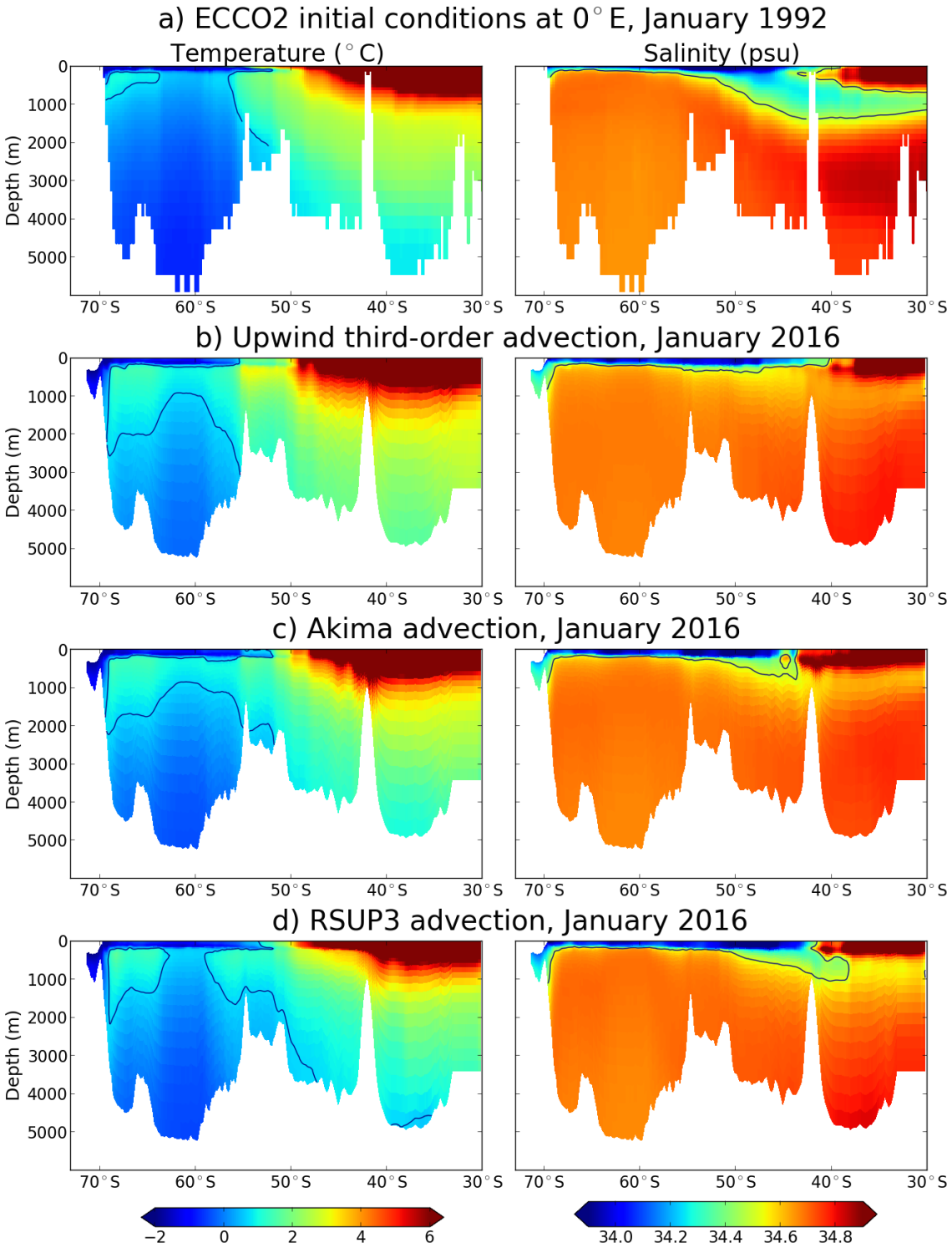

Figure 3.6: Temperature (°C) and salinity (psu) interpolated to 0°E. Black contours show the 0.75°C isotherm and the 34.5 psu isohaline. (a) Initial conditions from the ECCO2 reanalysis for January 1992. (b), (c), (d) Monthly average for January 2016 in three simulations using different tracer advection schemes: upwind third-order with flux limiters, Akima (the same simulation from Chapter 2), and RSUP3 respectively.

salinity slices through 0°E (as in Figure 2.6).

Antarctic Intermediate Water (AAIW, salinity < 34.5 psu, shown as a black contour) is characterised by the subsurface salinity minimum in the northern branch of the ACC. AAIW undergoes the most erosion in the upwind third-order simulation (Figure 3.6b), where increased salinity due to mixing with the underlying North Atlantic Deep Water (NADW) has left virtually no subsurface water below 34.5 psu after 24 years. The Akima advection scheme (Figure 3.6c) performs slightly better. AAIW is best preserved by the RSUP3 scheme (Figure 3.6d), although substantial erosion is still apparent compared to the initial conditions. Some of the residual salinification (between 0.05 and 0.07 psu) is due to the ECCO2 reanalysis, which provides lateral boundary conditions to MetROMS at 30°S, and which also exhibits some erosion of AAIW. It is also possible that underestimation of surface freshwater fluxes could be contributing to the increasing salinity of AAIW (*Griffies et al.*, 2009), although this would not explain the persistent freshening of the underlying NADW.

The increased southward spreading of warm Circumpolar Deep Water (CDW, temperature > 0.75°C, shown as a black contour) in MetROMS was also noted in Section 2.4.1.4. This phenomenon shows some sensitivity to advection schemes, with the upwind third-order simulation displaying the largest volume of warm CDW south of 55°S, and the RSUP3 simulation the least. RSUP3 also best preserves the cold Antarctic Bottom Water (AABW) in the northern part of the domain. While the increased volume of warm CDW is part of a general deep ocean warming south of 55°S, which may be due to biases in sea ice processes and/or bottom water formation, this sensitivity to advection schemes indicates that spurious diapycnal mixing could be part of the problem.

Section 3.3.2 suggested that the relatively low ACC transport simulated by MetROMS could be due to spurious diapycnal mixing, which weakens the meridional density gradient across the Southern Ocean through the erosion of deep water masses. The simulations analysed here support this hypothesis. Compared to the 2002-2016 mean Drake Passage transport of 126.8 Sv in the Akima simulation, transport is weaker in the upwind third-order simulation (123.5 Sv) and stronger in the RSUP3 simulation (136.4 Sv). However, transport in RSUP3 still falls below the most recent observational estimates of 173.3 ± 10.7 Sv (*Donohue et al.*, 2016).

Based on these results, while RSUP3 improves the preservation of deep water masses in this configuration of MetROMS, it does not appear to be a complete solution to water mass erosion. Additionally, RSUP3 imposes additional limits on the model timestep. The simulation presented here uses a baroclinic ocean timestep of 200

seconds, compared to 300 seconds for all other MetROMS simulations. Even this 200 second timestep is not stable in all circumstances, as other tests with RSUP3 using slightly different configurations of MetROMS (for example, with surface salinity restoring turned off) developed numerical instabilities. Due to the additional computational expense and the unreliable stability, combined with the merely moderate improvements to deep water mass preservation, the RSUP3 advection scheme was not used in the final configuration of MetROMS.

Lemarié et al. (2012) improved the stability of the RSUP3 scheme by implementing an implicit treatment of vertical fluxes in the CROCO (Coastal and Regional Ocean COmmunity model) branch of ROMS. Due to fundamental differences in the kernel between the CROCO and Rutgers branches of ROMS, it was decided that implementing *Lemarié et al.*'s work in MetROMS was beyond the scope of this project.

3.8 Influence of tides

As described in Section 2.4.3, both MetROMS and FESOM underestimate total basal melting of Antarctic ice shelves, which is likely partially due to the absence of tides in the models. Including tides in ice-shelf/ocean simulations has been shown to increase melt rates in a variety of circumstances (*Dinniman et al.*, 2016; *Makinson et al.*, 2011; *Gwyther et al.*, 2016), due to tidal currents increasing drag at the ice shelf base. In some cases, this increased drag also amplifies ice shelf refreezing (*Mueller et al.*, 2018; *Gwyther et al.*, 2015).

The size of MetROMS' circumpolar Antarctic domain and the unstable tendencies of its northern boundary prevent the explicit simulation of tides, which in ROMS requires specifying tidal elevations and/or velocities at the lateral boundaries (see Section 2.5). An alternative parameterisation of tidal effects on ice shelf melt rates was tested, which affects the friction velocity u^* in ice shelf cavities. The root-mean-squared (rms) tidal velocity u_{tide} is considered by u^* as follows:

$$u^* = \max\left(\sqrt{C_d\,(u^2 + v^2 + u_{tide}^2)}, u^*_{min}\right) \tag{3.1}$$

where all other terms are the same as in Equation 2.2. This follows the parameterisation of *Asay-Davis et al.* (2016) used by the ISOMIP+ experiments.

To calculate the rms tidal velocity, the amplitudes of horizontal transports A_U and A_V (in m^2/s) were obtained for each point in ice shelf cavities and each of 10 tidal

components, using the CATS 2008a_opt tidal model (*Padman et al.*, 2008). Since the root-mean square of a sinusoid of amplitude A, regardless of phase or period, is $\frac{A}{\sqrt{2}}$, u_{tide} becomes

$$u_{tide} = \frac{1}{h - z_{ice}} \sum_{n=1}^{10} \frac{\sqrt{A_U^2 + A_V^2}}{\sqrt{2}} \tag{3.2}$$

where $h - z_{ice}$ (bathymetry minus ice shelf draft) is the water column thicknes in m, and n is the tidal component.

With this parameterisation, tides influence ice shelf melt rates, but not ocean mixing. This produces a negative feedback which counteracts the initial increase in ice shelf melting (Figure 3.7). During the first 5 days of simulation, the tidal parameterisation increases total basal mass loss by 23% compared to the baseline simulation from Chapter 2. Neither simulation has had time to deviate from the initial temperature and salinity fields, so the effects of u^* can be assessed more or less in isolation. However, in a matter of days the increase in total basal mass loss drops to approximately 7%, and then slowly decays to approximately 4% after 10 years. This effect is due to generally colder temperatures in ice shelf cavities, which compensate for the increased u^* values. The initial increases in ice shelf melt produce excess cold, fresh meltwater which is not adequately mixed out of the cavities. As a result, the two simulations converge. Differences on the regional scale (not shown) are also minor.

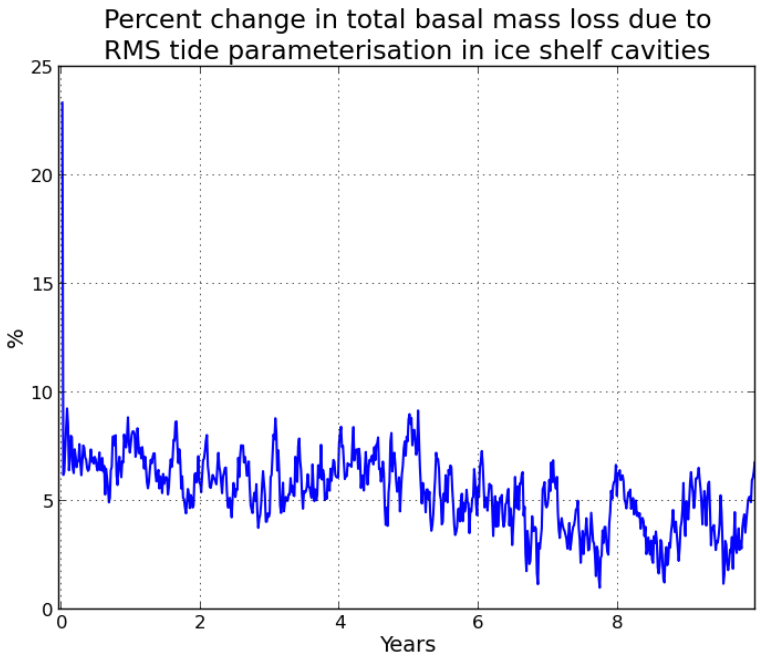

Figure 3.7: Timeseries (5-day averages) of percent change in total basal mass loss from all ice shelves. Results are calculated for a simulation parameterising the effects of tides on ice shelf melt rates, compared to the baseline simulation of Chapter 2.

These results contrast with regional ocean/ice-shelf simulations including explicit representations of tides, which have been found to increase basal mass loss by 25-100% (*Dinniman et al.*, 2016). This discrepancy suggests that parameterisations of tidal effects on ice shelf melt rates must also be implemented into the ocean mixing scheme, and that u^* cannot be considered in isolation. This parameterisation was therefore not included in the final configuration of MetROMS.

3.9 Topography smoothing in FESOM

Since an operational global configuration of FESOM already existed prior to this project, adapting the model for our purposes was significantly less challenging than with MetROMS. However, one significant complication arose during the generation of FESOM's unstructured mesh. As described in Section 2.2.3, the radii of the Gaussian filters used to smooth the bathymetry and ice shelf draft are scaled by the desired final resolution, which varies spatially. Creating this desired resolution requires some trial and error, as it depends on the placement of individual patches, the latitude of the rotated grid, and numerous parameters. Each attempt produces a scaling file which is used by the Gaussian filters for topographic smoothing. During the original generation of the two FESOM meshes presented in Chapter 2, the Gaussian smoothing was mistakenly never updated following the first attempt. That is, the topography was smoothed at a resolution which did not match the final resolution of either mesh. Furthermore, the same smoothing was used for both the low-resolution and high-resolution meshes. As a result, large areas of the Antarctic continental shelf were oversmoothed, particularly the Amundsen Sea as well as the Filchner-Ronne and Amery Ice Shelf cavities. The bathymetry was more affected than the ice shelf draft, as the latter only receives one pass of the Gaussian filter, and instead undergoes most of its smoothing via the slope-limiting procedure described in Section 2.2.3 which does not depend on the scaling file.

A deficiency in the FESOM mesh machinery was also discovered, in which land points were included in the Gaussian smoothing windows for the bathymetry. This had little effect on most regions of the Antarctic Ice Sheet, where the bedrock smoothly slopes across the grounding line. However, in steep-sided fjords such as the Amery Ice Shelf cavity and the deep ice regions near the Filchner-Ronne grounding line, smoothing into the land mask caused substantial shoaling of the bathymetry. Other FESOM meshes with much higher resolution in these regions as well as fewer passes of the Gaussian filters (*Timmermann and Goeller*, 2017) were largely unaffected by this problem, but it was a point of concern for the meshes used in this project.

When these problems came to light, both meshes were regenerated with the correct scaling for topographic smoothing, and with land points excluded from the smoothing windows. All the FESOM experiments in Chapters 2 and 5 were rerun. This section briefly compares the results of the high-resolution intercomparison simulation (Chapter 2) before and after the mesh was corrected.

The largest changes are seen in the Amundsen Sea, particularly in the Pine Island Ice Shelf region shown in Figure 3.8. A trough in the continental shelf is largely smoothed away in the old mesh (Figure 3.8a), which cuts off the pathway for CDW to travel onshore. As a result, the continental shelf is filled with cold LSSW near the surface freezing point (Figure 3.8b), with virtually no presence of warmer MCDW.

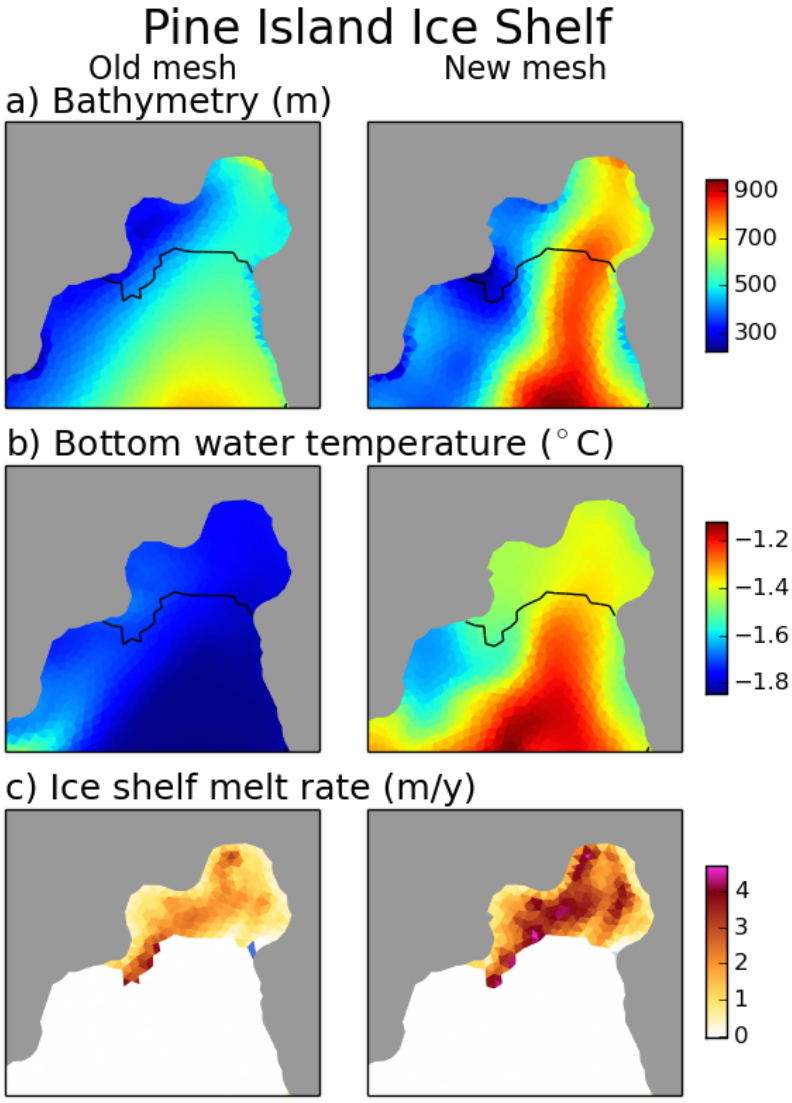

Figure 3.8: The Pine Island Ice Shelf in the high-resolution FESOM intercomparison experiment described in Chapter 2. Results are shown for the oversmoothed mesh (left) as well as for the final mesh where the oversmoothing has been rectified (right, same simulation as in Chapter 2). (a) Bathymetry (m). The black contour shows the ice shelf front. (b) Bottom water temperature (°C) averaged over 2002-2016. (c) Ice shelf melt rate (m/y) averaged over 2002-2016.

In the new mesh, the trough is better preserved, leading to increases in bottom water temperature of approximately 0.6°C on the continental shelf and 0.3°C in the ice shelf cavity. Ice shelf melt rates markedly increase (Figure 3.8c), with total basal mass loss from the Pine Island Ice Shelf increasing by 67%.

The Amery Ice Shelf cavity (Figure 3.9) is more affected by the consideration of the land mask during smoothing, due to the steep bedrock surrounding the cavity. In the old mesh, considering these points in the smoothing windows (combined with excessively large smoothing windows) causes the bathymetry to shoal substantially. Water column thickness near the back of the cavity is reduced by approximately 1000 m compared to the corrected mesh (Figure 3.9a). This inhibits the transport of inflowing MCDW to the grounding line, where cold ISW builds up instead (Figure 3.9b).

In the corrected mesh, stronger transport at the back of the cavity leads to warmer temperatures, and therefore increased ice shelf melt rates (Figure 3.9c). This effect is counteracted by lower melt rates in the outer two-thirds of the cavity, such that total basal mass loss from the entire ice shelf decreases by 13%. Similar processes are seen beneath the Filchner-Ronne Ice Shelf (not shown), which instead experiences a negligible increase (0.4%) in total basal mass loss.

In addition to these regional changes in ice shelf cavities, which can be directly attributed to local changes in the topography, the updated FESOM mesh exhibits several large-scale changes which indicate more complex teleconnections. Transport of the ACC through Drake Passage is reduced by 6% compared to the oversmoothed mesh, which is most likely due to baroclinic adjustment to changes in temperature and salinity. Finally, the corrected mesh simulates higher sea ice minima, with total February sea ice extent (1992-2016 mean) increasing by 31%. This is due to thicker coastal sea ice which better survives the summer melt, and which in turn is likely influenced by bathymetry-dependent circulation on the continental shelf.

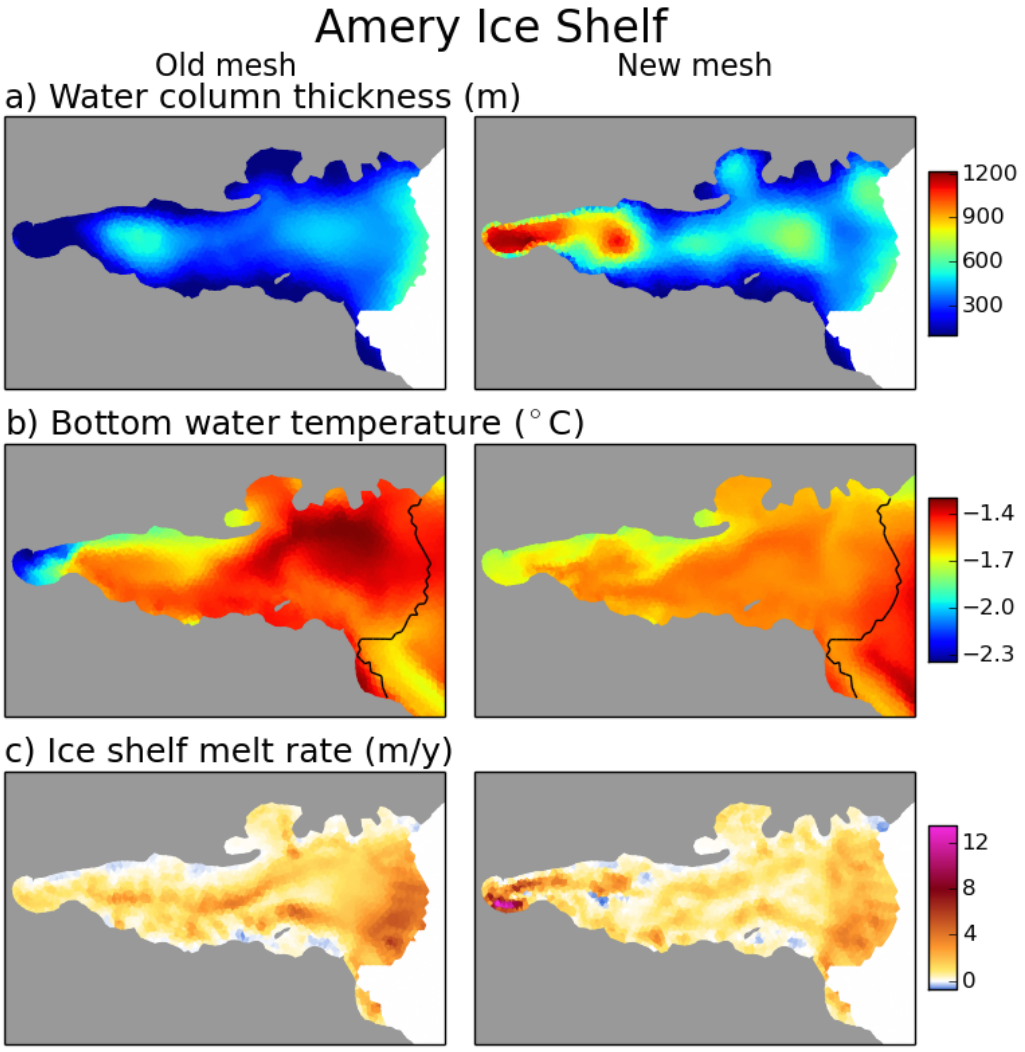

Figure 3.9: As in Figure 3.8, but for the Amery Ice Shelf cavity. (a) Water column thickness (m). (b) Bottom water temperature (°C) averaged over 2002-2016. The black contour shows the ice shelf front. (c) Ice shelf melt rate (m/y) averaged over 2002-2016.

3.10 Discussion and conclusions

As well as several unique defects due to well-buried bugs in the code, the circumpolar Antarctic configuration of MetROMS has experienced many of the same challenges as other Southern Ocean models over the course of its development, including unrealistic Drake Passage transport, deep convection in the Weddell Sea, and degradation of the boundaries between deep water masses. The case studies presented here explored the causes of these biases and their sensitivities to model design choices. Some of the resulting insights confirmed the results of previous studies with other models, while others represented new information which had not been previously discussed in the literature. Finally, the influence of topographic smoothing was demonstrated

in one case study with FESOM.

As shown in Chapter 2, MetROMS performs quite well on the Antarctic continental shelf and in ice shelf cavities, producing sub-ice circulation patterns and hydrography which are often more realistic than in FESOM. However, unresolved challenges in the deep ocean prevent long transient simulations with MetROMS. First, surface salinity restoring is required to prevent ever-expanding deep convection in the Weddell Sea, but such restoring would not be appropriate for future projections where surface salinity is not expected to conform to the present-day climatology. Second, spurious diapycnal mixing in the deep ocean causes progressive erosion of water masses over time, a form of model drift which subsequently weakens the ACC. Simulated conditions in the interior Southern Ocean are therefore unreliable on longer timescales, and may eventually influence the continental shelf and ice shelf cavities.

Future development of MetROMS could follow several pathways to address these issues. A permanent solution to Weddell Sea deep convection has so far proved elusive, but continued experimentation may reveal further improvements. Implementing the modified Pacanowski-Philander vertical mixing scheme used by FESOM (Section 2.2.4) may be beneficial, as *Timmermann and Beckmann* (2004) found this scheme to produce more realistic Weddell Sea hydrography than the KPP parameterisation. Another potential solution could be to tune CICE to produce higher sea ice concentration, which would damp the frazil-open water feedback currently overactive in MetROMS (Section 2.4.2.1). With regards to spurious diapycnal mixing, implementing the full RSUP3 tracer advection scheme of *Lemarié et al.* (2012) including its stability improvements is likely the best available option. This process would not be straightforward, due to structural differences in the ROMS kernel, but should yield improved representation of deep water masses. Finally, an explicit consideration of tides by MetROMS is worth pursuing, given the known influence of tides on sub-ice shelf processes (*Padman et al.*, 2009; *Makinson et al.*, 2011; *Mueller et al.*, 2018). The most appropriate implementation is likely the complete lunisolar tides of *Thomas et al.* (2001) and *Müller et al.* (2010), rather than approaches concerned with the lateral boundaries. An appropriate consideration of tides would be expected to increase basal melt rates in MetROMS, bringing them more in line with observational estimates.

When considering such possibilities for future development, one must consider the purpose of the given model. The processes to be studied, and the types of experiments to be completed, should guide the prioritisation of areas needing improvement. For example, if future research with MetROMS is limited to short-timescale, present-day process studies on the continental shelf, then deep ocean drift and surface salinity restoring would not be causes for concern. More relevant topics for

development would be the addition of tides, and potentially an increase in horizontal resolution. If future research instead pursues future projections similar to those completed with FESOM in Chapter 5, then MetROMS' performance in the deep ocean would require more attention. Ultimately both types of experiments are a research priority, so model development is likely to span all of these areas.

It is also important to note that different models invariably have different strengths and weaknesses due to key design elements which are not easily changed, such as vertical coordinate systems or fundamental numerical methods. Therefore, while continued development of individual models is essential, the use of several different models to study the same processes is a valuable strategy to better understand the climate system, and how best to model it.

Chapter 4

Spurious sea ice formation caused by oscillatory ocean tracer advection schemes

Preamble

One of the issues discussed in Chapter 3 warranted further attention: the link between oscillatory ocean tracer advection schemes and spurious sea ice formation (Section 3.5.3). Numerical oscillations in high-order advection schemes are a well-studied problem, but their impact on coupled sea ice models had not yet been investigated in the literature. There was no reason to believe that this mechanism of error was unique to MetROMS, so communication of the problem to the wider ocean/sea-ice modelling community was imperative.

This chapter is based on the paper "Spurious sea ice formation caused by oscillatory ocean tracer advection schemes" by Kaitlin A. Naughten, Benjamin K. Galton-Fenzi, Katrin J. Meissner, Matthew H. England, Gary B. Brassington, Frank Colberg, Tore Hattermann, and Jens B. Debernard, which was published in *Ocean Modelling* in June 2017. Compared to the published paper, the version reproduced here has several minor wording changes and clarifications, none of which affect the main conclusions of the study. I have secured copyright permission to reproduce the publication within this thesis.

I completed the majority of the work for this publication: installing and configuring MetROMS, discovering the mechanism of error, designing and running simulations, analysing results, and writing the paper. My supervisors Katrin Meissner, Ben Galton-Fenzi, and Matthew England gave me advice throughout the process. Gary

Brassington and Frank Colberg provided the flux limiter code which extends the upwind third-order advection scheme in ROMS. Tore Hattermann and Jens Debernard provided the MetROMS coupling code. All co-authors provided comments on the manuscript.

Note that since the simulations were completed and published earlier, the model configuration in this chapter is slightly different to Chapters 2 and 3. In particular, the improvements to MetROMS to prevent spurious deep convection in the Weddell Sea (Section 3.6) had not yet been implemented, with the exception of prescribed evaporation. However, the water column structure triggering convection takes several years to develop, while the simulations presented in this chapter are only 1 year long. They are therefore uncontaminated by spurious deep convection.

Abstract

Tracer advection schemes used by ocean models are susceptible to artificial oscillations: a form of numerical error whereby the advected field alternates between overshooting and undershooting the exact solution, producing false extrema. Here we show that these oscillations have undesirable interactions with a coupled sea ice model. When oscillations cause the near-surface ocean temperature to fall below the freezing point, sea ice forms for no reason other than numerical error. This spurious sea ice formation has significant and wide-ranging impacts on Southern Ocean simulations, including the disappearance of coastal polynyas, stratification of the water column, erosion of Winter Water, and upwelling of warm Circumpolar Deep Water. This significantly limits the model's suitability for coupled ocean-ice and climate studies. Using the terrain-following-coordinate ocean model ROMS (Regional Ocean Modelling System) coupled to the sea ice model CICE (Community Ice CodE) on a circumpolar Antarctic domain, we compare the performance of three different tracer advection schemes, as well as two levels of parameterised diffusion and the addition of flux limiters to prevent numerical oscillations. The upwind third-order advection scheme performs better than the centered fourth-order and Akima fourth-order advection schemes, with far fewer incidents of spurious sea ice formation. The latter two schemes are less problematic with higher parameterised diffusion, although some supercooling artifacts persist. Spurious supercooling was eliminated by adding flux limiters to the upwind third-order scheme. We present this comparison as evidence of the problematic nature of oscillatory advection schemes in sea ice formation regions, and urge other ocean/sea-ice modellers to exercise caution when using such schemes.

4.1 Introduction

A central element of ocean models is the advection of temperature and salinity, simulated using a number of different numerical methods (*Griffies et al.*, 2000). These advection schemes are susceptible to various types of numerical error (*Hecht et al.*, 2000; *Shchepetkin and McWilliams*, 1998; *Lilly*, 1965), including issues with stability, artifical dissipation (by which water masses over-mix), and artifical oscillations. It is the last such issue that we focus on here. Oscillations, also known as overshoots or dispersion, are characterised by tracer fields that appear jagged and erratic after advection, with false extrema (*Shchepetkin and McWilliams*, 1998). These oscillations most likely occur near steep gradients in the given tracer field, which can be poorly resolved at low resolution.

Oscillatory behaviour in various tracer advection schemes has been well-studied (*Hecht et al.*, 2000; *Shchepetkin and McWilliams*, 1998; *Pietrzak*, 1998), and its potential for undesirable feedbacks with ocean processes has been demonstrated (*Hecht*, 2010; *Farrow and Stevens*, 1995; *Gerdes et al.*, 1991). However, there are no published investigations of how oscillatory behaviour interacts with coupled ocean/sea-ice models. When simulating regions of sea ice formation, there is a major threshold associated with the freezing point. Oscillations which cause the ocean temperature to fall below the freezing point therefore have physical significance beyond simple numerical error, as acknowledged by *Hecht et al.* (2000). In some ways this situation is similar to the simulation of regions with strong freshwater inflow, where oscillations could cause negative salinity.

In this study, we use a terrain-following-coordinate ocean model (*Shchepetkin and McWilliams*, 2005; *Galton-Fenzi et al.*, 2012) with a coupled sea ice model (*Hunke et al.*, 2015) to show that oscillatory tracer advection schemes have a significant impact on sea ice formation. When oscillations cause the ocean temperature to fall below the freezing point, this spurious supercooling is then removed from the near-surface layers as frazil ice. This frazil forms even if the ocean is already shielded from atmospheric heat fluxes by a layer of solid sea ice. As a result, unphysically thick patches of sea ice occur. These thick patches of sea ice have a significant influence on other physical processes, including coastal polynyas, stratification of the water column, dense water formation, and the properties of deep water masses. Note that despite the similar terminology, this phenomenon is distinct from the temporal oscillations in ice-ocean Ekman transport discussed by *Roberts et al.* (2015).

Steep horizontal gradients in tracer fields are more common in the local coordinate space of sigma- or terrain-following-coordinate ocean models (*Griffies et al.*, 2000),

which discretise the vertical dimension using fractional depth of the water column rather than absolute depth. Here we use "horizontal" to describe a line or surface of constant vertical level on the terrain-following grid, rather than of constant depth. If the underlying bathymetry is steep, horizontally adjacent grid cells can lie at quite different depths. A sharp gradient in depth often translates to a sharp gradient in tracers such as temperature or salinity. By contrast, the same region modelled with z-coordinates would have weaker temperature and salinity gradients between horizontally adjacent grid cells, which would by definition lie at exactly the same depth. Since the ocean is, for the most part, well mixed in the horizontal but stratified in the vertical, there are more opportunities for sharp horizontal gradients in sigma-space than in z-space. As a consequence, sigma-coordinate and terrain-following coordinate ocean models may be particularly susceptible to artificial oscillations over areas of steep bathymetry.

Advection schemes are typically tested on idealised domains, often at very high resolution and sometimes with reduced dimensionality. In practice, however, advection schemes are ultimately incorporated into "realistic configurations", which we define here as three-dimensional forward models on observed domains, generally with rougher bathymetry and lower resolution than idealised setups. We believe it is valuable to communicate the effects of numerical error on realistic configurations, since they are the ones most often used to understand observations, make future projections, and ultimately inform policy. By understanding how errors present themselves in realistic domains, with realistic forcing and commonly used resolution, we hope to forewarn other members of the ocean modelling community who might otherwise experience similar problems, and to provide an acceptable solution.

4.2 Advection schemes

In a finite-volume discretisation of the primitive equations for ocean circulation, the concentration of a tracer at a given grid box represents the volume average over that grid box. The advection of the tracer depends on the advective fluxes through each face of the grid box. However, the calculation of these fluxes depends on the area-averaged concentration of the tracer over each face, and there is no exact solution for the interpolation of these values from the adjacent volume-averages. Several different numerical methods have been developed to address this interpolation, giving rise to different advection schemes. In our simulations we compare three different advection schemes from the standard distribution of ROMS (the Regional Ocean Modelling System) (*Shchepetkin and McWilliams*, 2005), as well as a limiter scheme designed to remove oscillations from one of the advection schemes.

4.2.1 Centered fourth-order

The centered fourth-order advection scheme (*Shchepetkin and McWilliams*, 2005) interpolates tracers to grid box faces using a midpoint-average modified by a gradient or curvative term. This interpolation is centered, and fourth-order accurate, in space. While this scheme is less prone to oscillations than its second-order counterpart (*Shchepetkin and McWilliams*, 1998), oscillations still occur (*Leonard and Mokhtari*, 1990).

4.2.2 Akima fourth-order

The Akima fourth-order advection scheme (*Shchepetkin and McWilliams*, 2005) differs from the centered fourth-order scheme only in its calculation of the gradient or curvature term, which utilises harmonic averaging rather than a simple midpoint average. *Shchepetkin and McWilliams* (2005) found that this scheme reduces oscillations compared to the centered fourth-order scheme.

4.2.3 Upwind third-order

There are several different schemes in the upwind third-order family; here we use the scheme known as UTOPIA (*Shchepetkin and McWilliams*, 2005; *Rasch*, 1994; *Leonard*, 1993). The interpolation of tracers to grid box faces is not centered in space, but rather is biased toward the upwind or upstream direction, which depends on the sign of the given velocity component. Upwind schemes in general suppress oscillations (*Griffies et al.*, 2000), as the truncation errors associated with upwind interpolation are dominated by dissipation rather than dispersion. In first-order upwind schemes, this can lead to unphysical diapycnal mixing which breaks down fronts between water masses. In comparison, third-order schemes exhibit significantly reduced artificial dissipation (*Leonard*, 1993). The residual is considered "implicit diffusion" which can often be compensated for by reducing or even eliminating explicitly parameterised diffusion (*Farrow and Stevens*, 1995; *Dinniman et al.*, 2015). Note that we use this scheme only for horizontal tracer advection; it is paired with the centered fourth-order advection scheme in the vertical.

4.2.4 Upwind limiters

While the upwind third-order scheme is known to significantly reduce oscillations compared to centered advection schemes, oscillations can still occur near sharp gradi-

ents (*Leonard*, 1993). These oscillations can be targeted and removed using a flux limiter scheme. Here we implement the "universal limiter" developed by *Leonard and Mokhtari* (1990) as part of the ULTRA-SHARP scheme; see also *Norris* (2000). This scheme calculates limits for the interpolated tracer values at each grid box face, and by enforcing these limits it clips false extrema, as follows:

Let C^* be the concentration of a tracer interpolated by the upwind third-order advection scheme to a given grid box face in the east-west direction. Let C_{WW}, C_W, C_E, and C_{EE} denote the volume-averaged (i.e. known) concentrations two cells west, one cell west, one cell east, and two cells east of this face. The flux limiters are then used to calculate a new concentration, C, as follows:

$$C = \begin{cases} \text{median}\left[C_E, C^*, \text{median}\left[C_W, C_E, C_{WW} + \alpha\left(C_W - C_{WW}\right)\right]\right] & \text{if } u \geq 0 \\ \text{median}\left[C_W, C^*, \text{median}\left[C_E, C_W, C_{EE} + \alpha\left(C_E - C_{EE}\right)\right]\right] & \text{if } u < 0 \end{cases} \tag{4.1}$$

where u is the zonal velocity at the grid box face. The equations are similar for the north-south faces. As with the baseline upwind third-order advection scheme, the upwind limiters are only applied in the horizontal.

Equation 4.1 defines three bounds on C, the first two of which are fixed, and the third which is modified by the parameter α which controls the amount of clipping. Smaller values of α lead to stricter clipping of oscillations, but may also clip some legitimate extrema. The specific choice of α is determined empirically. The original reference (*Leonard and Mokhtari*, 1990) set $\alpha = 10$, while we use $\alpha = 5$. Our solution showed little sensitivity to values of α greater than 5, and the smaller value is seen as the more conservative design choice.

Further details on the upwind limiter scheme and its implementation in ROMS can be found in an upcoming paper by *Brassington et al.* (2018).

4.2.5 Other advection schemes

Another popular tracer advection scheme among ROMS users is MPDATA (Multidimensional Positive Definite Advection Transport Algorithm) (*Smolarkiewicz*, 1984). This scheme is sign-preserving, and therefore unsuitable for temperature gradients across 0°C. In order to use MPDATA for the simulation of sea ice formation regions or ice shelf cavities, the temperature field would need to be transformed to ensure positivity. The advection could be done in Kelvins rather than degrees Celsius; alternatively, a smaller value surpassing the minimum freezing point (such as 5°C,

noting the depth-dependent freezing point in ice shelf cavities) could be added to temperature before advection and subtracted after. No other routines in the model would experience the extra 5°C, so the model physics would not be affected.

We experimented with the HSIMT scheme (High-order Spatial Interpolation at the Middle Temporal level) (*Wu and Zhu*, 2010), a non-oscillatory scheme that shares many properties with MPDATA, but is suitable for negative temperatures. Unfortunately, this scheme caused unacceptably high levels of spurious diapycnal mixing in our configuration (not shown). For different configurations, perhaps with higher resolution, HSIMT may be suitable. For all advection schemes, errors of both dissipative and dispersive nature are less likely at high resolution.

4.3 Model description

Our simulations are performed with the MetROMS model, which consists of the ROMS ocean model (Regional Ocean Modelling System) (*Shchepetkin and McWilliams*, 2005) including ice shelf thermodynamics (*Galton-Fenzi et al.*, 2012), coupled to the CICE sea ice model (Community Ice CodE) (*Hunke et al.*, 2015) using the MCT coupler (Model Coupling Toolkit) (*Larson et al.*, 2005; *Jacob et al.*, 2005). The coupling infrastructure was implemented by the Norwegian Meteorological Institute (*Debernard et al.*, 2017), and is described in Section 4.3.5.

4.3.1 Domain

We run MetROMS on a circumpolar Antarctic domain, with a northern boundary at 30°S. Horizontal resolution for both ROMS and CICE is $\frac{1}{4}^\circ$ scaled by cosine of latitude, and the South Pole is relocated to ensure approximately equal resolution around the coastline. This results in Cartesian resolutions ranging from 8-10 km on the Antarctic continental shelf to 15-20 km in the Antarctic Circumpolar Current (ACC). While this resolution is higher than most global coupled models, it is lower than many ROMS simulations, which often use smaller domains (such as the Amery Ice Shelf configuration of *Galton-Fenzi et al.* (2012) with resolution between 3-7 km; the Mertz Glacier Tongue configuration of *Cougnon et al.* (2013) with resolution between 2-3 km; and the Totten Ice Shelf configuration of *Gwyther et al.* (2014) with resolution between 2.5-3.5 km). Bathymetry, ice shelf draft, and land/sea masks were given by RTopo 1.05 (*Timmermann et al.*, 2010), and smoothed as in *Lemarié et al.* (2012) to ensure stability with terrain-following coordinates.

4.3.2 Forcing

ROMS and CICE are forced with the same atmospheric state, from which each component calculates bulk fluxes of heat, salt, and momentum. Over grid cells containing a mix of sea ice and open water, these fluxes are merged by the coupler.

Atmospheric forcing is provided by the ERA-Interim reanalysis (*Dee et al.*, 2011) and consists of 6-hourly fields for near-surface temperature, pressure, humidity, winds, and total cloud cover; and 12-hourly fields for rain, snow, and evaporation. The 6-hourly fields are linearly interpolated to each model timestep. The 12-hourly fields represent total water fluxes over the given 12-hour period, and are not interpolated in time but rather applied at a constant rate with a step change every 12 hours. For our one-year simulations we use 1992 forcing. We also apply an estimate of freshwater fluxes from iceberg melt, using the monthly-averaged 100-year climatology simulated by *Martin and Adcroft* (2010).

ROMS also requires lateral boundary conditions at the open northern boundary, 30°S. For this we use monthly averaged fields of temperature, salinity, and horizontal velocity from the ECCO2 cube92 reanalysis (*Menemenlis et al.*, 2008; *Wunsch et al.*, 2009) for 1992. Northern boundary conditions for sea surface height are given by the AVISO climatology (*AVISO*, 2011). The numerical treatment of these boundary conditions is discussed in Section 4.3.3.

4.3.3 Ocean configuration

ROMS is a split-explicit, free-surface, terrain-following-coordinate ocean model (*Shchepetkin and McWilliams*, 2005). We use the development version 3.7 of the Rutgers ROMS code, with the addition of ice shelf thermodynamics using the standard three-equation parameterisation (*Galton-Fenzi*, 2009; *Galton-Fenzi et al.*, 2012). Our grid has 31 terrain-following vertical levels, with higher resolution near the surface and bottom of the water column. Typical vertical resolutions are 1-3 m at the surface and 200-300 m in the deep interior ocean. In ice shelf cavities, vertical resolution is often finer than 1 m. With such thin vertical layers we require a baroclinic timestep of 5 minutes, with 30 barotropic timesteps for each baroclinic.

While we vary the tracer advection scheme in our experiments, advection of momentum uses the same scheme for all experiments: upwind third-order advection in the horizontal, and centered fourth-order advection in the vertical. Subgrid-scale mixing is parameterised using biharmonic viscosity (for momentum) and Laplacian diffusivity (for tracers). The horizontal mixing coefficients are 1000 m^4/s for bi-

harmonic viscosity, and either 15 or 150 m^2/s for Laplacian diffusivity (varying by experiment, see Section 4.3.7). These coefficients apply to the resolution of the largest grid cell (approx. 24 km) and are scaled linearly for smaller grid cells. We use the Large-McWilliams-Doney interior closure scheme (*Large et al.*, 1994) which includes the KPP boundary layer parameterisation.

Particular care must be taken at the open northern boundary, where instabilities can easily occur due to discontinuities between the lateral boundary conditions and the simulated fields. We follow the method used by the Southern Ocean State Estimate simulations (*Mazloff et al.*, 2010) on a similar circumpolar domain (Matthew Mazloff, personal communication). First, zonal velocity u is clamped to zero at the northern boundary to prevent waveguide artifacts. Second, the bathymetry is modified to be constant in y over the northernmost 15 rows of grid cells (approx. 3° latitude). In this way, boundary conditions for meridional velocity v can smoothly transition into the domain without immediately encountering variations in topography. Finally, a sponge layer is applied over these northernmost 15 rows, whereby the diffusivity coefficient linearly increases to 10 times its background value at the northern boundary, and the viscosity coefficient (which has units of m^4/s rather than m^2/s) to 100 times the background value. The numerical methods used to apply the northern boundary conditions consist of the Chapman scheme for sea surface height (*Chapman*, 1985), the Flather scheme for barotropic v (*Flather*, 1976), and the radiation-nudging scheme for baroclinic v, temperature, and salinity (*Marchesiello et al.*, 2001).

4.3.4 Sea ice configuration

CICE is a dynamic-thermodynamic sea ice model which has been successfully coupled to several global climate models (*Hunke et al.*, 2015). We use version 5.1.2 of the CICE code. Our simulations have 7 vertical ice layers plus 1 snow layer, and 5 ice thickness categories. The sea ice timestep is 30 minutes for both dynamic and thermodynamic processes.

Our configuration uses the "mushy" thermodynamics scheme (*Turner et al.*, 2013a). We use the level-ice melt pond parameterisation with Stefan refreezing. Radiation is treated by the Delta-Eddington scheme (*Briegleb and Light*, 2007).

For dynamics, we use the elastic-viscous-plastic scheme (*Hunke and Dukowicz*, 1997) as revised by *Bouillon et al.* (2013). Sea ice transport follows an incremental remapping approach (*Lipscomb and Hunke*, 2004). We use the ice strength formulation of *Rothrock* (1975), with the ridging participation and redistribution functions of

Lipscomb et al. (2007).

4.3.5 Coupling

ROMS and CICE run on separate processors, and communication between the two models is facilitated by the MCT coupler (*Larson et al.*, 2005; *Jacob et al.*, 2005). Since the same horizontal grid is used for the ocean and sea ice, the coupling is relatively straightforward. The only issue comes from the fact that ROMS uses the Arakawa C-grid while CICE uses the Arakawa B-grid (*Arakawa and Lamb*, 1977). That is, while ROMS and CICE share the same horizontal grid cells, the location of variables within that cell (i.e. at the centre, corners, or edges) is not the same. However, both the B- and C-grid have tracers in the centre of each cell. All coupling is therefore done on the tracer grid, with variables linearly interpolated to and from the centre of each cell where required.

ROMS and CICE exchange fields every 30 minutes of simulation (i.e., every sea ice timestep). All fields are averaged or integrated over the preceding 30-minute coupling interval. CICE passes ROMS the sea ice concentration, heat and salt fluxes, the shortwave radiation coming through the ice, and the ice-ocean stress vector. ROMS passes CICE the sea surface temperature and salinity, ocean velocity averaged over the upper 5 metres, sea surface height, and the freeze-melt potential.

The last variable warrants particular attention given the subject of this paper. Freeze-melt potential is the energy flux (in W/m^2) associated with the temperature difference from the freezing point, and is used by the sea ice model to form frazil ice (> 0) or melt existing sea ice (< 0). We follow the same algorithm as the POP (Parallel Ocean Program) z-coordinate ocean model (*Smith et al.*, 2010) to calculate freeze-melt potential, with minor modifications to account for the differing vertical coordinate system.

Freeze potential is integrated over the upper 5 metres of the water column, removing supercooling in these layers every ocean timestep. If warmer layers (above freezing) overlay colder layers, they are allowed to melt the frazil ice formed below. The surface layer is also allowed to melt frazil ice from previous ocean timesteps, within the same coupling interval. Any additional energy flux in the surface layer available to melt ice is accumulated each timestep as melt potential (< 0).

The salinity fluxes associated with both frazil ice formation and basal melting are calculated by CICE and returned to the ocean model as a surface salt flux. This design is required to ensure salt conservation, since the mushy thermodynamics scheme in CICE allows sea ice salinity to evolve. Also to match the mushy thermodynamics

in CICE, the freezing point T_f (in °C) is given by

$$T_f = \frac{S}{-18.48 + \frac{18.48}{1000} S} \tag{4.2}$$

where S is salinity in psu. Note that we neglect the depth-dependence of the freezing point, since this term is negligible over the upper 5 metres. Freeze-melt potential is not calculated in ice shelf cavities, which are masked out of the CICE domain. In ice shelf cavities the depth-dependence of the freezing point is vital, and supercooling is handled differently. For a full explanation see *Galton-Fenzi* (2009) and *Galton-Fenzi et al.* (2012).

4.3.6 Initialisation

ROMS is initialised with temperature and salinity from the ECCO2 cube92 reanalysis (*Menemenlis et al.*, 2008; *Wunsch et al.*, 2009) for January 1992. These fields are extrapolated into ice shelf cavities using a nearest-neighbour method in Cartesian space. Initial velocity and sea surface height are set to zero.

Sea ice is initialised using January 1992 observations from the NOAA/NSIDC Climate Data Record of Passive Microwave Sea Ice Concentration (*Meier et al.*, 2013). Wherever observed sea ice concentration exceeds 15%, we intialise with concentration 100%, sea ice thickness of 1 m, and snow thickness of 0.2 m. This method of sea ice initialisation is similar to that used by *Kjellsson et al.* (2015).

4.3.7 Experiments

We found that short simulations were sufficient to illustrate the impact of advection errors on sea ice formation and deep water masses. Therefore, each simulation we present here ran for one year under 1992 forcing. We ran six different simulations, varying the advection scheme, level of parameterised diffusion, and presence of upwind limiters, as summarised and named in Table 4.1.

Since the upwind third-order advection scheme has implicit diffusion, unlike the fourth-order centered and Akima schemes, we ran the latter two schemes with two levels of parameterised diffusion: low (Laplacian diffusivity of 15 m^2/s, the same as the upwind schemes) and high (150 m^2/s). These values are scaled by grid size, as described in Section 4.3.3, meaning the diffusivity coefficient for a typical grid cell will be smaller.

Experiment name	Tracer advection scheme	Laplacian diffusivity (m^2/s)	Upwind limiters	Walltime h:mm
U3_LIM	Upwind third-order	15	yes	4:32
U3	Upwind third-order	15	no	4:23
C4_LD	Centered fourth-order	15	n/a	4:22
A4_LD	Akima fourth-order	15	n/a	4:30
C4_HD	Centered fourth-order	150	n/a	4:30
A4_HD	Akima fourth-order	150	n/a	4:25

Table 4.1: Summary of simulations performed. Upwind limiters can only be combined with the upwind third-order scheme. Walltime refers to the hours and minutes required to complete each 1-year simulation. Simulations were run on the Raijin cluster of the Australian National Computational Infrastructure, using 608 cores (512 ocean + 96 sea ice) which are Intel Xeon Sandy Bridge/Broadwell 2.6 GHz.

In the following results, we treat U3_LIM as a baseline simulation to which all other simulations are compared. The presence of upwind limiters ensures there will be no spurious supercooling in this simluation. Note also that the upwind limiters have a negligible computational overhead, as shown in Table 4.1. Activating limiters in U3_LIM only causes a 3% increase in walltime compared to the U3 simulation.

4.4 Results and Discussion

4.4.1 Supercooling

In an accurate simulation of the Southern Ocean, we would not expect to see any supercooling below 5 metres depth, except possibly a small amount transported from the sub-ice shelf cavities (note that this legitimate supercooling will not be removed by the flux limiters). Since the ocean is cooled only at the surface, and ROMS removes supercooling from the upper 5 metres every 5 minutes, there should not be time for supercooling to propagate to deeper water masses. However, if these deeper water masses are near the freezing point, oscillatory advection errors could cause spurious supercooling.

An example of this phenomenon in experiment C4_LD is shown in Figure 4.1, which plots the difference from the freezing point at each cell in a slice through the model grid, at a single timestep. With no time-averaging, spatial averaging, or spatial interpolation, the presence of oscillatory advection errors is obvious. Rather than a smooth field, the model output appears noisy and discontinuous. Isolated columns of subsurface supercooling - some exceeding 0.5°C below the freezing point - are surrounded by much warmer water. Over a steep region of the continental slope, around 74.5°S, this supercooling extends as deep as 200 m.

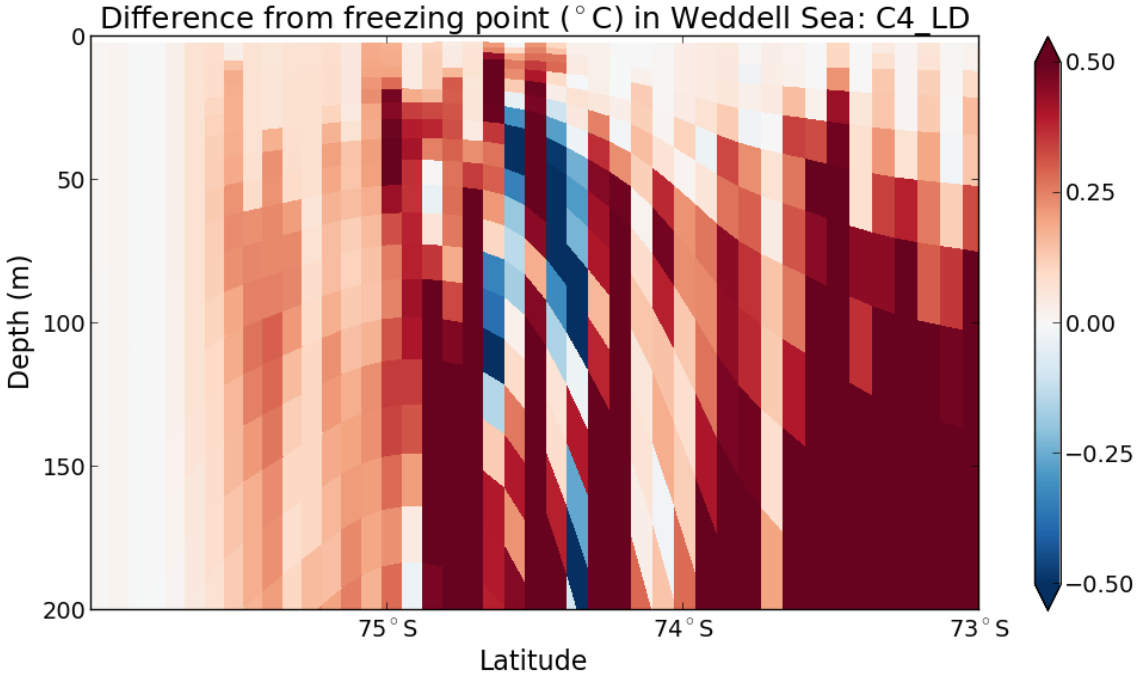

Figure 4.1: Difference from the surface freezing point, i.e. $T - T_f$, where T is ocean temperature and T_f is the surface freezing point as given by Equation 4.2. Values are shown on a single i-slice of the model grid through the Weddell Sea, for a single timestep on 26 June during the C4_LD simulation. In this region the grid is significantly rotated from regular longitude-latitude axes; longitudes in this plot range from 35°W in the southernmost cells to 40°W in the north.

Note that advection errors causing spurious formation of sea ice do not show up in Figure 4.1, since this supercooling is removed from the upper 5 metres of the water column as soon as it forms. Nonetheless, this figure illustrates the existence of oscillations and their unphysical nature. The salinity field (not shown) exhibits similar discontinuities, indicating that oscillations can deterioriate simulated fronts across the continental slope. Even disregarding the impact on sea ice formation, this behaviour presents a barrier to the accurate simulation of the interior ocean.

4.4.2 Sea ice formation

Frazil formation of sea ice should only occur where there is some amount of open water (i.e. sea ice concentration less than 100%), since supercooling of the ocean is driven by atmospheric heat fluxes. Again, there may be a small contribution from supercooled water exiting ice shelf cavities, but this should be restricted to grid cells adjacent to ice shelf fronts. Congelation, whereby seawater freezes directly onto the sea ice base due to conduction of heat through the ice, is calculated separately from frazil ice formation and at no stage involves supercooling in ROMS. Therefore, in an accurate simulation we would expect to see simulated frazil formation restricted to regions of open water, such as coastal polynyas and the northernmost edge of sea

ice extent during the freeze season.

The U3_LIM simulation performs reasonably well in this regard. Annually averaged frazil ice formation (Figure 4.2a) is strongest in coastal polynyas, particularly in the Ross and Weddell Seas. Areas of weaker frazil formation offshore correspond to the northernmost sea ice extent at different times of the year. Other simulations display significantly higher frazil formation than U3_LIM, particularly on the continental shelf, and sometimes far from the coast. These anomalies are most apparent for the C4_LD and A4_LD simulations (Figures 4.2c and 4.2e), and tend to line up with steep bathymetric features such as the continental shelf break.

Increasing the parameterised diffusion for the C4_HD and A4_HD simulations smoothes out many of the oscillations, and therefore removes most of the spurious frazil production (Figures 4.2d and 4.2f). However, there are still significant anomalies on the continental shelf. The upwind third-order scheme U3 with no limiters (Figure 4.2b) behaves similarly.

Figure 4.2 (following page): Annually averaged frazil ice formation during each 1-year simulation. Absolute frazil formation (cm/day) for the U3_LIM simulation is shown in (a); anomalies from U3_LIM for other simulations are shown in (b)-(f). Experiment names are explained in Table 4.1.

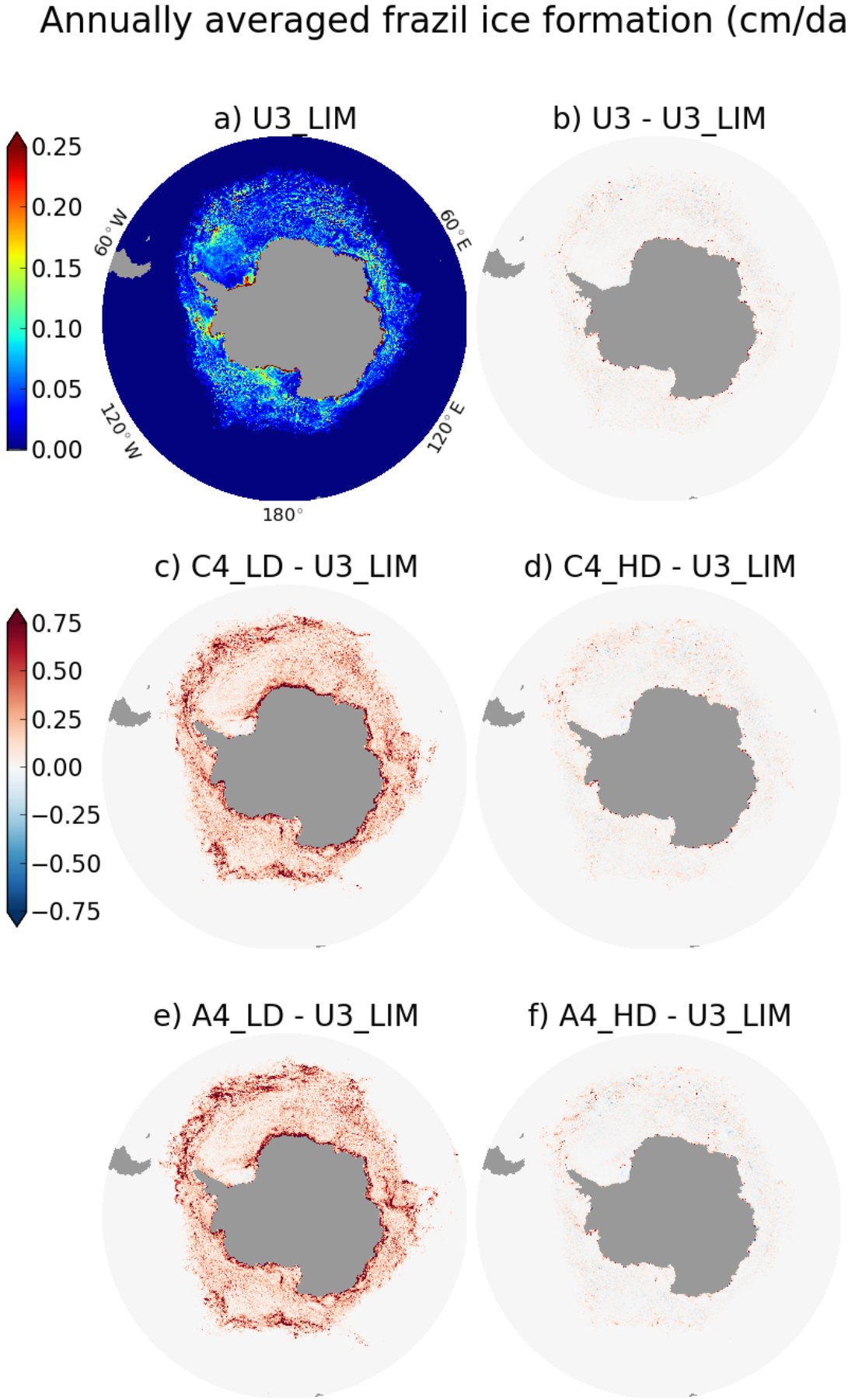
Annually averaged frazil ice formation (cm/day)
a) U3_LIM
b) U3 - U3_LIM
0.25
0.20
0.15
0.10
0.05
0.00
60°W
60°E
120°W
120°E
180°
c) C4_LD - U3_LIM
d) C4_HD - U3_LIM
0.75
0.50
0.25
0.00
−0.25
−0.50
−0.75
e) A4_LD - U3_LIM
f) A4_HD - U3_LIM

These anomalies in frazil ice formation for each simulation are reflected in the sea ice thickness. At the time of maximum sea ice area (23 August), the U3_LIM simulation displays a realistic distribution of effective sea ice thickness (Figure 4.3a), with thicker ice from the continental shelf exported by the Ross and Weddell Gyres, and thinner ice in polynya regions along the coastline. The C4_LD and A4_LD simulations (Figures 4.3c and 4.3e), by contrast, show thick packs of sea ice along the continental shelf break. Sea ice thickness in the offshore Weddell Sea is approximately tripled compared to the U3_LIM simulation. The regions of increased sea ice thickness differ somewhat from the regions of anomalous frazil formation seen in Figure 4.2, due to sea ice drift. However, given that other sea ice thermodynamic growth terms (congelation and snow-to-ice flooding) are similar in all six simulations, the thick ice is indeed driven by frazil formation.

These thick packs of sea ice are mostly eliminated by increasing the parameterised diffusion (C4_HD and A4_HD simulations; Figures 4.3d and 4.3f). However, thicker ice still exists along the continental shelf break of the Amundsen and Bellingshausen Seas, extending into the eastern Ross Sea. In other regions, such as offshore of the Amery Ice Shelf, sea ice is actually thinner than in U3_LIM. The upwind third-order scheme with no limiters (U3; Figure 4.3b) exhibits slightly thicker sea ice than U3_LIM along most of the continental shelf break.

Figure 4.3 (following page): As Figure 4.2, but showing effective sea ice thickness (concentration multiplied by height at each grid cell) on 23 August (daily average), which corresponds to the day of maximum sea ice area in the U3_LIM simulation. Cells where sea ice concentration is below 15% have been masked out of (a).

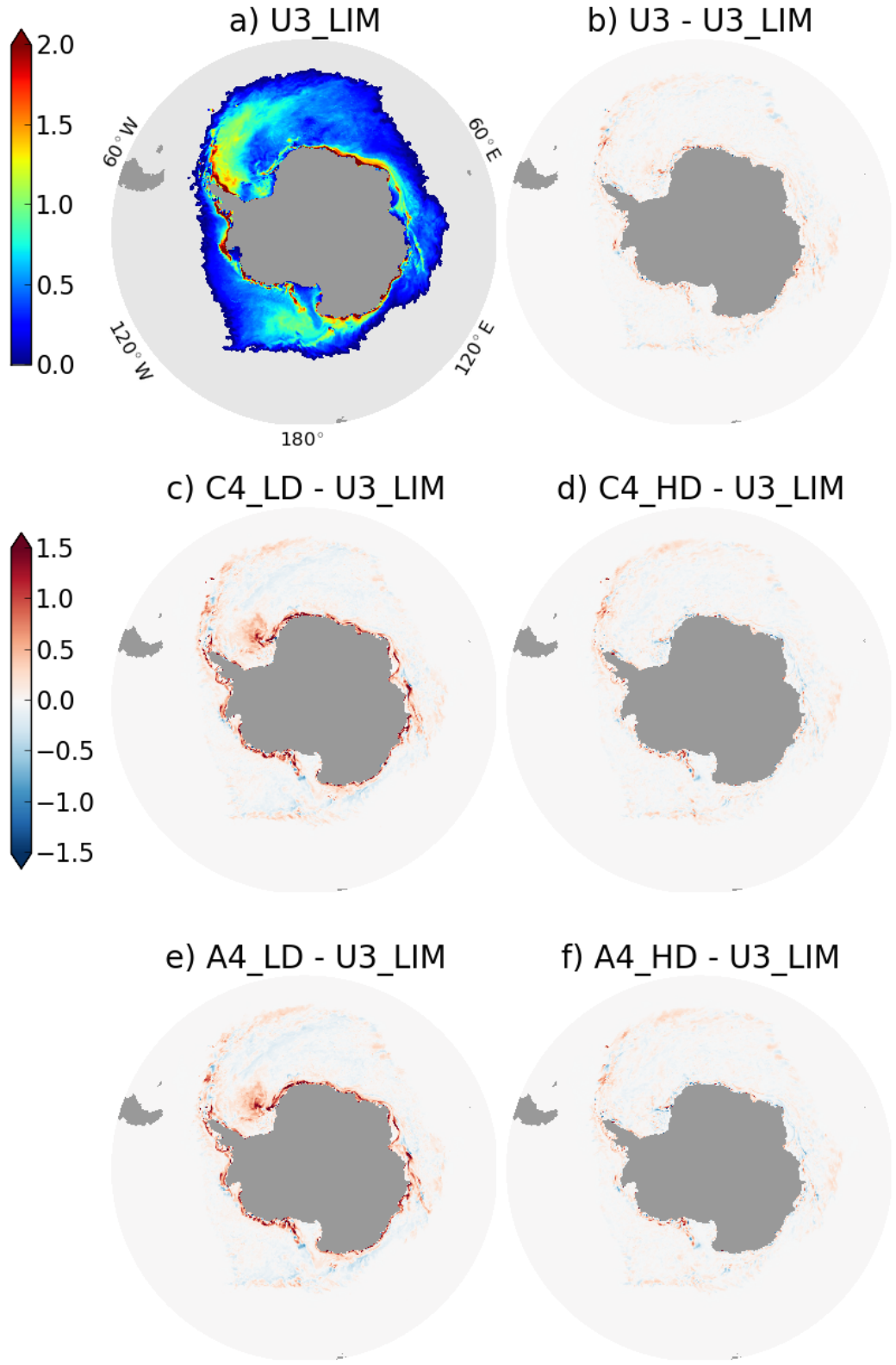
Effective sea ice thickness (m) on 23 August
a) U3_LIM
b) U3 - U3_LIM
c) C4_LD - U3_LIM
d) C4_HD - U3_LIM
e) A4_LD - U3_LIM
f) A4_HD - U3_LIM
2.0
1.5
1.0
0.5
0.0
−0.5
−1.0
−1.5
60°W
60°E
120°W
120°E
180°

4.4.3 Stratification

Sea ice which forms due to oscillatory advection errors alone will melt as soon as it drifts away from the spurious supercooling into warmer waters, which can occur in as little as 1 grid cell. In regions of persistent spurious supercooling causing thick sea ice, the rate of melting is significant. The resulting large freshwater flux stratifies the ocean, decreasing the mixed layer depth and suppressing deep convection. Note that sea ice melt cools, as well as freshens, the ocean surface.

Sea surface salinity at the sea ice maximum (23 August) is shown for the U3_LIM simulation in Figure 4.4a. The other simulations (Figures 4.4b through 4.4f) exhibit significant fresh anomalies (> 1 psu) in regions of spurious sea ice formation. For the C4_LD and A4_LD simulations (Figures 4.4c and 4.4e), these regions are so large that the meltwater freshens almost the entire domain. Freshening is particularly significant on the continental shelf, as well as east of the Drake Passage where meltwater from the Weddell Sea is swept into the ACC. For the C4_HD, A4_HD, and U3 simulations (Figures 4.4b, 4.4d, and 4.4f), this meltwater is restricted to the northern ACC east of the Drake Passage, as well as small patches on the western side of the Antarctic Peninsula.

Figure 4.4 (following page): As Figure 4.3, but for sea surface salinity. Note that ice shelf cavities are masked.

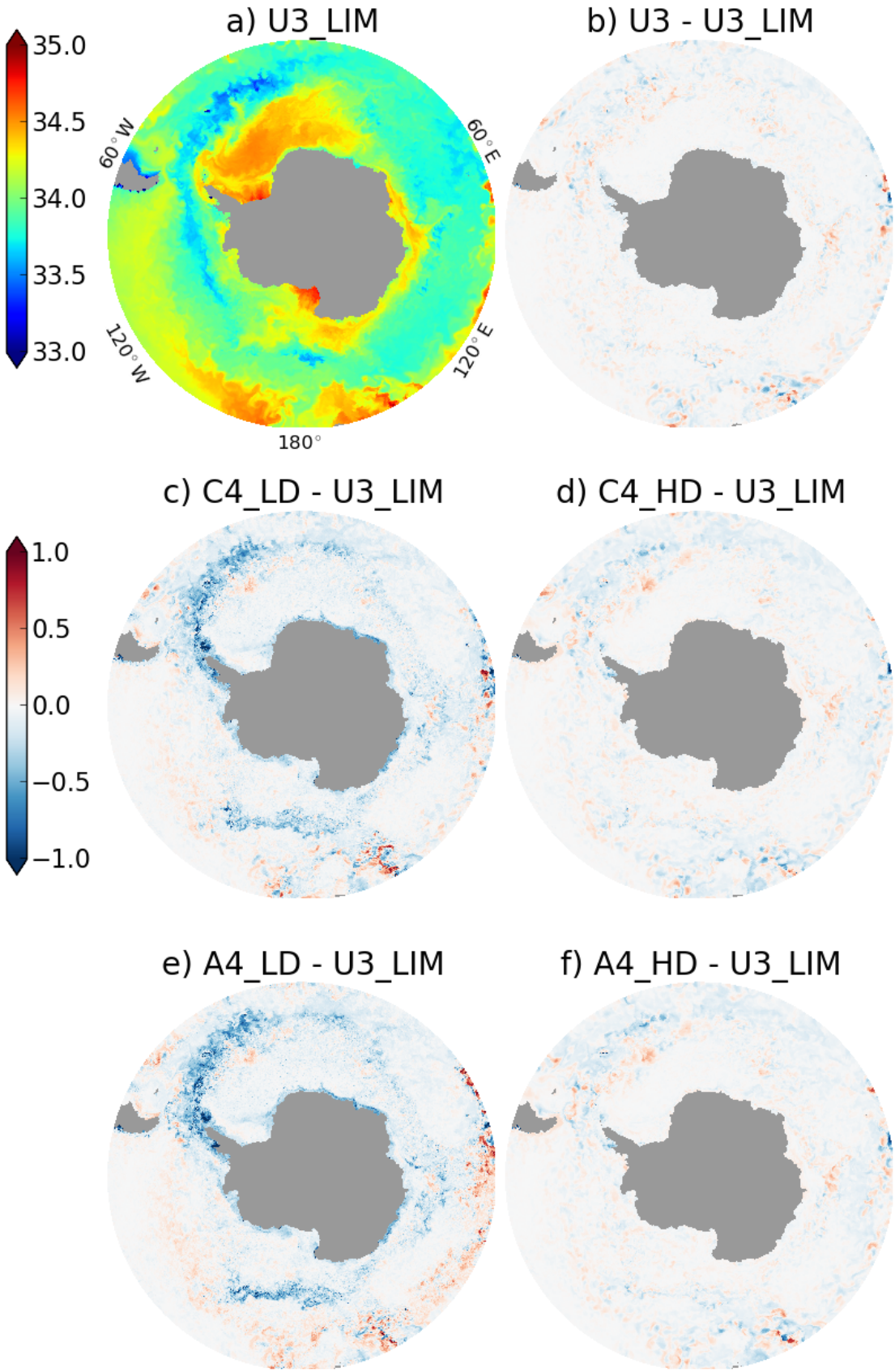
Sea surface salinity (psu) on 23 August
a) U3_LIM
b) U3 - U3_LIM
35.0
34.5
34.0
33.5
33.0
60°W
60°E
120°W
120°E
180°
c) C4_LD - U3_LIM
d) C4_HD - U3_LIM
1.0
0.5
0.0
−0.5
−1.0
e) A4_LD - U3_LIM
f) A4_HD - U3_LIM

Mixed layer depth, defined here as the depth of the oceanic boundary layer as calculated by the KPP parameterisation (*Large et al.*, 1994), is significantly affected by this surface freshening. During the sea ice maximum on 23 August, the U3_LIM simulation has deep mixed layers (> 300 m) in known regions of dense water formation (*Ohshima et al.*, 2013), most prominently the Ross and Weddell Seas as well as Prydz Bay near the Amery Ice Shelf (Figure 4.5a). The C4_LD and A4_LD simulations (Figures 4.5c and 4.5e) have much shallower mixed layers in these regions, as well as throughout the Weddell Sea and most of the ACC.

This behaviour is less pronounced for the C4_HD and A4_HD simulations (Figures 4.5d and 4.5f), although shallower mixed layers are still apparent in some regions of the continental shelf. No consistent anomalies are seen in mixed layer depth for the U3 simulation (Figure 4.5b).

Figure 4.5 (following page): As Figure 4.3, but for mixed layer depth (depth of the oceanic boundary layer as calculated by the KPP parameterisation). Note that ice shelf cavities are masked.

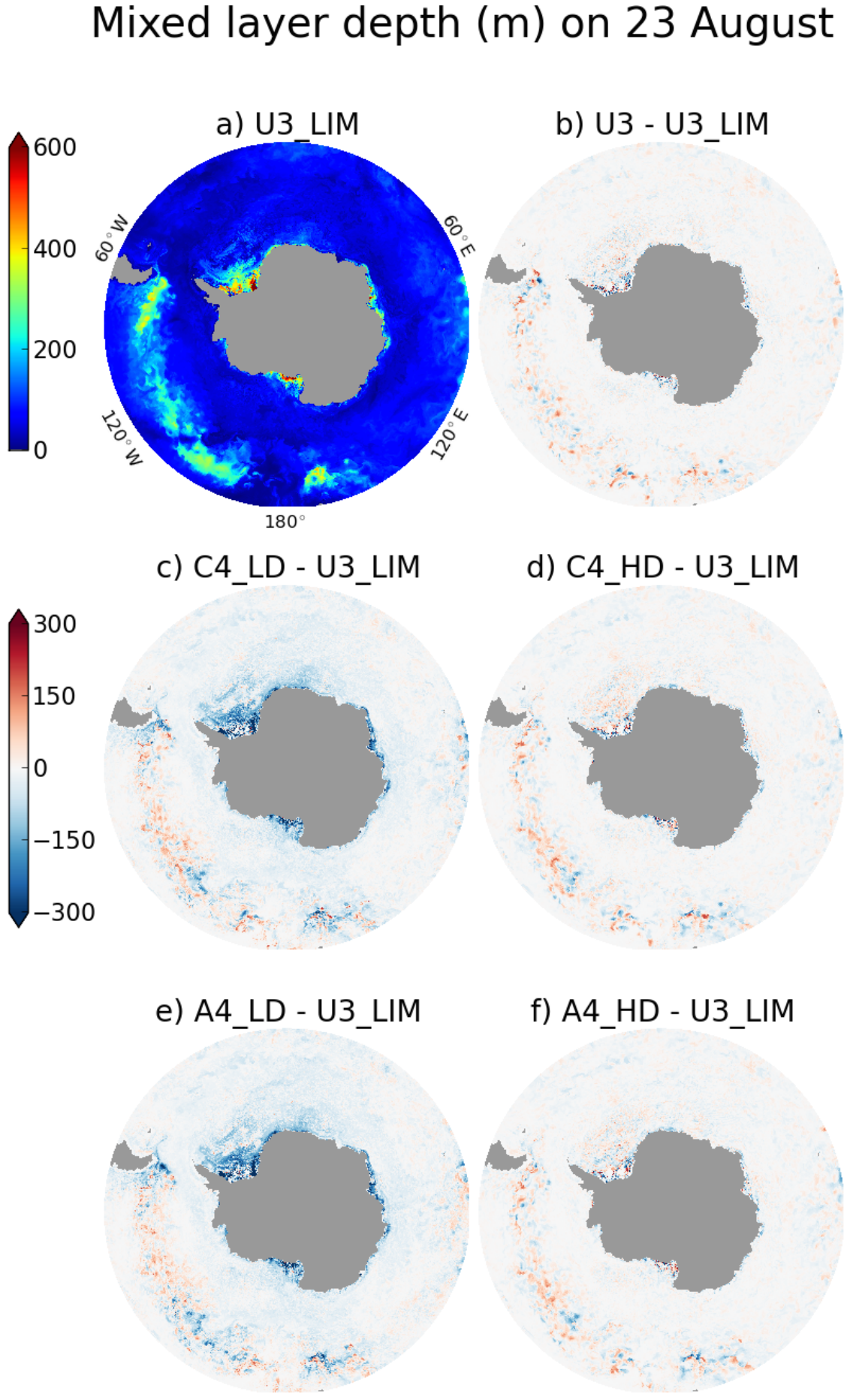
Mixed layer depth (m) on 23 August
a) U3_LIM
b) U3 - U3_LIM
600
400
200
0
60°W
60°E
120°W
120°E
180°
c) C4_LD - U3_LIM
d) C4_HD - U3_LIM
300
150
0
−150
−300
e) A4_LD - U3_LIM
f) A4_HD - U3_LIM

4.4.4 Coastal polynyas

Simulations with significant spurious supercooling are characterised by an almost complete absence of year-round coastal polynyas. Polynyas are regions of open water created by the strong southerly katabatic winds, which push sea ice away from the coast. As new sea ice forms in its place, the resulting brine rejection triggers deep convection, and warmer water from below upwells to the surface.

Spurious formation of sea ice suppresses coastal polynyas in two ways:

1. Dynamic: Thick sea ice forms due to spurious supercooling above steep bathymetry, particularly the continental shelf break. These thick packs of sea ice decrease the mobility of upstream sea ice, which often encompasses known coastal polynya regions. Export of sea ice from polynya regions is therefore inhibited.

2. Thermodynamic: The stabilising effect of meltwater from the transport of these thick patches of sea ice, as discussed in the previous section, suppresses deep convection in polynya regions. Upwelling of warmer water from below, which is necessary to prevent polynyas from immediately freezing over, is thereby suppressed.

Year-round coastal polynyas are present during the U3_LIM simulation in many regions along the Antarctic coastline. Figure 4.6a shows sea ice concentration for this simulation near the Amery Ice Shelf front (67°E-86°E) during the sea ice maximum on 23 August. Substantial polynyas are present in Barrier Bay (≈ 80°E), with several smaller polynyas dotted along the coastline.

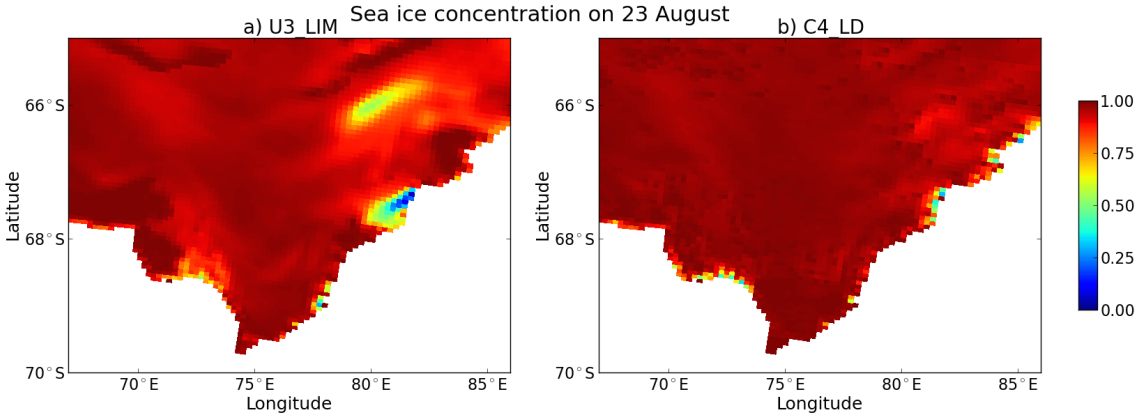

Figure 4.6: Sea ice concentration (fraction) on 23 August (daily average) near the Amery Ice Shelf front, including Barrier Bay (≈ 80°E). 23 August corresponds to the maximum sea ice extent in the U3_LIM simulation. Concentration for the U3_LIM simulation is shown in (a), and for the C4_LD simulation in (b). Experiment names are explained in Table 4.1.

These polynyas are significantly reduced in size during the C4_LD simulation (Figure 4.6b), with sea ice concentration near 1 almost everywhere. The high levels of spurious sea ice formation seen in C4_LD, and the resulting buttressing and stratifying effects, have nearly eliminated the coastal polynyas.

4.4.5 Deep water masses

As well as shutting down coastal polynyas, the stratification discussed in Section 4.4.3 causes the subsurface Winter Water layer to erode. Winter Water is the remnant of the winter mixed layer, overlaying warmer Circumpolar Deep Water and forming a subsurface temperature minimum. If the winter mixed layer is shallow, as seen in the C4_LD and A4_LD simulations, the thickness of this year-round layer is reduced.

Significant impacts are seen after only one year. Figure 4.7 shows zonal slices of temperature and salinity interpolated to 180°E (through the Ross Sea) on the last day of the U3_LIM simulation (31 December), and anomalies for the C4_LD simulation. A layer of Winter Water (temperature ≈ -0.5°C, salinity ≈ 34.4 psu) is visible in the

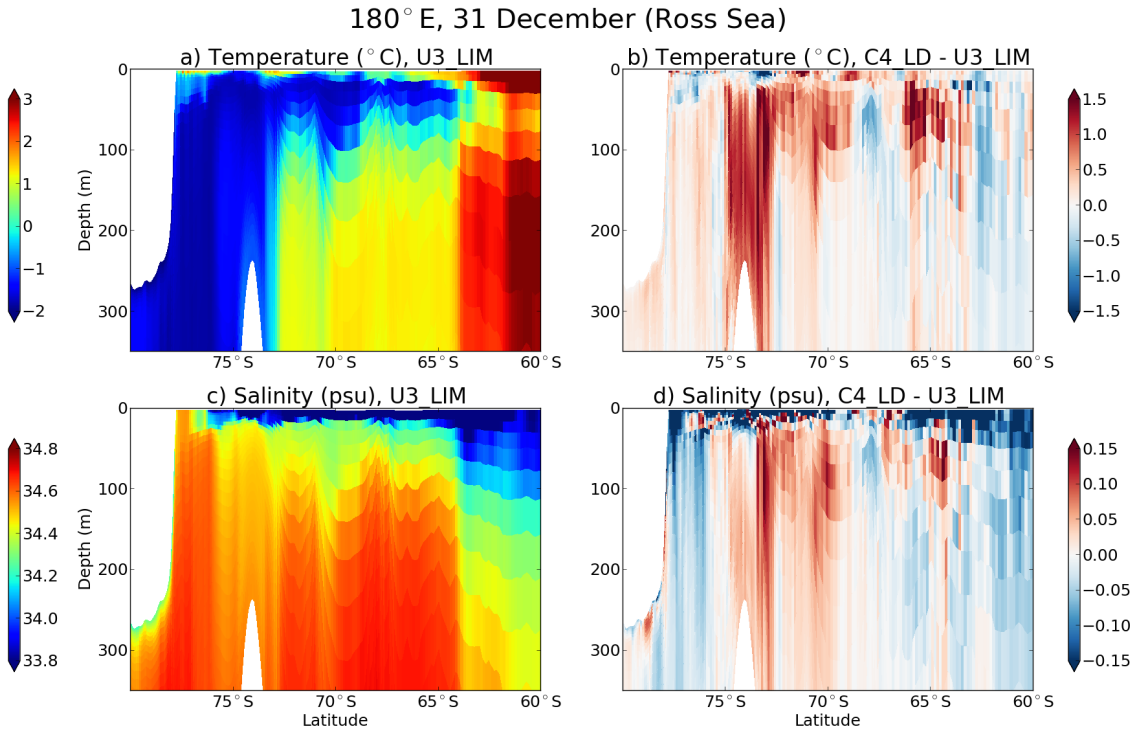

Figure 4.7: Latitude vs. depth slices of temperature (a,b) and salinity (c,d), interpolated to 180°E, which intersects the Ross Sea. Ice shelf cavities are explicitly simulated by ROMS, and the Ross Ice Shelf front can be seen on the left side of each plot. Values are averaged over the last day of simulation, 31 December. The U3_LIM simulation (a,c) and anomalies for the C4_LD simulation with respect to U3_LIM (b,d) are shown. Experiment names are explained in Table 4.1.

U3_LIM simulation (Figures 4.7a and 4.7c), with a tongue of cold water extending into the subsurface ACC, and warm salty Circumpolar Deep Water (temperature > 0°C, salinity > 34.5 psu (*Jacobs*, 2004)) below 100 m depth in the offshore water column. Dense water formation is also active in the Ross Sea polynya, visible as a column of uniform salinity (≈ 34.6 psu) immediately north of the Ross Ice Shelf front.

The Winter Water layer has been partially replaced by Circumpolar Deep Water in the C4_LD simulation (Figures 4.7b and 4.7d), which exhibits significant warm and saline anomalies above 100 m in the offshore water column. Warming of approximately 1°C is apparent over the continental slope (near 74°S), as Modified Circumpolar Deep Water begins to travel onto the continental shelf. Additionally, fresh anomalies north of the ice shelf front, concentrated near the surface, indicate a shutdown of dense water formation in this region due to stratification.

In longer simulations with C4_LD (not shown), Modified Circumpolar Deep Water eventually makes its way into ice shelf cavities, including the Ross. Area-averaged ice shelf melt rates dramatically increase, well beyond observational estimates, as warm water floods into the cavity. In contrast to these indirect effects of spurious supercooling on ice shelf melt rates, we do not see any significant evidence of direct effects, i.e. spurious supercooling causing refreezing onto the ice shelf base. Within ice shelf cavities, the ocean is shielded from the motion of wind and sea ice at the surface, and ocean velocities are therefore much slower. Oscillatory advection errors are much less likely when velocities are near-zero.

4.4.6 Effect of coupling interval

In our experiments, ROMS and CICE exchange fields every sea ice timestep, equal to 30 minutes. Some global climate models, such as the Community Earth System Model (which includes CICE), instead have a sea-ice/ocean coupling interval of 24 hours (*Roberts et al.*, 2015). This daily averaging of coupling fields is computationally inexpensive, but it also filters semi-diurnal feedbacks such as oscillations in ice-ocean Ekman transport, which can have a significant impact on sea ice dynamics as demonstrated by *Roberts et al.* (2015). Long coupling intervals also introduce lags into the model which can lead to instabilities and chaotic behaviour.

We found that spurious sea ice formation was sensitive to the length of the ice-ocean coupling interval. Simulations with 24-hour coupling intervals (not shown) experienced more significant anomalies than the 30-minute simulations analysed here. For all advection schemes, frazil formation as well as sea ice basal melt was

higher with 24-hour coupling than with 30-minute coupling, since the longer lags in the coupled system allowed both freeze potential and melt potential to overshoot. This compounded the effects of spurious supercooling in the C4_LD and A4_LD simulations. Anomalies in sea ice thickness, surface salinity, stratification, and dense water mass properties were more pronounced with 24-hour coupling than with 30-minute coupling. This indicates that long ice-ocean coupling intervals, as used by some global models, exacerbate spurious sea ice formation caused by oscillatory advection schemes.

4.5 Conclusions

We have shown that artificial oscillations in tracer advection schemes have undesirable interactions with a coupled sea ice model. Numerical oscillations cause spurious supercooling and sea ice formation, particularly over steep areas of bathymetry such as the continental shelf break, where thick packs of sea ice build up. The dynamic and thermodynamic impacts of this thick sea ice suppress coastal polynyas, stratify the water column, and cause Winter Water to erode and Circumpolar Deep Water to shoal. The long-term significance of these biases for the simulated climate state is unknown and is not the subject of this study.

The centered fourth-order and Akima fourth-order horizontal tracer advection schemes were the worst performing, with significantly more incidents of spurious supercooling and sea ice formation than the upwind third-order scheme. Increasing the parameterised diffusion improved the performance of both fourth-order schemes, but supercooling artifacts were still present. Spurious supercooling was only eliminated with the inclusion of a flux limiter for the upwind third-order scheme. However, only minor differences were apparent between the upwind third-order scheme with and without limiters, indicating that the limiters did not need to be activated very frequently.

Upwind limiters are a particularly attractive solution for preventing oscillations in high-resolution ocean models, because they allow parameterised diffusion to be very low or even nonexistent. For eddy-permitting or eddy-resolving simulations, explicit mixing can be destructive to the simulation of these eddies. The high levels of parameterised diffusion that we find necessary to add to the centered fourth-order and Akima fourth-order schemes to suppress oscillations would therefore be undesirable. On the other hand, oscillations should be less likely at higher resolution due to better resolution of steep gradients in tracer fields. In this case, substantial increases in parameterised diffusion may not actually be necessary.

When artificial oscillations breach thresholds such as the freezing point, they can no longer be considered superficial numerical error. In the extreme case, as we have shown, they can have detrimental effects on model physics. These results may be model-dependent, and in particular may be influenced by the terrain-following coordinates in our configuration. Nonetheless, we suggest that other users of coupled ocean/sea-ice models exercise caution when using oscillatory advection schemes and watch carefully for signs of spurious sea ice formation.

Chapter 5

Future projections of Antarctic ice shelf melting based on CMIP5 scenarios

Preamble

While MetROMS was ultimately deemed unsuitable for long transient simulations, future projections of ice shelf melt rates were still feasible using FESOM. This chapter takes the high-resolution configuration of FESOM from Chapter 2 and forces it with bias-corrected atmospheric output from CMIP5 projections of the 21st century.

This chapter is based on the paper "Future projections of Antarctic ice shelf melting based on CMIP5 scenarios" by Kaitlin A. Naughten, Katrin J. Meissner, Benjamin K. Galton-Fenzi, Matthew H. England, Ralph Timmermann, and Hartmut H. Hellmer, which is in press at *Journal of Climate* (). Compared to the published paper, the version reproduced here has several minor additions and clarifications, including the addition of Equation 5.1. None of these changes affect the main conclusions of the study. Cross-references to other thesis chapters have also been added, and the supplementary information (consisting of six figures) has been moved to Appendix A.

I completed the majority of the work for this publication: installing and configuring FESOM, designing and running simulations, analysing results, and writing the paper. My supervisors Katrin Meissner, Ben Galton-Fenzi, and Matthew England gave me advice throughout the process. Ralph Timmermann and Hartmut Hellmer provided the FESOM code, as well as helpful discussions about the preliminary

results. All co-authors provided comments on the manuscript.

Abstract

Basal melting of Antarctic ice shelves is expected to increase during the 21st century as the ocean warms, which will have consequences for ice sheet stability and global sea level rise. Here we present future projections of Antarctic ice shelf melting using FESOM (Finite Element Sea-ice/ice-shelf Ocean Model) forced with atmospheric output from CMIP5 (Coupled Model Intercomparison Project phase 5) models. CMIP5 models are chosen based on their agreement with historical atmospheric reanalyses over the Southern Ocean; the best-performing models are ACCESS 1.0 and the CMIP5 multi-model mean. Their output is bias-corrected for the RCP (Representative Concentration Pathway) 4.5 and 8.5 scenarios. During the 21st-century simulations, total ice shelf basal mass loss increases by between 41% and 129%. Every sector of Antarctica shows increased basal melting in every scenario, with the largest increases occurring in the Amundsen Sea. The main mechanism driving this melting is an increase in warm Circumpolar Deep Water on the Antarctic continental shelf. A reduction in wintertime sea ice formation simulated during the 21st century stratifies the water column, allowing a warm bottom layer to develop and intrude into ice shelf cavities. This effect may be overestimated in the Amundsen Sea due to a cold bias in the present-day simulation. Other consequences of weakened sea ice formation include freshening of High Salinity Shelf Water and warming of Antarctic Bottom Water. Furthermore, freshening around the Antarctic coast in our simulations causes the Antarctic Circumpolar Current to weaken and the Antarctic Coastal Current to strengthen.

5.1 Introduction

The Coupled Model Intercomparison Project phase 5 (CMIP5) (*Taylor et al.*, 2012) comprises the most comprehensive suite of future climate projections to date. A variety of Earth System Models, consisting of coupled components for the atmosphere, ocean, sea ice, and land surface, simulated future climate scenarios forced by standardised Representative Concentration Pathways (RCPs). These range from RCP 2.6, a "best-case scenario" where greenhouse gas concentrations stabilise by the mid-21st century, to RCP 8.5, a "business-as-usual scenario" where concentrations continue to accelerate. Global emissions of greenhouse gases are currently following the RCP 8.5 pathway (*Sanford et al.*, 2014).

However, none of the Earth System Models participating in CMIP5 included ice shelf interactions. Ice shelves, the floating extensions of the Antarctic Ice Sheet, buttress upstream glaciers and ultimately slow down sea level rise (*Dupont and Alley*, 2005). The fate of ice shelves, and consequently the ice sheet, in the 21st century and beyond largely depends on the oceanic transport of heat into ice shelf cavities (the regions of the ocean between ice shelves and the seafloor) and resulting basal melting. Here we employ an ocean model, FESOM (Finite-Element Sea-ice/ice-shelf Ocean Model) (*Wang et al.*, 2014; *Danilov et al.*, 2015; *Timmermann et al.*, 2012), which includes ice shelf cavities and simulates ice shelf basal melting and refreezing. FESOM is one of a number of ocean models which simulate ice shelf thermodynamics in this manner (see *Dinniman et al.* (2016) and references therein), but future projections with these models have so far been limited. By forcing FESOM with atmospheric output from the CMIP5 experiments, we obtain projections of ice shelf melt rates throughout the 21st century, as well as continental shelf water mass properties, sea ice processes, and Southern Ocean circulation.

FESOM has previously been used for future projections of ice shelf melting, forced with CMIP3 model output (the previous generation of climate projections to CMIP5). *Timmermann and Hellmer* (2013) presented FESOM simulations forced by output from the HadCM3 and ECHAM5 models, both present-day ("20C" scenario) and future ("E1" and "A1B" scenarios). The two CMIP3 models produced very different responses in FESOM, with the HadCM3 experiments exhibiting more realistic 20th-century salinities on the continental shelf, higher present-day melt rates, and a much larger response to 21st-century warming, particularly for the Filchner-Ronne Ice Shelf (FRIS). *Timmermann and Goeller* (2017) repeated the HadCM3 A1B scenario, as well as an extended 20C control experiment, with FESOM coupled to a regional ice sheet model over the FRIS catchment. However, it is unclear to what extent these projections of ice shelf melting are affected by systematic biases in the CMIP3 models. Given the strong sensitivity to model choice shown by *Timmermann and Hellmer* (2013), as well as the known issues with CMIP simulations in the Southern Ocean region (see Section 5.2), careful selection of CMIP5 models as well as bias-correction of the atmospheric forcing fields seems warranted.

In this study, we select CMIP5 models based on their climatological agreement with atmospheric reanalyses over the Southern Ocean (Section 5.2). We linearly bias-correct the CMIP5 output by applying anomalies in each variable over the 21st century, rather than their absolute values (Section 5.3.2). By forcing FESOM with two different RCPs and two choices of CMIP5 models, we assess the sensitivity of changes in ice shelf basal mass loss to the forcing scenario (Section 5.4.1). We investigate the mechanisms of warming in ice shelf cavities, with a particular focus on

the Amundsen Sea (Sections 5.4.3 and 5.4.4). We also assess water mass properties, with respect to ice shelf cavities (Section 5.4.2) as well as dense water exported from the continental shelf (Section 5.4.5). Changes in large-scale Southern Ocean circulation (Section 5.4.6) and sea ice (Section 5.4.7) are also discussed.

5.2 Selection of CMIP5 models for future forcing

CMIP5 models are well known to exhibit biases in the Southern Ocean region during their 20th-century ("historical") simulations. For example, every single model analysed by *Sallée et al.* (2013a) has a warm bias in Southern Ocean water masses, particularly near the surface. As a result, many CMIP5 models underestimate Antarctic sea ice extent, especially in summer (*Turner et al.*, 2013b). Furthermore, mixed layers in the Southern Ocean are too shallow year-round (*Sallée et al.*, 2013b). Biases specific to the atmosphere have also been identified. In particular, the Southern Hemisphere westerly winds are consistently too far north in CMIP5 models, and frequently too weak (*Bracegirdle et al.*, 2013; *Swart and Fyfe*, 2012). This bias is concerning for our simulations, since water masses near the Antarctic continental shelf break may be particularly sensitive to the position and strength of the westerlies (*Schmidtko et al.*, 2014; *Spence et al.*, 2014, 2017).

Given these biases, forcing an ocean model such as FESOM with raw atmospheric CMIP5 output may be problematic, and introduce additional uncertainties into our results. Furthermore, we spin up present-day FESOM simulations with the ERA-Interim atmospheric reanalysis (*Dee et al.*, 2011). Switching from ERA-Interim to raw CMIP5 output would then introduce an undesirable step change in forcing at the beginning of each RCP.

To avoid these problems, rather than forcing FESOM with CMIP5 output directly, we instead force with CMIP5 anomalies during each RCP, added to the ERA-Interim present-day climatology. This method assumes that projected changes are not state-dependent, i.e. the magnitude of future change does not depend on the simulated present-day climate. Projected changes in Southern Ocean temperature and salinity do not appear to be state-dependent, as shown by *Sallée et al.* (2013a). However, no such analysis has been conducted for atmospheric variables. Therefore, to minimise the risk of state-dependent future changes distorting our forcing fields, we choose CMIP5 models with the smallest possible biases in their present-day simulations.

Here we evaluate the performance of CMIP5 models compared to the ERA-Interim reanalysis for 10 atmospheric variables over the Southern Ocean, in a monthly climatology calculated over 1992-2005. We follow the method of *Gleckler et al.* (2008),

which uses the root-mean-squared (rms) error as a metric of model skill. Rather than calculating the rms error over the entire globe, we restrict our analysis to the region 30°S-80°S. It is important to note that ERA-Interim is not a perfect baseline for evaluation, as some biases are known to exist in its simulation of the Antarctic region. In particular, there are concerns regarding ERA-Interim's Southern Ocean cloud cover leading to a positive bias in summertime shortwave radiation (*Naud et al.*, 2014). On the other hand, *Nicolas and Bromwich* (2011) showed that ERA-Interim provides the most realistic surface hydrological cycle of any atmospheric reanalysis over the Southern Ocean.

Models are selected based on availability of the 10 atmospheric variables required to force our FESOM configuration (see caption of Figure 5.1), with monthly averages for the historical, RCP 4.5, and RCP 8.5 simulations. 19 models fit these criteria (Figure 5.1), and for each model we analyse a single ensemble member. We also apply the analysis to the multi-model mean (MMM) of the 19 models. For each model and each variable, we calculate the monthly climatology over 1992-2005 and linearly interpolate to the ERA-Interim grid. Following the equations of *Gleckler et al.* (2008), we calculate the rms error for each model and variable with respect to ERA-Interim over 30°S-80°S, as well as the "relative error" which normalises units across different variables. A relative error of 0.5, for example, indicates that the given model has an rms error 50% higher than the median across all models (excluding the multi-model mean), for the given variable. Similarly, a relative error of -0.5 indicates an rms error 50% lower than the median. Models in best agreement with ERA-Interim will consistently have relative error scores which are the most strongly negative.

Figure 5.1 summarises relative error for all models and variables in a portrait plot (as in Figure 3 of *Gleckler et al.* (2008)), where the best-performing models are dominated by blue squares. Notably, the multi-model mean (MMM) has lower relative error than any of its component models for most variables. The tendency of individual model errors to cancel out in the multi-model mean was also discussed by *Gleckler et al.* (2008). However, the multi-model mean is not necessarily dynamically consistent or conservative. Among the individual models, ACCESS-1.0 generally has the lowest relative errors, with ACCESS-1.3 not far behind. This result agrees with *Agosta et al.* (2015) who found ACCESS-1.3 and ACCESS-1.0 to be the CMIP5 models in best agreement with atmospheric reanalyses over the Antarctic continent. Based on our analysis, we chose to construct two sets of future forcing fields for FESOM, using output from either the CMIP5 multi-model mean or ACCESS-1.0. The details of constructing these forcing fields are given in Section 5.3.2.

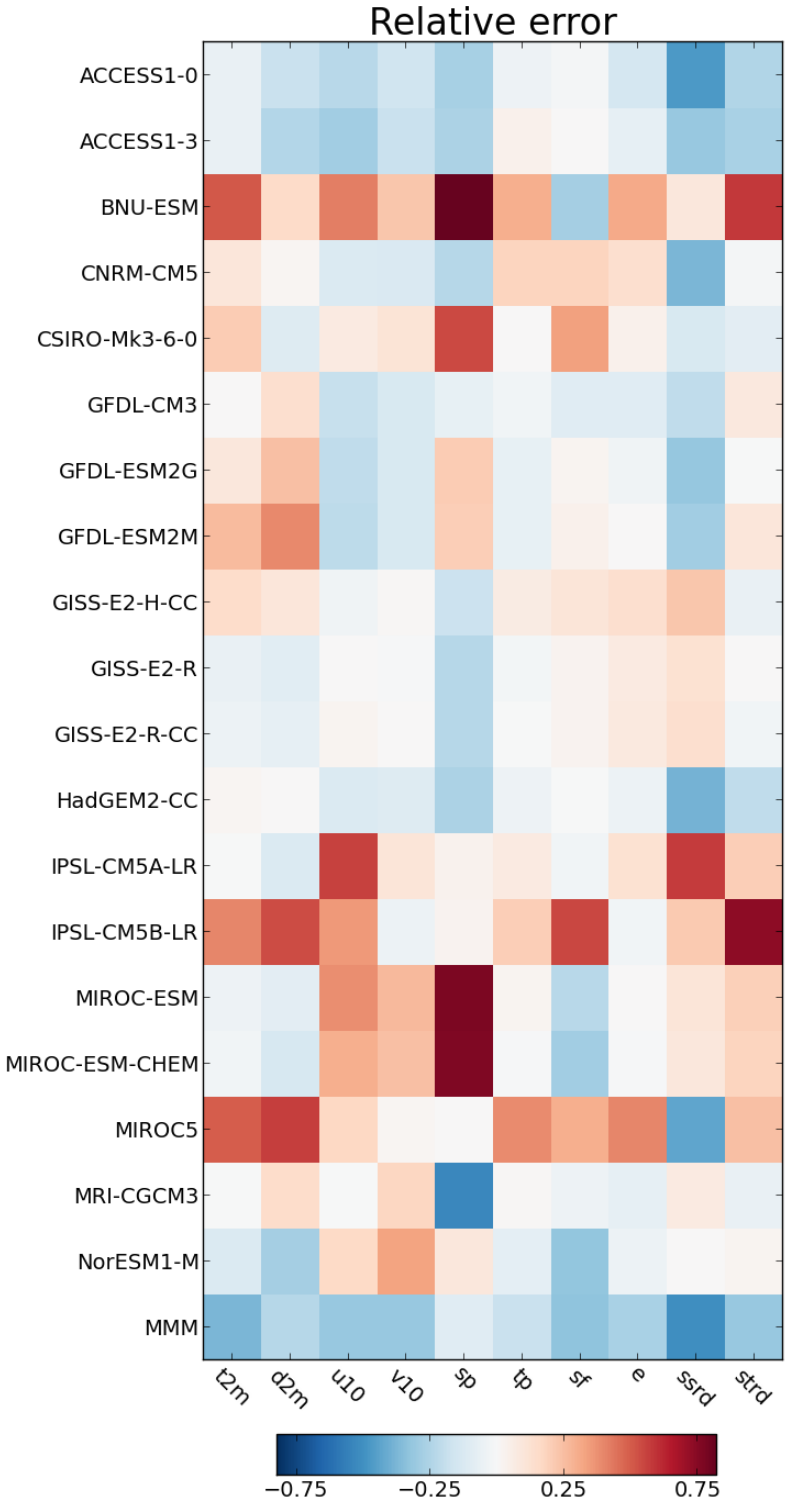

Figure 5.1: Relative error (defined in Section 5.2) for 19 CMIP5 models as well as the multi-model mean (MMM), calculated over the 1992-2005 monthly climatology of each model's "historical" simulation, with respect to the ERA-Interim reanalysis over the same time period. Results are shown for 9 atmospheric variables using ERA-Interim naming conventions: t2m (2 metre air temperature), d2m (2 metre dew point temperature), u10 and v10 (10 metre winds), sp (surface pressure), tp (total precipitation), sf (snowfall), e (evaporation), ssrd (downward shortwave solar radiation), and strd (downward longwave solar radiation).

5.3 Model description and experimental design

Simulations are performed with FESOM, a global ocean model notable for its unstructured mesh. Triangular elements allow for variable horizontal resolution, so that small-scale processes such as sub-ice shelf circulation can be resolved, while coarse resolution elsewhere in the domain minimises computational expense. The ocean component of FESOM is described by *Wang et al.* (2014), the sea ice component by *Danilov et al.* (2015), and the ice shelf component by *Timmermann et al.* (2012). Here we use the same configuration and parameter choices as in Chapter 2 but do not apply surface salinity restoring. Instead, as in previous publications with FESOM (*Timmermann and Hellmer*, 2013), surface salt fluxes are corrected such that the global mean is zero. Ice shelf cavities are not considered in this calculation, and do not receive any salt flux correction.

Ice shelf thermodynamics, i.e. heat and salt fluxes at the ice shelf base due to melting and refreezing, are simulated by FESOM using the three-equation parameterisation (*Hellmer and Olbers*, 1989; *Holland and Jenkins*, 1999), with velocity-dependent heat and salt transfer coefficients as detailed in Section 2.2.5. However, ice shelf geometry remains constant throughout all simulations, because any assumptions about changes in ice shelf draft would require coupling with an ice sheet model. This has recently been achieved with FESOM for the Filchner-Ronne region (*Timmermann and Goeller*, 2017), but is not yet operational for the entire continent. A partial solution could be to prescribe changes in ice shelf geometry to the ocean model, either at discrete restart points or in a continuously evolving manner, but this approach would also require significant model development. Regardless, it is likely that ice shelf geometry will indeed change throughout the 21st century, due to thinning and increased calving. Furthermore, FESOM does not consider the effects of tides, which are known to influence ice shelf melt rates (*Makinson et al.*, 2011; *Mueller et al.*, 2018), water mass exchanges at the ice shelf front (*Arzeno et al.*, 2014), and transport of heat onto the continental shelf (*Stewart et al.*, 2018).

5.3.1 Resolution

The FESOM mesh used in this study is the "high-resolution" option from Chapter 2. It has coarsest resolution in the abyssal Pacific, Atlantic, and Indian Oceans, ranging from 150 to 225 km (Figure 5.2a). Resolution is finer near coastlines, reaching approximately 75 km at low-latitude coastlines and 50 km for the Arctic and North Atlantic. The Southern Ocean contains the bulk of the computational nodes, with resolutions of 50 km or finer throughout the Antarctic Circumpolar Current (ACC).

Resolution continues to refine south of the ACC, and averages 5-7 km on the Antarctic continental shelf, including ice shelf cavities (Figure 5.2b). The Amundsen Sea has still finer resolution, of approximately 4 km. Note that this is still insufficient to resolve mesoscale eddies around Antarctica, which are understood to be a major source of heat transport onto the continental shelf (*Stewart and Thompson*, 2015; *Stewart et al.*, 2018).

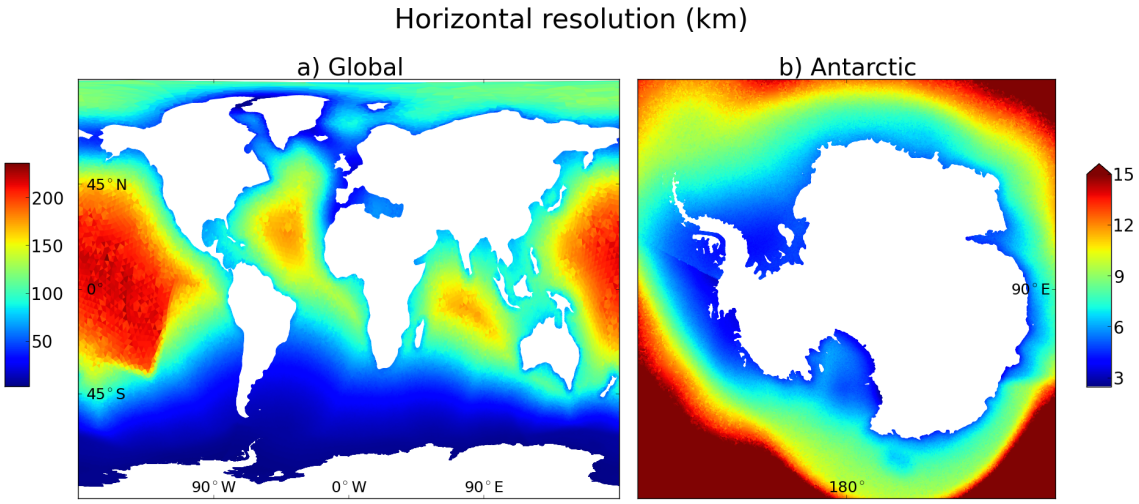

Figure 5.2: Horizontal resolution (km) in the FESOM mesh, defined as the square root of the area of each triangular element. (a) Global projection. (b) Circumpolar Antarctic projection; note the different colour scale. Values above 15 km in (b) are not differentiated.

Vertical discretisation comprises a hybrid sigma-z coordinate system. Sigma coordinates, with 22 vertical levels, are employed south of the 2500 m isobath surrounding Antarctica. This region covers the entire continental shelf, all ice shelf cavities, and part of the continental slope. The rest of the domain uses z-coordinates, with 38 unequally-spaced levels weighted towards the surface. All topographic data (bathymetry, ice shelf drafts, land-sea masks) are provided by RTopo-1.05 (*Timmermann et al.*, 2010).

5.3.2 Initial conditions and forcing

We use the same initial conditions as in Chapter 2. Temperature and salinity are provided by the ECCO2 reanalysis (*Menemenlis et al.*, 2008; *Wunsch et al.*, 2009) for January 1992, and extrapolated into ice shelf cavities. For the sea ice, initial conditions are based on the NOAA/NSIDC Climate Data Record for Passive Microwave Sea Ice Concentration (*Meier et al.*, 2013) for January 1992. Wherever observed sea ice concentration exceeds 0.15, the model is initialised with concentration 1, ice thickness of 1 m (in the Antarctic) or 2 m (in the Arctic), and snow thickness of 0.2 m. Initial sea ice velocity, ocean velocity, and sea surface height are set to zero.

Present-day atmospheric forcing is provided by the ERA-Interim reanalysis (*Dee et al.*, 2011), and consists of 6-hourly fields for near-surface air temperature, dew point temperature, pressure, and winds; and 12-hourly fields for incoming longwave and shortwave radiation, precipitation (split into rain and snow), and evaporation. We also apply an estimate of surface freshwater fluxes from iceberg melt, using the monthly climatology of *Martin and Adcroft* (2010).

Future simulations are forced using a combination of CMIP5 model output and ERA-Interim fields. The aim of this approach is twofold: to account for biases in the CMIP5 models' simulation of the mean climate state (as evaluated in Section 5.2), and to maintain the presence of sub-monthly variability in the atmospheric forcing. Variability at the sub-monthly timescale, particularly for winds, has been shown to be important for the accurate simulation of Antarctic sea ice (*Kim and Stössel*, 1998). However, the availability of CMIP5 atmospheric output at timescales finer than monthly averages is inconsistent. In fact, not a single CMIP5 model had sub-monthly output for all the variables and simulations we needed. For this reason, sub-monthly variability in our RCP forcing is derived from ERA-Interim, under the assumption that such variability will not change in an altered climate state.

The construction of the future forcing fields starts with monthly-averaged values for each variable. For each month of the RCP as simulated by a given CMIP5 model, we subtract that model's monthly climatology, calculated over the period 1992-2005 during the CMIP5 historical simulation. It is replaced by the ERA-Interim monthly climatology calculated over the same period. That is, we force FESOM with future anomalies as calculated by the CMIP5 model, rather than the absolute fields. Mean-state biases in the historical simulation as compared to ERA-Interim are therefore corrected in a linear fashion. This can be expressed as

$$F(\text{year},\text{month}) = F_C(\text{year},\text{month}) - \frac{1}{N}\sum_{A=1992}^{2005} F_C(A,\text{month}) + \frac{1}{N}\sum_{A=1992}^{2005} F_E(A,\text{month}) \tag{5.1}$$

where F_C is the atmospheric forcing from a given CMIP5 model, F_E is the atmospheric forcing from ERA-Interim, $N = 14$ is the number of years considered for the 1992-2005 climatology, and the result F is the corrected forcing.

Onto these monthly-averaged fields we superimpose variability on the 6- and 12-hour timescales, as derived from ERA-Interim. For each 6- or 12-hour timestep in the period 1994-2005, we calculate the anomaly from the monthly mean (for the given year, not the monthly climatology) as simulated by ERA-Interim. These anomalies are added to the monthly fields described above, in a repeating 12-year cycle throughout the RCP. The 12-year period 1994-2005 was chosen (rather than

1992-2005 as for the climatology) so it is aligned with the 4-year cycle of leap years. Since 2100 is not a leap year, the 12-year cycle is broken in 2100 and advanced by 1 year.

Freshwater fluxes from iceberg melting remain unchanged during the future simulations; the same monthly climatology is applied as for the present-day simulations. This design assumes that iceberg calving rates, as well as the spatial distribution of iceberg melting, will not change during the 21st century.

5.3.3 Experiments

We performed five simulations, summarised in Table 5.1. First, the present-day CONTROL simulation is forced solely with ERA-Interim, for which the forcing period 1992-2005 is repeated ten times. The first two repetitions (i.e. 28 years) are considered spinup; after this time, ice shelf melt rates have stabilised. The third repetition of the forcing is treated as the genuine 1992-2005 period. RCP simulations (2006-2100) split off from the end of the third forcing repetition, but the control simulation continues parallel to these RCP experiments, to provide an estimate of model drift. Experiments RCP 4.5 MMM and RCP 8.5 MMM are forced with the RCP 4.5 and 8.5 scenarios respectively, using output from the CMIP5 multi-model mean. The RCP 4.5 ACCESS and RCP 8.5 ACCESS simulations instead use output from the ACCESS 1.0 model.

Experiment	**Years**	**Forcing**	**Initialisation**
CONTROL	1992-2005, repeated 10 times	ERA-Interim	ECCO2 and NSIDC
RCP 4.5 MMM	2006-2100	RCP 4.5 (multi-model mean)	3rd repetition of CONTROL
RCP 4.5 ACCESS	2006-2100	RCP 4.5 (ACCESS 1.0)	3rd repetition of CONTROL
RCP 8.5 MMM	2006-2100	RCP 8.5 (multi-model mean)	3rd repetition of CONTROL
RCP 8.5 ACCESS	2006-2100	RCP 8.5 (ACCESS 1.0)	3rd repetition of CONTROL

Table 5.1: Summary of simulations performed.

For both RCPs, ACCESS 1.0 simulates greater 21st-century warming over the Southern Ocean than the multi-model mean. Therefore, in the results to follow, the RCP 4.5 ACCESS simulation displays somewhat stronger changes than RCP 4.5 MMM, and similarly for RCP 8.5. Additionally, the atmospheric forcing derived from ACCESS 1.0 exhibits interannual and decadal variability that is absent from the multi-model mean, which is reflected in our FESOM simulations. The multi-model mean averages out the variability in each of the 19 component models, including interan-

nual and decadal modes of variability which typically occur out of phase between different CMIP5 simulations. This means that projected future changes in these modes of variability, such as El Niño events (*Cai et al.*, 2014) which may affect the Amundsen Sea (*Steig et al.*, 2012; *Smith et al.*, 2017), will also not be captured by the MMM simulations.

5.3.4 Present-day evaluation

A comprehensive evaluation of this FESOM configuration was completed in Chapter 2. However, a brief summary of FESOM's performance and present-day biases around Antarctica is warranted.

First, simulated Antarctic sea ice extent agrees with observations in winter, but melts back too much in summer. The simulated pattern of sea ice formation generally agrees with observations, but sea ice production is too strong in the Amundsen, Ross, and Weddell Seas, while the small coastal polynyas of the Australian Sector are not well captured. Simulated transport of the Antarctic Circumpolar Current is slightly weaker than most recent observations.

With respect to ice shelf mass loss, our FESOM configuration underestimates total basal melting by nearly a factor of two compared to observational estimates. This is largely a regional bias confined to the Amundsen Sea, Bellingshausen Sea, and Australian sectors. By contrast, FESOM overestimates melting from the Amery and Ross Ice Shelves. Simulated melt rates from the Filchner-Ronne Ice Shelf (FRIS), the Larsen Ice Shelves, and the Eastern Weddell sector generally agree with observations. However, the simulated circulation in the FRIS cavity is less realistic. A point of concern with this FESOM configuration is the amount of topographic smoothing necessary for numerical stability, and the effect this may have on the model's cavity geometry.

As previously mentioned, the only difference between the configuration of Chapter 2 and the configuration presented here is the treatment of surface salt fluxes (surface salinity restoring versus global correction). This difference has virtually no effect on total ice shelf mass loss from Antarctica. However, some regional differences are more pronounced. The present-day control simulation analysed here shows higher melt rates in the Amundsen Sea sector (by up to 19% for Pine Island Ice Shelf) compared to the simulation of Chapter 2. This result suggests that surface salinity restoring contributes to the erosion of warm bottom water, a process discussed more fully in Section 5.4.4. The increased melting in the Amundsen Sea is offset by reduced melt rates downstream in the eastern Ross Sea, including the Sulzberger and Nickerson

Ice Shelves.

5.4 Results

5.4.1 Ice shelf basal mass loss

In our RCP simulations, total basal mass loss from all Antarctic ice shelves increases by between 41% and 129% depending on the scenario. These percentages are calculated by comparing the 2091-2100 average (last 10 years of the RCPs) to the 1996-2005 average (10 years preceding the RCPs). The increased melting is more pronounced in the simulations forced with ACCESS 1.0 (67% and 129% for RCP 4.5 and RCP 8.5 respectively) than in the simulations forced with the multi-model mean (41% and 90%). This tendency can be attributed to the greater atmospheric warming in ACCESS 1.0, as noted in Section 5.3.3.

Figure 5.3 partitions the increased mass loss into eight sectors: the Filchner-Ronne Ice Shelf (FRIS), the Eastern Weddell Region (all ice shelves between FRIS and the Amery), the Amery Ice Shelf, the Australian Sector (all ice shelves between the Amery and the Ross), the Ross Sea, the Amundsen Sea, the Bellingshausen Sea, and the Larsen Ice Shelves. The largest increases in ice shelf melting are seen in the Amundsen Sea, particularly in the RCP 8.5 simulations where basal mass loss triples to quadruples. The regional processes causing this increased melting are discussed further in Section 5.4.4. The Ross Sea is the least affected sector in all four simulations, with increases from 16% to 71%. Changes here are smaller due to strong convection in the Ross Polynya, which erodes the heat content of any warming onshore flow. Convection near other cold-cavity ice shelves, namely FRIS and the Amery Ice Shelf, is weaker and therefore its protective effect is more easily overwhelmed by warming processes (see Section 5.4.3).

To assess the significance of the changes shown in Figure 5.3, we have also calculated linear trends over the RCP simulations (2006-2100). These trends are significant at the 95% level for all sectors and all RCP scenarios, with the exception of the Larsen sector for which the trend is not significant during RCP 4.5 MMM and RCP 4.5 ACCESS. In the control simulation, the only significant trend in basal mass loss is for the Bellingshausen Sea sector, where melt rates increase at approximately one-fifth of the rate seen in the least dramatic RCP simulation (RCP 4.5 MMM).

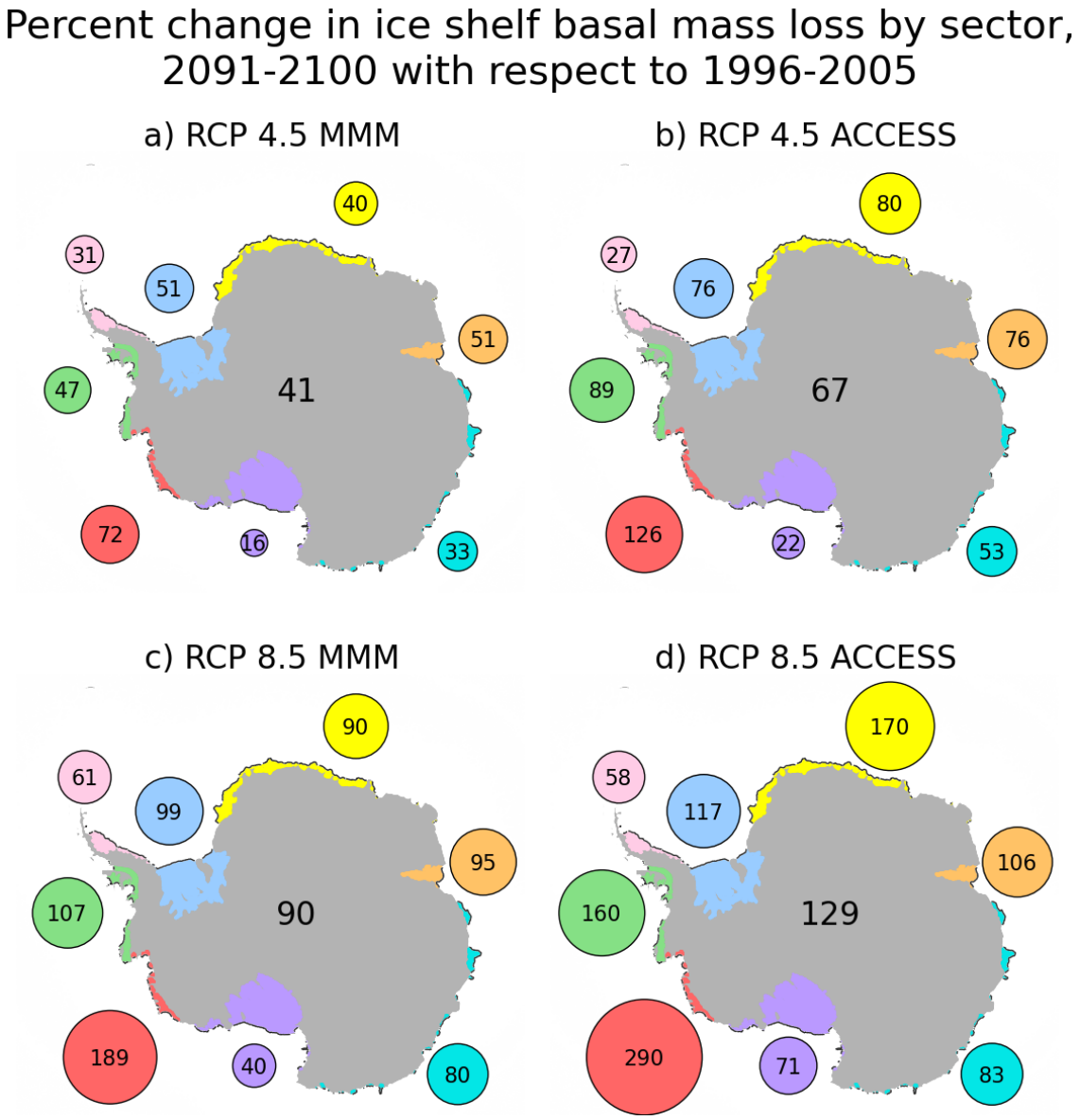

Figure 5.3: Percent change in ice shelf basal mass loss for each RCP simulation. Changes are calculated between the 1996-2005 average (10 years preceding RCPs) and 2091-2100 average (last 10 years of each RCP). The results are split into eight sectors of Antarctica, colour-coded as follows: Filchner-Ronne Ice Shelf (blue), Eastern Weddell Region (yellow), Amery Ice Shelf (orange), Australian Sector (teal), Ross Sea (purple), Amundsen Sea (red), Bellingshausen Sea (green), Larsen Ice Shelves (pink). The area of each coloured circle is proportional to the value written inside it, which is the percent change in basal mass loss for that sector. The number written in the centre of the continent is the percent change in ice shelf basal mass loss over all of Antarctica.

5.4.2 Water masses in ice shelf cavities

Changes in ice shelf basal mass loss can be better understood by examining the evolution of different water masses in ice shelf cavities during the 21st century. Figure 5.4 defines six different water masses based on discrete temperature and salinity boundaries. Ice Shelf Water (ISW) has temperature below the surface freezing point, and can only be formed as a result of ice shelf basal melting. Antarctic Surface Water (AASW) is relatively fresh and is warmed by the sun in the absence of sea ice. Low Salinity Shelf Water (LSSW) and High Salinity Shelf Water (HSSW) are the products of sea ice formation, with temperatures near the surface freezing point; HSSW is more affected by brine rejection, and thus has higher salinity. Circumpolar Deep Water (CDW), which upwells in the offshore Southern Ocean, is the warmest water mass in ice shelf cavities. As it crosses the continental shelf, it can be modified to varying degrees by mixing with colder water masses, forming Modified Circumpolar Deep Water (MCDW). Defining these different water masses leads to a natural distinction between cold-cavity ice shelves (where melting is driven by HSSW or LSSW, producing significant ISW) and warm-cavity ice shelves (where melting is driven by CDW or MCDW).

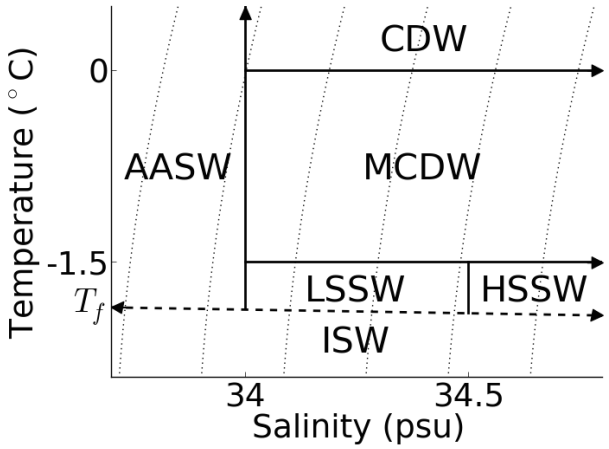

Figure 5.4: Schematic showing discrete potential temperature and salinity boundaries used to categorise water masses in ice shelf cavities in Figure 5.5. The dashed line T_f is the surface freezing point. The dotted curves show potential density contours. ISW = Ice Shelf Water, AASW = Antarctic Surface Water, LSSW = Low Salinity Shelf Water, HSSW = High Salinity Shelf Water, MCDW = Modified Circumpolar Deep Water, CDW = Circumpolar Deep Water.

Note that in Figure 5.4, the only threshold with physical significance is the surface freezing point. Other boundaries are somewhat arbitrary, such as the threshold salinity differentiating LSSW from HSSW, or the temperature range of MCDW. Here we use the same definitions as in Section 2.4.1.3, with the addition of CDW as a separate water mass from MCDW. The salinity thresholds are also the same as in *Galton-Fenzi* (2009).

For each water mass in ice shelf cavities, we calculated its heat content relative to the in-situ freezing point, hereafter abbreviated as HCf:

$$\text{HCf} = \int (T - T_{if})\, \rho\, c_{pw}\, dV \tag{5.2}$$

where T is potential temperature (°C), T_{if} is the in-situ freezing point (°C), ρ is the potential density (kg/m^3), $c_{pw} = 4180$ J K^{-1} kg^{-1} is the specific heat of seawater, and dV is the volume (m^3) of the given cell (a triangular prism). The integral is performed over all cells in ice shelf cavities in the given region (e.g. the Ross Sea), whose temperature and salinity values satisfy the definition of the given water mass. The in-situ freezing point is calculated as follows:

$$T_{if} = -0.0575\, S + 0.0901 - 7.61 \times 10^{-4}\, z \tag{5.3}$$

where S is salinity (psu) and z is depth (metres, positive). In Equations 5.2 and 5.3, T, ρ, S, and z are averaged over the six vertices of the given cell.

Note that HCf is influenced by the volume of the given water mass as well as its temperature and its position in the water column (which affects the in-situ freezing point). HCf represents the amount of energy (in Joules) available to melt ice at the given depth, but changes in total HCf are not equivalent to changes in basal mass loss, because the latter is also influenced by the flushing rate and by ocean velocities at the ice-ocean interface. Note that even ISW generally has a positive HCf, since its temperature typically lies between the surface and in-situ freezing points.

Timeseries of HCf for each water mass in ice shelf cavities, for the eight sectors defined in Figure 5.3 as well as the total for all ice shelves, are shown in Figure 5.5 for the RCP 8.5 MMM simulation. The timeseries have been scaled as percentages of the initial (1992-2005 mean) total HCf of all water masses in the given region.

Beneath the Filchner-Ronne Ice Shelf, HSSW is replaced by fresher LSSW during the 21st century, due to weaker sea ice formation. ISW also declines, which could indicate a shorter residence time with faster flushing of the cavities, and/or a warmer source water mass from which the heat is not fully extracted, so that the volume of water cooled below the surface freezing point is reduced. All three water masses exhibit slight warming (not shown), but total HCf in the cavity only increases by 20% (2091-2100 mean), which is relatively low compared to other cavities. The changes in HCf of individual water masses are therefore dominated by changes in proportional volume rather than temperature. The Ross Sea exhibits similar behaviour, with total HCf increasing by only 6% which indicates an even greater dominance of volume over temperature.

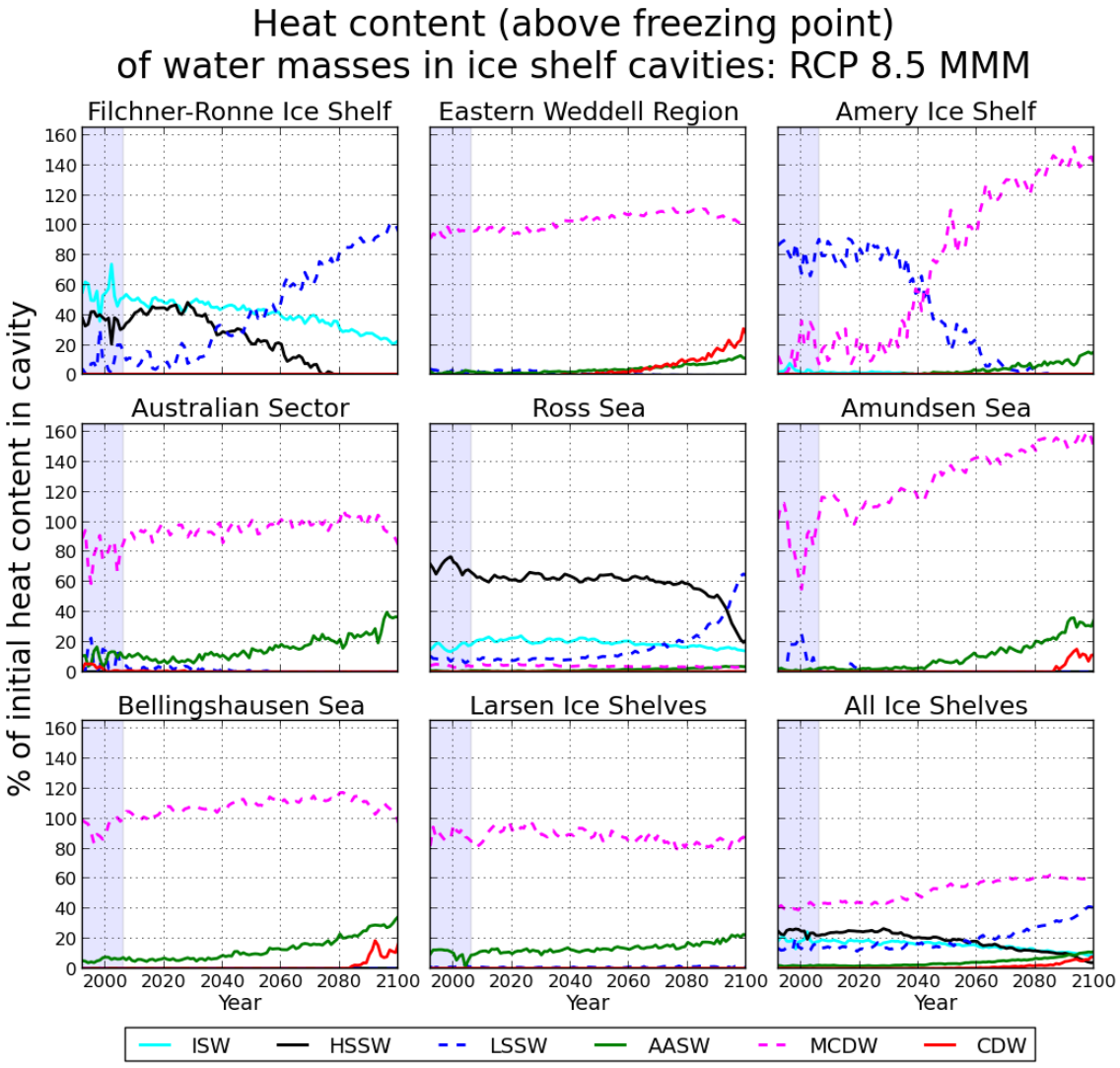

Figure 5.5: Annually-averaged timeseries of the heat content of different water masses (categorised in Figure 5.4) in ice shelf cavities during the RCP 8.5 MMM simulation. Heat content is calculated relative to the in-situ freezing point, and therefore represents the amount of energy in Joules available to melt ice at the given depth. Here it is scaled as a percentage of the initial (1992-2005 mean) heat content of all water masses in the given region (again relative to the in-situ freezing point). Results are shown for the eight sectors defined in Figure 5.3, as well as the total for all ice shelves. The years 1992-2005, preceding the RCP period, are shaded in light blue. Versions of this figure for the other three RCP simulations are available in Appendix A (Figures A.1 to A.3).

The Amery Ice Shelf cavity is initially dominated by LSSW, but during the first half of the 21st century this is replaced by relatively cool MCDW just above the $-1.5°C$ threshold. During the second half of the 21st century, this MCDW warms so that its HCf continues to rise; by 2091-2100, total HCf in the cavity has increased by 56%. An increasing presence of fresh AASW is also evident. The Australian Sector is initially more dominated by MCDW, but exhibits a loss of LSSW similar to the Amery. Enhanced HCf from AASW is more evident in this region, due to increases in both volume and temperature.

In both the Eastern Weddell Region and the Bellingshausen Sea, HCf from MCDW slightly increases during most of the 21st century. The volume of MCDW is actually stable or declining during this time, as some of it is replaced by fresher AASW, but its temperature is increasing. During the last 20 years of the simulation, this warming reaches the point where the HCf of MCDW declines due to replacement by CDW.

The most pronounced changes are seen in the Amundsen Sea, where total HCf doubles during the 21st century. The cavities in this region are initially dominated by LSSW and cool MCDW, but substantial warming of MCDW (by approx. 1°C) causes its HCf to increase throughout the 21st century, with an eventual contribution from CDW. This occurs despite a decrease in the volume of MCDW, due to replacement by fresher AASW (related to the increasing stratification described in Section 5.4.4). That is, more heat is contained in a smaller volume of MCDW, as it is less modified.

The Larsen Ice Shelves show the least pronounced changes in HCf, with a slight shift from MCDW to AASW due to freshening. There is very little contribution from warming, as total HCf increases by only 6%.

5.4.3 Mechanisms of warming in ice shelf cavities

Enhanced ice shelf basal melting is primarily the result of ocean warming in ice shelf cavities, but this warming can occur through several different processes. Figure 5.6 highlights these processes for a single scenario (RCP 8.5 MMM), comparing the period 2091-2100 to 1996-2005 as before. Figure 5.6a plots the maximum warming attained at any depth for each horizontal point in ice shelf cavities (note the non-linear colour scale), while Figure 5.6b plots the fractional depth below the ice shelf base of this maximum warming (0 is the ice shelf base, 1 is the seafloor). Figure 5.6c plots a seasonality metric based on monthly climatologies (defined in the figure caption), where 0 indicates no seasonality in the warming signal.

Two main mechanisms of warming can be identified: (1) surface-dominated and (2) bottom-dominated (corresponding to Mode 3 and Mode 2 ice shelf melting respectively, as in *Jacobs et al.* (1992)). Surface-dominated warming is characterised by fractional depths near 0 and high seasonality. Warming in this case is driven by a decline in summer sea ice cover, which exposes a greater fraction of the ocean surface to incoming solar radiation and changes in incoming longwave radiation. This surface water warms and may subduct beneath ice shelves. Regions affected by surface-dominated warming include the Filchner, Larsen, and Wilkins Ice Shelves, the eastern half of the Eastern Weddell Region, the Australian Sector, and the Ross

Ice Shelf front.

Conversely, bottom-dominated warming has fractional depths near 1 and low seasonality. This type of warming indicates an increased presence of CDW or MCDW, whose temperature is unaffected by the seasonal cycle. Bottom-dominated warming tends to have a larger magnitude than surface-dominated warming in our simulations, as seen by larger values in Figure 5.6a. The Amundsen Sea is the most affected region, and is explored in more detail in the next section. Also affected are the Abbot and Amery Ice Shelves, the western half of the Eastern Weddell Region, and the Ronne Ice Shelf.

Unlike other 21st-century projections with FESOM which were forced with output from the HadCM3 model (*Timmermann and Hellmer*, 2013; *Timmermann and Goeller*, 2017), our simulations do not show a redirection of the Antarctic Coastal Current beneath the Filchner-Ronne Ice Shelf. Comparing FESOM results between experiments forced with HadCM3 and ECHAM5 output, *Timmermann and Hellmer* (2013) showed that the occurrence of this transition is highly sensitive to the atmospheric forcing. Our simulations show a combination of processes driving melting beneath FRIS. The largest increases in melt occur immediately east of Berkner Island, due to inflow of warmer AASW. The Ronne Ice Shelf cavity is also slightly affected by bottom-dominated warming, due to an eastward shift in sea ice formation near the ice shelf front (see Section 5.4.7). Reduced convection in the Ronne Depression allows a warmer bottom layer to develop, consisting of warm LSSW or highly modified MCDW (maximum temperature $-1.4°C$ in RCP 8.5 ACCESS), which subsequently flows into the Ronne Ice Shelf cavity.

Figure 5.6 (following page): Details of warming in ice shelf cavities during the RCP 8.5 MMM simulation. (a) Maximum ocean warming attained at any depth, between the 1996-2005 average and the 2091-2100 average. Nodes with cooling throughout the entire water column (mainly near the back of the Ross Ice Shelf) are masked in white in all three panels. Note the nonlinear colour scale. (b) Fractional depth below the ice shelf base of this maximum warming, where 0 is the ice shelf base and 1 is the seafloor. (c) Seasonality of this warming, calculated using monthly climatologies for 1996-2005 and 2091-2100, at the depth shown in (b) for each horizontal node. The seasonality metric is defined as the difference in warming between the months with maximum and minimum warming at the given node, divided by the annual warming shown in (a). A value of 0 thus indicates no seasonality, while a value of 3 indicates a seasonal cycle in the warming signal which is three times the annual mean warming. Rn = Ronne Ice Shelf; Fi = Filchner Ice Shelf; EWed = Eastern Weddell Region; Am = Amery Ice Shelf; Aus = Australian Sector; Rs = Ross Ice Shelf; AS = Amundsen Sea; Ab = Abbot Ice Shelf; Wk = Wilkins Ice Shelf; Lr = Larsen Ice Shelves. Versions of this figure for the other three RCP simulations are available in Appendix A (Figures A.4 to A.6).

RCP 8.5 MMM, 2091-2100 minus 1996-2005

a) Maximum warming over depth (° C)

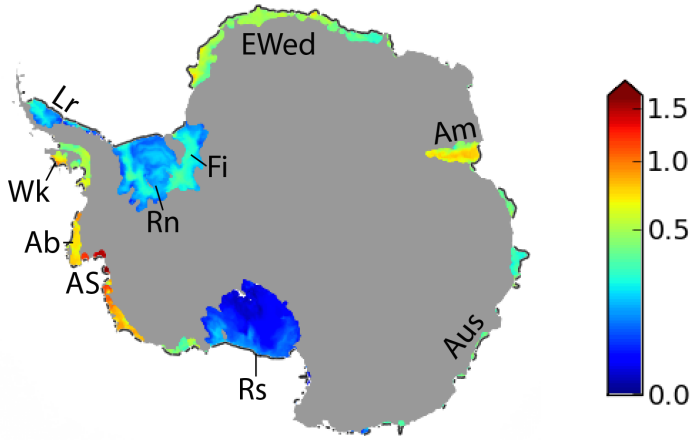

b) Fractional depth below ice shelf base of maximum warming

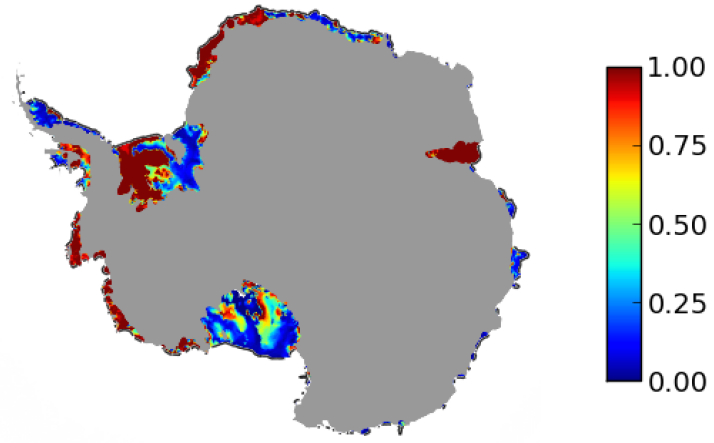

c) Seasonality metric

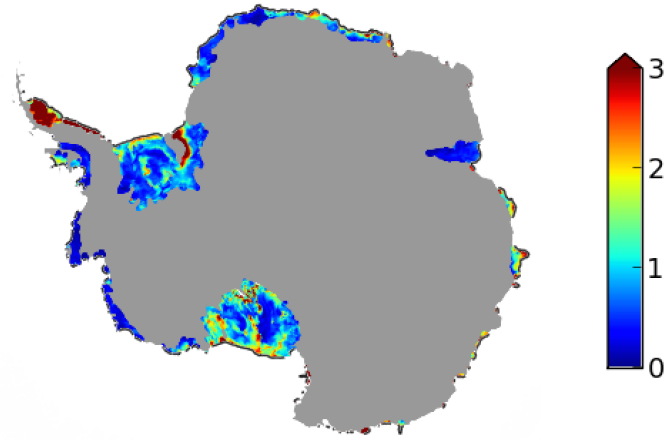

5.4.4 CDW in the Amundsen Sea

A region of particular interest in our simulations is the Amundsen Sea sector, which experiences the largest increase in ice shelf basal mass loss of any Antarctic region, due to strong bottom-dominated warming. Prior to the RCPs (1996-2005), our FESOM configuration exhibits a cold bias in the Amundsen Sea, with bottom water temperatures around -1°C on the continental shelf (Figure 5.7a). By comparison, observations in this region suggest temperatures around 1°C (*Jacobs et al.*, 2011; *Jenkins et al.*, 2010; *Dutrieux et al.*, 2014). As a result, our FESOM configuration underestimates ice shelf melt rates in the Amundsen Sea compared to observation-based estimates (Section 2.4.3.6). This model bias is largely due to unrealistically strong sea ice formation in the Amundsen Sea, which fills the continental shelf with cold LSSW and erodes most of the warm signal from MCDW in the bottom layer. Other possible contributors to this cold bias are a spuriously large mixing along sigma coordinate lines (*Nakayama et al.*, 2014), as well as unresolved mesoscale eddies which would otherwise transport heat across the shelf break (*Stewart and Thompson*, 2015).

By the end of all four RCP simulations, this cold bias has been largely overtaken by warming. Significant warm anomalies are apparent in bottom water temperature on the Amundsen Sea continental shelf, particularly in front of the Pine Island and Thwaites Ice Shelves (Figure 5.7a). The RCP 8.5 ACCESS simulation experiences the strongest warming, of up to 1.8°C. Ice shelf melt rates increase (Figure 5.7b), with total basal mass loss from the Pine Island and Thwaites Ice Shelves approximately quadrupling during the RCP 8.5 ACCESS simulation. The warm anomalies coincide with salinification of up to 0.15 psu in the bottom layer (Figure 5.7c). This combination of increased temperature and salinity indicates that the warming is due to an enhanced presence of CDW on the continental shelf.

This increase in CDW is driven by stratification, as shown in Figure 5.8 with meridional slices of temperature and salinity through 104°W, during September when convection is strongest. Prior to the RCPs (1996-2005, left column), temperature and salinity on the continental shelf are relatively uniform with depth. Sea ice form-

Figure 5.7 (following page): Conditions in the Amundsen Sea region, showing absolute variables for the 1996-2005 average (left column) and the anomalies with respect to this baseline for the 2091-2100 average in each RCP simulation (middle four columns) and the CONTROL experiment (right column). (a) Bottom water temperature (°C). The dashed black line shows the 1500 m isobath, which approximates the continental shelf break. (b) Ice shelf melt rate (m/y). The anomaly colour scale is capped at 18 m/y for visibility; the true maximum anomaly is 24.8 m/y. IS = Ice Shelf. (c) Bottom water salinity (psu).

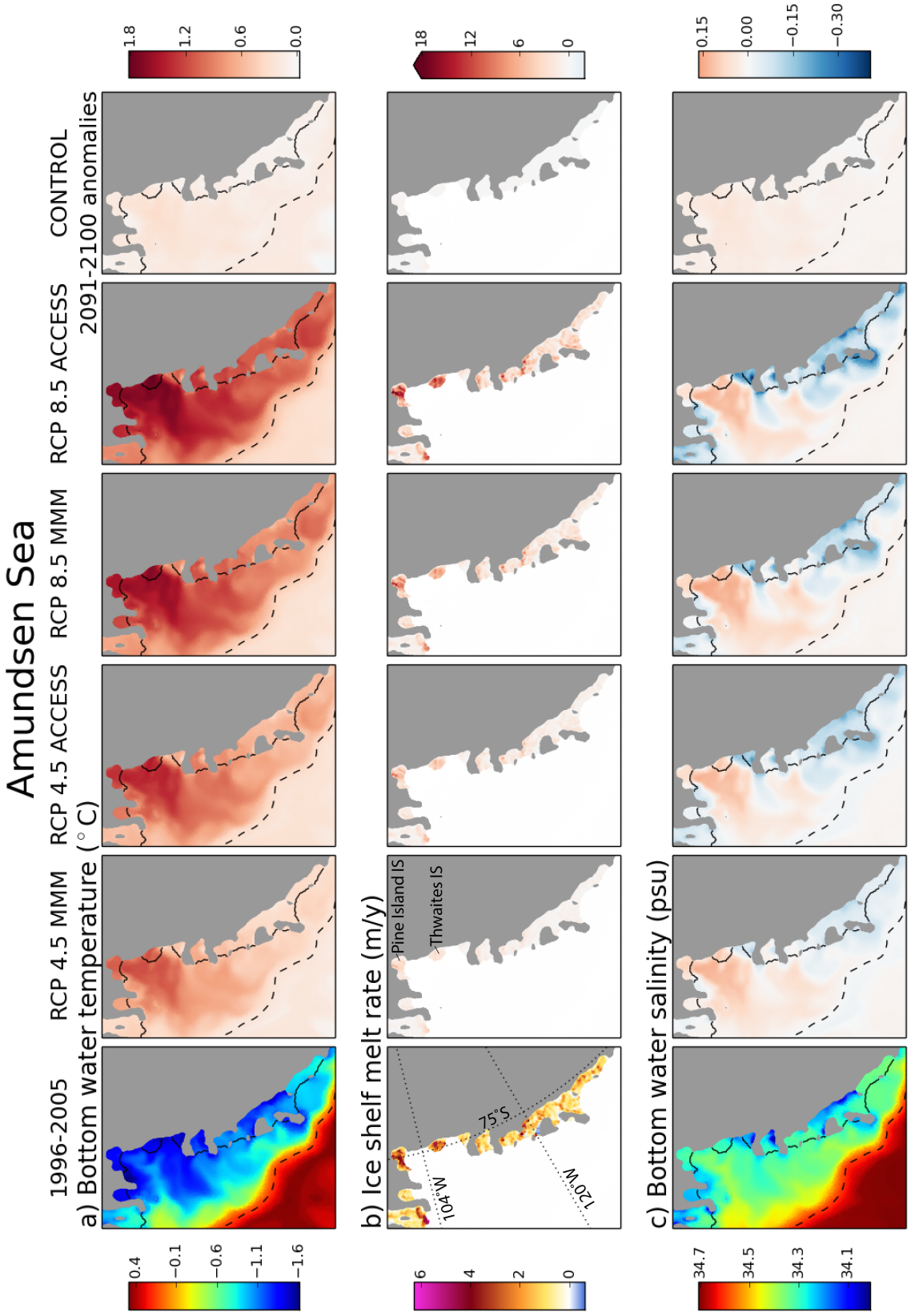
Amundsen Sea
1996-2005
RCP 4.5 MMM
RCP 4.5 ACCESS
RCP 8.5 MMM
RCP 8.5 ACCESS
CONTROL
2091-2100 anomalies
a) Bottom water temperature (°C)
0.4
−0.1
−0.6
−1.1
−1.6
1.8
1.2
0.6
0.0
b) Ice shelf melt rate (m/y)
Pine Island IS
Thwaites IS
75°S
104°W
120°W
6
4
2
0
18
12
6
0
c) Bottom water salinity (psu)
34.7
34.5
34.3
34.1
0.15
0.00
−0.15
−0.30

ation has destabilised the entire water column, so the warmth of the bottom layer is lost to the atmosphere due to deep convection. However, by the end of RCP 8.5 ACCESS (2091-2100, right column), the water column has stratified. The cold surface water is now too fresh to form a deep mixed layer, so the underlying CDW ($> 0°C$) is preserved. Analysis of the surface freshwater budget reveals the primary cause of this freshening to be reduced sea ice formation.

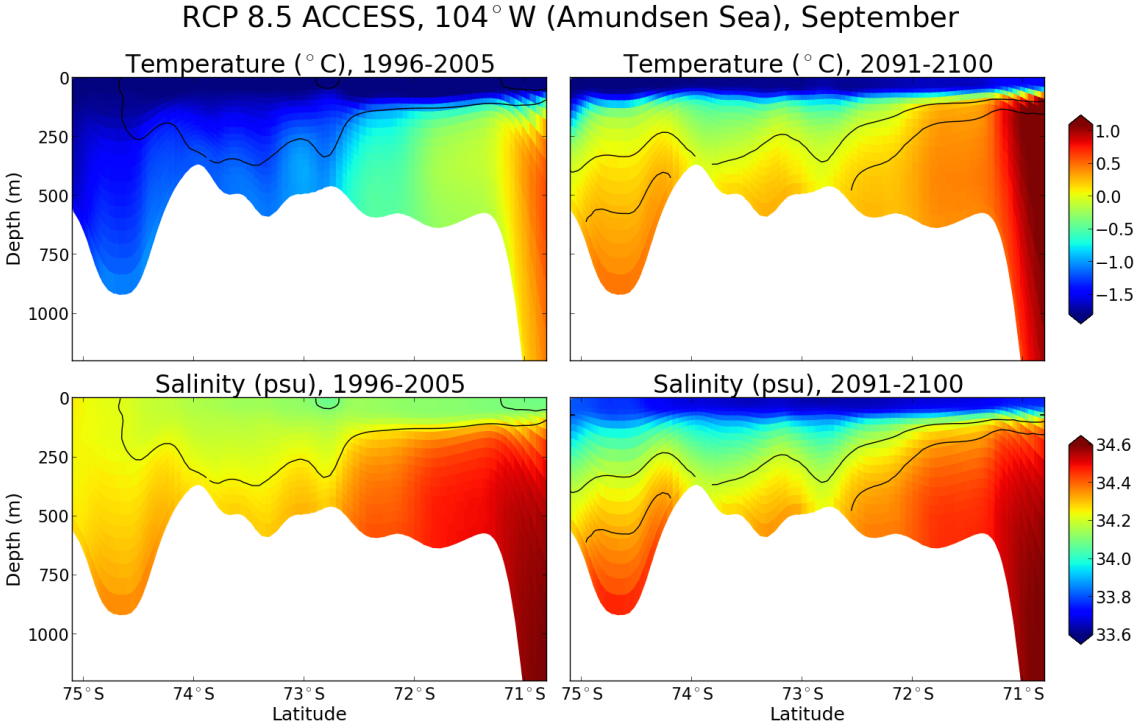

Figure 5.8: Meridional slices of temperature (°C, top row) and salinity (psu, bottom row) interpolated to 104°W through the Amundsen Sea (line of longitude marked in Figure 5.7b). Results are shown for the September monthly average, in the 1996-2005 climatology (left) as well as the 2091-2100 climatology (right) for the RCP 8.5 ACCESS simulation. The black lines show potential density contours for 1027.45 kg/m^3 and 1027.55 kg/m^3.

In reality, the present-day Amundsen Sea may not be capable of experiencing much further warming, since it is already inundated with unmodified CDW. The warming seen in our simulations should therefore be interpreted as the reversal of a model bias, rather than as a reliable projection for the Amundsen Sea region. However, the mechanism of warming - reduced sea ice formation stratifying the water column and permitting greater onshore transport of CDW and MCDW - is still valid, and could apply to many regions of Antarctica. In our simulations, this mechanism is visible to a lesser extent in the Bellingshausen Sea, the Amery Ice Shelf cavity, and the western half of the Eastern Weddell region (Brunt, Riiser-Larsen, Ekstrom, Jelbart, and Fimbul Ice Shelves). It is also useful to note that the model's Amundsen Sea cold bias is sensitive to atmospheric forcing (as also found by *Nakayama et al.* (2014) for a different configuration of FESOM), and is not necessarily an intrinsic feature

of this model configuration.

Transport of CDW onto the continental shelf can also be affected by changes in wind stress, which affect Ekman upwelling at the shelf break (*Schmidtko et al.*, 2014). In particular, strengthening and poleward shifting of the Southern Hemisphere westerly winds has been suggested as a mechanism to cause warming on the continental shelf of West Antarctica (*Spence et al.*, 2014, 2017). Among our experiments, the RCP 8.5 MMM scenario experiences the most pronounced changes in winds. Here the bias-corrected atmospheric forcing shows a similar strengthening, but a smaller southward shift, of the Southern Hemisphere westerlies compared to the idealised wind changes applied by *Spence et al.* (2014). In order to quantify the effects of changing wind stress on ice shelf melting in our simulations, we performed an additional experiment identical to RCP 8.5 MMM, but with no changes in the winds. That is, the wind fields were held fixed at the 1992-2005 monthly climatology, with submonthly variability superimposed as before, but zero monthly anomalies throughout the RCP. By 2091-2100, ice shelf basal mass loss from the Amundsen Sea sector was 2.8% lower than in the original RCP 8.5 MMM simulation, and basal mass loss from the entire continent was 0.6% higher. Therefore, the changes in ice shelf melting we simulate during the 21st century do not appear to be primarily caused by changes in wind stress. This is in agreement with the results of *Donat-Magnin et al.* (2017) who found that including ice shelf thermodynamics in a regional model of the Amundsen Sea reduced the sensitivity of continental shelf temperatures to changes in the winds.

5.4.5 Changes in HSSW and AABW

Temperature-salinity distributions of water masses south of 65°S are shown in Figure 5.9, averaged over the period 1996-2005 (left column) as well as 2091-2100 for each RCP experiment and the control experiment. Figure 5.9a zooms into the HSSW part of the distribution, which freshens in all four RCP scenarios. The magnitude of this freshening ranges from approximately 0.05 psu in RCP 4.5 MMM to almost 0.5 psu in RCP 8.5 ACCESS. In fact, by the end of RCP 8.5 ACCESS no water at all would be classified as HSSW using the definition in Figure 5.4 (salinity $\geq$ 34.5 psu), neglecting the seasonal cycle. By contrast, HSSW in the control simulation becomes slightly saltier, by approximately 0.05 psu.

HSSW is the product of strong sea ice formation and the resultant brine rejection, and its decline in the RCP simulations is driven by warmer winter air temperatures causing weaker sea ice formation (Section 5.4.7). The resulting water masses shift toward LSSW properties, which are less affected by brine rejection, and consequently

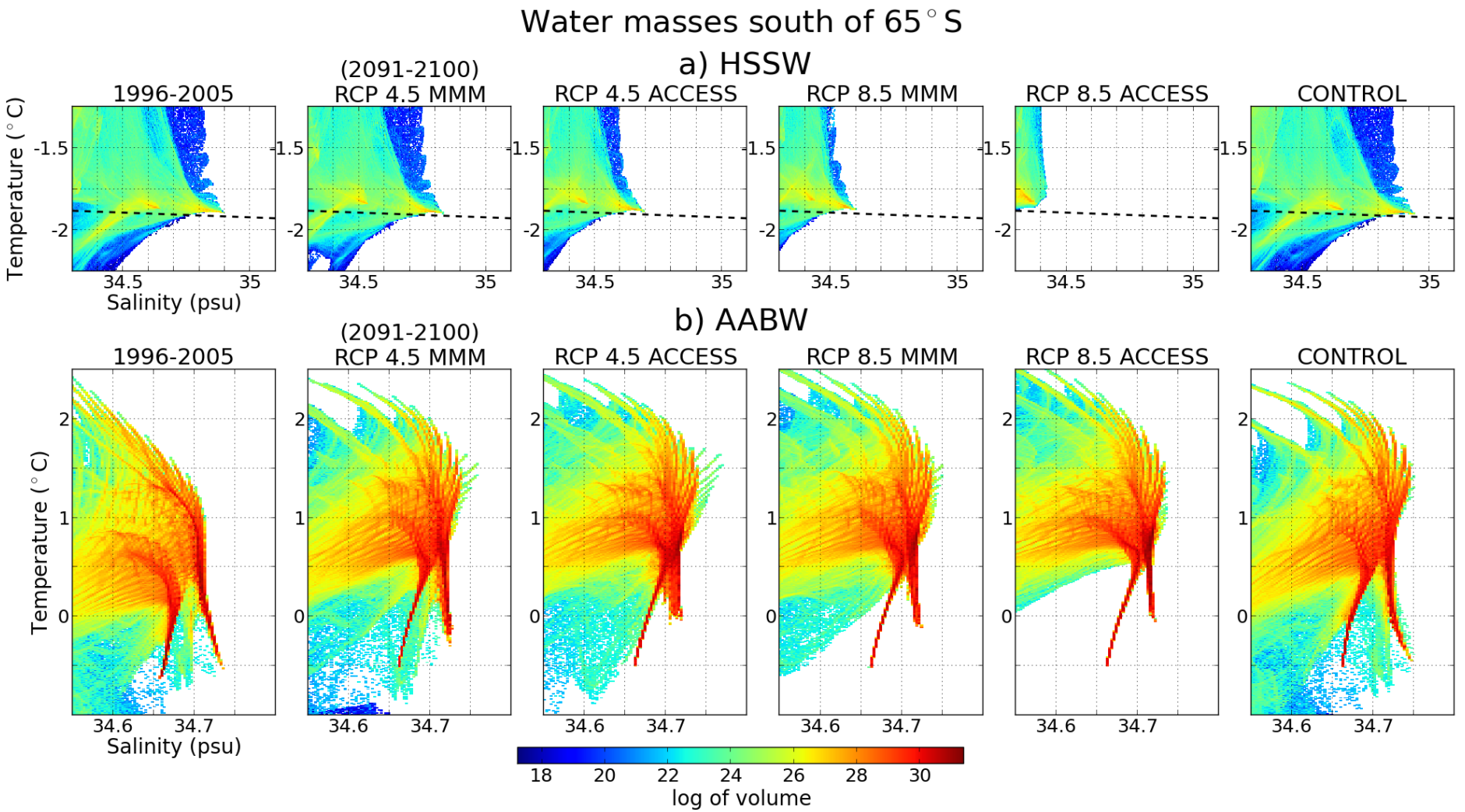

Figure 5.9: Temperature-salinity distribution of water masses south of 65°S, averaged over the years 1996-2005 (leftmost column), as well as 2091-2100 for each RCP experiment and the CONTROL experiment. Each triangular prism south of 65°S in the FESOM mesh is sorted into 1000×1000 temperature and salinity bins. The colour scale shows the log of the volume (m^3) of each bin, and the dashed lines in (a) show the surface freezing point. Results are shown zoomed into two different regions of the distribution: (a) HSSW (High Salinity Shelf Water); (b) AABW (Antarctic Bottom Water).

fresher and less dense. Export of cold water down the continental slope, which feeds AABW, is therefore inhibited, and AABW would be expected to warm as a result.

Figure 5.9b zooms into the AABW part of the distribution, which is characterised by a double-forked feature. The fresher fork is Weddell Sea Bottom Water (WSBW), and the saltier fork is Ross Sea Bottom Water (RSBW) (Section 2.4.1.3). Both forks display warming during the RCP simulations, as expected. This warming is more pronounced for RSBW, with changes of approximately 0.5°C in the RCP 8.5 ACCESS simulation.

In the CONTROL experiment, no significant drift is seen for the cold WSBW and RSBW forks, but the warmer varieties of AABW and CDW (> 0°C) become warmer as well as saltier. This drift is affected by deep ocean processes operating on centennial to millennial timescales, which are not expected to stabilise during our relatively short spinup of 28 years.

5.4.6 Changes in large-scale circulation

Our simulations show a weakening of the Antarctic Circumpolar Current (ACC) in response to 21st-century climate change. Over the period 1996-2005, the mean transport through Drake Passage (67°W) is 144 Sv. By 2091-2100, this has weakened by 13%, 16%, 13%, and 17% in RCP 4.5 MMM, RCP 4.5 ACCESS, RCP 8.5 MMM, and RCP 8.5 ACCESS respectively. The absolute reductions in transport are 19 Sv, 23 Sv, 19 Sv, and 24 Sv respectively. The control simulation also shows a weakening of 8% (11 Sv), which may be due to diapycnal mixing in the deep ocean (Section 2.4.1.1). The more pronounced ACC weakening seen in the RCP simulations indicates that forced changes, as well as drift, are underway. These changes cannot be attributed to weakening of the Southern Hemisphere westerly winds, because in fact these winds strengthen slightly in all four forcing scenarios. Rather, near-surface freshening around the Antarctic continent reduces the meridional density gradient across the Southern Ocean, causing zonal transport to weaken. The same phenomenon was apparent in the climate change simulations of *Hattermann and Levermann* (2010), although after 150 years it was overwhelmed by the effects of deep ocean warming which ultimately drove a strengthening of the ACC.

While freshening around Antarctica reduces the density gradient across the Southern Ocean, it strengthens the density gradient across the continental slope, which in our simulations causes the Antarctic Coastal Current to strengthen. We estimate the speed of this current in 1-degree longitude bins, by selecting the maximum time-averaged surface speed of all nodes within the given bin which are south of

64°S with bathymetry shallower than 2500 m. For the 1996-2005 average, the mean Antarctic Coastal Current speed across all longitude bins is 0.13 m/s. During each RCP scenario, the mean percentage increase in speed across all longitude bins (2091-2100 versus 1996-2005) is 11%, 27%, 29%, and 52% for RCP 4.5 MMM, RCP 4.5 ACCESS, RCP 8.5 MMM, and RCP 8.5 ACCESS respectively. The largest changes occur between 80°W and 180°W, which contains the Bellingshausen, Amundsen, and eastern Ross Seas. Since the Amundsen and Bellingshausen Seas exhibit the greatest increases in ice shelf basal melting (Section 5.4.1), it is logical that the resulting meltwater would strengthen the coastal current locally as well as immediately downstream in the eastern Ross Sea. During the same period in the CONTROL experiment, residual drift causes the Antarctic Coastal Current to slightly slow, by an average of 3% over all longitude bins.

Due to the counteracting effects of the weakening ACC and strengthening coastal current, our simulations show no consistent trends in subpolar gyre strength for either the Ross or Weddell Sea. The Ross Gyre weakens in RCP 4.5 MMM but strengthens in RCP 8.5 MMM (both significant at the 95% level), with no significant trends in the simulations forced with ACCESS. Conversely, the Weddell Gyre strengthens in RCP 4.5 ACCESS and weakens in RCP 8.5 ACCESS, with no significant trends in the simulations forced with the multi-model mean. Both gyres weaken during the CONTROL experiment, due to the weakening ACC but stable coastal current.

5.4.7 Changes in sea ice

Our configuration of FESOM underestimates the present-day Antarctic sea ice minimum by approximately a factor of two (Section 2.4.2.1), which is a common bias among coupled ocean/sea-ice models (*Downes et al.*, 2015). In some years of the control simulation, February Antarctic sea ice extent is near zero. With very little summer sea ice left to lose, analysing changes in the Antarctic sea ice minimum during the RCP experiments would be of limited use.

Changes in the sea ice maximum are more robust, as our FESOM configuration more or less reproduces observed September sea ice extent (Section 2.4.2.1). Figure 5.10 plots September sea ice concentration averaged over 1996-2005, as well as the anomalies during 2091-2100 for each RCP simulation and the control experiment. The northern edge of the sea ice pack retreats in all four RCP simulations, with the greatest declines in the Amundsen and Bellingshausen Seas (as observed in recent decades (*Meier et al.*, 2013)) and off the coast of East Antarctica.

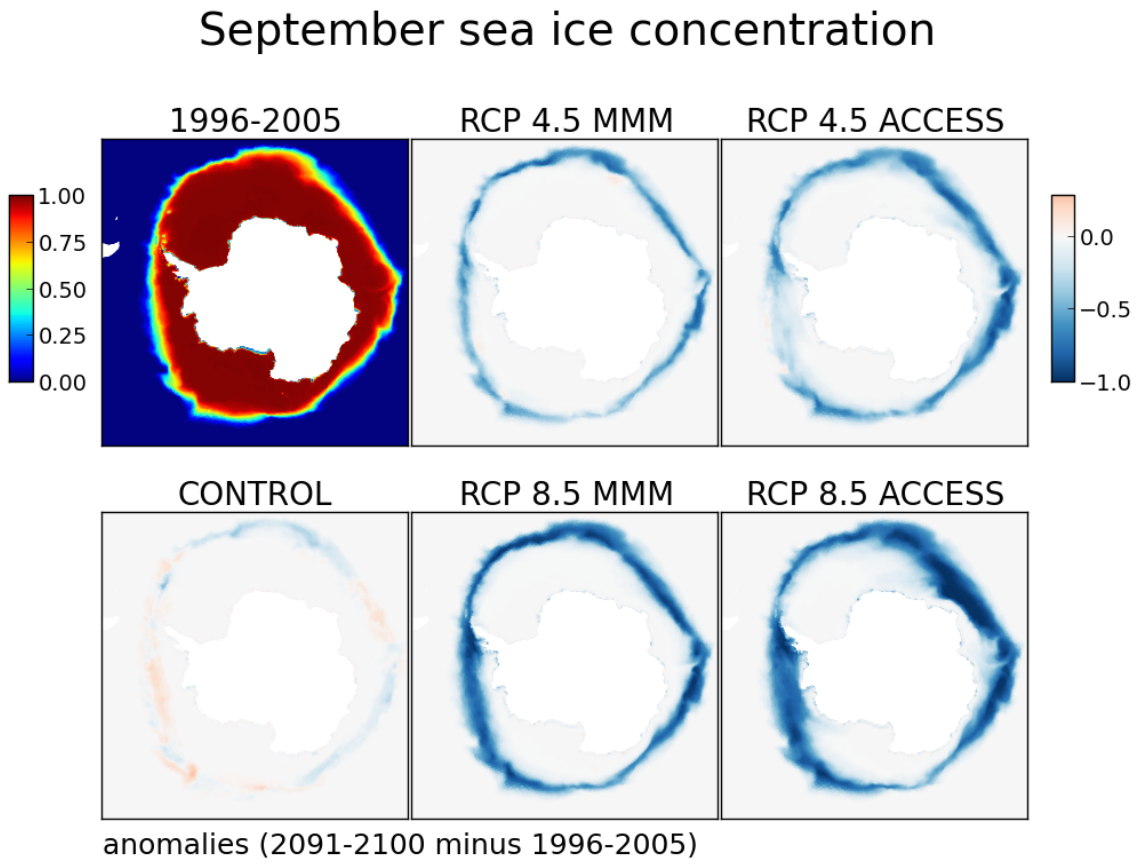

Figure 5.10: Sea ice concentration (fraction) averaged over September, the month of maximum sea ice extent. Absolute concentration is shown for the 1996-2005 average, and anomalies for 2091-2100 with respect to 1996-2005 are shown for the four RCP simulations and the CONTROL simulation.

These anomalies represent a decline in September total Antarctic sea ice extent (calculated as the area of mesh elements with sea ice concentration exceeding 0.15) of 18%, 18%, 30%, and 35% for RCP 4.5 MMM, RCP 4.5 ACCESS, RCP 8.5 MMM, and RCP 8.5 ACCESS respectively. These declines are similar to the sea ice projections simulated directly by the CMIP5 multi-model mean and ACCESS 1.0 (Ariaan Purich, personal communication) which indicates that ice shelf meltwater has minimal effect on sea ice changes in our simulations. This is in contrast to the results of *Merino et al.* (2018) who found that prescribing ice shelf and iceberg meltwater led to non-negligible changes in simulated sea ice extent.

Changes in sea ice formation and melt during the RCP 8.5 MMM simulation are shown in Figure 5.11, with seasonal averages for the 1996-2005 baseline (Figure 5.11a) as well as anomalies for 2091-2100 (Figure 5.11b). Positive anomalies indicate more freezing or less melting, depending on the sign of the initial field, and vice versa for negative anomalies. In general, freezing and melting both weaken, indicating a reduction in intensity of the sea ice cycle.

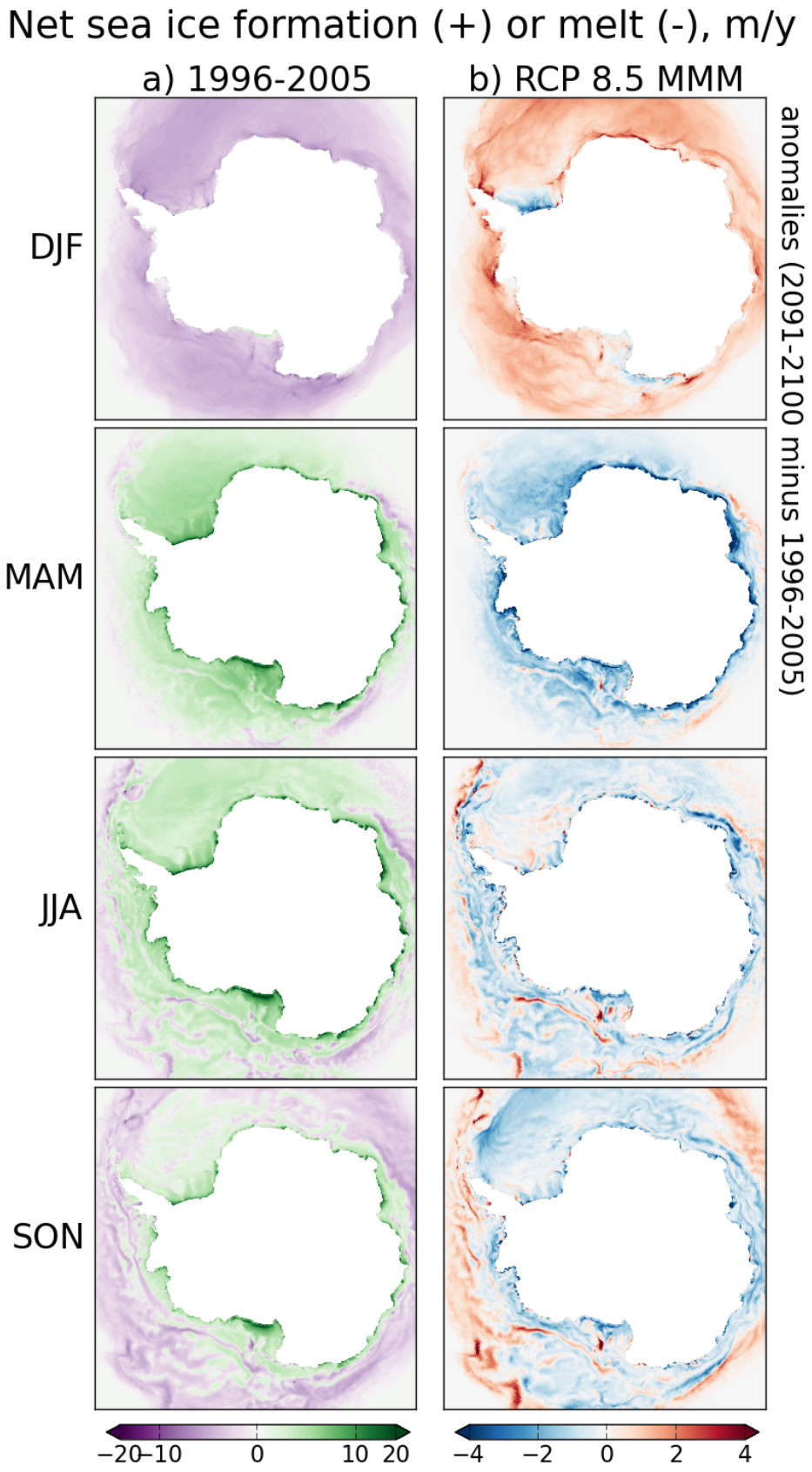

Figure 5.11: (a) Net sea ice formation (positive) or melt (negative) in m/y for each season in the 1996-2005 mean. Note the nonlinear colour scale. (b) Anomalies for 2091-2100 with respect to 1996-2005 in the RCP 8.5 MMM simulation.

Summer (DJF) is dominated by reduced melting, as there is less sea ice available to melt, except in the southern Weddell and Ross Seas which experience increased melting of multiyear ice. Similarly, offshore regions show year-round reductions in melting. Warmer temperatures also cause the transition zone between freezing and melting to shift southward, which is particularly visible in spring (SON). The cooler seasons show widespread weakening of sea ice formation on the continental shelf, as noted in previous sections. In the Ross and Weddell Seas some shifts in the regions of strongest sea ice formation are visible, characterised by adjacent positive and negative anomalies. In particular, wintertime (JJA) sea ice formation shifts eastward out of the Ronne Depression, and northward in the Ross Sea.

Across the seasonal cycle, the net effect of these changes is to reduce the transport of freshwater away from the Antarctic coast, with consequent effects on Southern Ocean density gradients as described in Section 5.4.6.

5.5 Summary and discussion

In our simulations, ice shelf basal melting increases in every sector of Antarctica and in every 21st-century forcing scenario. Perhaps the most significant result in our simulations is the effect of reduced sea ice formation on ice shelf basal melting, which confirms and extends the findings of *Timmermann and Hellmer* (2013). In the simulated present-day climate, sea ice formation drives convection on the continental shelf which protects ice shelf cavities from warm CDW and MCDW intruding from offshore. During the simulated 21st century, warmer winters with less sea ice formation cause increased stratification of the water column. Shallower mixed layers allow a warm bottom layer of CDW or MCDW to develop in many regions, most notably the Amundsen Sea. In the warmest scenario (RCP 8.5 ACCESS), ice shelf basal mass loss from the Amundsen Sea quadruples as a result. The simulations of *Timmermann and Hellmer* (2013) and *Timmermann and Goeller* (2017) showed a similar mechanism, but mainly affecting the southern Weddell Sea rather than the Amundsen Sea, and aided by a redirected coastal current.

Some ice shelf cavities affected by this bottom-dominated warming, such as the Eastern Weddell Region and the Amery Ice Shelf, also exhibit excessive MCDW in present-day simulations (Sections 2.4.3.2 and 2.4.3.3) which is possibly due to oversmoothing of the continental slope. Conversely, the Amundsen Sea has unrealistically strong modification of CDW in present-day simulations, as described in Section 5.4.4. These present-day biases may affect the simulated future changes, and our projections should therefore be interpreted with caution.

For other ice shelves, such as the Ross and the Filchner, simulated increases in melting are instead driven by warmer AASW which subducts beneath the ice shelf front. This process is tied to reductions in sea ice, as an increased area of open water raises sea surface temperatures due to solar heating. The same process was found in the future projections of *Timmermann and Goeller* (2017) for the FRIS region, although increased melting in these simulations was mainly caused by MCDW. Chapter 2 also highlighted concerns with oversmoothed ice shelf fronts, particularly the Ross, allowing relatively warm surface waters to enter the cavity too easily. This may mimic the effects of tides, which are absent in FESOM, on water mass exchanges at the ice shelf front. Nonetheless, some amount of increased melting from warming AASW would be expected regardless of geometry.

Trends in simulated water mass proportions in ice shelf cavities reflect the increased presence of CDW, warmer MCDW, and AASW, which can all be attributed to reductions in sea ice formation or extent. We also simulate a reduction in HSSW, which is replaced by fresher LSSW due to weaker sea ice formation in the Ross and Weddell Seas. Freshening of HSSW on the continental shelf is also apparent in temperature-salinity distributions. Export of HSSW off the continental shelf is inhibited due to its lower density, and as a result the colder varieties of AABW (Ross Sea and Weddell Sea Bottom Water) warm.

We simulate a weakening of the Antarctic Circumpolar Current due to freshening around the Antarctic continent (again caused by weakened sea ice formation), which reduces the meridional density gradient across the Southern Ocean. Across the continental slope, a stronger density gradient causes the Antarctic Coastal Current to increase in speed.

Most of the changes during the 21st century are more pronounced in the simulations forced with ACCESS 1.0 as compared to the CMIP5 multi-model mean. This is due to the greater warming over the Southern Ocean simulated by ACCESS 1.0. As expected, changes are also more pronounced in the RCP 8.5 scenario than the RCP 4.5 scenario, with the exception of ACC weakening which is approximately the same between the two scenarios. We do not simulate any major threshold changes in FESOM's response to 21st-century forcing. Rather, the four simulations exhibit largely the same patterns of behaviour along a continuum of severity. This may be due to the stand-alone nature of our simulations, as coupling with an atmosphere and/or ice sheet model would allow for other nonlinear positive feedbacks to develop.

This work builds on previous studies with FESOM, where future projections were integrated using the atmospheric output of CMIP3 models without bias-correction. Simulations forced with the HadCM3 model (*Timmermann and Hellmer*, 2013; *Tim-*

mermann and Goeller, 2017) revealed a tipping point in the southern Weddell Sea, whereas our results show more gradual changes. FESOM simulations forced with uncorrected output from the CMIP5 model HadGEM2 (*Timmermann and Kauker*, 2014) also show gradual increases in ice shelf melting around Antarctica, with no tipping points. These differences in behaviour illustrate the sensitivity of sub-ice shelf processes to atmospheric forcing, and the importance of constraining climate projections in order to better predict the response of the ice shelves and ice sheet. At the time of writing, the only other published future projections of ice shelf melting forced with CMIP output are from the BRIOS model (*Hellmer et al.*, 2012, 2017). These simulations use the same HadCM3 forcing as the FESOM CMIP3 simulations mentioned above, and display similar behaviour.

While our bias-correction method was successful in this instance, it should be applied with caution by others in the future. In particular, CMIP5 models should be chosen whose historical simulations are as close to atmospheric reanalyses as possible, so that the bias-correction term is small. This approach minimises the risk of applying state-dependent future changes which depend on underlying biases in the CMIP5 models, and also avoids potential artifacts in the corrected forcing such as unrealistic wind fields. As noted in Section 5.2, biases in ERA-Interim over the Southern Ocean may also influence our constructed forcing fields. However, in most cases the biases of atmospheric reanalyses such as ERA-Interim are likely to be small compared to those of global climate models unconstrained by observations. Furthermore, our initial conditions for the deep ocean are not yet equilibrated to the forcing period 1992-2005, which is itself a perturbation from the preindustrial climate. Therefore, some forced trends may be influencing our CONTROL simulation.

Finally, our experiments assume that ice shelf geometry will not change during the 21st century. This assumption is clearly problematic, as ice shelves are already responding to climate change with thinning (*Paolo et al.*, 2015) and collapse (*Rott et al.*, 1996; *Rack and Rott*, 2004; *Hogg and Gudmundsson*, 2017). Furthermore, the coupled ice-sheet/ocean simulations of *Timmermann and Goeller* (2017) indicate that an evolving ice shelf draft tends to enhance, not damp, increases in basal melt rates during warming scenarios. *Donat-Magnin et al.* (2017) also found that prescribed grounding line retreat in the Amundsen Sea region led to increased melt rates, due to stronger buoyancy-driven circulation within the cavities.

Our projections of melt rates have particularly troubling implications for the marine sectors of the ice sheet which are grounded below sea level, including the Amundsen Basin as well as the Wilkes and Aurora Basins (both within the Australian Sector in our analysis, and exhibiting similar behaviour). Standalone ice sheet modelling has demonstrated the vulnerability of these marine basins to ocean warming (*Feldmann*

and Levermann, 2015; *Mengel and Levermann*, 2014; *Sun et al.*, 2016), illustrating the need for fully coupled ice-sheet/ocean simulations to provide more reliable future projections. The potential collapse of marine sectors of the Antarctic Ice Sheet, and corresponding global sea level rise, is one of the most profound yet poorly understood impacts of climate change, and further model development is essential to better predict this behaviour in the 21st century and beyond.

Chapter 6

Concluding remarks

The Antarctic continental shelf and ice shelf cavities are some of the least observed regions of the global ocean, but are of crucial importance for future sea level rise. Sub-ice shelf circulation and water mass properties determine basal melt rates and ultimately the stability of the Antarctic Ice Sheet. These processes are influenced by sea ice, which drives the ice pump through the formation of HSSW and LSSW, but also indirectly affects other modes of melting. The absence of sea ice allows AASW to warm and melt the ice shelf front, while the strength of sea ice formation influences how easily CDW can intrude into cavities. Much of our understanding of ice-shelf, ocean, and sea ice interactions is based on numerical modelling, but this modelling has not yet been incorporated into fully coupled GCMs. As such, the model intercomparison projects from which GCMs benefit so greatly, and the standardised future climate projections by which GCMs inform society, have not yet been extended to include sub-ice shelf processes.

This thesis contributed to the field of ice-shelf/ocean/sea-ice modelling in three major ways, fulfilling the aims set out in Section 1.4. First, a new circumpolar Antarctic configuration of MetROMS was developed, combining the ROMS ice shelf branch with a state-of-the-art, externally coupled sea ice model. Despite numerous challenges in development spanning both the ocean and sea ice components (Chapters 3 and 4), the final configuration performed reasonably well, especially on the continental shelf and in ice shelf cavities. Second, a comprehensive intercomparison of MetROMS and FESOM was completed (Chapter 2), representing the only published intercomparison of ice-shelf/ocean models over a realistic domain and with interactive sea ice. Third, projections of ice shelf melt rates in the 21st century were produced with FESOM (Chapter 5), using carefully selected and bias-corrected atmospheric forcing from CMIP5 projections. The remainder of this discussion summarises the main conclusions of each chapter, and outlines possibilities for future

work.

Chapter 2 compared Antarctic ice shelf, ocean, and sea ice processes in MetROMS and FESOM using standardised simulations over the period 1992-2016, and evaluated the models against observations where possible. FESOM's sensitivity to horizontal resolution was also assessed. Even though MetROMS and FESOM implement fundamentally different numerical methods (finite-volume versus finite-element), their output was broadly similar, with many of the same biases. Such similarity suggests that perhaps some of the biases lie with ERA-Interim and/or the underlying observations, and that atmospheric forcing is a first-order control on sea ice conditions, which then influence sub-ice shelf processes. This hypothesis could be tested by expanding the intercomparison to use several different atmospheric forcing products, and assessing their impact on the simulations. On the other hand, MetROMS and FESOM have a number of deficiencies in common despite their different underlying numerical methods, including unresolved eddies, the absence of tides, and excessive diapycnal mixing. These shared attributes may also explain some of the similarities in their output.

Perhaps the most pertinent bias shared by MetROMS and FESOM was their underestimation of total ice shelf basal melting. While observations are still scarce, making true melt rates uncertain, both MetROMS and FESOM fall well outside the range of recent observational estimates for ice shelf basal mass loss integrated over the Antarctic continent. Some of this bias could be explained by the lack of tides in both models. However, the underestimation was most pronounced in the Amundsen and Bellingshausen Sea sectors, where the models were unable to capture observed intrusions of unmodified CDW. This is likely due to a combination of insufficient horizontal resolution (in MetROMS and low-resolution FESOM), spuriously large mixing along sigma coordinate lines (in FESOM), and biases in the atmospheric forcing (*Nakayama et al.*, 2014). Other common biases between the two models included relatively weak ACC transport and insufficient summer sea ice cover.

Two models is the absolute minimum required for an intercomparison, which would ideally comprise a larger number of models. However, it was not realistic to install, configure, and run simulations with more than two models during the course of this PhD. The intercomparison could be expanded if external partners, from a variety of institutions, ran standardised simulations independently and contributed their results to a central database. This procedure occurs in larger intercomparison projects such as CMIP5, as well as the family of OMIPs (Ocean Model Intercomparison Projects) being undertaken on an ungoing basis in the ocean modelling community.

Chapter 3 chronicled the development pathway of the circumpolar Antarctic con-

figuration of MetROMS, with case studies of challenges overcome during the process, and sensitivity studies showing the effects of unsuitable parameterisations. Some of the issues in the simulation were not completely resolved, including a tendency towards unrealistic deep convection in the Weddell Sea, erosion of deep water masses caused by spurious diapycnal mixing, and the inability to adequately simulate tides. A detailed discussion of potential pathways to address these issues was presented in Section 3.10.

One case study was also presented with FESOM, showing the impacts of excessive topographic smoothing resulting from a mishap during mesh generation. Substantial regional differences in water mass properties and ice shelf melt rates were apparent, compared to the high-resolution simulation from Chapter 2 with the corrected mesh. Given this demonstrated sensitivity to topographic smoothing, and keeping in mind that the corrected mesh is still smoother than the MetROMS grid, it would be worth pursuing options to reduce FESOM's smoothing in the future. The simplest course of action would be to reduce the number of passes of the Gaussian filters (as in *Timmermann and Goeller* (2017)), although this may impose stricter requirements on the model timestep. Alternatively, a selective Hanning filter similar to in the ROMS grid (Section 2.2.3) would prevent the topography from being smoothed beyond the minimum requirements for stability at a given length of timestep. It is also possible that a recent reformulation of FESOM's dynamical core (*Danilov et al.*, 2017) requires less topographic smoothing to ensure numerical stability, although this version of the code does not yet include ice shelf cavities.

Chapter 4 demonstrated the relationship between oscillatory ocean tracer advection schemes and spurious sea ice formation, which had never before been explored in the literature, but which presented substantial difficulties for MetROMS. The centered fourth-order and Akima fourth-order advection schemes, unless damped with higher parameterised diffusion, were prone to dispersive error causing spurious supercooling, and subsequently erroneous sea ice formation. As a result, sea ice became thicker and less mobile, coastal polynyas largely disappeared, the water column became increasingly stratified, and the subsurface Winter Water layer was eroded by warm Circumpolar Deep Water. The upwind third-order advection scheme, which is dominated by dissipative rather than dispersive error, was naturally less prone to this problem. Extending the upwind scheme with flux limiters removed all spurious supercooling and provided a baseline for comparison.

In the future, it would be useful to investigate whether other models are affected by this issue to the same extent as MetROMS. There are several reasons to believe that MetROMS is particularly susceptible. First, its terrain-following coordinates tend to equate steep bathymetry with steep horizontal (along-level) gradients in temperature

and salinity, leading to more opportunities for oscillatory advection errors compared to a z-coordinate model. Furthermore, the freeze potential formulation in MetROMS is likely to make sea ice formation especially sensitive to spurious supercooling. MetROMS assumes that supercooled ocean cells instantaneously form frazil ice, so that the supercooling is completely removed from the near-surface ocean every timestep. In other models, the adjustment is more gradual, such as in FESOM where the sea-ice/ocean heat flux is parameterised as a function of the temperature difference and the friction velocity. Although different models may have different levels of sensitivity to this mechanism of error, it has also been identified in at least one z-coordinate model (Xylar Asay-Davis, personal communication), confirming that the problem is not unique to MetROMS.

Chapter 5 presented future projections of ice shelf basal melt rates in FESOM, forced with bias-corrected atmospheric output from CMIP5 models. Based on an rms error analysis over the Southern Ocean, ACCESS 1.0 and the CMIP5 multi-model mean were found to be in best agreement with ERA-Interim. Four 21st-century atmospheric forcing scenarios were constructed for FESOM, and every scenario caused ice shelf basal melting to increase in every sector of Antarctica. Much of this melting, particularly in the Amundsen Sea, was driven by reduced sea ice formation, which caused the water column to stratify and allowed increased transport and preservation of CDW on the continental shelf. A number of other simulated changes were attributed to reduced sea ice formation, including freshening of HSSW, warming of RSBW and WSBW, weakening of the ACC, and strengthening of the Antarctic Coastal Current. However, sea ice formation in the Ross Polynya remained strong enough to largely protect the Ross Ice Shelf cavity from warming, as the heat content of inflowing CDW was eroded by the convection of cold shelf waters.

To date, FESOM remains one of only two ice-shelf/ocean/sea-ice models which have published future projections forced with CMIP output (*Timmermann and Hellmer*, 2013; *Timmermann and Goeller*, 2017; *Hellmer et al.*, 2012, 2017). The other such model is BRIOS (Bremerhaven Regional Ice-Ocean Simulations), a predecessor of FESOM which shares many of the same parameterisations. In order to increase our confidence in these future projections, it would be desirable to produce them using a wider variety of models. However, such models must be suitable for long transient simulations, which is not currently the case for the circumpolar Antarctic configuration of MetROMS. As discussed in Chapter 3, MetROMS' problems with Weddell Sea deep convection and spurious diapycnal mixing would need to be resolved before MetROMS could be considered for century-scale projections.

The other obvious pathway to improve future projections of ice shelf melt rates would be to consider an evolving ice shelf draft. The first such projections with FE-

SOM, coupled asynchronously to the ice sheet model RIMBAY (Revised Ice Model Based on frAnk pattYn), were recently published by *Timmermann and Goeller* (2017). The domain of RIMBAY was restricted to the Filchner-Ronne catchment, and all other ice shelf cavities had static geometry. However, this setup indicates that ice-sheet/ocean coupling over the entire continent is within reach in FESOM. Development is also underway to couple ROMS to the ice sheet model Elmer/Ice (*Gladstone et al.*, 2017), indicating that a long-term goal could be the combination of ROMS, CICE, and Elmer-Ice over a realistic circumpolar domain.

Overall remarks

Comparing the two models used in this thesis, MetROMS tended to perform better on the continental shelf and in ice shelf cavities, while FESOM performed better in the deep ocean. MetROMS' simulated water mass properties, sub-ice shelf circulation, and basal melt patterns were typically in better agreement with observations. However, FESOM exhibited better preservation of deep water masses. Since biases in the deep Southern Ocean will eventually impact the Antarctic continental shelf, the question of which model is "better" largely depends on the length of the simulation considered.

What is the best pathway forward for each model? Chapter 3 noted that improvements to MetROMS should be prioritised based on the types of experiments the model performs in the future. If it is mainly used for present-day process studies on the continental shelf, a proper consideration of tides would be the most useful addition. If MetROMS instead pursues long transient simulations, including future projections, addressing its shortcomings in the deep ocean would be vital. In FESOM, the most pressing issue to rectify is the oversmoothing of topography, as detailed above. Since sub-ice shelf processes are especially sensitive to cavity geometry, a more accurate representation of topography would be expected to improve FESOM's performance in these regions, as well as on the continental shelf.

Using two different models to tackle the same questions yields many insights which would not be reached by using only one. This thesis used two models to study the present-day Antarctic margin, but only one model to project its future behaviour, and one model to investigate the numerical phenomenon of spurious sea ice formation. Ideally, modelling studies would always use at least two models, and intercomparison projects would use many more. However, this goal presents logistical challenges related to time, computational cost, and the clear presentation of results.

Finally, it is the expectation of the author that this field will be radically overhauled

in the coming years, as ice-sheet/ocean coupling continues to advance. Static ice shelves will eventually no longer be the norm, and it will be necessary for all ocean modellers studying ice shelf cavities to have a basic understanding of ice sheet dynamics, rather than considering thermodynamics in isolation. A more complete representation of ocean-cryosphere interactions in both regional and global models will lead to a better understanding of processes on the Antarctic continental shelf, a greater diversity of models suitable for future projections, and ultimately an improved ability to predict and anticipate future sea level rise.

Appendix A

Additional figures for future simulations

Figures 5.5 and 5.6 showed results for the RCP 8.5 MMM simulation. The following are versions of the same figures for the other three RCP simulations.

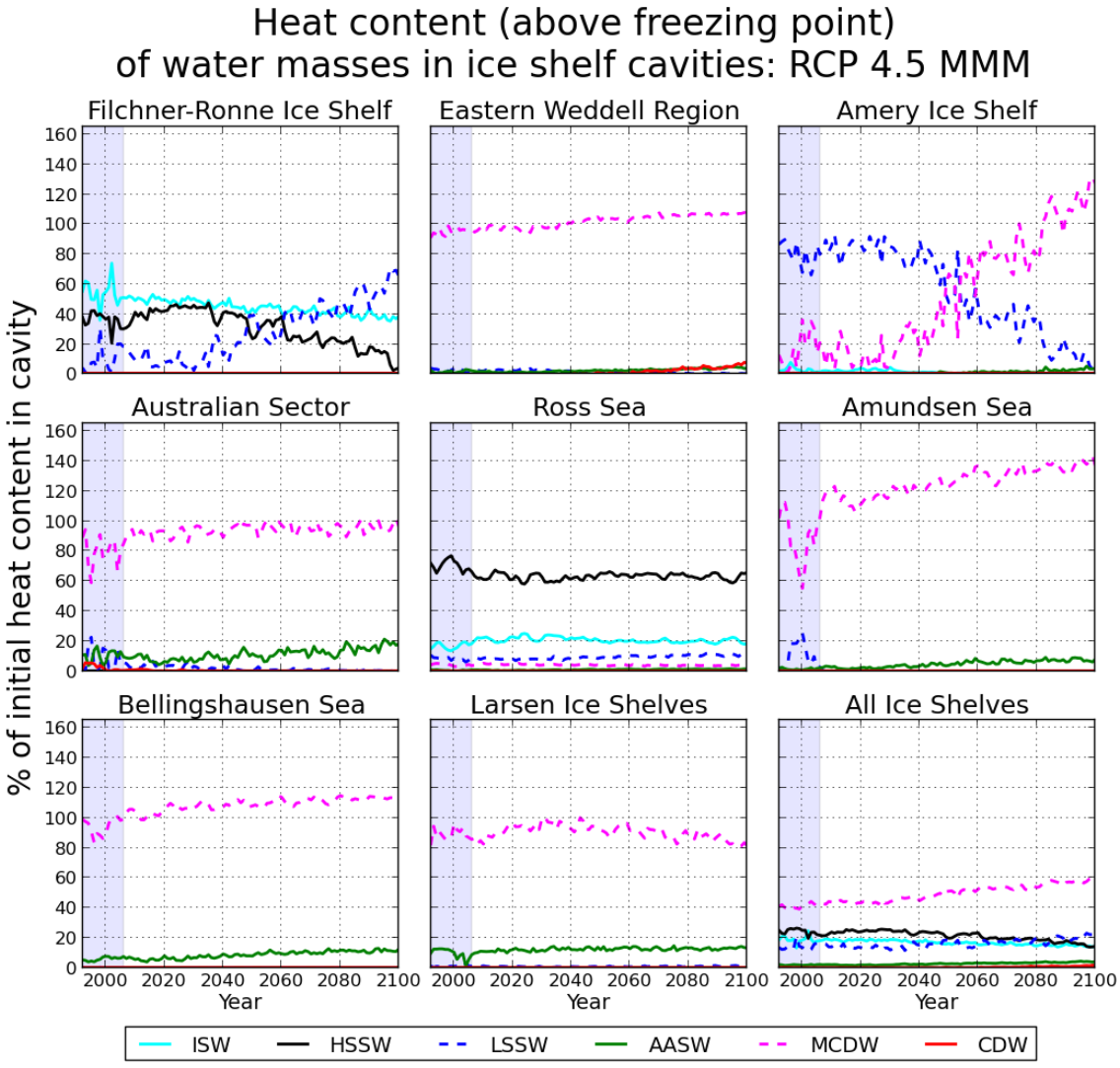

Figure A.1: As Figure 5.5, for the RCP 4.5 MMM simulation.

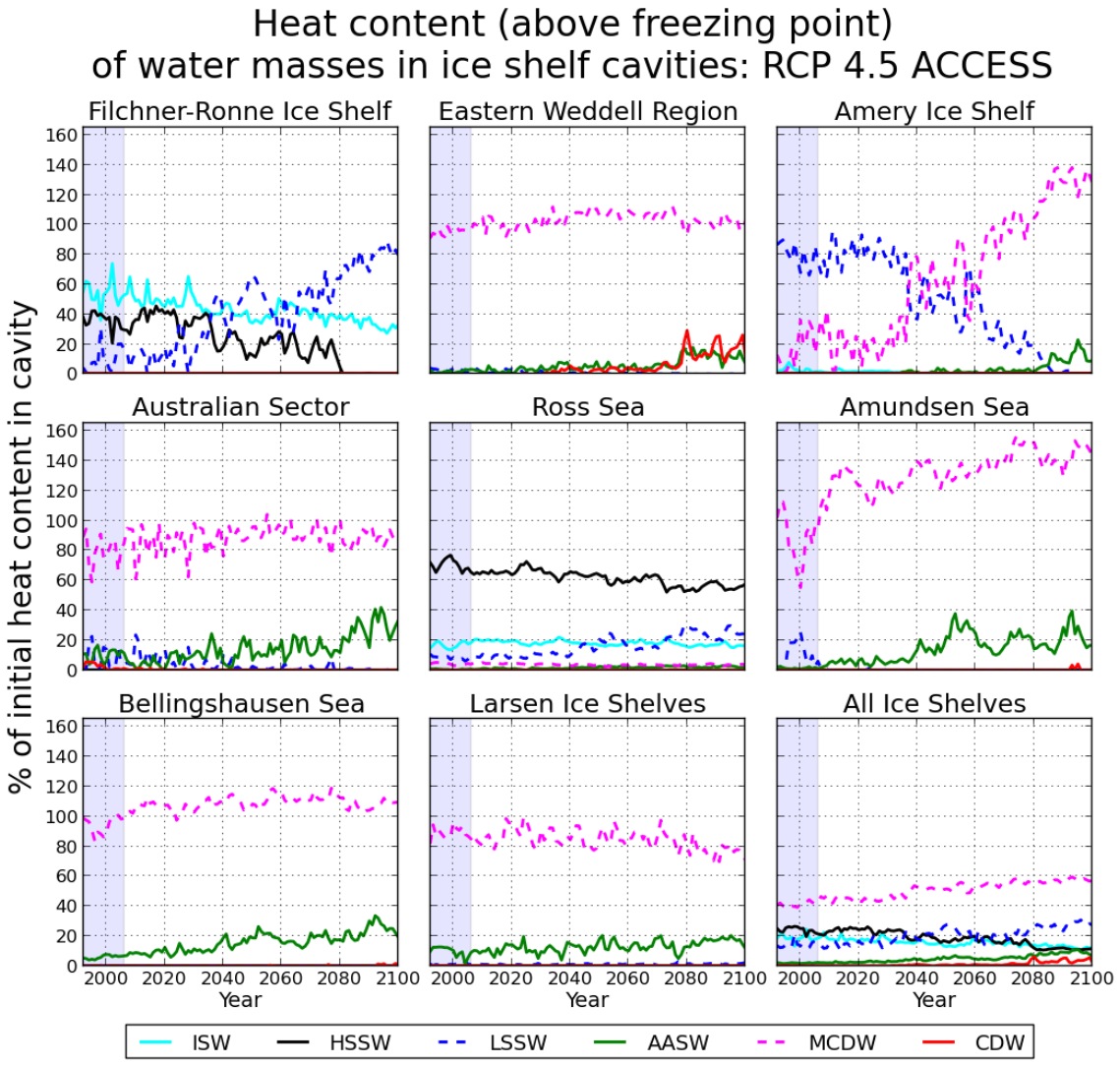

Figure A.2: As Figure 5.5, for the RCP 4.5 ACCESS simulation.

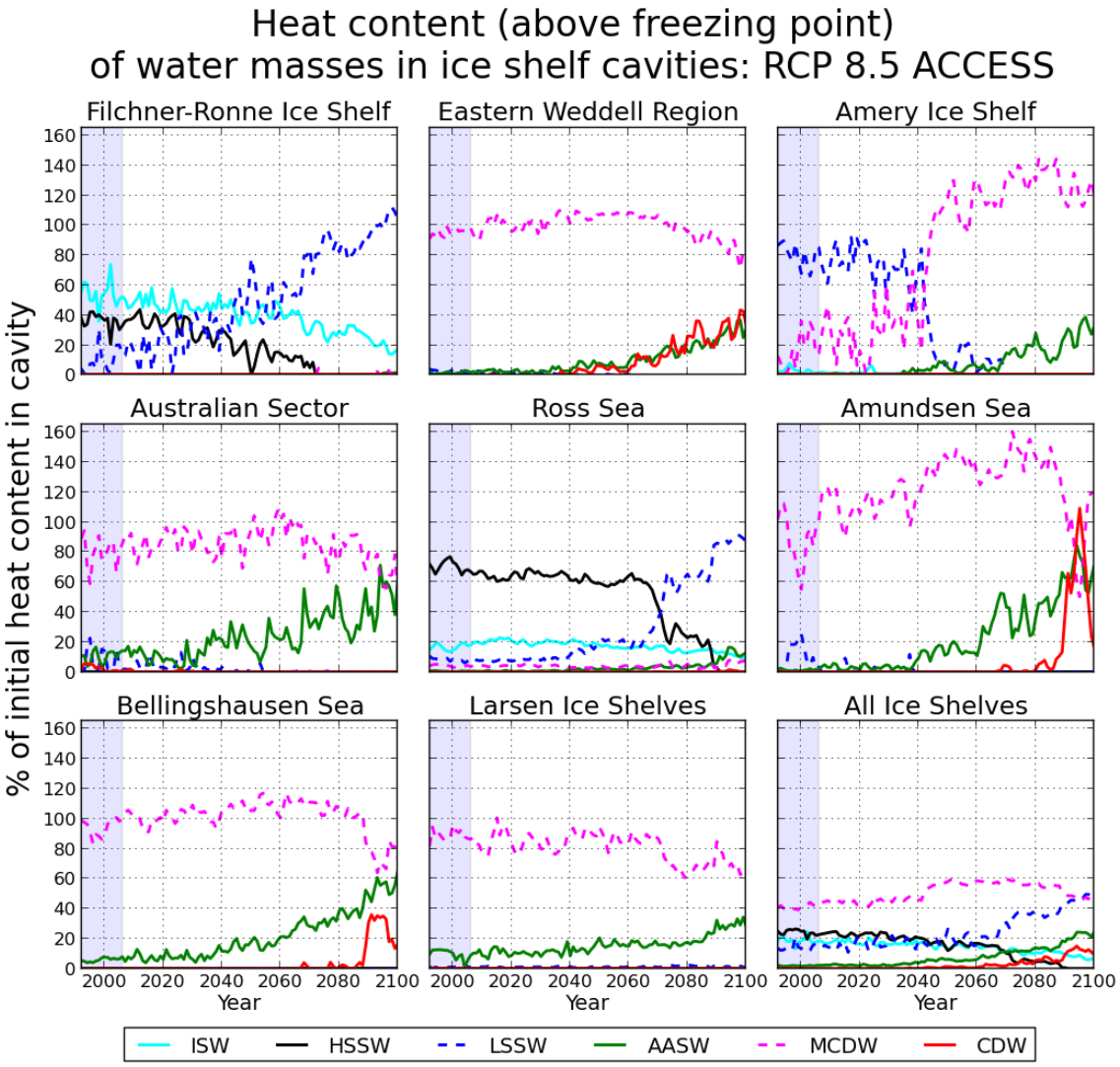

Figure A.3: As Figure 5.5, for the RCP 8.5 ACCESS simulation.

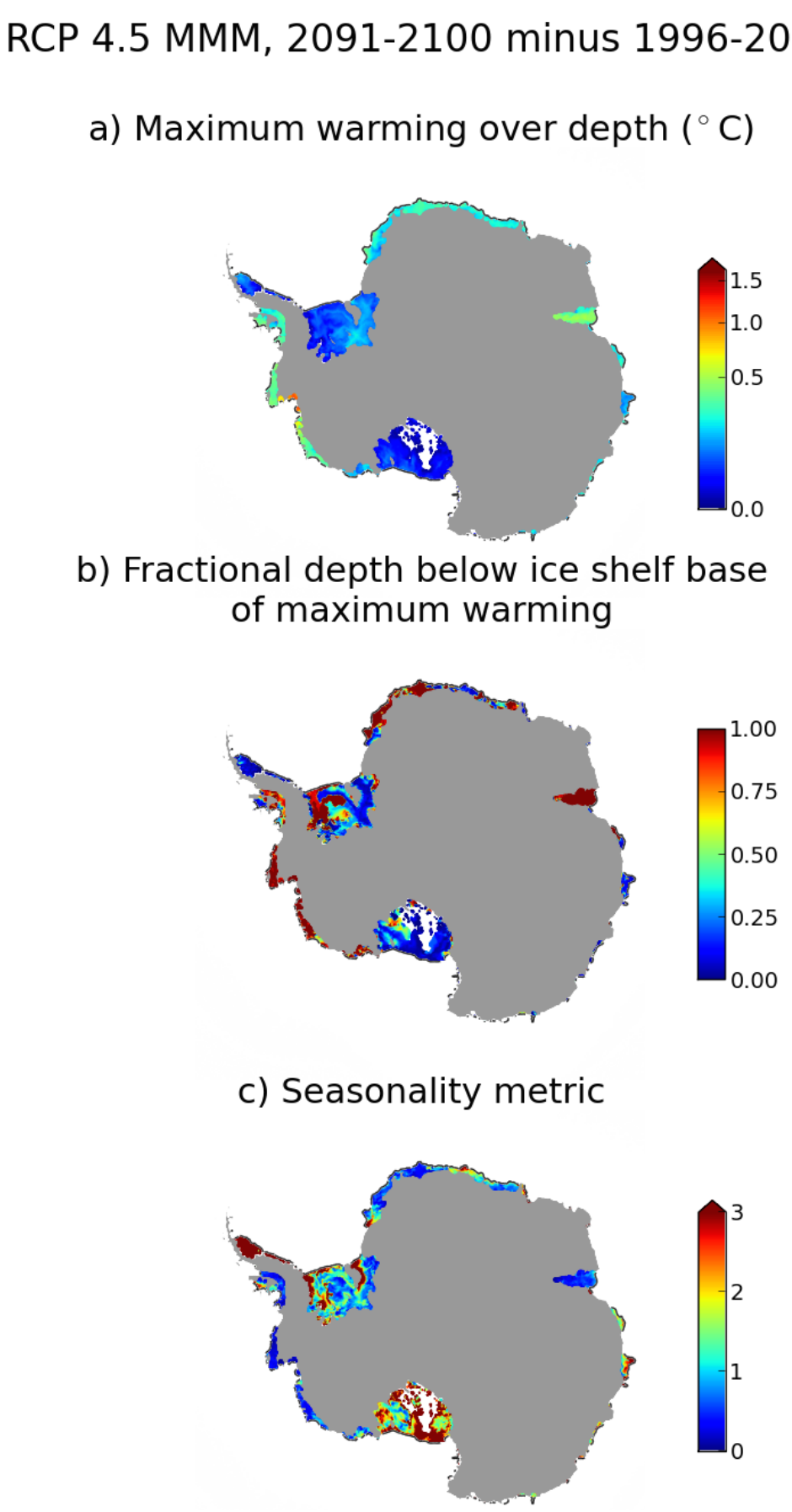

Figure A.4: As Figure 5.6, for the RCP 4.5 MMM simulation.

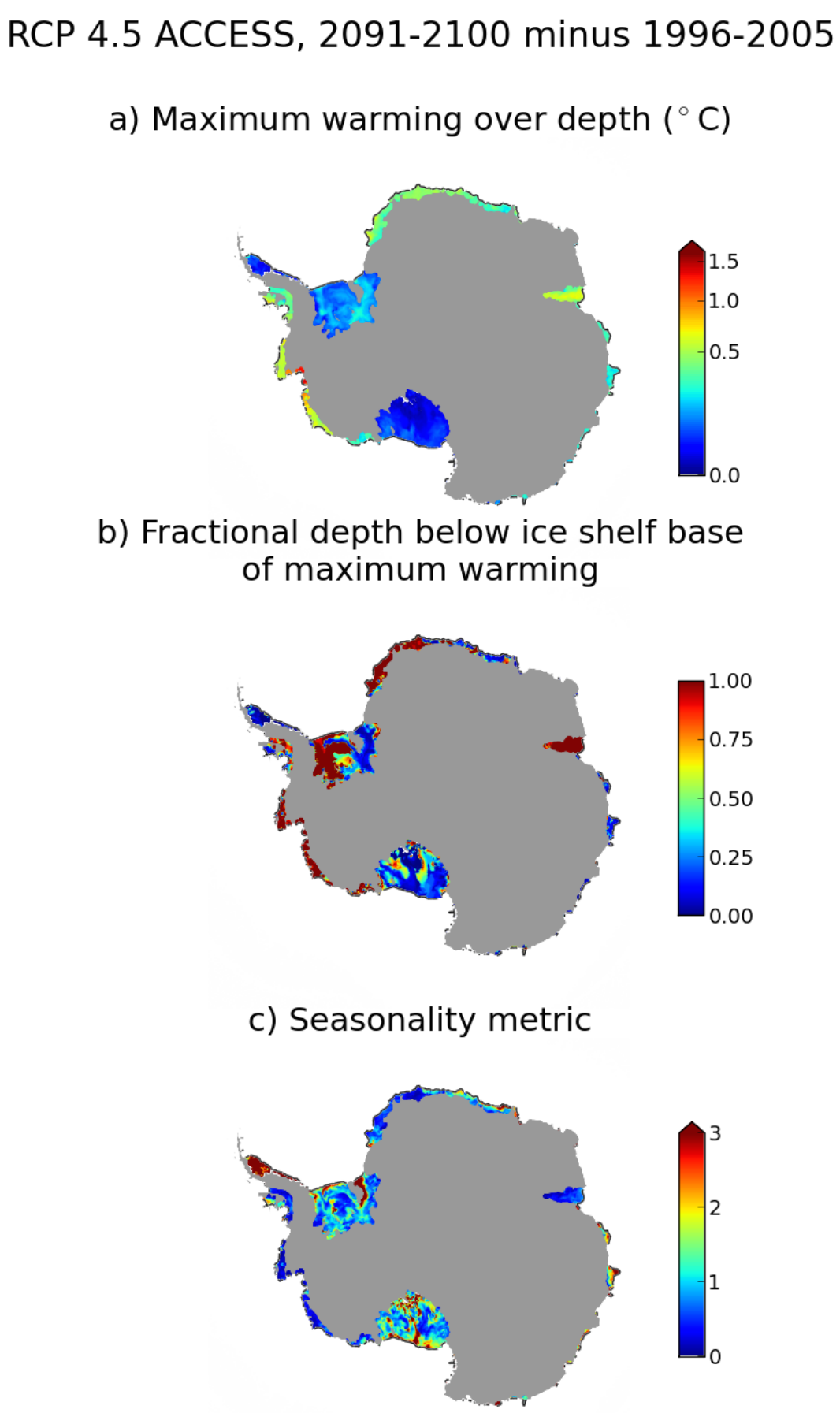

Figure A.5: As Figure 5.6, for the RCP 4.5 ACCESS simulation.

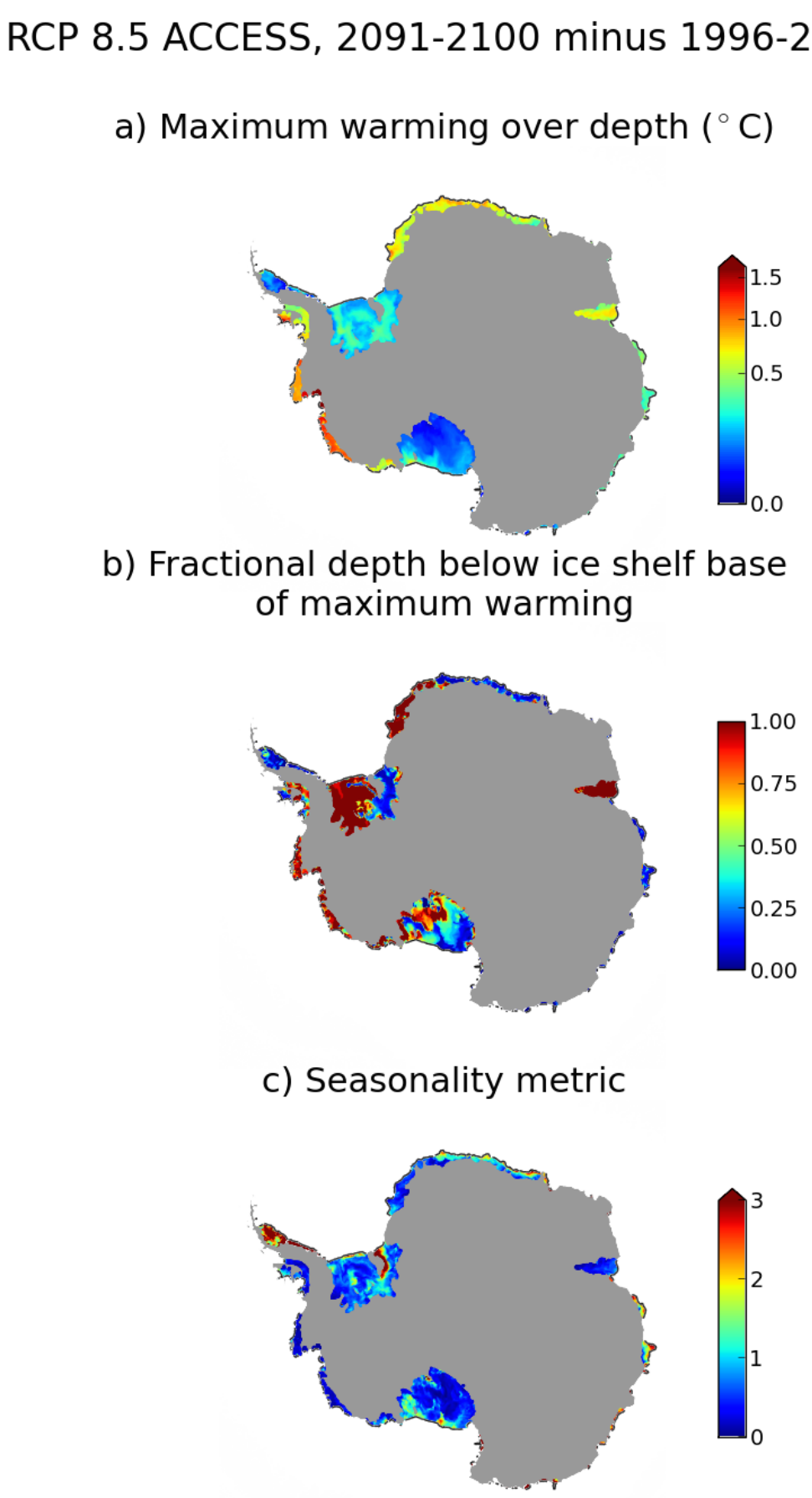

Figure A.6: As Figure 5.6, for the RCP 8.5 ACCESS simulation.

Bibliography

Agosta, C., X. Fettweis, and R. Datta (2015), Evaluation of the CMIP5 models in the aim of regional modelling of the Antarctic surface mass balance, *Cryosphere*, *9*, 2311–2321, doi:10.5194/tc-9-2311-2015.

Aguiar, W., M. M. Mata, and R. Kerr (2017), On the deep convection events and Antarctic Bottom Water formation in ocean reanalysis products, *Ocean Science Discussions*, doi:10.5194/os-2017-9.

Arakawa, A., and V. R. Lamb (1977), Computational design of the basic dynamical processes of the UCLA general circulation model, *Methods in Computational Physics: Advances in Research and Applications*, *17*, 173–265.

Arango, H. G. (2010), ROMS Framework and Algorithms, in *ROMS/TOMS User Workshop*, Honolulu, Hawaii.

Arzeno, I. B., R. C. Beardsley, R. Limeburner, B. Owens, L. Padman, S. R. Springer, C. L. Stewart, and M. J. M. Williams (2014), Ocean variability contributing to basal melt rate near the ice front of Ross Ice Shelf, Antarctica, *Journal of Geophysical Research: Oceans*, *119*, 4214–4233, doi:10.1002/2014JC009792.

Asay-Davis, X. S., S. L. Cornford, G. Durand, B. K. Galton-Fenzi, R. M. Gladstone, G. H. Gudmundsson, T. Hattermann, D. M. Holland, D. Holland, P. R. Holland, D. F. Martin, P. Mathiot, F. Pattyn, and H. Seroussi (2016), Experimental design for three interrelated marine ice sheet and ocean model intercomparison projects: MISMIP v. 3 (MISMIP +), ISOMIP v. 2 (ISOMIP +) and MISOMIP v. 1 (MISOMIP1), *Geoscientific Model Development*, *9*, 2471–2497, doi:10.5194/gmd-9-2471-2016.

Assmann, K. M., H. H. Hellmer, and A. Beckmann (2003), Seasonal variation in circulation and water mass distribution on the Ross Sea continental shelf, *Antarctic Science*, *15*(1), 3–11, doi:10.1017/S0954102003001007.

AVISO (2011), AVISO Level 4 Absolute Dynamic Topography for Climate Model Comparison. Ver. 1., doi:10.5067/DYNTO-1D1M1.

Barthélemy, A., H. Goosse, P. Mathiot, and T. Fichefet (2012), Inclusion of a katabatic wind correction in a coarse-resolution global coupled climate model, *Ocean Modelling*, *48*, 45–54, doi:10.1016/j.ocemod.2012.03.002.

Bodas-Salcedo, A., T. Andrews, A. V. Karmalkar, and M. A. Ringer (2016), Cloud liquid water path and radiative feedbacks over the Southern Ocean, *Geophysical Research Letters*, *43*, 10,938–10,946, doi:10.1002/2016GL070770.

Bouillon, S., T. Fichefet, V. Legat, and G. Madec (2013), The elastic-viscous-plastic method revisited, *Ocean Modelling*, *71*, 2–12, doi:10.1016/j.ocemod.2013.05.013.

Bracegirdle, T. J., E. Shuckburgh, J.-B. Sallée, Z. Wang, A. J. S. Meijers, N. Bruneau, T. Phillips, and L. J. Wilcox (2013), Assessment of surface winds over the Atlantic, Indian, and Pacific Ocean sectors of the Southern Ocean in CMIP5 models: Historical bias, forcing response, and state dependence, *Journal of Geophysical Research: Atmospheres*, *118*, 547–562, doi:10.1002/jgrd.50153.

Brassington, G. B., F. Colberg, K. A. Naughten, K. Fennel, P. Yu, J. Wilkin, and H. G. Arango (2018), Extending the ROMS third-order upwind advection scheme with limiters, *Ocean Modelling*, *draft*.

Briegleb, B. P., and B. Light (2007), A Delta-Eddington multiple scattering parameterization for solar radiation in the sea ice component of the Community Climate System Model: NCAR Tech. Note NCAR/TN-472+STR, *Tech. rep.*, National Center for Atmospheric Research.

Budgell, W. P. (2005), Numerical simulation of ice-ocean variability in the Barents Sea region: Towards dynamical downscaling, *Ocean Dynamics*, *55*, 370–387, doi:10.1007/s10236-005-0008-3.

Cai, W., S. Borlace, M. Lengaigne, P. Van Rensch, M. Collins, G. Vecchi, A. Timmermann, A. Santoso, M. J. Mcphaden, L. Wu, M. H. England, G. Wang, E. Guilyardi, and F. F. Jin (2014), Increasing frequency of extreme El Niño events due to greenhouse warming, *Nature Climate Change*, *4*, 111–116, doi:10.1038/nclimate2100.

Chapman, D. C. (1985), Numerical Treatment of Cross-Shelf Open Boundaries in a Barotropic Coastal Ocean Model, *Journal of Physical Oceanography*, *15*, 1060–1075, doi:10.1175/1520-0485(1985)015⟨1060:NTOCSO⟩2.0.CO;2.

Church, J. A., P. U. Clark, A. Cazenave, J. M. Gregory, S. Jevrejeva, A. Levermann, M. A. Merrifield, G. A. Milne, R. S. Nerem, P. D. Nunn, A. J. Payne, W. T. Pfeffer, D. Stammer, and A. S. Unnikrishnan (2013), Sea Level Change, in *Climate Change*

2013: The Physical Science Basis. Contribution of Working Group I to the Fifth Assessment Report of the Intergovernmental Panel on Climate Change, pp. 1137–1216, Cambridge University Press.

Cook, C. P., T. van de Flierdt, T. Williams, S. R. Hemming, M. Iwai, M. Kobayashi, F. J. Jimenez-Espejo, C. Escutia, J. J. González, B.-K. Khim, R. M. McKay, S. Passchier, S. M. Bohaty, C. R. Riesselman, L. Tauxe, S. Sugisaki, A. L. Galindo, M. O. Patterson, F. Sangiorgi, E. L. Pierce, H. Brinkhuis, A. Klaus, A. Fehr, J. A. P. Bendle, P. K. Bijl, S. A. Carr, R. B. Dunbar, J. A. Flores, T. G. Hayden, K. Katsuki, G. S. Kong, M. Nakai, M. P. Olney, S. F. Pekar, J. Pross, U. Röhl, T. Sakai, P. K. Shrivastava, C. E. Stickley, S. Tuo, K. Welsh, and M. Yamane (2013), Dynamic behaviour of the East Antarctic ice sheet during Pliocene warmth, *Nature Geoscience*, *6*, 765–769, doi:10.1038/ngeo1889.

Cougnon, E. A., B. K. Galton-Fenzi, A. J. S. Meijers, and B. Legrésy (2013), Modeling interannual dense shelf water export in the region of the Mertz Glacier Tongue (1992-2007), *Journal of Geophysical Research: Oceans*, *118*, 5858–5872, doi:10.1002/2013JC008790.

Cunningham, S. A., S. G. Alderson, B. A. King, and M. A. Brandon (2003), Transport and variability of the Antarctic Circumpolar Current in Drake Passage, *Journal of Geophysical Research*, *108*(C5), 8084, doi:10.1029/2001JC001147.

Danilov, S., Q. Wang, R. Timmermann, N. Iakovlev, D. Sidorenko, M. Kimmritz, T. Jung, and J. Schröter (2015), Finite-Element Sea Ice Model (FESIM), version 2, *Geoscientific Model Development*, *8*, 1747–1761, doi:10.5194/gmd-8-1747-2015.

Danilov, S., D. Sidorenko, Q. Wang, and T. Jung (2017), The Finite-volumE Sea ice-Ocean Model (FESOM2), *Geoscientific Model Development*, *10*, 765–789, doi:10.5194/gmd-10-765-2017.

De Rydt, J., and G. H. Gudmundsson (2016), Coupled ice shelf-ocean modeling and complex grounding line retreat from a seabed ridge, *Journal of Geophysical Research: Earth Surface*, *121*, 865–880, doi:10.1002/2015JF003791.

Debernard, J. B., N. M. Kristensen, S. Maartensson, K. Wang, and G. A. Waagbo (2017), metno/metroms: Intermediate release, doi:10.5281/zenodo.290667.

Deconto, R. M., and D. Pollard (2016), Contribution of Antarctica to past and future sea-level rise, *Nature*, *531*, 591–597, doi:10.1038/nature17145.

Dee, D. P., S. M. Uppala, A. J. Simmons, P. Berrisford, P. Poli, S. Kobayashi, U. Andrae, M. A. Balmaseda, G. Balsamo, P. Bauer, P. Bechtold, A. C. M. Beljaars, L. van de Berg, J. Bidlot, N. Bormann, C. Delsol, R. Dragani, M. Fuentes,

A. J. Geer, L. Haimberger, S. B. Healy, H. Hersbach, E. V. Hólm, L. Isaksen, P. Kållberg, M. Köhler, M. Matricardi, A. P. McNally, B. M. Monge-Sanz, J. J. Morcrette, B. K. Park, C. Peubey, P. de Rosnay, C. Tavolato, J. N. Thépaut, and F. Vitart (2011), The ERA-Interim reanalysis: configuration and performance of the data assimilation system, *Quarterly Journal of the Royal Meteorological Society*, *137*, 553–597, doi:10.1002/qj.828.

Depoorter, M. A., J. L. Bamber, J. A. Griggs, J. T. M. Lenaerts, S. R. M. Ligtenberg, M. R. van den Broeke, and G. Moholdt (2013), Calving fluxes and basal melt rates of Antarctic ice shelves, *Nature*, *502*, 89–92, doi:10.1038/nature12567.

Dinniman, M. S., J. M. Klinck, and W. O. Smith (2011), A model study of Circumpolar Deep Water on the West Antarctic Peninsula and Ross Sea continental shelves, *Deep Sea Research II*, *58*, 1508–1523, doi:10.1016/j.dsr2.2010.11.013.

Dinniman, M. S., J. M. Klinck, L.-S. Bai, D. H. Bromwich, K. M. Hines, and D. M. Holland (2015), The Effect of Atmospheric Forcing Resolution on Delivery of Ocean Heat to the Antarctic Floating Ice Shelves, *Journal of Climate*, *28*, 6067–6085, doi:10.1175/JCLI-D-14-00374.1.

Dinniman, M. S., X. S. Asay-Davis, B. K. Galton-Fenzi, P. R. Holland, and A. Jenkins (2016), Modeling Ice Shelf/Ocean Interaction in Antarctica: a review, *Oceanography*, *29*(4), 144–153, doi:10.5670/oceanog.2016.106.

Donat-Magnin, M., N. C. Jourdain, P. Spence, J. Le Sommer, H. Gallée, and G. Durand (2017), Ice-Shelf Melt Response to Changing Winds and Glacier Dynamics in the Amundsen Sea Sector, Antarctica, *Journal of Geophysical Research: Oceans*, *122*, 10,206–10,224, doi:10.1002/2017JC013059.

Donohue, K. A., K. L. Tracey, D. R. Watts, M. P. Chidichimo, and T. K. Chereskin (2016), Mean Antarctic Circumpolar Current transport measured in Drake Passage, *Geophysical Research Letters*, *43*, 11,760–11,767, doi:10.1002/2016GL070319.

Downes, S. M., R. Farneti, P. Uotila, S. M. Griffies, S. J. Marsland, D. Bailey, E. Behrens, M. Bentsen, D. Bi, A. Biastoch, C. Böning, A. Bozec, V. M. Canuto, E. P. Chassignet, G. Danabasoglu, S. Danilov, N. Diansky, H. Drange, P. G. Fogli, A. Gusev, A. Howard, M. Ilicak, T. Jung, M. Kelley, W. G. Large, A. Leboissetier, M. Long, J. Lu, S. Masina, A. Mishra, A. Navarra, A. J. George Nurser, L. Patara, B. L. Samuels, D. Sidorenko, P. Spence, H. Tsujino, Q. Wang, and S. G. Yeager (2015), An assessment of Southern Ocean water masses and sea ice during 1988-2007 in a suite of interannual CORE-II simulations, *Ocean Modelling*, *94*, 67–94, doi:10.1016/j.ocemod.2015.07.022.

Dupont, T. K., and R. B. Alley (2005), Assessment of the importance of ice-shelf buttressing to ice-sheet flow, *Geophysical Research Letters*, *32*, L04503, doi:10.1029/2004GL022024.

Dutrieux, P., J. De Rydt, A. Jenkins, P. R. Holland, H. K. Ha, S. H. Lee, E. J. Steig, Q. Ding, E. P. Abrahamsen, and M. Schröder (2014), Strong sensitivity of Pine Island ice-shelf melting to climatic variability, *Science*, *343*, 174–178, doi:10.1126/science.1244341.

Dutton, A., A. E. Carlson, A. J. Long, G. A. Milne, P. U. Clark, R. M. Deconto, B. P. Horton, S. Rahmstorf, and M. E. Raymo (2015), Sea-level rise due to polar ice-sheet mass loss during past warm periods, *Science*, *349*(6244), aaa4019, doi:10.1126/science.aaa4019.

England, M. H. (1993), Representing the Global-Scale Water Masses in Ocean General Circulation Models, *Journal of Physical Oceanography*, *23*, 1523–1552, doi:10.1175/1520-0485(1993)023⟨1523:RTGSWM⟩2.0.CO;2.

England, M. H., J. S. Godfrey, A. C. Hirst, and M. Tomczak (1993), The Mechanism for Antarctic Intermediate Water Renewal in a World Ocean Model, *Journal of Physical Oceanography*, *23*, 1553–1560, doi:10.1175/1520-0485(1993)023⟨1553:TMFAIW⟩2.0.CO;2.

Engwirda, D., M. Kelley, and J. Marshall (2017), High-order accurate finite-volume formulations for the pressure gradient force in layered ocean models, *Ocean Modelling*, *116*, 1–15, doi:10.1016/j.ocemod.2017.05.003.

Fairall, C. W., E. F. Bradley, D. P. Rogers, J. B. Edson, and G. S. Young (1996), Bulk parameterization of air-sea fluxes for Tropical Ocean-Global Atmosphere Coupled-Ocean Atmosphere Response Experiment, *Journal of Geophysical Research*, *101*(C2), 3747–3764, doi:10.1029/95JC03205.

Farrow, D. E., and D. P. Stevens (1995), A New Tracer Advection Scheme for Bryan and Cox Type Ocean General Circulation Models, *Journal of Physical Oceanography*, *25*, 1731–1741.

Feldmann, J., and A. Levermann (2015), Collapse of the West Antarctic Ice Sheet after local destabilization of the Amundsen Basin, *Proceedings of the National Academy of Sciences*, *112*(46), 14,191–14,196, doi:10.1073/pnas.1512482112.

Fetterrer, F., K. Knowles, W. Meier, and M. Savoie (2016), Sea Ice Index, Version 2, doi:10.7265/N5736NV7.

Fetterrer, F., K. Knowles, W. Meier, M. Savoie, and A. K. Windnagel (2017), Sea Ice Index, Version 3, doi:10.7265/N5K072F8.

Flather, R. (1976), A tidal model of the northwest European continental shelf, *Memoires de la Societe Royale de Sciences de Liege*, *6*, 141–164.

Foldvik, A., J. H. Middleton, and T. D. Foster (1990), The tides of the southern Weddell Sea, *Deep Sea Research*, *37*(8), 1345–1362, doi:10.1016/0198-0149(90)90047-Y.

Foldvik, A., T. Gammelsrød, S. Østerhus, E. Fahrbach, G. Rohart, M. Schröder, K. W. Nicholls, L. Padman, and R. A. Woodgate (2004), Ice shelf water overflow and bottom water formation in the southern Weddell Sea, *Journal of Geophysical Research*, *109*, C02015, doi:10.1029/2003JC002008.

Fraser, A. D., R. A. Massom, K. J. Michael, B. K. Galton-Fenzi, and J. L. Lieser (2012), East Antarctic Landfast Sea Ice Distribution and Variability, 2000-08, *Journal of Climate*, *25*, 1137–1156, doi:10.1175/JCLI-D-10-05032.1.

Fretwell, P., H. D. Pritchard, D. G. Vaughan, J. L. Bamber, N. E. Barrand, R. Bell, C. Bianchi, R. G. Bingham, D. D. Blankenship, G. Casassa, G. Catania, D. Callens, H. Conway, A. J. Cook, H. F. J. Corr, D. Damaske, V. Damm, F. Ferraccioli, R. Forsberg, S. Fujita, Y. Gim, P. Gogineni, J. A. Griggs, R. C. A. Hindmarsh, P. Holmlund, J. W. Holt, R. W. Jacobel, A. Jenkins, W. Jokat, T. Jordan, E. C. King, J. Kohler, W. Krabill, M. Riger-Kusk, K. A. Langley, G. Leitchenkov, C. Leuschen, B. P. Luyendyk, K. Matsuoka, J. Mouginot, F. O. Nitsche, Y. Nogi, O. A. Nøst, S. V. Popov, E. J. Rignot, D. M. Rippin, A. Rivera, J. L. Roberts, N. Ross, M. J. Siegert, A. M. Smith, D. Steinhage, M. Studinger, B. Sun, B. K. Tinto, B. C. Welch, D. Wilson, D. A. Young, C. Xiangbin, and A. Zirizzotti (2013), Bedmap2: Improved ice bed, surface and thickness datasets for Antarctica, *The Cryosphere*, *7*, 375–393, doi:10.5194/tc-7-375-2013.

Gade, H. G. (1979), Melting of Ice in Sea Water: A Primitive Model with Application to the Antarctic Ice Shelf and Icebergs, *Journal of Physical Oceanography*, *9*, 189–198, doi:10.1175/1520-0485(1979)009⟨0189:MOIISW⟩2.0.CO;2.

Galton-Fenzi, B. K. (2009), Modelling Ice-Shelf/Ocean Interaction, Ph.D. thesis, University of Tasmania.

Galton-Fenzi, B. K., C. Maraldi, R. Coleman, and J. R. Hunter (2008), The cavity under the Amery Ice Shelf, East Antarctica, *Journal of Glaciology*, *54*(188), 881–887, doi:10.3189/002214308787779898.

Galton-Fenzi, B. K., J. R. Hunter, R. Coleman, S. J. Marsland, and R. C. Warner (2012), Modeling the basal melting and marine ice accretion of the Amery Ice Shelf, *Journal of Geophysical Research*, *117*, C09031, doi:10.1029/2012JC008214.

Gent, P. R., and J. C. McWilliams (1990), Isopycnal Mixing in Ocean Circulation Models, *Journal of Physical Oceanography*, *20*, 150–155, doi:10.1175/1520-0485(1990)020⟨0150:IMIOCM⟩2.0.CO;2.

Gent, P. R., J. Willebrand, T. J. McDougall, and J. C. McWilliams (1995), Parameterizing Eddy-Induced Tracer Transports in Ocean Circulation Models, *Journal of Physical Oceanography*, *25*, 463–474, doi:10.1175/1520-0485(1995)025⟨0463:PEITTI⟩2.0.CO;2.

Gerdes, R., C. Köberle, and J. Willebrand (1991), The influence of numerical advection schemes on the results of ocean general circulation models, *Climate Dynamics*, *5*, 211–226.

Gladstone, R. M., L. Jong, B. K. Galton-Fenzi, D. E. Gwyther, and J. C. Moore (2017), Simulating the interactions between marine ice sheets and their surrounding oceans, in *Forum for Research into Ice Shelf Processes*, Bergen, Norway.

Gleckler, P. J., K. E. Taylor, and C. Doutriaux (2008), Performance metrics for climate models, *Journal of Geophysical Research*, *113*, D06104, doi:10.1029/2007JD008972.

Golledge, N. R., D. E. Kowalewski, T. R. Naish, R. H. Levy, C. J. Fogwill, and E. G. W. Gasson (2015), The multi-millennial Antarctic commitment to future sea-level rise, *Nature*, *526*, 421–425, doi:10.1038/nature15706.

Golledge, N. R., R. H. Levy, R. M. McKay, and T. R. Naish (2017), East Antarctic ice sheet most vulnerable to Weddell Sea warming, *Geophysical Research Letters*, *44*, 2343–2351, doi:10.1002/2016GL072422.

Goosse, H., and T. Fichefet (2001), Open-ocean convection and polynya formation in a large-scale ice-ocean model, *Tellus*, *53A*, 94–111, doi:10.1034/j.1600-0870.2001.01061.x.

Gordon, A. L. (1978), Deep Antarctic Convection West of Maud Rise, *Journal of Physical Oceanography*, *8*, 600–612, doi:10.1175/1520-0485(1978)008⟨0600:DACWOM⟩2.0.CO;2.

Gordon, A. L., B. A. Huber, and J. Busecke (2015), Bottom water export from the western Ross Sea, 2007 through 2010, *Geophysical Research Letters*, *42*, 5387–5394, doi:10.1002/2015GL064457.

Graham, J. A., M. S. Dinniman, and J. M. Klinck (2016), Impact of model resolution for on-shelf heat transport along the West Antarctic Peninsula, *Journal of Geophysical Research: Oceans*, *121*, 7880–7897, doi:10.1002/2016JC011875.

Greenbaum, J. S., D. D. Blankenship, D. A. Young, T. G. Richter, J. L. Roberts, A. R. A. Aitken, B. Legrésy, D. M. Schroeder, R. C. Warner, T. D. van Ommen, and M. J. Siegert (2015), Ocean access to a cavity beneath Totten Glacier in East Antarctica, *Nature Geoscience*, *8*, 294–298, doi:10.1038/NGEO2388.

Griffies, S. M., and R. W. Hallberg (2000), Biharmonic Friction with a Smagorinsky-Like Viscosity for Use in Large-Scale Eddy-Permitting Ocean Models, *Monthly Weather Review*, *128*, 2935–2946, doi:10.1175/1520-0493(2000)128⟨2935:BFWASL⟩2.0.CO;2.

Griffies, S. M., C. Böning, F. O. Bryan, E. P. Chassignet, R. Gerdes, H. Hasumi, A. C. Hirst, A.-M. Treguier, and D. Webb (2000), Developments in ocean climate modelling, *Ocean Modelling*, *2*, 123–192, doi:10.1016/S1463-5003(00)00014-7.

Griffies, S. M., A. Biastoch, C. Böning, F. O. Bryan, G. Danabasoglu, E. P. Chassignet, M. H. England, R. Gerdes, H. Haak, R. W. Hallberg, W. Hazeleger, J. H. Jungclaus, W. G. Large, G. Madec, A. Pirani, B. L. Samuels, M. Scheinert, A. Sen Gupta, C. A. Severijns, H. L. Simmons, A.-M. Treguier, M. Winton, S. G. Yeager, and J. Yin (2009), Coordinated Ocean-ice Reference Experiments (COREs), *Ocean Modelling*, *26*, 1–46, doi:10.1016/j.ocemod.2008.08.007.

Gwyther, D. E. (2016), Modelling regional ice shelf/ocean interaction with ROMS, in *ROMS Asia-Pacific Workshop*, Hobart, Australia.

Gwyther, D. E., B. K. Galton-Fenzi, J. R. Hunter, and J. L. Roberts (2014), Simulated melt rates for the Totten and Dalton ice shelves, *Ocean Science*, *10*, 267–279, doi:10.5194/os-10-267-2014.

Gwyther, D. E., B. K. Galton-Fenzi, M. S. Dinniman, J. L. Roberts, and J. R. Hunter (2015), The effect of basal friction on melting and freezing in ice shelf-ocean models, *Ocean Modelling*, *95*, 38–52, doi:10.1016/j.ocemod.2015.09.004.

Gwyther, D. E., E. A. Cougnon, B. K. Galton-Fenzi, J. L. Roberts, J. R. Hunter, and M. S. Dinniman (2016), Modelling the response of ice shelf basal melting to different ocean cavity environmental regimes, *Annals of Glaciology*, *57*(73), 131–141, doi:10.1017/aog.2016.31.

Haas, C., M. Nicolaus, S. Willmes, A. P. Worby, and D. Flinspach (2008), Sea ice and snow thickness and physical properties of an ice floe in the western Weddell

Sea and their changes during spring warming, *Deep-Sea Research Part II*, *55*, 963–974, doi:10.1016/j.dsr2.2007.12.020.

Haidvogel, D. B., and A. Beckmann (1999), *Numerical Ocean Circulation Modeling*, Imperial College Press, London.

Haney, R. L. (1991), On the Pressure Gradient Force over Steep Topography in Sigma Coordinate Ocean Models, *Journal of Physical Oceanography*, *21*, 610–619, doi:10.1175/1520-0485(1991)021⟨0610:OTPGFO⟩2.0.CO;2.

Hattermann, T., and A. Levermann (2010), Response of Southern Ocean circulation to global warming may enhance basal ice shelf melting around Antarctica, *Climate Dynamics*, *35*, 741–756, doi:10.1007/s00382-009-0643-3.

Hattermann, T., O. A. Nøst, J. M. Lilly, and L. H. Smedsrud (2012), Two years of oceanic observations below the Fimbul Ice Shelf, Antarctica, *Geophysical Research Letters*, *39*, L12605, doi:10.1029/2012GL051012.

Hecht, M. W. (2010), Cautionary tales of persistent accumulation of numerical error: Dispersive centered advection, *Ocean Modelling*, *35*, 270–276, doi:10.1016/j.ocemod.2010.07.005.

Hecht, M. W., B. A. Wingate, and P. Kassis (2000), A better, more discriminating test problem for ocean tracer transport, *Ocean Modelling*, *2*, 1–15, doi:10.1016/S1463-5003(00)00004-4.

Hellmer, H. H., and D. J. Olbers (1989), A two-dimensional model for the thermohaline circulation under an ice shelf, *Antarctic Science*, *1*(4), 325–336, doi:10.1017/S0954102089000490.

Hellmer, H. H., S. S. Jacobs, and A. Jenkins (1998), Oceanic erosion of a floating Antarctic glacier in the Amundsen Sea, in *Ocean, Ice, and Atmosphere: Interactions at the Antarctic Continental Margin*, edited by S. S. Jacobs and R. F. Weiss, pp. 319–339, American Geophysical Union, Washington, D.C., doi:10.1029/AR075p0341.

Hellmer, H. H., F. Kauker, R. Timmermann, J. Determann, and J. Rae (2012), Twenty-first-century warming of a large Antarctic ice-shelf cavity by a redirected coastal current., *Nature*, *485*, 225–228, doi:10.1038/nature11064.

Hellmer, H. H., F. Kauker, R. Timmermann, and T. Hattermann (2017), The Fate of the Southern Weddell Sea Continental Shelf in a Warming Climate, *Journal of Climate*, *30*, 4337–4350, doi:10.1175/JCLI-D-16-0420.1.

Herraiz-Borreguero, L., J. A. Church, I. Allison, B. Pena-Molino, R. Coleman, M. Tomczak, and M. Craven (2016), Basal melt, seasonal water mass transformation, ocean current variability, and deep convection processes along the Amery Ice Shelf, *Journal of Geophysical Research: Oceans*, *121*, 4946–4965, doi: 10.1002/2016JC011858.

Heuzé, C., K. J. Heywood, D. P. Stevens, and J. K. Ridley (2013), Southern Ocean bottom water characteristics in CMIP5 models, *Geophysical Research Letters*, *40*, 1409–1414, doi:10.1002/grl.50287.

Heuzé, C., J. K. Ridley, D. Calvert, D. P. Stevens, and K. J. Heywood (2015), Increasing vertical mixing to reduce Southern Ocean deep convection in NEMO3.4, *Geoscientific Model Development*, *8*, 3119–3130, doi:10.5194/gmd-8-3119-2015.

Hogg, A. E., and G. H. Gudmundsson (2017), Impacts of the Larsen-C Ice Shelf calving event, *Nature Climate Change*, *7*, 540–542, doi:10.1038/nclimate3359.

Holland, D. M., and A. Jenkins (1999), Modeling Thermodynamic Ice-Ocean Interactions at the Base of an Ice Shelf, *Journal of Physical Oceanography*, *29*, 1787–1800, doi:10.1175/1520-0485(1999)029⟨1787:MTIOIA⟩2.0.CO;2.

Holland, P. R., H. F. J. Corr, D. G. Vaughan, A. Jenkins, and P. Skvarca (2009), Marine ice in Larsen Ice Shelf, *Geophysical Research Letters*, *36*, L11604, doi: 10.1029/2009GL038162.

Holland, P. R., N. Bruneau, C. Enright, M. Losch, N. T. Kurtz, and R. Kwok (2014), Modeled trends in Antarctic Sea Ice Thickness, *Journal of Climate*, *27*, 3784–3801, doi:10.1175/JCLI-D-13-00301.1.

Hunke, E. C., and J. K. Dukowicz (1997), An Elastic-Viscous-Plastic Model for Sea Ice Dynamics, *Journal of Physical Oceanography*, *27*, 1849–1867, doi:10.1175/1520-0485(1997)027⟨1849:AEVPMF⟩2.0.CO;2.

Hunke, E. C., D. A. Hebert, and O. Lecomte (2013), Level-ice melt ponds in the Los Alamos sea ice model, CICE, *Ocean Modelling*, *71*, 26–42, doi:10.1016/j.ocemod.2012.11.008.

Hunke, E. C., W. H. Lipscomb, A. K. Turner, N. Jeffery, and S. Elliott (2015), CICE: the Los Alamos Sea Ice Model Documentation and Software User's Manual LA-CC-06-012, *Tech. rep.*, Los Alamos National Laboratory.

Hunter, J. R. (2006), Specification for Test Models of Ice Shelf Cavities, *Tech. rep.*, Antarctic Climate & Ecosystems Cooperative Research Centre.

Jacob, R., J. Larson, and E. Ong (2005), M x N Communication and Parallel Interpolation in Community Climate System Model Version 3 Using the Model Coupling Toolkit, *International Journal of High Performance Computing Applications*, *19*(3), 293–307, doi:10.1177/1094342005056116.

Jacobs, S. S. (2004), Bottom water production and its links with the thermohaline circulation, *Antarctic Science*, *16*(4), 427–437, doi:10.1017/S095410200400224X.

Jacobs, S. S., and J. C. Comiso (1989), Sea Ice and Oceanic Processes on the Ross Sea Continental Shelf, *Journal of Geophysical Research*, *94*(C12), 18,195–18,211, doi:10.1029/JC094iC12p18195.

Jacobs, S. S., A. L. Gordon, and J. L. Ardai (1979), Circulation and melting beneath the Ross Ice Shelf, *Science*, *203*, 439–443, doi:10.1126/science.203.4379.439.

Jacobs, S. S., H. H. Hellmer, C. S. M. Doake, A. Jenkins, and R. M. Frolich (1992), Melting of ice shelves and the mass balance of Antarctica, *Journal of Glaciology*, *38*(130), 375–387, doi:10.3189/S0022143000002252.

Jacobs, S. S., A. Jenkins, C. F. Giulivi, and P. Dutrieux (2011), Stronger ocean circulation and increased melting under Pine Island Glacier ice shelf, *Nature Geoscience*, *4*, 519–523, doi:10.1038/ngeo1188.

Jenkins, A. (1991), A One-Dimensional Model of Ice Shelf-Ocean Interaction, *Journal of Geophysical Research*, *96*(C11), 20,671–20,677, doi:10.1029/91JC01842.

Jenkins, A. (2011), Convection-Driven Melting near the Grounding Lines of Ice Shelves and Tidewater Glaciers, *Journal of Physical Oceanography*, *41*, 2279–2294, doi:10.1175/JPO-D-11-03.1.

Jenkins, A. (2016), A Simple Model of the Ice Shelf-Ocean Boundary Layer and Current, *Journal of Physical Oceanography*, *46*, 1785–1803, doi:10.1175/JPO-D-15-0194.1.

Jenkins, A., and S. S. Jacobs (2008), Circulation and melting beneath George VI Ice Shelf, Antarctica, *Journal of Geophysical Research*, *113*, C04013, doi:10.1029/2007JC004449.

Jenkins, A., P. Dutrieux, S. S. Jacobs, S. D. McPhail, J. R. Perrett, A. T. Webb, and D. White (2010), Observations beneath Pine Island Glacier in West Antarctica and implications for its retreat, *Nature Geoscience*, *3*, 468–472, doi:10.1038/ngeo890.

Jordan, J. R., P. R. Holland, D. Goldberg, K. Snow, R. Arthern, P. Heimbach, and A. Jenkins (2017), Ocean-Forced Ice-Shelf Thinning in a Synchronously Coupled Ice-Ocean Model, *Journal of Geophysical Research: Oceans*, *accepted*, doi:10.1002/2017JC013251.

Joughin, I., and R. B. Alley (2011), Stability of the West Antarctic ice sheet in a warming world, *Nature Geoscience*, *4*, 506–513, doi:10.1038/ngeo1194.

Joughin, I., and L. Padman (2003), Melting and freezing beneath Filchner-Ronne Ice Shelf, Antarctica, *Geophysical Research Letters*, *30*(9), 1477, doi:10.1029/2003GL016941.

Khazendar, A., M. P. Schodlok, I. G. Fenty, S. R. M. Ligtenberg, E. J. Rignot, and M. R. van den Broeke (2013), Observed thinning of Totten Glacier is linked to coastal polynya variability, *Nature Communications*, *4*, 2857, doi:10.1038/ncomms3857.

Kim, S., and A. Stössel (1998), On the representation of the Southern Ocean water masses in an ocean climate model, *Journal of Geophysical Research*, *103*(C11), 24,891–24,906, doi:10.1029/98JC02413.

Kjellsson, J., P. R. Holland, G. J. Marshall, P. Mathiot, Y. Aksenov, A. C. Coward, S. Bacon, A. P. Megann, and J. K. Ridley (2015), Model sensitivity of the Weddell and Ross seas, Antarctica, to vertical mixing and freshwater forcing, *Ocean Modelling*, *94*, 141–152, doi:10.1016/j.ocemod.2015.08.003.

Koltermann, K. P., V. V. Gouretski, and K. Jancke (2011), Hydrographic Atlas of the World Ocean Circulation Experiment (WOCE). Volume 3: Atlantic Ocean (eds. M. Sparrow, P. Chapman and J. Gould), *Tech. rep.*, International WOCE Project Office, Southampton, UK.

Kurtz, N. T., and T. Markus (2012), Satellite observations of Antarctic sea ice thickness and volume, *Journal of Geophysical Research*, *117*, C08025, doi:10.1029/2012JC008141.

Kusahara, K., and H. Hasumi (2014), Pathways of basal meltwater from Antarctic ice shelves: A model study, *Journal of Geophysical Research: Oceans*, *119*, 5690–5704, doi:10.1002/2014JC009915.

Kusahara, K., H. Hasumi, and T. Tamura (2010), Modeling sea ice production and dense shelf water formation in coastal polynyas around East Antarctica, *Journal of Geophysical Research*, *115*, C10006, doi:10.1029/2010JC006133.

Kusahara, K., G. D. Williams, R. A. Massom, P. Reid, and H. Hasumi (2017), Roles of wind stress and thermodynamic forcing in recent trends in Antarctic sea ice and Southern Ocean SST: An ocean-sea ice model study, *Global and Planetary Change*, *158*, 103–118, doi:10.1016/j.gloplacha.2017.09.012.

Kwok, R., and G. F. Cunningham (2008), ICESat over Arctic sea ice: Estimation of snow depth and ice thickness, *Journal of Geophysical Research*, *113*, C08010, doi:10.1029/2008JC004753.

Langhorne, P. J., K. G. Hughes, A. J. Gough, I. J. Smith, M. J. M. Williams, N. J. Robinson, C. L. Stevens, W. Rack, D. Price, G. H. Leonard, A. R. Mahoney, C. Haas, and T. G. Haskell (2015), Observed platelet ice distributions in Antarctic sea ice: An index for ocean-ice shelf heat flux, *Geophysical Research Letters*, *42*, 5442–5451, doi:10.1002/2015GL064508.

Langley, K. A., J. Kohler, A. Sinisalo, M. J. Øyan, S. E. Hamran, T. Hattermann, K. Matsuoka, O. A. Nøst, and E. Isaksson (2014), Low melt rates with seasonal variability at the base of Fimbul Ice Shelf, East Antarctica, revealed by in situ interferometric radar measurements, *Geophysical Research Letters*, *41*, 8138–8146, doi:10.1002/2014GL061782.

Large, W. G., J. C. McWilliams, and S. C. Doney (1994), Oceanic Vertical Mixing - a Review and a Model with a Nonlocal Boundary-Layer Parameterization, *Reviews of Geophysics*, *32*(4), 363–403, doi:10.1029/94rg01872.

Larson, J., R. Jacob, and E. Ong (2005), The Model Coupling Toolkit: A New Fortran90 Toolkit for Building Multiphysics Parallel Coupled Models, *International Journal of High Performance Computing Applications*, *19*(3), 277–292, doi:10.1177/1094342005056115.

Lemarié, F., J. Kurian, A. F. Shchepetkin, M. Jeroen Molemaker, F. Colas, and J. C. McWilliams (2012), Are there inescapable issues prohibiting the use of terrain-following coordinates in climate models?, *Ocean Modelling*, *42*, 57–79, doi:10.1016/j.ocemod.2011.11.007.

Lenaerts, J. T. M., M. R. van den Broeke, W. J. van de Berg, E. van Meijgaard, and P. K. Munneke (2012), A new, high-resolution surface mass balance map of Antarctica (1979-2010) based on regional atmospheric climate modeling, *Geophysical Research Letters*, *39*, L04501, doi:10.1029/2011GL050713.

Leonard, B. P. (1993), Positivity-Preserving Numerical Schemes for Multidimensional Advection, *Tech. rep.*, NASA.

Leonard, B. P., and S. Mokhtari (1990), ULTRA-SHARP Nonoscillatory Convection Schemes for High-Speed Steady Multidimensional Flow, *Tech. rep.*, NASA.

Lewis, E. L., and R. G. Perkin (1986), Ice pumps and their rates, *Journal of Geophysical Research*, *91*(C10), 11,756–11,762, doi:10.1029/JC091iC10p11756.

Lilly, D. K. (1965), On the Computational Stability of Numerical Solutions of Time-Dependent Non-Linear Geophysical Fluid Dynamics Problems, *Monthly Weather Review*, *93*(1), 11–25, doi:10.1175/1520-0493(1965)093⟨0011:OTCSON⟩2.3.CO;2.

Lipscomb, W. H., and E. C. Hunke (2004), Modeling Sea Ice Transport Using Incremental Remapping, *Monthly Weather Review*, *132*, 1341–1354, doi:10.1175/1520-0493(2004)132⟨1341:MSITUI⟩2.0.CO;2.

Lipscomb, W. H., E. C. Hunke, W. Maslowski, and J. Jakacki (2007), Ridging, strength, and stability in high-resolution sea ice models, *Journal of Geophysical Research*, *112*, C03S91, doi:10.1029/2005JC003355.

Makinson, K., P. R. Holland, A. Jenkins, K. W. Nicholls, and D. M. Holland (2011), Influence of tides on melting and freezing beneath Filchner-Ronne Ice Shelf, Antarctica, *Geophysical Research Letters*, *38*, L06601, doi:10.1029/2010GL046462.

Marchesiello, P., J. C. McWilliams, and A. F. Shchepetkin (2001), Open boundary conditions for long-term integration of regional oceanic models, *Ocean Modelling*, *3*, 1–20, doi:10.1016/S1463-5003(00)00013-5.

Marchesiello, P., L. Debreu, and X. Couvelard (2009), Spurious diapycnal mixing in terrain-following coordinate models: The problem and a solution, *Ocean Modelling*, *26*, 156–169, doi:10.1016/j.ocemod.2008.09.004.

Martin, T., and A. Adcroft (2010), Parameterizing the fresh-water flux from land ice to ocean with interactive icebergs in a coupled climate model, *Ocean Modelling*, *34*, 111–124, doi:10.1016/j.ocemod.2010.05.001.

Martinson, D. G., and D. C. McKee (2012), Transport of warm Upper Circumpolar Deep Water onto the Western Antarctic Peninsula Continental Shelf, *Ocean Science*, *8*, 433–442, doi:10.5194/os-8-433-2012.

Mathiot, P., B. Barnier, H. Gallée, J. M. Molines, J. L. Sommer, M. Juza, and T. Penduff (2010), Introducing katabatic winds in global ERA40 fields to simulate their impacts on the Southern Ocean and sea-ice, *Ocean Modelling*, *35*, 146–160, doi:10.1016/j.ocemod.2010.07.001.

Mathiot, P., A. Jenkins, C. Harris, and G. Madec (2017), Explicit representation and parametrised impacts of under ice shelf seas in the z* coordinate ocean model NEMO 3.6, *Geoscientific Model Development*, *10*, 2849–2874, doi:10.5194/gmd-10-2849-2017.

Mazloff, M. R., P. Heimbach, and C. Wunsch (2010), An Eddy-Permitting Southern Ocean State Estimate, *Journal of Physical Oceanography*, *40*, 880–899, doi:10.1175/2009JPO4236.1.

McPhail, S. D., M. E. Furlong, M. Pebody, J. R. Perrett, P. Stevenson, A. T. Webb, and D. White (2009), Exploring beneath the PIG Ice Shelf with the Autosub3 AUV, in *OCEANS '09 IEEE Bremen: Balancing Technology with Future Needs*, p. 6, IEEE, Piscataway, USA, doi:10.1109/OCEANSE.2009.5278170.

McPhee, M. G., G. A. Maykut, and J. H. Morison (1987), Dynamics and thermodynamics of the ice/upper ocean system in the marginal ice zone of the Greenland Sea, *Journal of Geophysical Research*, *92*(C7), 7017–7031, doi:10.1029/JC092iC07p07017.

Meehl, G. A., G. J. Boer, C. Covey, M. Latif, and R. J. Stouffer (2000), The Coupled Model Intercomparison Project (CMIP), *Bulletin of the American Meteorological Society*, *81*(2), 313–318, doi:10.1175/1520-0477(2000)081⟨0313:TCMIPC⟩2.3.CO;2.

Meier, W., F. Fetterrer, M. Savoie, S. Mallory, R. Duerr, and J. Stroeve (2013), NOAA/NSIDC Climate Data Record of Passive Microwave Sea Ice Concentration, Version 2, doi:10.7265/N55M63M1.

Menemenlis, D., J.-M. Campin, P. Heimbach, C. Hill, T. Lee, A. T. Nguyen, M. P. Schodlok, and H. Zhang (2008), ECCO2: High resolution global ocean and sea ice data synthesis, *Mercator Ocean Quarterly Newsletter*, *31*, 13–21.

Mengel, M., and A. Levermann (2014), Ice plug prevents irreversible discharge from East Antarctica, *Nature Climate Change*, *4*, 451–455, doi:10.1038/nclimate2226.

Merino, N., N. C. Jourdain, J. Le Sommer, H. Goosse, P. Mathiot, and G. Durand (2018), Impact of increasing antarctic glacial freshwater release on regional sea-ice cover in the Southern Ocean, *Ocean Modelling*, *121*, 76–89, doi:10.1016/j.ocemod.2017.11.009.

Miller, K. G., J. D. Wright, J. V. Browning, A. Kulpecz, M. Kominz, T. R. Naish, B. S. Cramer, Y. Rosenthal, W. R. Peltier, and S. Sosdian (2012), High tide of the warm Pliocene: Implications of global sea level for Antarctic deglaciation, *Geology*, *40*(5), 407–410, doi:10.1130/G32869.1.

Moffat, C., B. Owens, and R. C. Beardsley (2009), On the characteristics of Circumpolar Deep Water intrusions to the west Antarctic Peninsula Continental Shelf, *Journal of Geophysical Research*, *114*, C05017, doi:10.1029/2008JC004955.

Mueller, R. D., L. Padman, M. S. Dinniman, S. Y. Erofeeva, H. A. Fricker, and M. A. King (2012), Impact of tide-topography interactions on basal melting of Larsen C Ice Shelf, Antarctica, *Journal of Geophysical Research: Oceans*, *117*, C05005, doi:10.1029/2011JC007263.

Mueller, R. D., T. Hattermann, S. L. Howard, and L. Padman (2018), Tidal influences on a future evolution of the Filchner-Ronne Ice Shelf cavity in the Weddell Sea, Antarctica, *The Cryosphere*, *12*, 453–476, doi:10.5194/tc-12-453-2018.

Müller, M., H. Haak, J. H. Jungclaus, J. Sündermann, and M. Thomas (2010), The effect of ocean tides on a climate model simulation, *Ocean Modelling*, *35*, 304–313, doi:10.1016/j.ocemod.2010.09.001.

Nakayama, Y., R. Timmermann, M. Schröder, and H. H. Hellmer (2014), On the difficulty of modeling Circumpolar Deep Water intrusions onto the Amundsen Sea continental shelf, *Ocean Modelling*, *84*, 26–34, doi:10.1016/j.ocemod.2014.09.007.

Naud, C. M., J. F. Booth, and A. D. Del Genio (2014), Evaluation of ERA-Interim and MERRA cloudiness in the Southern Ocean, *Journal of Climate*, *27*, 2109–2124, doi:10.1175/JCLI-D-13-00432.1.

Naughten, K. A., B. K. Galton-Fenzi, K. J. Meissner, M. H. England, G. B. Brassington, F. Colberg, T. Hattermann, and J. B. Debernard (2017), Spurious sea ice formation caused by oscillatory ocean tracer advection schemes, *Ocean Modelling*, *116*, 108–117, doi:10.1016/j.ocemod.2017.06.010.

Naughten, K. A., K. J. Meissner, B. K. Galton-Fenzi, M. H. England, R. Timmermann, H. H. Hellmer, T. Hattermann, and J. B. Debernard (2018), Intercomparison of Antarctic ice-shelf, ocean, and sea-ice interactions simulated by MetROMS-iceshelf and FESOM 1.4, *Geoscientific Model Development*, *11*, 1257–1292, doi:10.5194/gmd-11-1257-2018.

Nicholls, K. W., and M. R. Johnson (2001), Oceanographic conditions south of Berkner Island, beneath Filchner-Ronne Ice Shelf, Antarctica, *Journal of Geophysical Research*, *106*(C6), 11,481–11,492, doi:10.1029/2000JC000350.

Nicholls, K. W., and S. Østerhus (2004), Interannual variability and ventilation timescales in the ocean cavity beneath Filchner-Ronne Ice Shelf, Antarctica, *Journal of Geophysical Research*, *109*, C04014, doi:10.1029/2003JC002149.

Nicholls, K. W., K. Makinson, and S. Østerhus (2004), Circulation and water masses beneath the northern Ronne Ice Shelf, Antarctica, *Journal of Geophysical Research*, *109*, C12017, doi:10.1029/2004JC002302.

Nicholls, K. W., E. P. Abrahamsen, J. J. H. Buck, P. A. Dodd, C. Goldblatt, G. Griffiths, K. J. Heywood, N. E. Hughes, A. Kaletzky, G. F. Lane-Serff, S. D. McPhail, N. W. Millard, K. I. C. Oliver, J. R. Perrett, M. R. Price, C. J. Pudsey, K. Saw, K. Stansfield, M. J. Stott, P. Wadhams, A. T. Webb, and J. P. Wilkinson (2006), Measurements beneath an Antarctic ice shelf using an autonomous underwater vehicle, *Geophysical Research Letters*, *33*, L08612, doi:10.1029/2006GL025998.

Nicholls, K. W., S. Østerhus, K. Makinson, T. Gammelsrød, and E. Fahrbach (2009), Ice-ocean processes over the continental shelf of the southern Weddell Sea, Antarctica: a review, *Reviews of Geophysics*, *47*, 1–23, doi:10.1029/2007RG000250.

Nicolas, J. P., and D. H. Bromwich (2011), Precipitation Changes in High Southern Latitudes from Global Reanalyses: A Cautionary Tale, *Surveys in Geophysics*, *32*, 475–494, doi:10.1007/s10712-011-9114-6.

Norris, S. E. (2000), A Parallel Navier Stokes Solver for Natural Convection and Free Surface Flow, Ph.D. thesis, University of Sydney.

Ohshima, K. I., Y. Fukamachi, G. D. Williams, S. Nihashi, F. Roquet, Y. Kitade, T. Tamura, D. Hirano, L. Herraiz-Borreguero, I. C. Field, M. A. Hindell, S. Aoki, and M. Wakatsuchi (2013), Antarctic Bottom Water production by intense sea-ice formation in the Cape Darnley polynya, *Nature Geoscience*, *6*, 235–240, doi:10.1038/ngeo1738.

O'Leary, M. J., P. J. Hearty, W. G. Thompson, M. E. Raymo, J. X. Mitrovica, J. M. Webster, and M. J. O'Leary (2013), Ice sheet collapse following a prolonged period of stable sea level during the last interglacial, *Nature Geoscience*, *6*, 796–800, doi:10.1038/ngeo1890.

Oreskes, N., K. Shrader-Frechette, and K. Belitz (1994), Verification, Validation, and Confirmation of Numerical Models in the Earth Sciences, *Science*, *263*, 641–646, doi:10.1126/science.263.5147.641.

Pacanowski, R. C., and S. G. H. Philander (1981), Parameterization of Vertical Mixing in Numerical Models of Tropical Oceans, *Journal of Physical Oceanography*, *11*, 1443–1451, doi:10.1175/1520-0485(1981)011⟨1443:POVMIN⟩2.0.CO;2.

Padman, L., S. Y. Erofeeva, H. A. Fricker, and S. L. Howard (2008), CATS2008a_opt: Circum-Antarctic Tidal Simulation, Inverse Model Version 2008a.

Padman, L., S. L. Howard, A. H. Orsi, and R. D. Muench (2009), Tides of the northwestern Ross Sea and their impact on dense outflows of Antarctic Bottom Water, *Deep Sea Research II*, *56*, 818–834, doi:10.1016/j.dsr2.2008.10.026.

Paolo, F. S., H. A. Fricker, and L. Padman (2015), Volume loss from Antarctic ice shelves is accelerating, *Science*, *348*(6232), 327–331, doi:10.1126/science.aaa0940.

Parkinson, C. L., and W. M. Washington (1979), A large-scale numerical model of sea ice, *Journal of Geophysical Research*, *84*(C1), 311–337, doi:10.1029/JC084iC01p00311.

Pellichero, V., J.-B. Sallée, S. Schmidtko, F. Roquet, and J.-B. Charrassin (2017), The ocean mixed layer under Southern Ocean sea-ice: Seasonal cycle and forcing, *Journal of Geophysical Research: Oceans*, *122*, 1608–1633, doi:10.1002/2016JC011970.

Petty, A. A., D. L. Feltham, and P. R. Holland (2013), Impact of Atmospheric Forcing on Antarctic Continental Shelf Water Masses, *Journal of Physical Oceanography*, *43*, 920–940, doi:10.1175/JPO-D-12-0172.1.

Petty, A. A., P. R. Holland, and D. L. Feltham (2014), Sea ice and the ocean mixed layer over the Antarctic shelf seas, *The Cryosphere*, *8*, 761–783, doi:10.5194/tc-8-761-2014.

Pietrzak, J. (1998), The Use of TVD Limiters for Forward-in-Time Upstream-Biased Advection Schemes in Ocean Modeling, *Monthly Weather Review*, *126*, 812–830, doi:10.1175/1520-0493(1998)126⟨0812:TUOTLF⟩2.0.CO;2.

Pipitone, J., and S. Easterbrook (2012), Assessing climate model software quality: A defect density analysis of three models, *Geoscientific Model Development*, *5*, 1009–1022, doi:10.5194/gmd-5-1009-2012.

Pritchard, H. D., S. R. M. Ligtenberg, H. A. Fricker, D. G. Vaughan, M. R. van den Broeke, and L. Padman (2012), Antarctic ice-sheet loss driven by basal melting of ice shelves, *Nature*, *484*, 502–505, doi:10.1038/nature10968.

Rack, W., and H. Rott (2004), Pattern of retreat and disintegration of the Larsen B Ice Shelf, *Annals of Glaciology*, *39*, 505–510, doi:10.3189/172756404781814005.

Rasch, P. J. (1994), Conservative Shape-Preserving Two-Dimensional Transport on a Spherical Reduced Grid, *Monthly Weather Review*, *122*, 1337–1350, doi:10.1175/1520-0493(1994)122⟨1337:CSPTDT⟩2.0.CO;2.

Raymo, M. E., and J. X. Mitrovica (2012), Collapse of polar ice sheets during the stage 11 interglacial, *Nature*, *483*, 453–456, doi:10.1038/nature10891.

Reddy, T. E., D. M. Holland, and K. R. Arrigo (2010), Ross ice shelf cavity circulation, residence time, and melting: Results from a model of oceanic chlorofluorocarbons, *Continental Shelf Research*, *30*, 733–742, doi:10.1016/j.csr.2010.01.007.

Rignot, E. J., G. Casassa, P. Gogineni, W. Krabill, A. Rivera, and R. Thomas (2004), Accelerated ice discharge from the Antarctic Peninsula following the collapse of Larsen B ice shelf, *Geophysical Research Letters*, *31*, L18401, doi:10.1029/2004GL020697.

Rignot, E. J., I. Velicogna, M. R. van den Broeke, A. Monaghan, and J. T. M. Lenaerts (2011), Acceleration of the contribution of the Greenland and Antarctic ice sheets to sea level rise, *Geophysical Research Letters*, *38*, L05503, doi:10.1029/2011GL046583.

Rignot, E. J., S. S. Jacobs, J. Mouginot, and B. Scheuchl (2013), Ice-Shelf Melting Around Antarctica, *Science*, *341*, 266–270, doi:10.1126/science.1235798.

Rignot, E. J., J. Mouginot, M. Morlighem, H. Seroussi, and B. Scheuchl (2014), Widespread, rapid grounding line retreat of Pine Island, Thwaites, Smith, and Kohler glaciers, West Antarctica, from 1992 to 2011, *Geophysical Research Letters*, *41*, 3502–3509, doi:10.1002/2014GL060140.

Rintoul, S. R., K. Speer, M. Sparrow, M. P. Meredith, E. Hofmann, E. Fahrbach, C. Summerhayes, A. P. Worby, M. H. England, R. G. Bellerby, S. Speich, D. P. Costa, J. Hall, M. A. Hindell, G. Hosie, K. Stansfield, Y. Fukamachi, T. de Bruin, A. Naveira Garabato, K. Alverson, V. Ryabinin, H. C. Shin, and S. Gladyshev (2010), Southern Ocean Observing System (SOOS): Rationale and strategy for sustained observations of the Southern Ocean, in *Proceedings of OceanObs'09: Sustained Ocean Observations and Information for Society*, vol. 2, edited by J. Hall, D. E. Harrison, and D. Stammer, ESA Publication WPP-306, Venice, doi:10.5270/OceanObs09.cwp.74.

Rintoul, S. R., A. Silvano, B. Pena-Molino, E. van Wijk, M. Rosenberg, J. S. Greenbaum, and D. D. Blankenship (2016), Ocean heat drives rapid basal melt of the Totten Ice Shelf, *Science Advances*, *2*, e1601610, doi:10.1126/sciadv.1601610.

Roberts, A., A. Craig, W. Maslowski, R. Osinski, A. Duvivier, M. Hughes, B. Nijssen, J. Cassano, and M. Brunke (2015), Simulating transient ice-ocean Ekman transport in the Regional Arctic System Model and Community Earth System Model, *Annals of Glaciology*, *56*(69), 211–228, doi:10.3189/2015AoG69A760.

Robertson, R., L. Padman, and G. D. Egbert (1998), Tides in the Weddell Sea, in *Ocean, Ice, and Atmosphere: Interactions at the Antarctic Continental Margin*,

edited by S. S. Jacobs and R. F. Weiss, pp. 341–369, American Geophysical Union, Washington, D.C., doi:10.1029/AR075p0341.

Roemmich, D., G. Johnson, S. Riser, R. Davis, J. Gilson, W. Owens, S. Garzoli, C. Schmid, and M. Ignaszewski (2009), The Argo Program: Observing the Global Ocean with Profiling Floats, *Oceanography*, *22*(2), 34–43, doi:10.5670/oceanog.2009.36.

Roquet, F., C. Wunsch, G. Forget, P. Heimbach, C. Guinet, G. Reverdin, J.-B. Charrassin, F. Bailleul, D. P. Costa, L. A. Huckstadt, K. T. Goetz, K. M. Kovacs, C. Lydersen, M. Biuw, O. A. Nøst, H. Bornemann, J. Ploetz, M. N. Bester, T. McIntyre, M. C. Muelbert, M. A. Hindell, C. R. McMahon, G. D. Williams, R. Harcourt, I. C. Field, L. Chafik, K. W. Nicholls, L. Boehme, and M. A. Fedak (2013), Estimates of the Southern Ocean general circulation improved by animal-borne instruments, *Geophysical Research Letters*, *40*, 6176–6180, doi:10.1002/2013GL058304.

Rothrock, D. A. (1975), The Energetics of the Plastic Deformation of Pack Ice by Ridging, *Journal of Geophysical Research*, *80*(33), 4514–4519.

Rott, H., P. Skvarca, and T. Nagler (1996), Rapid Collapse of Northern Larsen Ice Shelf, Antarctica, *Science*, *271*, 788–792, doi:10.1126/science.271.5250.788.

Russell, J. L., R. J. Stouffer, and K. W. Dixon (2006), Intercomparison of the Southern Ocean circulations in IPCC coupled model control simulations, *Journal of Climate*, *19*, 4560–4575, doi:10.1175/JCLI3869.1.

Sallée, J.-B., E. Shuckburgh, N. Bruneau, A. J. S. Meijers, T. J. Bracegirdle, Z. Wang, and T. Roy (2013a), Assessment of Southern Ocean water mass circulation and characteristics in CMIP5 models: Historical bias and forcing response, *Journal of Geophysical Research: Oceans*, *118*, 1830–1844, doi:10.1002/jgrc.20135.

Sallée, J.-B., E. Shuckburgh, N. Bruneau, A. J. S. Meijers, T. J. Bracegirdle, and Z. Wang (2013b), Assessment of Southern Ocean mixed-layer depths in CMIP5 models: Historical bias and forcing response, *Journal of Geophysical Research: Oceans*, *118*, 1845–1862, doi:10.1002/jgrc.20157.

Sanford, T., P. C. Frumhoff, A. Luers, and J. Gulledge (2014), The climate policy narrative for a dangerously warming world, *Nature Climate Change*, *4*, 164–166, doi:10.1038/nclimate2148.

Scambos, T. A., J. A. Bohlander, C. A. Shuman, and P. Skvarca (2004), Glacier acceleration and thinning after ice shelf collapse in the Larsen B embayment, Antarctica, *Geophysical Research Letters*, *31*, L18402, doi:10.1029/2004GL020670.

Schmidtko, S., K. J. Heywood, A. F. Thompson, and S. Aoki (2014), Multidecadal warming of Antarctic waters, *Science*, *346*(6214), 1227–1232, doi:10.1126/science.1256117.

Semtner, A. J. (1976), A Model for the Thermodynamic Growth of Sea Ice in Numerical Investigations of Climate, *Journal of Physical Oceanography*, *6*, 379–389, doi:10.1175/1520-0485(1976)006⟨0379:AMFTTG⟩2.0.CO;2.

Sen Gupta, A., A. Santoso, A. S. Taschetto, C. C. Ummenhofer, J. Trevena, and M. H. England (2009), Projected changes to the Southern Hemisphere ocean and sea ice in the IPCC AR4 climate models, *Journal of Climate*, *22*, 3047–3078, doi:10.1175/2008JCLI2827.1.

Shchepetkin, A. F., and J. C. McWilliams (1998), Quasi-Monotone Advection Schemes Based on Explicit Locally Adaptive Dissipation, *Monthly Weather Review*, *126*(6), 1541–1580, doi:10.1175/1520-0493(1998)126⟨1541:QMASBO⟩2.0.CO;2.

Shchepetkin, A. F., and J. C. McWilliams (2003), A method for computing horizontal pressure-gradient force in an oceanic model with a nonaligned vertical coordinate, *Journal of Geophysical Research*, *108*(C3), 3090, doi:10.1029/2001JC001047.

Shchepetkin, A. F., and J. C. McWilliams (2005), The regional oceanic modeling system (ROMS): A split-explicit, free-surface, topography-following-coordinate oceanic model, *Ocean Modelling*, *9*, 347–404, doi:10.1016/j.ocemod.2004.08.002.

Shepherd, A. P., E. R. Ivins, A. Geruo, V. R. Barletta, M. J. Bentley, S. Bettadpur, K. H. Briggs, D. H. Bromwich, R. Forsberg, N. Galin, M. Horwath, S. S. Jacobs, I. Joughin, M. A. King, J. T. M. Lenaerts, J. Li, S. R. M. Ligtenberg, A. Luckman, S. B. Luthcke, M. McMillan, R. Meister, G. A. Milne, J. Mouginot, A. Muir, J. P. Nicolas, J. Paden, A. J. Payne, H. D. Pritchard, E. J. Rignot, H. Rott, L. Sandberg Sørensen, T. A. Scambos, B. Scheuchl, E. J. O. Schrama, B. Smith, A. V. Sundal, J. H. van Angelen, W. J. van de Berg, M. R. van den Broeke, D. G. Vaughan, I. Velicogna, J. Wahr, P. L. Whitehouse, D. J. Wingham, D. Yi, D. A. Young, and H. J. Zwally (2012), A Reconciled Estimate of Ice-Sheet Mass Balance, *Science*, *338*, 1183–1189, doi:10.1126/science.1228102.

Silvano, A., S. R. Rintoul, B. Pena-Molino, and G. D. Williams (2017), Distribution of water masses and meltwater on the continental shelf near the Totten and Moscow University ice shelves, *Journal of Geophysical Research: Oceans*, *122*, 2050–2068, doi:10.1002/2016JC012115.

Smagorinsky, J. (1963), General Circulation Experiments With the Primitive Equations I. The Basic Experiment, *Monthly Weather Review*, *91*(3), 99–164, doi:10.1175/1520-0493(1963)091⟨0099:GCEWTP⟩2.3.CO;2.

Smagorinsky, J. (1993), Some historical remarks on the use of non-linear viscosities, in *Large Eddy Simulation of Complex Engineering and Geophysical Flows*, edited by B. Galperin and S. Orszag, pp. 3–36, Cambridge University Press, Cambridge.

Smedsrud, L. H., and A. Jenkins (2004), Frazil ice formation in an ice shelf water plume, *Journal of Geophysical Research*, *109*, C03025, doi:10.1029/2003JC001851.

Smith, J. A., T. J. Andersen, M. Shortt, A. M. Gaffney, M. Truffer, T. P. Stanton, R. Bindschadler, P. Dutrieux, A. Jenkins, C. D. Hillenbrand, W. Ehrmann, H. F. J. Corr, N. Farley, S. Crowhurst, and D. G. Vaughan (2017), Sub-ice-shelf sediments record history of twentieth-century retreat of Pine Island Glacier, *Nature*, *541*, 77–80, doi:10.1038/nature20136.

Smith, R., P. Jones, B. P. Briegleb, F. O. Bryan, G. Danabasoglu, J. Dennis, J. K. Dukowicz, C. Eden, B. Fox-Kemper, P. R. Gent, M. W. Hecht, S. Jayne, M. Jochum, W. G. Large, K. Lindsay, M. E. Maltrud, N. Norton, S. Peacock, M. Vertenstein, and S. G. Yeager (2010), The Parallel Ocean Program (POP) reference manual: Ocean component of the Community Climate System Model (CCSM), *Tech. rep.*, Los Alamos National Laboratory.

Smolarkiewicz, P. K. (1984), A Fully Multidimensional Positive Definite Advection Transport Algorithm with Small Implicit Diffusion, *Journal of Computational Physics*, *54*, 325–362, doi:10.1016/0021-9991(84)90121-9.

Spence, P., S. M. Griffies, M. H. England, A. M. Hogg, O. A. Saenko, and N. C. Jourdain (2014), Rapid subsurface warming and circulation changes of Antarctic coastal waters by poleward shifting winds, *Geophysical Research Letters*, *41*, 4601–4610, doi:10.1002/2014GL060613.

Spence, P., R. M. Holmes, A. M. Hogg, S. M. Griffies, K. D. Stewart, and M. H. England (2017), Localized rapid warming of West Antarctic subsurface waters by remote winds, *Nature Climate Change*, *7*, 595–603, doi:10.1038/nclimate3335.

St-Laurent, P., J. M. Klinck, and M. S. Dinniman (2013), On the Role of Coastal Troughs in the Circulation of Warm Circumpolar Deep Water on Antarctic Shelves, *Journal of Physical Oceanography*, *43*, 51–64, doi:10.1175/JPO-D-11-0237.1.

Steig, E. J., Q. Ding, D. S. Battisti, and A. Jenkins (2012), Tropical forcing of Circumpolar Deep Water Inflow and outlet glacier thinning in the Amundsen Sea Embayment, West Antarctica, *Annals of Glaciology*, *53*, 19–28, doi:10.3189/2012AoG60A110.

Stewart, A. L., and A. F. Thompson (2015), Eddy-mediated transport of warm Circumpolar Deep Water across the Antarctic Shelf Break, *Geophysical Research Letters*, *42*, 432–440, doi:10.1002/2014GL062281.

Stewart, A. L., A. Klocker, and D. Menemenlis (2018), Circum-Antarctic Shoreward Heat Transport Derived From an Eddy- and Tide-Resolving Simulation, *Geophysical Research Letters*, *45*, 1–12, doi:10.1002/2017GL075677.

Sun, S., S. L. Cornford, D. E. Gwyther, R. M. Gladstone, B. K. Galton-Fenzi, L. Zhao, and J. C. Moore (2016), Impact of ocean forcing on the Aurora Basin in the 21st and 22nd centuries, *Annals of Glaciology*, *57*(73), 79–86, doi:10.1017/aog.2016.27.

Swart, N. C., and J. C. Fyfe (2012), Observed and simulated changes in the Southern Hemisphere surface westerly wind-stress, *Geophysical Research Letters*, *39*, L16711, doi:10.1029/2012GL052810.

Talley, L. D. (2007), Hydrographic Atlas of the World Ocean Circulation Experiment (WOCE). Volume 2: Pacific Ocean (eds. M. Sparrow, P. Chapman and J. Gould), *Tech. rep.*, International WOCE Project Office, Southampton, UK.

Tamura, T., K. I. Ohshima, and S. Nihashi (2008), Mapping of sea ice production for Antarctic coastal polynyas, *Geophysical Research Letters*, *35*, L07606, doi:10.1029/2007GL032903.

Tamura, T., K. I. Ohshima, A. D. Fraser, and G. D. Williams (2016), Sea ice production variability in Antarctic coastal polynyas, *Journal of Geophysical Research: Oceans*, *121*, 2967–2979, doi:10.1002/2015JC011537.

Taylor, K. E., R. J. Stouffer, and G. A. Meehl (2012), An overview of CMIP5 and the experiment design, *Bulletin of the American Meteorological Society*, *93*(4), 485–498, doi:10.1175/BAMS-D-11-00094.1.

Thoma, M., A. Jenkins, D. M. Holland, and S. S. Jacobs (2008), Modelling Circumpolar Deep Water intrusions on the Amundsen Sea continental shelf, Antarctica, *Geophysical Research Letters*, *35*, L18602, doi:10.1029/2008GL034939.

Thomas, M., J. Sündermann, and E. Maier-Reimer (2001), Consideration of ocean tides in an OGCM and impacts on subseasonal to decadal polar motion excitation, *Geophysical Research Letters*, *28*(12), 2457–2460, doi:10.1029/2000GL012234.

Timmermann, R., and A. Beckmann (2004), Parameterization of vertical mixing in the Weddell Sea, *Ocean Modelling*, *6*, 83–100, doi:10.1016/S1463-5003(02)00061-6.

Timmermann, R., and S. Goeller (2017), Response to Filchner-Ronne Ice Shelf cavity warming in a coupled ocean-ice sheet model. Part I: The ocean perspective, *Ocean Science*, *13*, 765–776, doi:10.5194/os-13-765-2017.

Timmermann, R., and H. H. Hellmer (2013), Southern Ocean warming and increased ice shelf basal melting in the twenty-first and twenty-second centuries based on coupled ice-ocean finite-element modelling, *Ocean Dynamics*, *63*, 1011–1026, doi:10.1007/s10236-013-0642-0.

Timmermann, R., and F. Kauker (2014), Reducing the uncertainty in projections of future ice shelf basal melting, in *EGU General Assembly*, Vienna, Austria.

Timmermann, R., S. Danilov, J. Schröter, C. Böning, D. Sidorenko, and K. Rollenhagen (2009), Ocean circulation and sea ice distribution in a finite element global sea ice-ocean model, *Ocean Modelling*, *27*, 114–129, doi:10.1016/j.ocemod.2008.10.009.

Timmermann, R., A. Le Brocq, T. Deen, E. Domack, P. Dutrieux, B. K. Galton-Fenzi, H. H. Hellmer, A. Humbert, D. Jansen, A. Jenkins, A. Lambrecht, K. Makinson, F. Niederjasper, F. O. Nitsche, O. A. Nøst, L. H. Smedsrud, and W. H. F. Smith (2010), A consistent dataset of Antarctic ice sheet topography, cavity geometry, and global bathymetry, *Earth System Science Data*, *2*, 261–273, doi:10.5194/essdd-3-231-2010.

Timmermann, R., Q. Wang, and H. H. Hellmer (2012), Ice-shelf basal melting in a global finite-element sea-ice/ice-shelf/ocean model, *Annals of Glaciology*, *53*(60), 303–314, doi:10.3189/2012AoG60A156.

Trenberth, K. E., and J. T. Fasullo (2010), Simulation of Present-Day and Twenty-First-Century Energy Budgets of the Southern Oceans, *Journal of Climate*, *23*, 440–454, doi:10.1175/2009JCLI3152.1.

Tsamados, M., D. L. Feltham, and A. V. Wilchinsky (2013), Impact of a new anisotropic rheology on simulations of Arctic sea ice, *Journal of Geophysical Research: Oceans*, *118*, 91–107, doi:10.1029/2012JC007990.

Turner, A. K., E. C. Hunke, and C. M. Bitz (2013a), Two modes of sea-ice gravity drainage: A parameterization for large-scale modeling, *Journal of Geophysical Research: Oceans*, *118*, 2279–2294, doi:10.1002/jgrc.20171.

Turner, J., T. J. Bracegirdle, T. Phillips, G. J. Marshall, and J. S. Hosking (2013b), An Initial Assessment of Antarctic Sea Ice Extent in the CMIP5 Models, *Journal of Climate*, *26*, 1473–1484, doi:10.1175/JCLI-D-12-00068.1.

Venables, H. J., and M. P. Meredith (2014), Feedbacks between ice cover, ocean stratification, and heat content in Ryder Bay, western Antarctic Peninsula, *Journal of Geophysical Research: Oceans*, *119*, 5323–5336, doi:10.1002/2013JC009669.

Wåhlin, A. K., X. Yuan, G. Björk, and C. Nohr (2010), Inflow of Warm Circumpolar Deep Water in the Central Amundsen Shelf, *Journal of Physical Oceanography*, *40*, 1427–1434, doi:10.1175/2010JPO4431.1.

Wang, Q., S. Danilov, and J. Schröter (2008), Finite element ocean circulation model based on triangular prismatic elements, with application in studying the effect of topography representation, *Journal of Geophysical Research*, *113*, C05015, doi:10.1029/2007JC004482.

Wang, Q., S. Danilov, H. H. Hellmer, D. Sidorenko, J. Schröter, and T. Jung (2013), Enhanced cross-shelf exchange by tides in the western Ross Sea, *Geophysical Research Letters*, *40*, 5735–5739, doi:10.1002/2013GL058207.

Wang, Q., S. Danilov, D. Sidorenko, R. Timmermann, C. Wekerle, X. Wang, T. Jung, and J. Schröter (2014), The Finite Element Sea Ice-Ocean Model (FESOM) v.1.4: formulation of an ocean general circulation model, *Geoscientific Model Development*, *7*, 663–693, doi:10.5194/gmd-7-663-2014.

Wen, J., Y. Wang, W. Wang, K. C. Jezek, H. Liu, and I. Allison (2010), Basal melting and freezing under the Amery Ice Shelf, East Antarctica, *Journal of Glaciology*, *56*(195), 81–90, doi:10.3189/002214310791190820.

Whitworth, T., A. H. Orsi, S.-J. Kim, W. D. Nowlin, and R. A. Locarnini (1998), Water masses and mixing near the Antarctic slope front, in *Ocean, Ice, and Atmosphere: Interactions at the Antarctic Continental Margin*, vol. 75, edited by S. S. Jacobs and R. F. Weiss, pp. 1–27, American Geophysical Union, Washington, D.C., doi:10.1029/AR075p0001.

Williams, K. D., A. Bodas-Salcedo, M. Déqué, S. Fermepin, B. Medeiros, M. Watanabe, C. Jakob, S. A. Klein, C. A. Senior, and D. L. Williamson (2013),

The Transpose-AMIP II Experiment and Its Application to the Understanding of Southern Ocean Cloud Biases in Climate Models, *Journal of Climate*, *26*, 3258–3274, doi:10.1175/JCLI-D-12-00429.1.

Worby, A. P., C. A. Geiger, M. J. Paget, M. L. van Woert, S. F. Ackley, and T. L. DeLiberty (2008), Thickness distribution of Antarctic sea ice, *Journal of Geophysical Research*, *113*, C05S92, doi:10.1029/2007JC004254.

Wu, H., and J. Zhu (2010), Advection scheme with 3rd high-order spatial interpolation at the middle temporal level and its application to saltwater intrusion in the Changjiang Estuary, *Ocean Modelling*, *33*, 33–51, doi:10.1016/j.ocemod.2009.12.001.

Wunsch, C., P. Heimbach, R. Ponte, and I. Fukumori (2009), The Global General Circulation of the Ocean Estimated by the ECCO-Consortium, *Oceanography*, *22*(2), 88–103, doi:10.5670/oceanog.2009.41.

Zwally, H. J., and M. B. Giovinetto (2011), Overview and Assessment of Antarctic Ice-Sheet Mass Balance Estimates: 1992-2009, *Surveys in Geophysics*, *32*, 351–376, doi:10.1007/s10712-011-9123-5.

Zweng, M. M., J. R. Reagan, J. I. Antonov, A. V. Mishonov, T. P. Boyer, H. E. Garcia, O. K. Baranova, D. R. Johnson, D. Seidov, and M. M. Bidlle (2013), World Ocean Atlas 2013, Volume 2: Salinity, *Tech. rep.*, NOAA.